Rubber Bearings For Precision Positioning Systems

by

Augusto E. Barton Martinelli
B.S., Mechanical Engineering (1999)
Pontificia Universidad Catolica del Peru

Submitted to the Department of Mechanical Engineering
in partial fulfillment of the requirements for the degree of

Master of Science in Mechanical Engineering

at the

MASSACHUSETTS INSTITUTE OF TECHNOLOGY
[September 2005]
August 2005

Author .....
Department of Mechanical Engineering
August 9, 2005

Certified by .....
David L. Trumper
Professor of Mechanical Engineering
Thesis Supervisor

Accepted by .....
Lallit Anand
Chairman, Department Committee on Graduate Students,
Department of Mechanical Engineering

Rubber Bearings For Precision Positioning Systems

by

Augusto E. Barton Martinelli

B.S., Mechanical Engineering (1999)

Pontificia Universidad Catolica del Peru

Submitted to the Department of Mechanical Engineering
on August 9, 2005, in partial fulfillment of the
requirements for the degree of
Master of Science in Mechanical Engineering

Abstract

In this thesis we investigate the use of thin rubber sheets or laminates of metal and rubber sheets as bearings in precision positioning systems. Such bearings have the potential to replace more conventional flexures fabricated for instance from metal. Rubber bearings also potentially have advantages in for example ease and low-cost of fabrication, overload robustness, and compact form.

To study the properties of these we have designed a test fixture. This fixture allows us to measure the shear and compression characteristics of these bearings in their static sense, as a function of frequency, and of various design parameters. The test fixture has been used to test several types of rubber material. The tests performed include compression and shear tests of rubber laminates' static stiffness, dynamic stiffness, preload effects, step response, hysteresis, fatigue tests, and manufactureability.

Different low-cost manufacturing methods of the rubber bearings have been suggested and preliminary tests have been done. The feasibility of these manufacturing methods has been confirmed, and the advantages and disadvantages of each identified.

On the basis of the experimental results a rotary precision positioning system utilizing a rotary laminated rubber bearing, was designed, fabricated and tested. The bearing of this device consists of multiple laminates of metal and rubber sheets packaged within a preload mechanism. This preload mechanism assures the bearing radial stiffness and compact form. It also assures a low cost alternative versus the use of conventional flexural bearings. Tests have shown that a steady-state angular travel of 2.5 mrad-pk can be accomplished and two types of controllers have been used to obtain a closed-loop bandwidth in the range of 1 kHz and 1.5 kHz.

Thesis Supervisor: David L. Trumper
Title: Professor of Mechanical Engineering

Acknowledgments

I will like to thank Professor David Trumper for his guidance and support as my research advisor these past two years. I have learned a lot from him and working in his lab.

I want to thank the National Science Foundation, and the Lawrence Livermore Laboratory for funding this research project.

My Precision Motion Control labmates Rick Montesanti, Xiadong Lu, Marten Byl, Katie Lilienkamp, Dave Otten, Aaron Mazzeo, Vijay Shilpiekandula, Dave Cuff, Larry Hawe, and Joe Cattell have given me a lot of help. It has been great working with all of you, thank you. Special thanks to Rick for being so willing to give me advise and support in every aspect including personal.

Thanks to Laura Zaganjori and Denise Moody for the all the administrative help, and for handling all the research related purchases in a professional manner.

Professor Samir Nayfeh helped me understand the dynamic properties of rubber, and gave me great literature references.

Mark Belanger helped me in the fabrication as well in the design of my parts to make them easier to manufacture. Thanks Mark.

My experience at MIT has been really challenging and interesting. I have learned a great deal here, and it has been great been here. But my greatest joy during my stay at MIT has been the birth of my twin son and daughter, Santiago and Paula. You have changed my life completely, making me now a happier person.

My family has been of great support for me, and I will like to give a special thanks

to my Mom, Dad, and sisters.

All of this work will not have been possible without the support and care of my wife Carolina, to whom I owe everything. I love you.

Contents

List of Figures

List of Tables

Chapter 1

Introduction

The main focus of this thesis is to gain a better understanding of the properties of laminate rubber bearings, and of their use in precision positioning systems. These laminate rubber bearings are a promising alternative to the use of conventional flexural bearings.

To study the properties of rubber bearings we have designed and fabricated the test fixture shown in 1-1. This fixture allows us to measure the shear and compression characteristics of bearings in their static sense, as a function of frequency, and of various design parameters. The test fixture has been used to test several types of rubber materials including Buna-N, Silicone, Neoprene, Viton, and Latex/Natural Rubber. The performed tests include compression and shear tests of rubber laminates' static stiffness, dynamic stiffness, preload effects, step response, hysteresis, and fatigue tests.

The results of these tests have shown the potential of rubber bearings as bearing for precision positioning systems due to the high compression to shear stiffness ratio that can be achieved. Based on the experimental results a rotary precision positioning system utilizing a rotary laminated rubber bearing was designed, fabricated and tested. A photograph of the device can be seen in Figure 1-2.

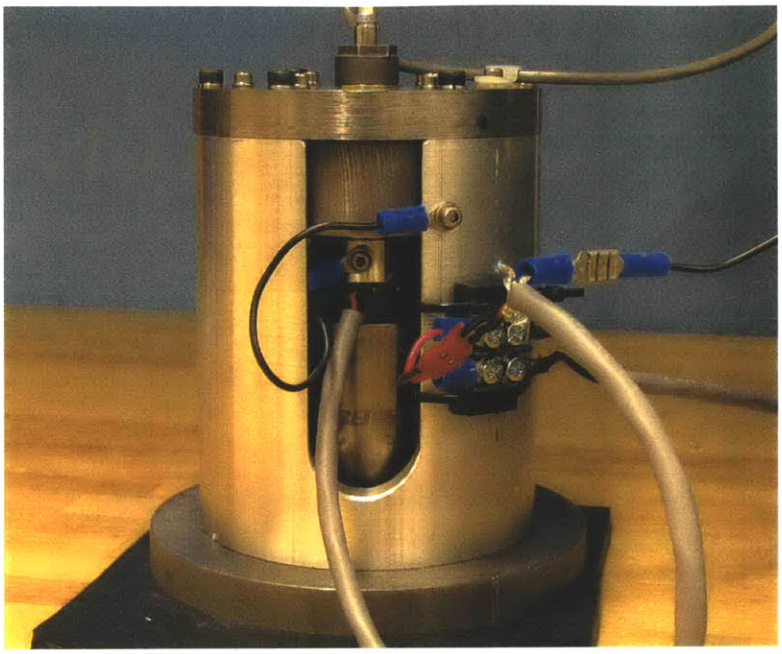

Figure 1-1: Photograph of Rubber Bearing Test Device.

1.1 Motivation for the Research

Current bearings used in precision machines include aerostatic, flexural, hydrostatic, magnetic, rolling element, and sliding contact. Laminate rubber bearings are an alternative bearing that can be designed and fabricated in a compact form, with low cost. Also the rubber bearings don't require additional supporting services like pressurized air or fluid.

Rubber bearings are already used in several engineering applications, including bridge bearings which have lasted for decades [9], and elastomeric dampers for helicopter blades, which have been widely studied [4] [8].

Previous work done by Rivin [17] has proved the potential of laminate rubber bearings as a bearing for precision machines, due to the high static compression to shear modulus ratio E_c/G. Rivin has shown that this ratio can reach values of $100 - 1000$ for ultra-thin rubber laminates for thicknesses between $0.8 - 0.1$ mm. As noted by

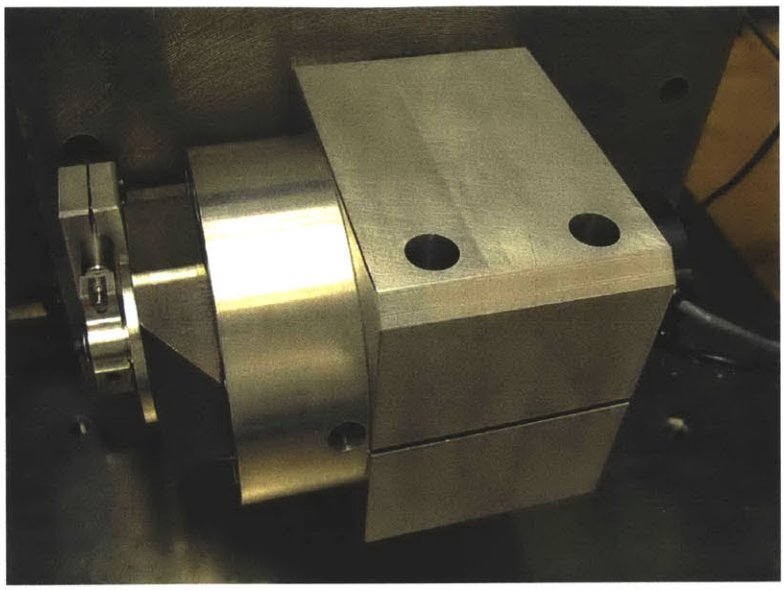

Figure 1-2: Photograph of Rotary Fast Tool Servo.

Rivin [17] the properties of rubber-metal laminates make them "ideally suited for many machine-design application" (p.447), including limited travel bearings. The tests performed by Rivin were all static, and part of his recommendations are that future researchers should address the many other issues involved in rubber bearing application, which is a motivation for this research.

1.2 Objectives of the Research

The objective of this thesis is to gain a better understanding of thin laminate rubber bearings behavior. These have been studied in their static sense by Eugene I. Rivin [17].

The use of rubber for damping has had a large amount of research, including their dynamic behavior [17] [11] [14]. All of these research efforts show how rubber stiffness increases with frequency, with dependence on the type of material and operating temperature. The type of dynamic tests available for elastomeric materials, including

rubber, are somehow limited to the purpose of obtaining information about their loss characteristics. These tests are generally performed at frequencies on the order of tens of Hertz.

The designed rubber test fixture shown in Figure 1-1, is used to perform static and dynamic tests of several rubber materials in compression and shear up to 5 kHz. The performed tests include: static stiffness, dynamic stiffness, step response, hysteresis, and fatigue tests.

Manufacturability tests are also performed to assure the rubber bearings low cost.

There is a wide variety of rubber materials which could be candidates for rubber bearings. To select an adequate material for the rubber bearing, several materials were selected and subjected to several tests to evaluate their applicability as a rubber bearing.

Based on the experience gained testing the rubber materials a rotary precision positioning system utilizing a rotary laminated rubber bearing was designed, fabricated, and tested. The designed precision rotary positioning system is a low cost alternative to a similar earlier device designed by Montesanti [13] which uses metal flexures. Montesanti's rotary precision positioning system consists of a Rotary Fast Tool Servo, used for diamond turning. It has a maximum stroke of 50 μm pk-pk at low frequencies and has demonstrated a 2.5 μm pk-pk stroke at 2 kHz while under operation.

1.3 Outline

Chapter 2 gives a literature review of relevant theory related to rubber properties. This serves to interpret the results obtained with the rubber test device as well as

understanding some issues involved in designing rubber bearings. Chapter 3 describes the design of the test fixture used to test rubber specimens in compression and shear. The design considerations for the design of the device are presented, as well as the most important calculations. Chapter 4 and 5 present the rubber test device compression and shear test results, respectively. Further the effects of different parameters in the compression and shear properties of the rubber bearings are analyzed. Chapter 6 makes further analysis of the properties rubber bearings. It also presents several manufacturing methods for the laminate rubber bearings, and different topologies of the linear and rotary bearings. Chapter 7 shows the design, assembly, and testing of a rotary Fast Tool Servo (or precision positioning system), using laminate rubber bearings. The design of the control system and all the related electronics is also presented here. Finally, in Chapter 8 we discuss the results of the rubber compression and shear tests, as well as the measured performance of the designed rotary fast tool servo. Also suggestions for future work are presented.

Chapter 2

Literature review

In order to design a precision machine using rubber bearings it is important to be able to predict their performance. The performance of rubber bearings depend on several variables including frequency, temperature, shape, strain levels and preload. Being able to quantify this dependence and understand its physical meaning is key. In this chapter relevant characteristics of viscoelastic materials (including rubber) behavior is presented.

2.1 Rubber compounding

In the selection of rubber materials for the use in rubber bearings one needs to understand how the properties of rubber can be modified to obtain the desired characteristics. Rubbers are part of a group called polymers, which is defined by Jones [11] as "materials composed of long interwined and cross-linked molecular chains"(p.39).

The way to impart the desired properties to a rubber compound is by adding chemicals called cross-linking agents during vulcanization. This are listed by Gent [9] as reinforcements, anti-degradants, process aids, extenders, and specialty additives, such as tackifiers, blowing agents, and colorants.

If the compounding of your own rubber material is realizable then its properties could be modified to fit certain requirements. Often one relies on already compounded rubbers, and not all suppliers will provide you with a list of the cross-linking agents used in the compounding of their vulcanized rubber. Even the properties of the rubber supplied by a manufacturer may vary from batch to batch. For this reason it is very important to rely on experimentation.

As described by [12], the fillers are used in the majority of rubbers used in engineering applications, and may comprise up to one third of the total volume, being generally one of the many kinds of carbon black which can be reinforcing or non-reinforcing. The reinforcing blacks improve tear and abrasion properties, and increase the Young's modulus, hysteresis and creep. The non-reinforcing ones have little effect on tear and abrasion, but give moderate increases in Young's modulus, hysteresis and creep.

2.2 Stiffness of rubber springs

In this section methods for calculating the stiffness of rubber springs will be presented. This will help in the design of rubber bearings for precision machines, and serve as basis of comparison with the experimental results gathered with the Rubber Test device.

2.2.1 Homogeneous Compression

Homogeneous compression is possible when a rubber block is compressed between surfaces that permit the rubber block to freely expand laterally, as shown on Figure 2-1. When considering rubber as incompressible with a Poisson ratio $\nu = \frac{1}{2}$ then $A_x t_x = At$ and the applied compressive force becomes:

$$F = \frac{AE_0x}{t-x} \tag{2.1}$$

where F is the applied compressive force and E_0 is the Young's modulus. The detailed derivation of (2.1) is done by Lindley [16] (p.5).

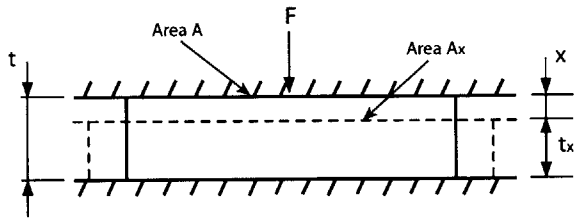

Figure 2-1: Homogeneous compression.

According to Lindley [16] for strains below $10-20\%$ the homogenous compressive strain is well represented by Hooke's Law

$$F = \frac{AE_0x}{t} \tag{2.2}$$

2.2.2 Compression stiffness of rubber bonded to metal

Bonding rubber to metal significantly increases the compression stiffness due to the increased constraints imparted on the rubber deformation. This is of great importance when trying to achieve high compression to shear stiffness ratios, which is ideal for rubber bearings. Lindley [16] presents different methods of bonding rubber to metal like brass plating, proprietary bonding cements, or other types of adhesives. Friction could sometimes be enough to prevent slippage of the load carrying surfaces, but it is not recommended by Lindley [12], since slippage may occur for high shape factors $S > \mu/2$, where μ is the coefficient of friction.

Rubber has a Poisson ratio ν which is only slightly below $\frac{1}{2}$. Because of this rubber can be treated as a first approximation as incompressible. If rubber bonded to metal (or any other rigid member) is subject to compression then any decrease in thickness will be accompanied by bulging of the rubber at the force free surfaces. The compression stiffness in this case will depend on the shape of the rubber, which can be represented by its shape factor S, and is defined as the ratio of one loaded area to the total force-free area as shown on Figure 2-2.

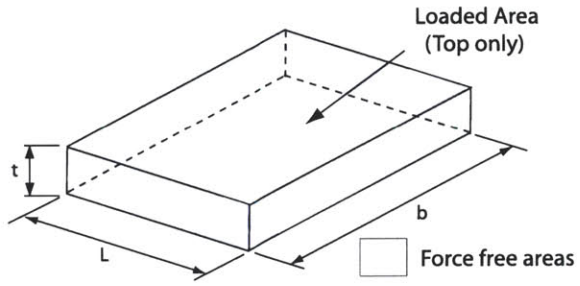

Figure 2-2: Figure showing loaded and force free areas of a block under compression.

Under the assumption that rubber is incompressible the compression modulus for a circular disk and rectangular blocks of infinite length is given by Freakley [8] (p.116):

$$E_c = E_0(1 + 2kS^2) \tag{2.3}$$

for circular disks, and

$$E_c = \frac{4}{3}E_0(1 + kS^2) \tag{2.4}$$

for rectangular blocks of infinite length (or one-dimensional strain).

Here E_0 is the Young's modulus, S is the shape factor, and k is a compression coefficient. The coefficient k is an empirically determined material property, which

corrects for experimental deviation. Typical values of k are given in Table 2.1.

Rubber may be considered as incompressible for some applications, but for blocks with high shape factors, bulk compression must be taken into account, since if it is not considered (2.3) and (2.4) are unbounded. The compression modulus E_c of rubber blocks taking into account the bulk modulus E_∞, is given by Lindley [16] (p.9):

$$E_c = \left[\frac{1}{E_0(1+2kS^2)} + \frac{1}{E_\infty}\right]^{-1} \tag{2.5}$$

for circular disks, and

$$E_c = \left[\frac{3}{4E_0(1+kS^2)} + \frac{1}{E_\infty}\right]^{-1} \tag{2.6}$$

for rectangular blocks of infinite length (or one-dimensional strain)

As a reference, the materials properties for natural rubber are given in Table 2.1 (Source: Gent [9]).

For a rectangular block as shown in Figure 2-2 the shape factor is

$$S = \frac{Lb}{2t(L+b)} \tag{2.7}$$

For a circular disk of radius a as shown in Figure 2-3 the shape factor is

$$S = \frac{a}{2t} \tag{2.8}$$

Finally, for a compression strip of width b and thickness t, where the strain in the direction of its length is negligible, the shape factor is defined by Lindley [12] as

Table 2.1: Hardness and elastic moduli for natural rubber (note: The Shore A hardness is a value given only as a reference, the data given corresponds to the IRHD scale)(Source: Gent [9])

Hardeness (IRHD ±2)	Shore A (see note)	Shear modulus G (kPa)	Young's modulus E_0 (kPa)	Bulk modulus E_∞ (MPa)	Comp. coeff. k
30	26	296	896	979	0.93
35	31	365	1158	979	0.89
40	36	441	1469	979	0.85
45	43	524	1765	979	0.8
50	48	621	2137	1007	0.73
55	53	793	3172	1062	0.64
60	58	1034	4344	1124	0.57
65	63	1344	5723	1179	0.54
70	68	1689	7170	1241	0.53
75	74	2186	9239	1303	0.52

$$S = \frac{b}{2t} \tag{2.9}$$

Lindley [12] (p.41) derives the compression stiffness of a solid rubber ring of rectangular section shown in Figure 2-4 considering a one-dimensional strain as (2.4) giving the following:

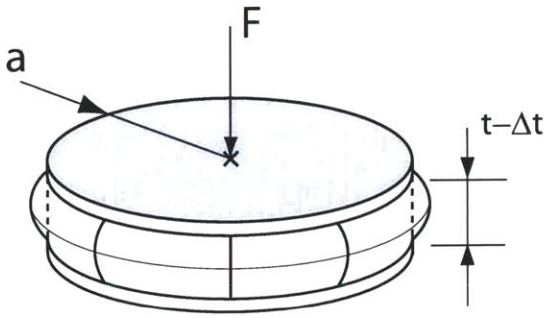

Figure 2-3: Compression of a bonded disk.

$$K = \frac{4}{3} E_0 \pi D_m \frac{b}{t} \left[1 + \frac{kb^2}{4t^2} \right] \tag{2.10}$$

where $D_m = \frac{1}{2}(D + d)$, and $b = \frac{1}{2}(D - d)$.

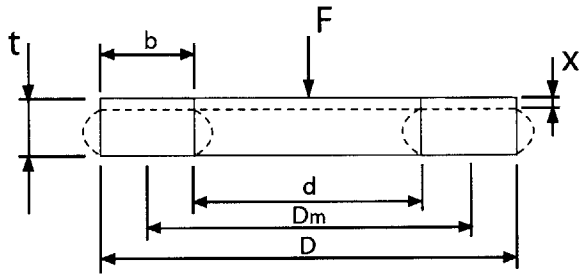

Figure 2-4: Compression of a ring of rectangular section.

2.2.3 Tension stiffness

A tensile loading condition must be avoided in the design of rubber bearings, since according to Lindley [16] the use of rubber springs in tension is not a common practice, since in tension are susceptible to ozone cracking, and support much lower loads than in compression.

Lindley [16] observes that the stiffness of a bonded rubber unit in tension can be calculated using the same equations used for compression. The stiffness is also dependent of the shape factor and the rubber unit bulges inward instead of outward, as in compression.

2.2.4 Shear stiffness

Rubber bearings are utilized in shear and it is preferable that its shear stiffness behaves linearly within its working strain range. It is noted by Lindley [16] that the

shear-strain curves of rubber are linear for strains below 50%. However hard vulcanizates tend to be less linear as shown in Figure 2-5.

This doesn't limit the use of hard vulcanizates as materials for rubber bearings in precision machines since their strain is expected to be way below 50% or even lower than 1%, depending on the application. This large strain capability is a strong advantage of rubber bearings as compared with metal flexure bearings, which are limited to material strain on the order of 0.1%.

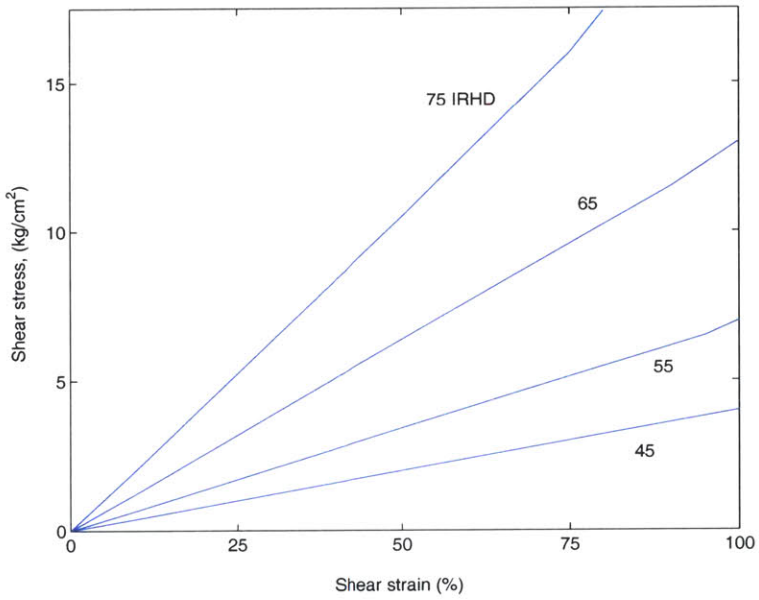

Figure 2-5: Shear stress-strain curves for rubbers of different hardness (Source: Lindley [16]).

The shear stiffness K_s is simply given by

$$K_s = \frac{F}{x} = \frac{GA}{t} \tag{2.11}$$

where G is the shear modulus, A is the surface area subject to shear, and t is the rubber thickness.

According to Freakley [8], (2.11) is applicable within the linear strain range stated earlier. However, when the ratio of thickness to length exceeds 1/4, the deflection due to bending becomes significant and must be considered.

2.3 Dynamic properties of rubber

The design of rubber bearings for precision machines requires a good knowledge of their dynamic properties which can be affected by several factors including, additives, temperature, preload, frequency of oscillation, type of strain, and amplitude of oscillation.

2.3.1 The nature of viscoelastic behavior

Viscoelastic materials behave cannot be modeled either as an elastic solid nor liquid bodies, their behavior can be seen as a combination of both types of bodies. As noted by Ferry [7] elastic solid stress is directly proportional to strain in small deformations but independent of the rate of strain, while viscous liquid stress is directly proportional to rate of strain but independent of the strain itself.

Viscoelastic materials do not maintain a constant strain under constant stress but deform slowly with time, or creep [7]. Viscoelastic materials under cyclic deformation give rise to properties such as stiffness and energy dissipation, which means that some energy is stored and recovered in each cycle and some is dissipated as heat [7] [11]. This means that when viscoelastic materials are subject to a sinusoidal stress the strain will be out of phase from the stress.

Ferry [7] observes that a polymer is composed of threadlike molecules which have a greater volume than atomic dimensions. Also that a qualitative way to view a polymer structure is to consider "long-range contour relationships, somewhat more local

relationships seen with a more detailed scale, and so on, eventually including the orientation of bonds in the chain backbone with respect to each other on a scale of atomic dimensions" (p.2) as shown on Figure 2-6. When a polymer is subject to stress, rearrangements on a local scale are relatively rapid, and very slow on the long-range scale.

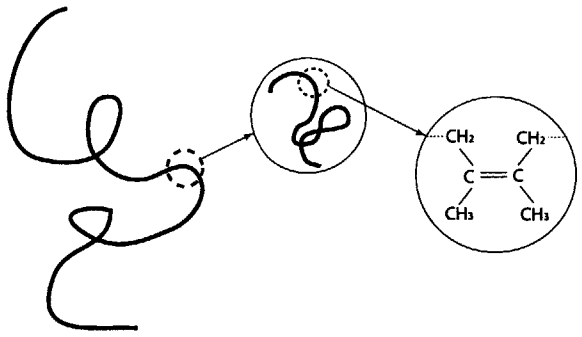

Figure 2-6: Representation of Long-range and short-range contour relationships in a flexible threadlike molecule, adapted from [7]. (Natural rubber molecule shown).

Because of the rearrangements time-frame related with the rearrangement of local and long-range scale, when a polymer is subject to a low frequency excitation the long-range rearrangements predominate. And when subject to a high frequency excitation the local scale rearrangements predominate. This means that the polymer will attain smaller strains with the same stress magnitude as the frequency of excitation is increased.

2.3.2 Simple Shear

The shear strain $\gamma_{12} = \gamma_{21} = \tan\alpha \approx \alpha$, and shear stress σ_{12} are functions of time. Ferry [7] notes that they are related by a constitutive equation based on the principle that the effects of sequential changes in strain are additive:

$$\sigma_{21}(t) = \int_{-\infty}^{t} G(t-t')\dot{\gamma}_{21}(t')\,dt' \tag{2.12}$$

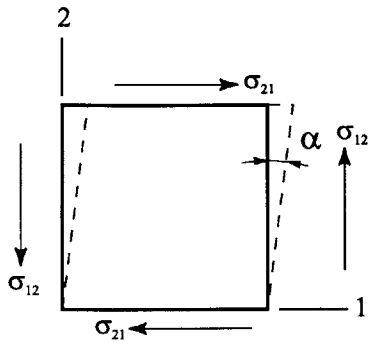

Figure 2-7: Simple shear of a cubical element, seen from 1-2 plane.

and that the strain can be expressed in terms of of the history of the time derivative of the stress $\dot{\sigma_{21}}$ as:

$$\gamma_{21}(t) = \int_{-\infty}^{t} J(t-t')\dot{\sigma_{21}}(t')\,dt' \tag{2.13}$$

where $\dot{\gamma_{21}}$ is the shear rate, $G(t)$ is called the relaxation modulus, and $J(t)$ is called the creep compliance.

If the shear stress is applied in the form of a step then the shear strain can be expressed as stated by Ferry as [7] (p.10) as $\gamma_{21}(t) = \sigma J(t)$, where $J(t)$ increases in a significant manner with time, resulting in a strain versus time as shown in Figure 2-8.

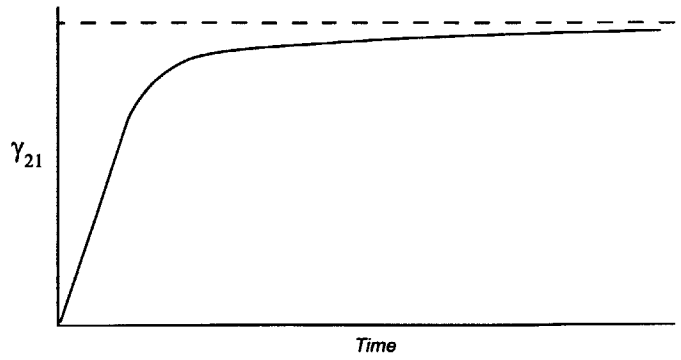

Figure 2-8: Time profile of a shear creep experiment (from tested Neoprene rubber).

The creep behavior of rubber under a step stress can give some insight on its frequency response. Ferry [7] notes that periodic stress applied at a frequency ω is qualitatively equivalent to a transient experiment at time $t = 1/\omega$.

2.3.3 Sinusoidal excitation in Simple Shear

When designing a precision machine using rubber bearings it is necessary to know how rubber behaves when subject to a sinusoidal excitation. This becomes essential to design a controller for the machine.

When applying a sinusoidal shear stress $\sigma(t)$ with frequency ω, the output strain $\gamma(t)$ comes out sinusoidal and out of phase, both being related as shown by Ferry [7] (p.12)

$$\sigma(t) = \gamma^0 |G^*| \cos(\omega t + \delta) \tag{2.14}$$

provided that the viscoelastic behavior is linear. Here G^* is defined as the complex modulus and has the following form $G^* = G' + iG''$. Also $G'(\omega)$ is defined as the shear storage modulus, $G''(\omega)$ as the shear loss modulus, and $\tan\delta = G''/G'$.

Viscoelastic materials of high molecular weight can show a drop of the shear compliance with frequency of many powers of 10. Examples are given by Ferry [7] (p.33-47), including a lightly vulcanized Hevea rubber, showing this behavior.

2.3.4 Bulk Compression

The change of shape in simple shear is not accompanied by change in volume. Other deformation geometries like bulk compression are characterized by a change in volume and shape. For the case of bulk compression the voluminal strain $\Delta_v(t)$ is as a

consequence of an applied pressure $P(t)$ is time dependant as shown by Ferry [7](p.20) for very small strains as

$$-P(t) = \int_{-\infty}^{t} K(t-t')\dot{\Delta}_v(t')\,dt' \tag{2.15}$$

where $\Delta_v = (V - V_0)/V_0 \approx \frac{3}{2}\gamma_{kk}$ and $K(t)$ is termed the bulk relaxation modulus.

The applied pressure $P(t)$ and voluminal strain $\Delta_v(t)$ are related as shown by same author as

$$P(t) = -\Delta_v K(t) \tag{2.16}$$

$$\Delta_v(t) = -PB(t) \tag{2.17}$$

where B(t) is the bulk compression creep compliance.

When testing the compression stiffness of high shape factor specimens it is important to understand their behavior. This show less increase of compression stiffness than the shear stiffness with frequency. As stated by [7] "Bulk compression would not be expected to involve changes in long-range molecular configuration or contour shape" (p.22). Viscoelastic materials of high molecular weight can show drops of the Bulk compliance with frequency of less than 10. Examples are given by Ferry [7] (p.49,561), including natural rubber vulcanized by sulfur which shows a drop of Bulk compliance of less than a factor of 2.

2.3.5 Simple extension

Simple extension is defined as an elongation in one direction accompanied by shrinking of the two mutually perpendicular directions of the same magnitude.

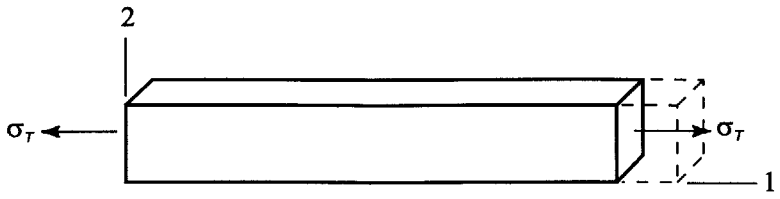

Figure 2-9: Simple extension.

The longitudinal strain γ_{11} is related to the tensile stress σ_T by the constitutive equation derived by Ferry [7] (p.22)

$$\sigma_T = \gamma_{11}\left[G(t) + \int_{-\infty}^{t} G(t-t')\dot{\nu}(t')\,dt'\right] \tag{2.18}$$

$$\tag{2.19}$$

The quantity in brackets is denominated $E(t)/2$, and the tensile strain ϵ is equal to $\frac{1}{2}\gamma_{11}$ getting to the following:

$$\sigma_T = \epsilon E(t) \tag{2.20}$$

$$\epsilon(t) = \sigma_T D(t) \tag{2.21}$$

where $E(t)$ is the tensile relaxation modulus and $D(t)$ is the tensile creep compliance.

For a perfect elastic solid at equilibrium, the equilibrium Young's modulus is related to the shear and bulk moduli by the classical elastic theory:

$$E_e = \frac{9G_eK_e}{G_e + 3K_e} = 2G_e(1+\nu_e) \tag{2.22}$$

but for the case of viscoelastic materials where G, K, and ν are time-dependent,

$E(t)$ must be specified in terms of G and ν as shown by (2.18)

For polymeric systems, in certain broad ranges of time scale, $K(t)$ is often greater than $G(t)$ by two orders of magnitude or more. This condition corresponds to a Poisson ratio close to 1/2, and in that case $E(t)$ and $D(t)$ become:[7]

$$E(t) = 3G(t) \tag{2.23}$$

$$D(t) = J(t)/3 \tag{2.24}$$

This means that the results from simple extension experiments will give the same information as the shear experiments. But Ferry [7] observes that "for any viscoelastic material, there will in general be some conditions (especially short times or high frequencies) under which G and K are similar in magnitude and the approximations of (2.23) and (2.24) will not be applicable. This situation corresponds to a value of ν substantially less than 1/2; the minimum value ordinarily observed is about 0.2 for homogeneous, isotropic materials" (p.24). He further implies that (2.23) and (2.24) are also limited to small deformations, and small rates of deformation, where the last implies low frequency, since for large deformations or large strain rates, the simple extension and shear experiments show very different behavior.

The observations from Ferry must be taken into consideration when reading complex modulus data from tested materials, since the presented data might be assuming a similar shear extension and shear behavior, which might not be adequate for your application.

It is observed by Nashif [14] that elastomeric materials at low frequencies (or high temperatures) have a Poisson ratio $\nu \approx 0.5$, which gives $E = 3G$, but the Poisson ratio decreases with frequency. An example is given where the 3M-467 adhesive, reaches a poisson ratio of $\nu \approx 0.33$, and so $E \approx 2.67G$.

2.3.6 Bulk Longitudinal deformation

Bulk longitudinal deformation occurs when the volume is subject to an elongation or compression in one direction and the two other mutually perpendicular dimensions are constrained to remain constant.

Ferry [7] notes that the condition of bulk longitudinal deformation is met by the compression of a flat sample. Rubber bearings fabricated with thin rubber and the load carrying surfaces bonded to rigid members, subject to compression loads can be considered to be subject to this type of deformation. Ferry further states that viscoelastic behavior in bulk longitudinal deformation will in general combine the features of shear and bulk viscoelasticity, however bulk effects will predominate. So similar behavior to that of bulk deformation is expected.

2.3.7 Classical Models for viscoelastic behavior

As shown by (2.14) the modulus of viscoelastic materials can be expressed in complex form, and so the stiffness:

$$k^* = k(1 + i\eta) \tag{2.25}$$

where η is known as the loss factor. As shown by Jones [11] viscoelastic behavior can be approximated by simple models such as the Maxwell and Voigt models, as shown on Figure 2-10. Defining the parameters of the Maxwell and Voigt models is fairly simple when using few of this elements, but poor approximations are accomplished.

The complex stiffness of the different types of models are summarized in Table 2.2. Jones [11] observes that the number of elements used can be increased in order to model the complex modulus behavior, which requires the identification of a large

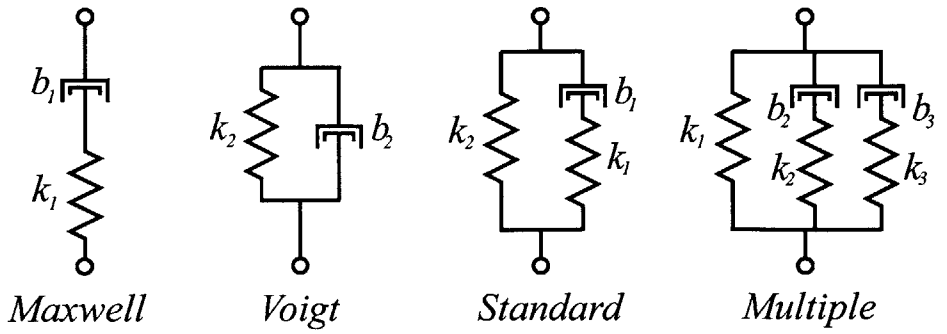

Figure 2-10: Classical models of viscoelastic behavior, adapted from [14].

Table 2.2: Complex stiffness of standard viscoelastic models, Source: Jones [11]

Model	Complex stiffness k^*
Maxwell	$\frac{i\omega k_1 b_1}{k_1+i\omega b_1}$
Voigt	$k_2 + i\omega b_2$
Standard	$\frac{i\omega k_1 b_1}{k_1+i\omega b_1} + k_2$
Multiple	$k_0 + \frac{i\omega k_1 b_1}{k_1+i\omega b_1} + \frac{i\omega k_2 b_2}{k_2+i\omega b_2} + \ldots$

number of parameters.

2.3.8 Effects of Temperature

Temperature affects the properties of viscoelastic materials and is considered one of the most important environmental factors. Nashif [14] states that "when the temperature is reduced the thermal motions of the molecules become slower and, since rubber-like deformation depends on these motions, the response to stress changes becomes more sluggish, the rubber appearing stiffer, ie. its modulus increases. At a sufficiently low temperature substantially no molecular motions occur and the behavior then resembles that of a glass, in which deformation is due to the straining of interatomic bonds". (p.89)

The effects of temperature are shown on Figure 2-11, where four distinct regions are observed. Most rubber like materials, such as cross-linked polymers are charac-

terized by the glassy, transition, and rubbery regions as noted by Nashif [14]

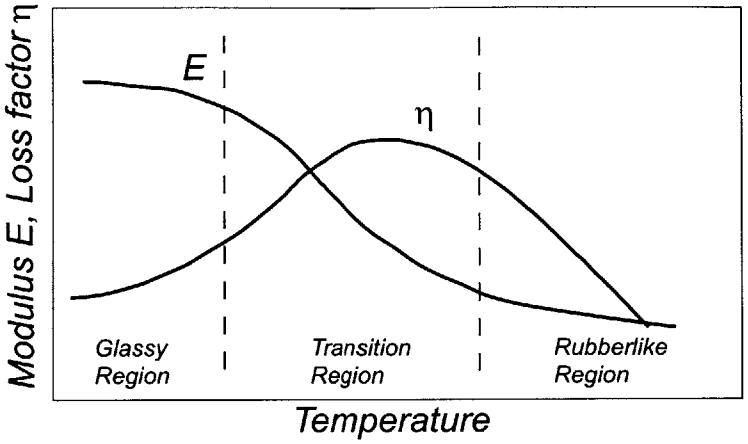

Figure 2-11: Variation of storage modulus and loss factor with temperature, adapted from [14].

2.3.9 Effects of Frequency

The modulus of rubber-like materials always increases with frequency [14]. The increase of modulus with frequency takes place in three regions as shown in Figure 2-12. The first is the rubbery region which takes place at low frequencies and where the modulus takes the lowest value. The second one is the transition region where the modulus increases dramatically. The third one is the glassy which takes place at high frequencies and is where the modulus takes its highest values. The loss factor increases with increasing frequency in the rubbery region, taking its highest value in the transition region, and then starts decreasing with increasing frequency in the glassy region.

2.3.10 Representation of Frequency-Temperature effects

Because of the inverse relationship between temperature and frequency effects on dynamic properties a superposition principle is used [14]. Based on this principle,

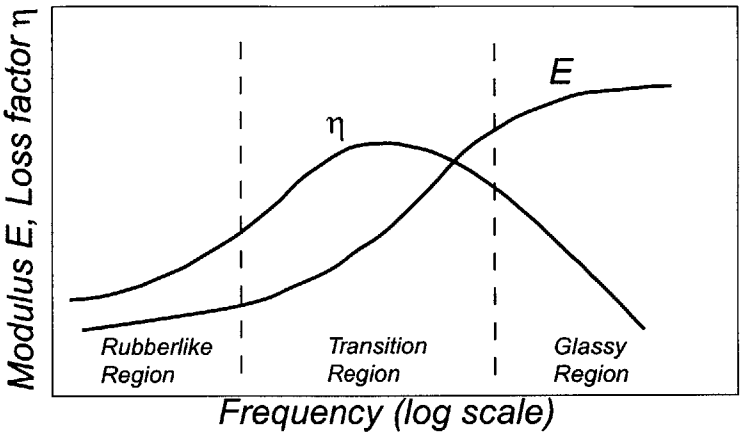

Figure 2-12: Variation of complex modulus and loss factor with frequency, adapted from [14].

measurements of properties as a function of frequency made at different temperatures can be collapsed on one master graph called nomogram.

These nomograms are useful to predict dynamic behavior, but care must be taken to find out what are the limitations of these nomograms. The tests undertaken for creating this type of nomograms might be at conditions which do not cover the scope of your application. This might differ in the type of deformation, strain amplitude, frequency range of tests, etc.

2.3.11 Effects of Cyclic Dynamic Strain

The variation of the modulus and loss factor with dynamic strain amplitude is similar to that of temperature, but the effect is much smaller than that of temperature as observed by Jones [14]. Figure 2-13 shows how the modulus decreases with increasing dynamic strain. The three regions shown are called the linear, the transition, and the equilibrium zone. The composition of the material affects the variation of the modulus with dynamic strain. As shown in Figure 2-14 when the amount of fillers is increased then its nonlinearity is greater.

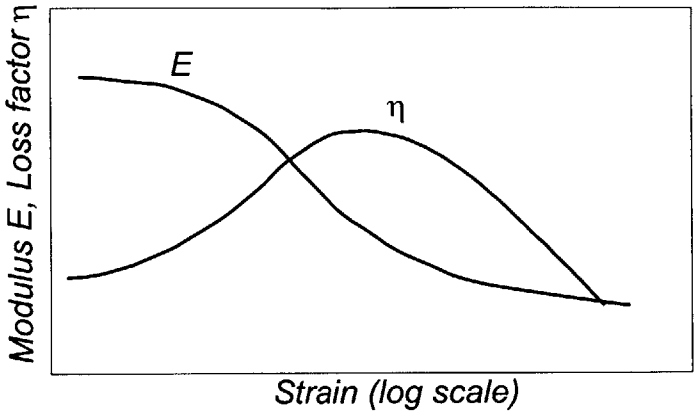

Figure 2-13: Variation of complex modulus and loss factor with strain amplitude, adapted from [14].

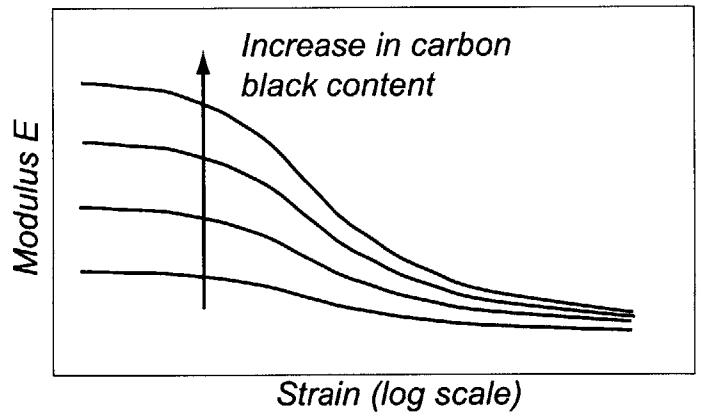

Figure 2-14: Variation of storage modulus and loss factor with strain amplitude for different contents of carbon black, adapted from [14].

2.3.12 Effect of Pressure and Temperature in Viscoelastic behavior

It is observed by Nashif [14] that the dynamic or complex modulus increases with static preload, whereas the loss factor decreases, and that this effect is usually more

important in the rubbery region, which will be at low frequency as shown in Figure 2-15.

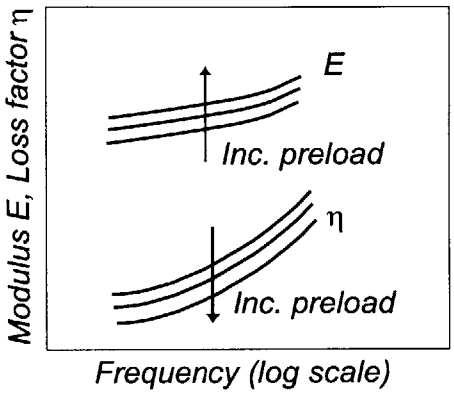

Figure 2-15: Variation of complex modulus and loss factor with preload, adapted from [14].

As shown by Gent [9], components of high shape factor subject to a compressive strain increase their static shear stiffness as compressive load is applied. This effect is greater for higher shape factors.

2.3.13 Tests for Dynamic mechanical properties of polymers

In this section different types of devices for testing dynamic mechanical properties of polymers will be presented. A brief description of them and their specifications will accompany.

Yersley Oscillograph

As presented by Gent [9] the Yersley Oscillograph consists of a rocking arm that can deform a rubber sample either in compression or in shear as shown in Figure 2-16. A pen attached to the arm records the rocking motion to yield an oscillogram. The test is applicable to materials with static moduli below 2 MPa in compression or 1 MPa in shear to produce about 20% deformation.

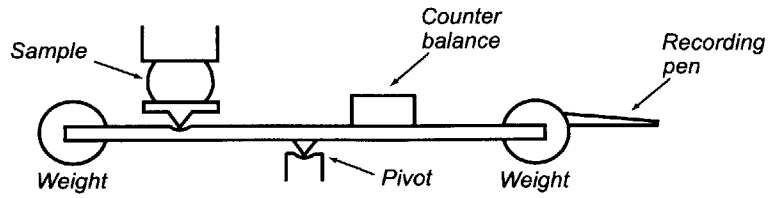

Figure 2-16: Schematic of Yersley Oscillograph, adapted from [9].

It is further implied by Gent [9] that this setup provides a fair understanding of the the relative dynamic stiffness and damping properties of different rubber compositions. This setup is limited by the fact that it provides a decreasing force input and that testing occurs at low frequencies, between 3 and 6 Hz.

Resonant Beam

The resonant beam presented by Gent [9] consists of a beam pivoted at one end and driven by a vibration exciter on the other end. The sample is placed in between as shown in Figure 2-17. The beam is driven at a controlled displacement at resonance which permits large displacements with minimum force. This device permits finding the static stiffness and damping properties (at a given frequency) of the sample. The frequency range of this device is 10 to 30 Hz.

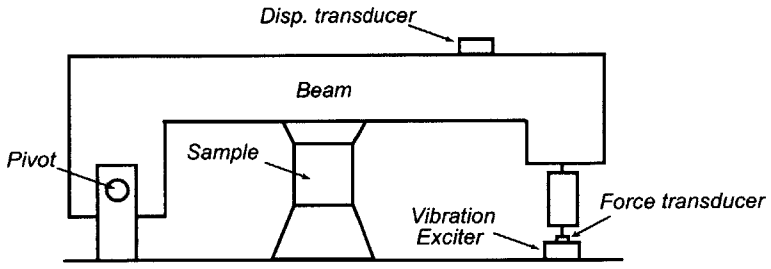

Figure 2-17: Schematic of resonant beam test device, adapted from [9].

Servo-hydraulic testers

Servo-hydraulic testers like the one shown by Gent [9] provide in a single device the capability of high force and large displacements. Different types of specimens can be tested in this machine like a rubber mount in compression or shear, and a tire. A displacement transducer senses the motion while a load cell in the stationary side measures force as shown in Figure 2-18. The frequency range is limited to several hundred Hz. A similar device is shown by Payne [16] where a maximum frequency of 50 Hz can be obtained with a peak-to-peak amplitude of 0.1 inches.

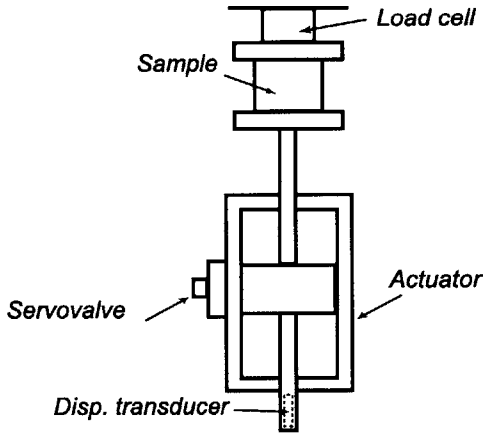

Figure 2-18: Schematic of a servo-hydraulic tester, adapted from [9].

Electromagnetic shaker

This machine shown by Payne [16] consists of a 50 lb electromagnetic shaker mounted on a horizontal axis. Two samples are tested at the same time in this machine, with one just used as a reactance, allowing preload to be applied. The other is placed between two force transducers, and two accelerometers are attached to the moving side of the sample. This machine can vibrate up to 2000 Hz. Power limitations of this machine gave a peak-to-peak amplitude of 0.1 inches at 50 Hz.

Transducer measurements by Electrical Impedance

This interesting method presented by Ferry [7] measures complex voltage/current ratios without the need to determine absolute values of force displacement, or velocity, and can be applied for soft solids. The Fitzgerald transducer apparatus presented by Ferry is an example which provides considerable versatility and precision. This device tests two disc-shaped samples in shear inside a thick cylindrical driving tube and a heavy, freely suspended floating mass as shown on Figure 2-19. The tube and masses are suspended by fine wires, which keep them centered, and permit longitudinal motion. The driving tube is electromagnetically driven, producing a longitudinal oscillation with small amplitude. The floating mass moves at a smaller amplitude, whose magnitude and phase are determined by its inertia and their supports elastance. The mechanical impedance of the oscillating system is calculated based on the measured impedance of one of the driving coils, which is measured with the aid of a bridge while in motion. The Fitzgerald apparatus has been used at frequencies from 10 to 6000 Hz.

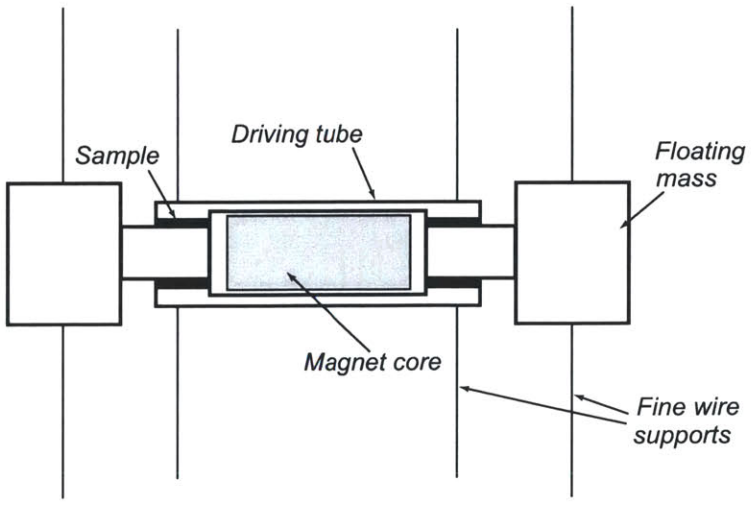

Figure 2-19: Schematic of Fitzgerald Electromagnetic transducer, adapted from [7].

Torsion test ASTM D5279

Useful information was found on the EARSC website [5]. Here they present the ASTM torsion test, also called the rheovibron test, which is used to measure the mechanical properties of polymers in torsion. The specimen which has a rectangular cross section is gripped longitudinally between two clamps. The lower one is connected to the drive motor, and the upper one to a torque transducer. This device is equipped with a thermal chamber which permits testing through temperatures ranging from $-100°C$ to $100°C$. The frequency limit of this device is 10 Hz. The results from this test as stated by EARSC [5] "provide useful measures of the glass transition and peak loss factor and can be used to approximate dynamic performance at higher frequencies."

As well a photo of such an instrument is shown in the following website $< http : //www.ptli.com/testlopedia/tests/DMA - D4440.asp >$ from Plastics Technology Laboratories, INC.

2.4 Mechanical Fatigue of rubber

Fatigue life properties of rubber become essential for the use of rubber bearing in precision machines. Understanding how mechanical fatigue is identified and the factors that affect it helps in the design of the rubber bearing.

Gent [9] notes that mechanical fatigue is demonstrated in rubbery materials by a progressive weakening of physical properties as a result of slow crack growth during application of dynamic loads or deformation. Gent also notes that the main causes of fatigue cracking in rubber are mechanical, thermal, environmental (oxygen, ozone, and ultraviolet radiation), and chemical.

2.4.1 Fatigue Life

Fatigue life is the number cycles required to break an specimen into two pieces at a given stress or strain. Fatigue characteristics of materials are denoted by $S - N$ curves where S denotes stress σ or strain ε , depending if the fatigue test is stress or strain controlled, and N is the number of cycles to failure.

Gent [9] observes that when reducing the dynamic stress or strain to a certain value the fatigue life of rubber approaches infinity, as shown on a typical $S - N$ curve for rubber in Figure 2-20. This concept is called limiting stress or strain. This concept is really important since if infinite life can be assured in a rubber bearing then replacement of it could be avoided increasing the rubber bearing reliability.

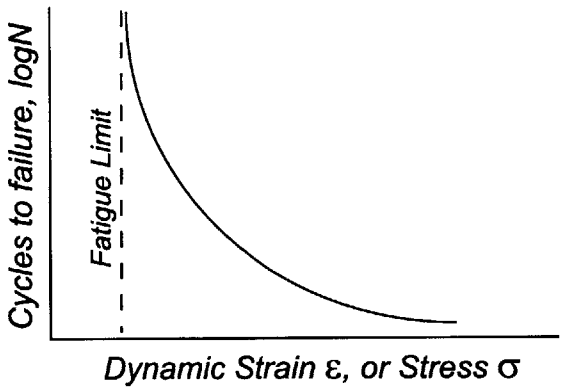

Figure 2-20: S-N curve for rubber: S is the peak to peak amplitude dynamic stress or strain, and N the number of cycles; adapted from [9].

2.4.2 Fatigue crack propagation

As described by Gent [9] fatigue crack propagation described by the crack growth rate dC/dN, has four characteristic regions as shown in Figure 2-21.

Region I is were the tearing energy G is less than the threshold tear energy G_0, hence no mechanical crack growth occurs, and the crack growth is caused only by

ozone (which occurs above a critical tensile stress), and is described by [9] (p.145)

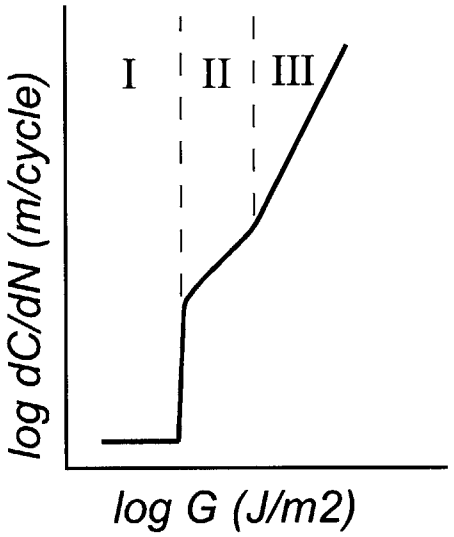

Figure 2-21: Cyclic crack growth rate dC/dN; data of unfilled Natural Rubber adapted from [9].

$$\frac{dC}{dN} = k_z O_z = R_z; \qquad G < G_0 \tag{2.26}$$

where O_z is the ozone concentration.

In region II, crack growth is dependent on both ozone and mechanical factors in an approximately additive and linear fashion. Hence, [9] (p.145)

$$\frac{dC}{dN} = R_z + A(G - G_0); \qquad G_0 < G < G_A \tag{2.27}$$

where A is a crack growth constant for region II.

In region III, a power law dependency between crack growth rate and G has been found for many rubbers as follows, [9] (p.145)

$$\frac{dC}{dN} = BG^{\beta}; \qquad G_A < G < G_C \tag{2.28}$$

where B and β are constants, being β a value between 2 and 6, for most rubber vulcanizates.

In region IV dC/dN approaches the velocity of elastic waves in rubber, about $50m/s$ [9].

2.5 Examples of use of rubber bearings

2.5.1 Bridge Bearings

As noted by Gent [9] laminated polychloroprene and natural rubber bearings have been in service in US and Canada for more than 30 years. The primary function of bridge bearings is to accommodate expansion and contraction, due to changes in temperature and humidity, and of rotation caused by bending under traffic loads [8].

The laminated rubber bearings consist of rubber laminates bonded to metal intermediate plates. This bearings provide high compressive stiffness to support the high loads from the bridges, as well as having low shear stiffness to accommodate the bridge expansion or contraction.

Stiffness measurements have been performed on bridge bearings after being in service for 20 years, showing no evidence of significant change in either shear or compression stiffness [9].

2.5.2 Rubber bearings used in helicopters

One use of rubber bearings in helicopters is their use in helicopter blades, where they are called elastomeric lead-lag dampers. As noted by Brackbill [4] elastomeric lead-lag dampers have been used on helicopters since 1970. Helicopters with soft-inplane rotor systems are subject to ground and air resonance instabilities, which are remedied with the use of the lead-lag dampers.

Other use of rubber bearings in helicopters is in their rotor head systems. As noted by Freakley [8] the elastomeric rotor head is a low-maintenance articulated rotor. Freakley further notes that "the main elastomeric bearing, consisting of a large number of shims separated by thin natural rubber layers, yields the large shape factor necessary for the small deflections under centrifugal loading, whereas the spherical section of the shims permits the required motions of the blade in shear."(p.498)

Chapter 3

Design of Test Hardware

In this chapter the design of the test hardware used for testing rubber specimens in compression and shear is presented. The design considerations taken for the design of the device are presented, as well as the most important calculations.

3.1 Compression Test Hardware

The design of the compression test hardware is presented in this section. A solid model of the compression test device is shown in Figure 3-1.

3.1.1 Functional Requirements

The compression test hardware has the purpose of testing thin rubber specimens under compression, with a thickness in the range of $0.5 - 1$ mm. The rubber specimens are of different materials and subject to static and dynamic tests ranging up to 5 kHz.

The applied force is required to be measured as well as the change in the rubber thickness. Due to the high compression stiffness of thin rubber specimens, the mechanical components must be robust in order to measure accurately the change in rubber thickness.

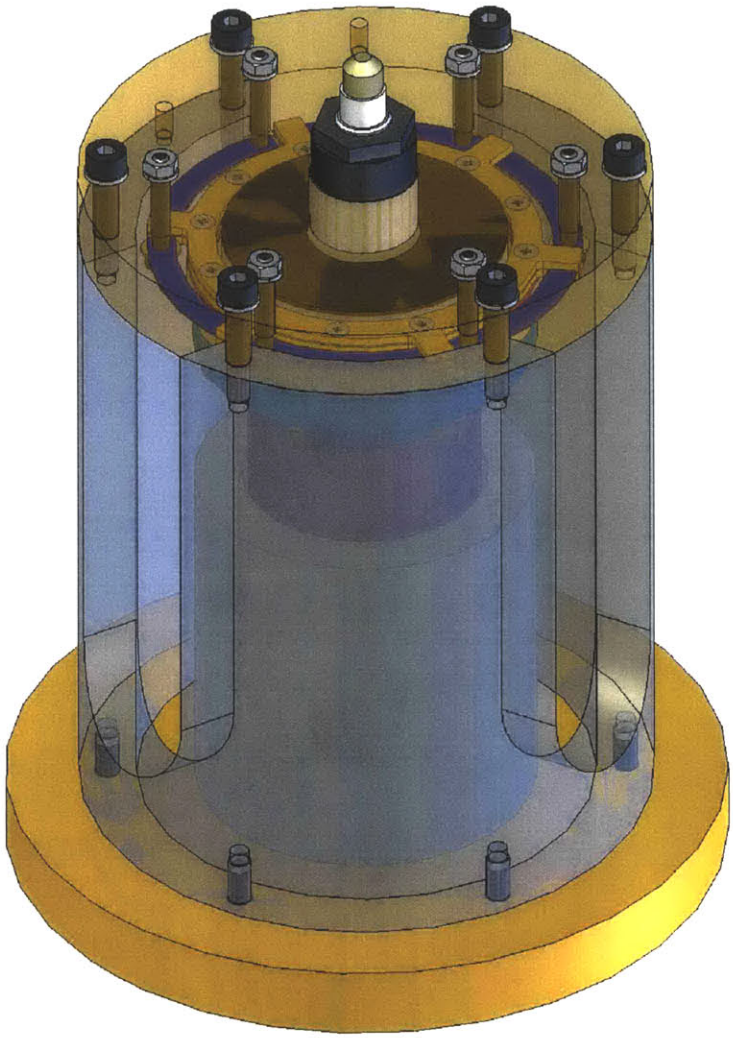

Figure 3-1: Solid model of compression test device (Some parts shown transparent to clarify assembly).

A sample with a static stiffness of 50 N/μm is taken as a reference to design the apparatus. Since dynamic tests are desired, the rubber specimen requires to be preloaded so that a sinusoidal force can be applied keeping the specimen always under load. The temperature rise of the whole apparatus must be kept to a minimum to prevent measurement errors.

3.1.2 Actuator

The chosen actuator is a voice coil actuator, as shown on figure 3-2. The BEI Kimco, model LA24-33-000A, voice coil actuator was chosen because of being readily available in our lab. The actuator has a force constant of $K_m = 7.1$ N/A which let us apply a force of nearly 7 N when keeping the current below 1 A.

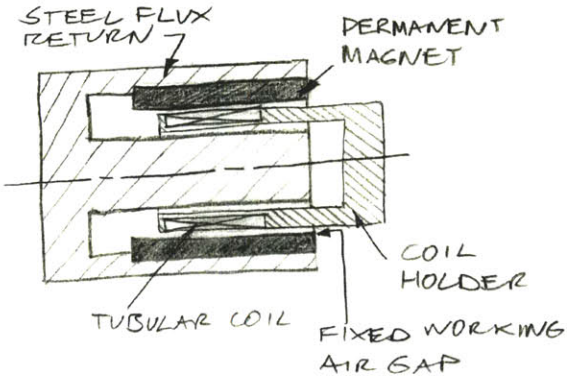

Figure 3-2: Voice coil actuator schematic.

The current is limited to 1 A to avoid overheating the hardware. This will keep the heat dissipation from the voice coil 5.5Ω resistance below 5.5 W, which can be readily dissipated.

The voice coil inductance is 2.3 mH and must to be taken into consideration at frequencies higher than 300 Hz depending on the load. For that reason current will be measured and used to calculate the force applied by the actuator.

3.1.3 Preload mechanism

The rubber specimens require to be preloaded in order to be subject to sinusoidal forces. The preload mechanism must be compact, in order to keep the device stiffness high; and easy to assemble to reduce the disassembly and assembly time between tests of different samples.

Different options were evaluated for the preload mechanism, including the use of small helical coil springs, and flexures. The problems with the use of the springs were the space requirements and assembly difficulties. The use of a flexure type preload was preferred because of the reduced space requirements, easy assembly, and the ability of increasing the preload force by stacking flexures.

The designed preload flexure consists of a set of six independent flexures which are arranged circumferentially around a center ring. The flexures are bolted and clamped to the target as shown in Figure 3-3. The clamps are designed with fingers to clamp the steel flexures such that stress concentrations are reduced.

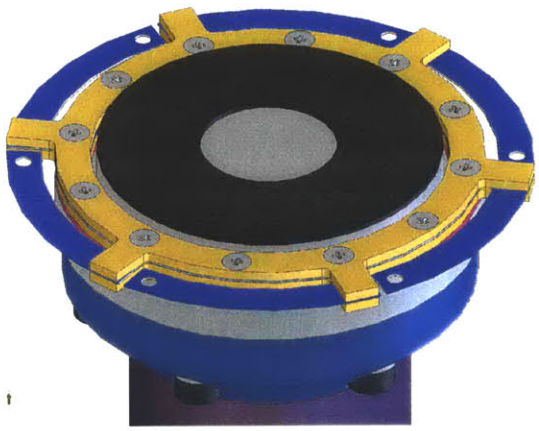

Figure 3-3: Preload flexure assembly.

Preload flexure sizing

For the sizing of the preload flexure, we use a model of a beam with one of the ends fixed and the other one guided as shown in Figure 3-4. The equations for this model will be as follows [19]:

$$M_A = \frac{WL}{2}; \tag{3.1}$$

$$y_A = \frac{-WL^3}{12EI}; \tag{3.2}$$

$$R_B = W; \tag{3.3}$$

$$M_B = \frac{-WL}{2}; \tag{3.4}$$

$$\tag{3.5}$$

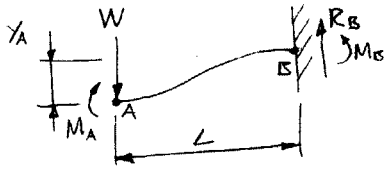

Figure 3-4: Model of flexure.

The stiffness of each flexure will be $k = W/y_A = 12EI/L^3$ with a total stiffness of the preload flexure as $k_T = Nk$, with $I = 1/12bt^3$, and the number of flexures $N = 6$.

Based on preliminary calculations and material availability, 1095C Blue Tempered 0.381 mm (0.015 in) thick Spring Steel is the chosen material for the preload flexure. The design allowable stress for the material is $900MPa$. The flexure section width is chosen based on the space limitations and allowable stress. The preload force is required to be large enough to keep the sample under compression while applying to it a sinusoidally varying force, and to assure a uniform contact of the rubber specimen contacting surfaces. The required force for that task is estimated to be of the order of $60N$; based on a 5 μ total flatness error of ground steel flat stock, a 50 Nμ stiff rubber specimen. It is estimated that one quarter of the specimen is lying on a non-uniform surface, and so the preload assures the contact of the load carrying surfaces with the steel surfaces. This estimate also considers one side of the rubber specimen being bonded.//

A single preload flexure was designed to provide $60N$ of preload force, and at the same time have a low stiffness compared to the rubber specimens. With the following final dimensions for the flexure, as shown in Figure 3-5:

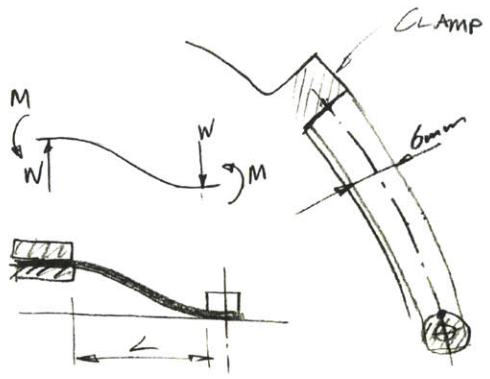

Figure 3-5: Model of flexure.

$$b = 6mm \tag{3.6}$$

$$t = 0.381mm \tag{3.7}$$

$$L = 25.2mm \tag{3.8}$$

we get the following results:

$$I = \frac{1}{12}(6\text{mm})(0.381\text{mm})^3 = 27.65 \cdot 10^{-3}\text{mm}^4 \tag{3.9}$$

$$k = \frac{12(2.1 \cdot 10^{-3}\text{N/mm}^2)(27.65 \cdot 10^{-3}\text{mm}^4)}{(25.2\text{mm})^3} = 4.34\text{N/mm} \tag{3.10}$$

$$k_T = 6x4.34\text{N/mm} = 26\text{N/mm} \tag{3.11}$$

$$M_A = \frac{10\text{N} \cdot 25.2\text{mm}}{2} = 126\text{Nmm} \tag{3.12}$$

$$\sigma_f = \frac{M_A t}{2I} = \frac{126\text{Nmm} \cdot 0.381\text{mm}}{2 \cdot 27.65 \cdot 10^{-3}\text{mm}^4} \tag{3.13}$$

$$\sigma_f = 868\text{MPa} < 900\text{MPa}(OK) \tag{3.14}$$

The preload flexure needs to deflect 2.3 mm in order to provide the $60N$ force. It was fabricated according to the design parameters, and tested satisfactorily for a 3.1 mm deflection.

Table 3.1: Preload flexures estimated Preload force

Flexures	Deflection (mm)	Preload (N)
1/2 flexure	2.37	31
1 flexure	2.37	62
1 1/2 flexures	1.99	78
2 flexures	1.99	103

The preload force has been tabulated in Table 3.1 for a 0.8 mm thick sample plus one top clamp (0.060 in thick) plus two lower clamps (each 0.060 in thick) and a total flexure stiffness of 26 N/mm.

Flexure bolts sizing

The flexures of the preload flexure are clamped with a single bolt which is subject to both a normal force and moment. Because of this special loading, the need to use small size bolts, and the restricted dimensions of the flexure, the sizing of these bolts is analyzed in detail.

Three stacked preload flexures are considered for the sizing of the bolts which results in a preload force of 180 N. This means that the bolt will experience a normal force of 30 N and a moment of 384 Nmm.

Figure 3-6 shows the bolts dimensions, which are taken as reference to calculate the bolt compliance δ_b and joint compliance δ_j [3]

$$\delta_b = \frac{1}{E}\left(\frac{0.4d}{\pi D_H^2/4} + \frac{l_1}{A_m} + \frac{0.5d}{A_m}\right) \tag{3.15}$$

$$\delta_j = \frac{l_j}{E \cdot A_s}, \; with \; A_s = \frac{\Pi}{4}(D_H + 0.1{l_j}^2 - {d_h}^2) \tag{3.16}$$

where E is the bolt material Young's modulus, d is the minimum thread diameter,

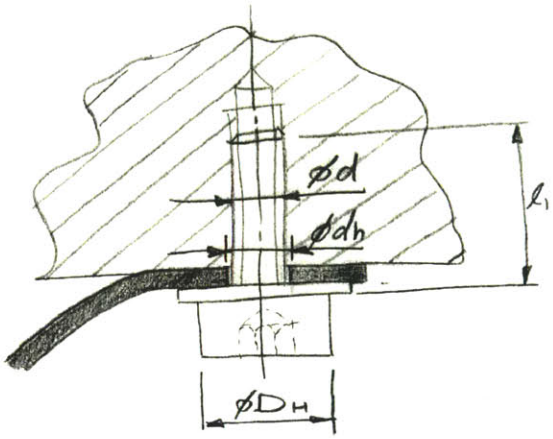

Figure 3-6: Felxure bolt.

A_m the area of the minor thread diameter.

The bolt settling deflection f_z and force F_z are calculated as follows:

$$f_z = 3.29 \cdot (\frac{l_1}{d})^{0.34} \cdot 10^{-3} mm \tag{3.17}$$

$$F_z = \frac{f_z}{\delta_b + \delta_j} \tag{3.18}$$

Finally the minimum and maximum bolt mounting force is calculated [3]

$$F_{Mmin} = (F_{req} + F_z) \tag{3.19}$$

$$F_{Mmax} = \alpha_A \cdot F_{Mmin} \tag{3.20}$$

With the following data $E = 2.1 \cdot 10^5 MPa$, $d = 1.5mm$, $A_m = 1.8mm^2$, $l_1 = 75mm$, $D_H = 3.8mm$, $l_j = 75mm$, and $d_h = 2.4mm$; we find the following compliances δ and settling force F_z:

$$\delta_b = 200.6 \cdot 10^{-6} \text{mm/N} \tag{3.21}$$

$$A_s = 95.8 \text{mm}^2 \tag{3.22}$$

$$\delta_j = 3.7 \cdot 10{-}6\text{mm/N} \tag{3.23}$$

$$f_z = 12.4 \cdot 10^{-3}\text{mm} \tag{3.24}$$

$$F_z = 61\text{N} \tag{3.25}$$

$$\tag{3.26}$$

Figure 3-7 shows how the pressure distribution in the bolted joint sums up. The design consideration for this bolted joint is that all the joint interface stays in compression. For that $\frac{F_{req}}{A} > \frac{W}{A} + \frac{9M_i}{4bA}$, which implies that $F_{req} > 30\text{N} + 9 \cdot 384\text{Nmm}/(4 \cdot 5\text{mm}) = 203\text{N}$. Then the $F_{imin} = SF \cdot F_{req} + F_z = 2 \cdot 203\text{N} + 61\text{N}$ giving $F_{imin} = 467\text{N}$. And the $F_{imax} = \alpha_A \cdot F_i min$, with $\alpha_A = 2.5$ for being the bolt preloaded manually, giving $F_{imax} = 1168$ N. The yield strength is matched in an M2 bolt at a preload force of 2420 N meaning that a safety factor of 2.1 is accomplished.

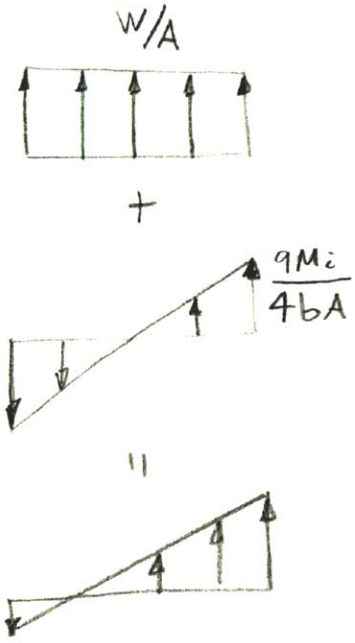

Figure 3-7: Flexure bolt joint pressure distribution under load.

3.1.4 Top plate sizing

The rubber specimens are compressed between the target and the top plate by the aid of the preload flexure. This top circular plate is bolted on the circumference and subject to a uniform central force due to the force transmitted by the rubber specimen. The top plate is required to be stiff compared to the rubber specimen. A rubber specimen static compression stiffness of 50 N/μm is taken as a reference. The design stiffness for the top plate is on the order of 1000 N/μm.

To size the top plate the expression given by Roark [19] to find the deflections of a circular plate fixed on the outer edge is used

$$y_b = \frac{wa^3}{D}\left(\frac{C_1 L_6}{C_4} - L_3\right) \tag{3.27}$$

$$\theta_b = \frac{Wa^2}{DC_4} L_6 \tag{3.28}$$

where C_1, L_6 and C_4 are factors which depend on the geometry of the plate as defined by [19]; $D = \frac{Et^3}{12(1-\nu^2)}$ is the plate stiffnes constant, with t being the plate thickness, and ν the Poisson ratio. The model of the plate is shown in Figure 3-8, which shows a center hole which is the one existing in the top plate for the cap gage.

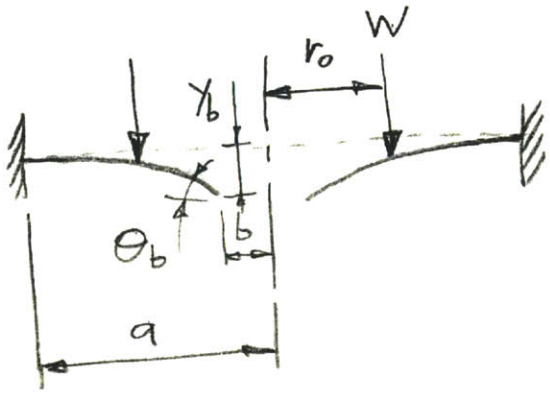

Figure 3-8: Circular plate with outer edge fixed, and inner edge free.

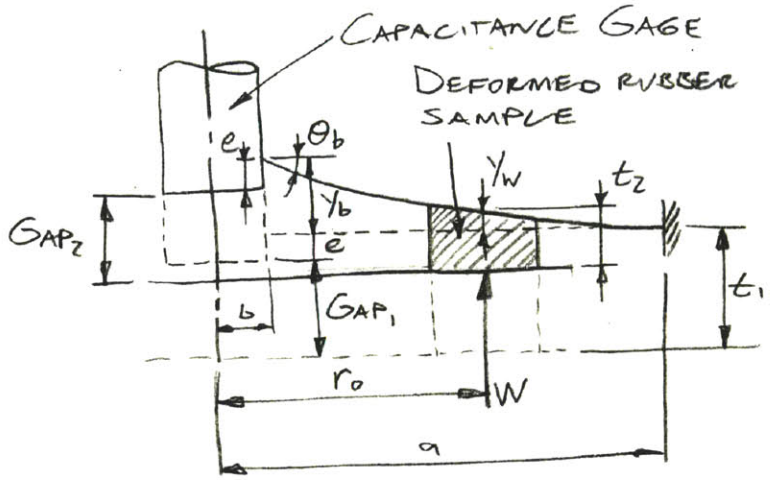

Figure 3-9: Model of top plate and sample deformation.

When the sample is under a load W it will be subject to a reduction in thickness $\Delta t = W/k$, where k is the sample stiffness. The plate will also deflect as shown in Figure 3-9. Due to the plate deformation the capacitance gage will actually measure a reduction of thickness $\Delta t_m = \Delta t - (y_b - y_w)$. The deflection y_w is estimated as $y_w = \frac{y_b}{a^3}(a - r_0)^3$. So the measurement error will be $(\Delta t_m - \Delta t)$ which gives a percentage error expressed by

$$\frac{(\Delta t_m - \Delta t)}{\Delta t} 100\% = -\frac{y_b \left[1 - \frac{(a-r_0)^3}{a^3}\right]}{W/k} \tag{3.29}$$

Taking into consideration the following parameters: the top plate material Young's modulus and Poisson ratio $E = 2.1 \cdot 10^5$ MPa and $\nu = 0.3$ (for steel), a plate thickness $t = 12.7$ mm, dimensions $b = 4$ mm, $a = 45$ mm, $r_0 = 15$ mm, and a sample compression stiffness $k = 50$ N/μm gives as measurement error of -1.07%. This measurement error is adequate for the considered static stiffness.

An estimate of the top plate natural frequency is of the order of 15 kHz, which is acceptable for making measurements of the rubber specimens dynamic stiffness up to 5 kHz. The estimate is done by using the equivalent mass and stiffness method,

derived with an approximate finite element method.

3.1.5 Body design

The body is designed to serve as the principal structure of the test device. Three windows are incorporated to ease the device assembly and voice coil holder alignment with respect to the permanent magnet.

A photograph of the target-flexure-sample-voice coil actuator assembly inside the body is shown in Figure 3-10.

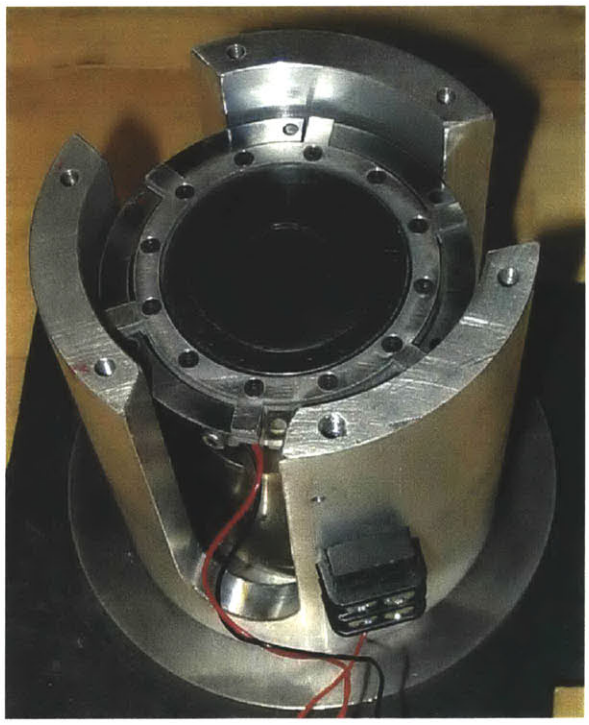

Figure 3-10: Photograph of the target-flexure-sample-voice coil actuator assembly inside the body.

3.1.6 Force indirect measurement

Because of the voice coil resistance, inductance, and back emf, the force requires to be measured indirectly by measuring the current. The current is measured with the aid of a 0.1Ω resistor, with a $25W$ power rating. The chosen resistor has a comparable low resistance to the one of the voice coil in order to unalter the voice coil performance. A schematic circuit of the current sensing is shown in Figure 3-13.

3.1.7 Displacement measurement

The displacement measurement is done with the aid of an ADE 2804 passive capacitance probe in conjunction with an ADE 3800 module. This capacitance probe from ADE [1] is a transducer which forms a capacitor with the target surface. And because the area of the formed capacitor is constant, variations in capacitance are related to variations in the distance between the probe and the target surface. Further the module has an output voltage proportional to the distance between the probe and the target. The output voltage is $0V$ when the probe is at its nominal standoff, $-10V$ at near standoff, and $+10V$ at far standoff. In our system the nominal standoff is 50 μm, and the probe has a measuring range of ± 25 μm from this standoff.

The target used for the probe is the rubber specimen holder. For that reason the rubber specimens are circular with a circular hole at the center, to allow the gage to sense the displacement of the metal target with no intervening rubber.

The gage is clamped on the top plate with the aid of a quick-grip keyless bushing like the one shown in Figure 3-11. This type of clamp was chosen in order to maintain the top plate stiffness, ease quick assembly and disassembly, and hold the gage firmly near the target. A cross section of the clamp, cap gage, and top plate assembly is show in Figure 3-12.

Figure 3-11: Quick-grip keyless bushing.

The stand-off of the capacitance gage must be set up to 50 μm from the target within at least 5 μm. This can be done by placing plastic shims between the target and capacitance or by a clamping mechanism that allows a precise adjustment of the cap gage position without compromising the connection stiffness. The first option is not possible because of the lack of access to the gap between the cap gage and the target. But the quick-grip keyless bushing permits a fine adjustments of the gap between the target and probe by increasing it while tightening the bushing nut. The way to set up the probe stand-off is by first placing the cap gage close to the target and then tighten the bushing nut until the cap gage module outputs 0 V (which corresponds to the 50 μm stand-off). If a tighter grip of the cap gage is desired then the bushing could be pushed in when near to the measuring range of the cap gage and then tighten the bushing nut until the cap gage module outputs 0 V. This procedure is not easy to follow the first time you try it, but it doesn't require many repetitions to make it an easy task.

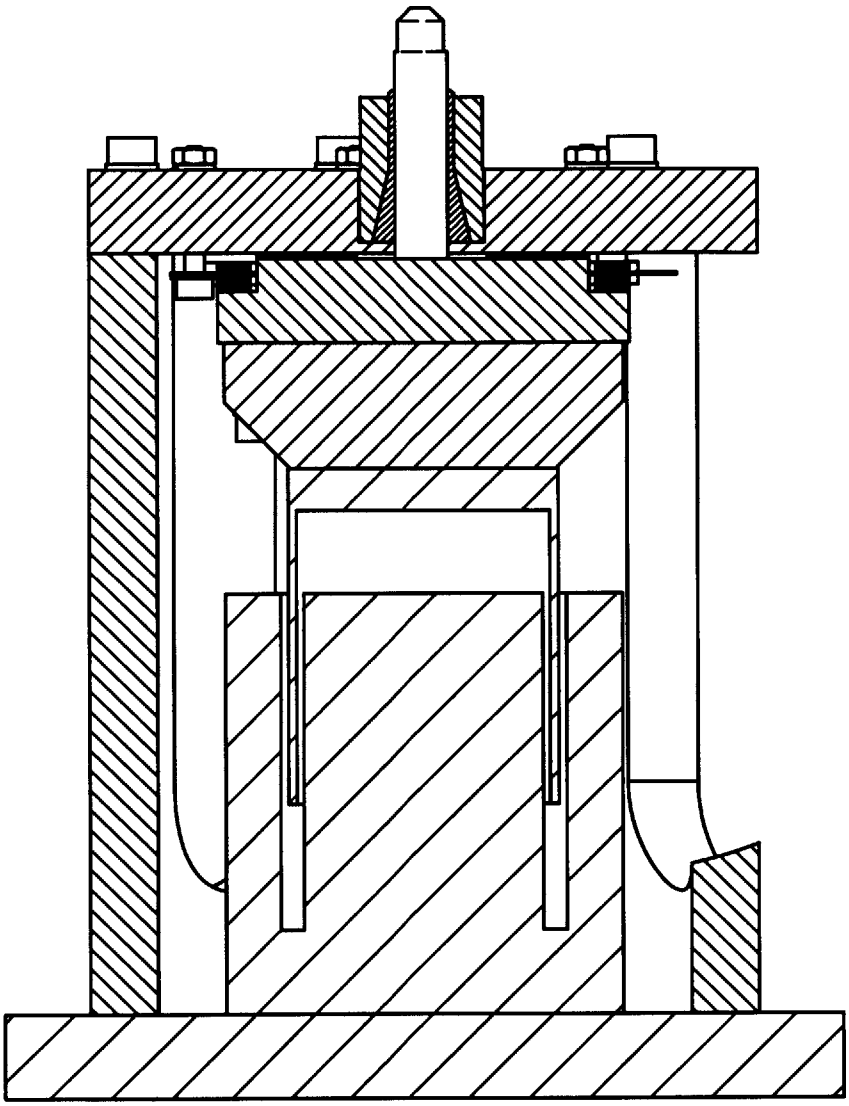

Figure 3-12: Cross section of compression rubber test device.

The ADE 3800 capacitance gaging module is set up for:

Sensor diameter: 2 mm

Total Measurement Range: 50 μm (± 25 μm)

Output Voltage Range: $20V(\pm 10V)$

Output Measurement Range: 50 μm (± 25 μm)

Output Scale Factor = OVR/OMR = $0.4V/\mu$m

Standoff: 50 μ

Bandwidth: $5kHz$

3.1.8 Power Amplifier

For our test setup a constant force magnitude supply from the voice coil actuator, for the test frequency range, is ideal. For that to be possible the current magnitude needs to stay constant. A maximum current of $0.8A$ is chosen in order to keep the power dissipation of the voice coil low. The voice coil actuator circuit model is shown in Figure 3-13, yielding the following differential equation:

$$v_m(t) - i(t)(R_s + R_m) - L_m \frac{d}{dt} i(t) - e(t) = 0 \tag{3.30}$$

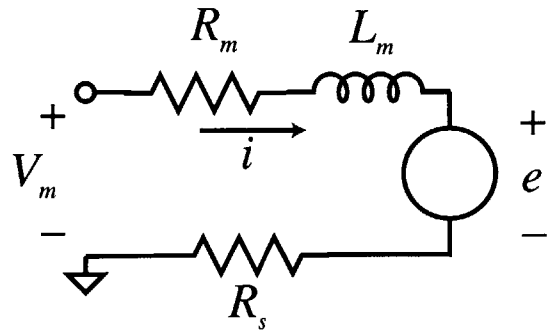

Figure 3-13: Voice coil actuator circuit.

where $e(t) = K_m \frac{d}{dt} x(t)$ is the back-emf. The magnitude of the back-emf is defined by $|e(t)| = K_m \omega |x(t)|$ where $|x(t)| < 1 \cdot 10^{-6}$ m, $K_m = 7.1$ V/A, and $\omega < 31416$ rad/s(5 kHz), which gives a back-emf $|e(t)| < 0.22$V. The back-emf is very low compared to even the voltage drop across the resistors R_s and R_m for the chosen current of 0.8 A, of 0.8 A$(5.5\Omega + 0.1\Omega) = 4.48$ V. For that reason then we simplify (3.30) as follows:

$$v_m(t) - i(t)(R_s + R_m) - L_m \frac{d}{dt} i(t) = 0 \tag{3.31}$$

Taking the Laplace transform of (3.31):

$$V_m(s) - I(s)(R_s + R_m) - L_m s I(s) = 0 \tag{3.32}$$

$$\frac{I(s)}{V(s)} = \frac{1/(R_s + R_m)}{(L_m/(R_s + R_m))s + 1} \tag{3.33}$$

For the given values of $R_s = 0.1\Omega$, $R_m = 5.5\Omega$, and $L_m = 2.3$ mH, gives as a pole with a break frequency at 388 Hz. The Bode plot for $I(s)/V(s)$ is shown in Figure 3-14.

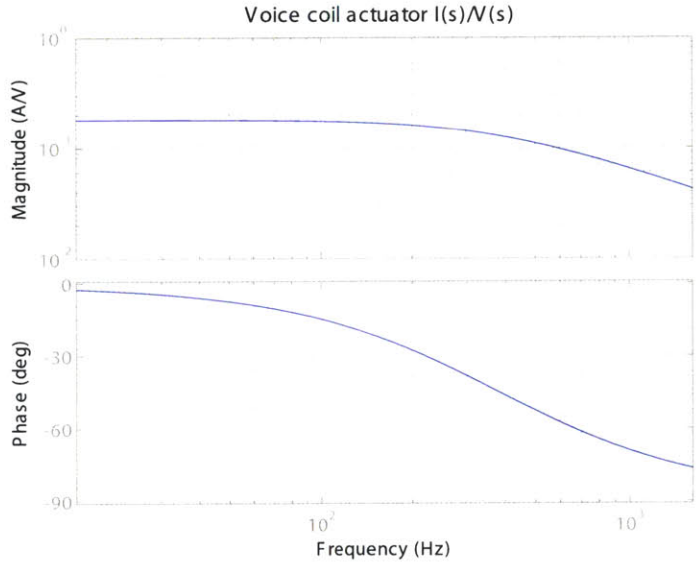

Figure 3-14: Voice coil actuator $I(s)/V(s)$ Bode plot.

3.1.9 Electrical connections

To avoid ground loops a grounding technique was followed as shown in Figure 3-15. The technique followed is to keep supply commons separate and meet only at one single point connected to ground. As a result "each supply current returns only on its associated common, and not on other commons or the ground wire," as stated by Trumper [18] (Sec. 5.5.1)

This grounding technique helped reduce the ground loops and electrical noise of

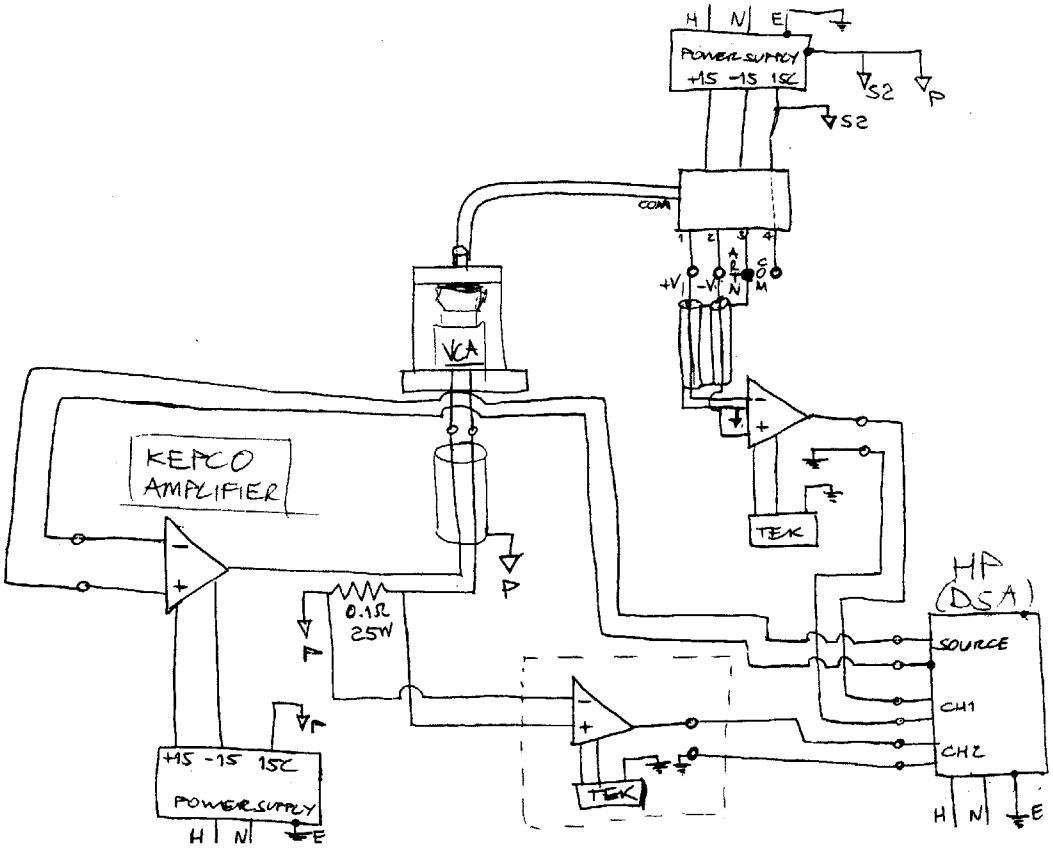

Figure 3-15: Schematic of electrical connections for the rubber test device.

the position signal. The measured electrical noise from the cap gage is on the order of 2 mV pk-pk, which is equivalent to 5 nm pk-pk displacement. This noise measurement is taken with the capacitance gage module filter set up at 5 kHz, and further low pass filtering of 50 kHz.

3.2 Shear Test Hardware

The design of the shear test hardware is presented in this section. A solid model of the shear test device is shown in Figure 3-16.

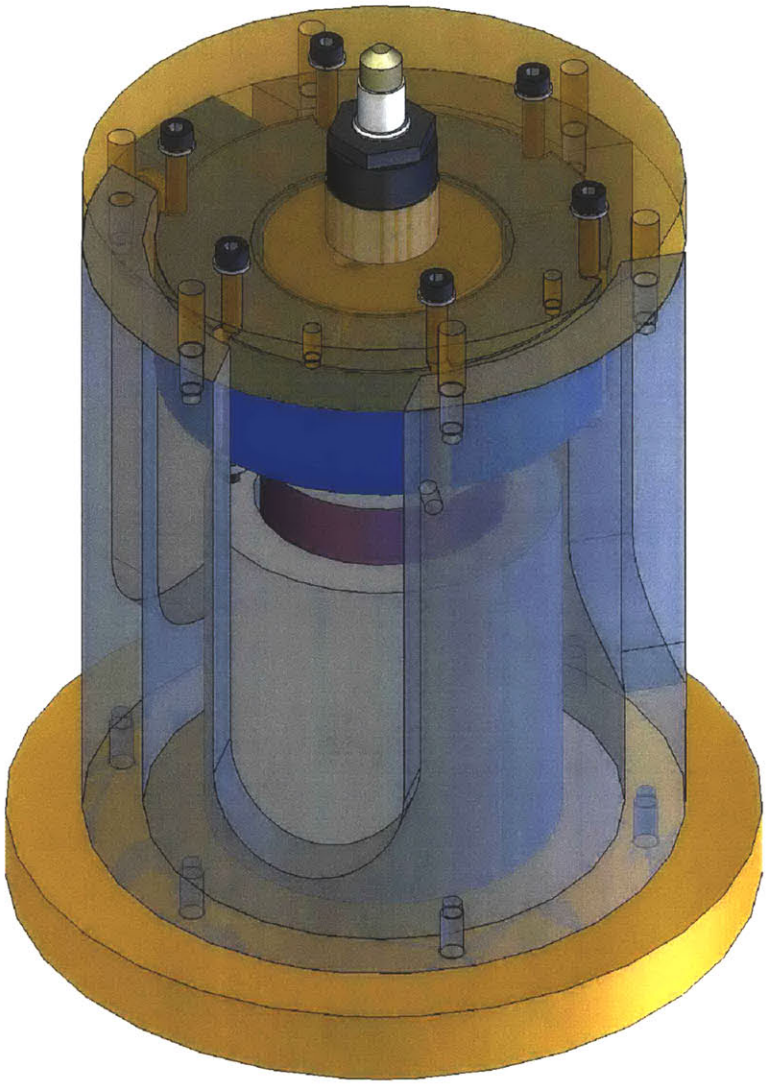

Figure 3-16: Solid model of shear test device (Some parts shown transparent to clarify assembly).

3.2.1 Functional Requirements

The shear test hardware has the purpose of testing thin rubber specimens under shear. This hardware utilizes basically the same main hardware as the compression test hardware in order to make the device more versatile and to reduce its development time and cost.

The shear test hardware uses the same actuator, body, bottom plate, top plate, and cap gage as the compression test hardware. The only hardware that requires a new design is the target shaft and sample holder. The rubber specimens are placed between the target shaft and sample holder. The sample holder should be able to preload the rubber samples to different preload values in order to take into account its effect in the rubber bearings performance. The rubber specimens will range in thickness from $1 - 0.5$ mm.

A photograph of the sample holder with the target shaft, with the sample in between both and the voice coil actuator coil holder is shown in Figure 3-17.

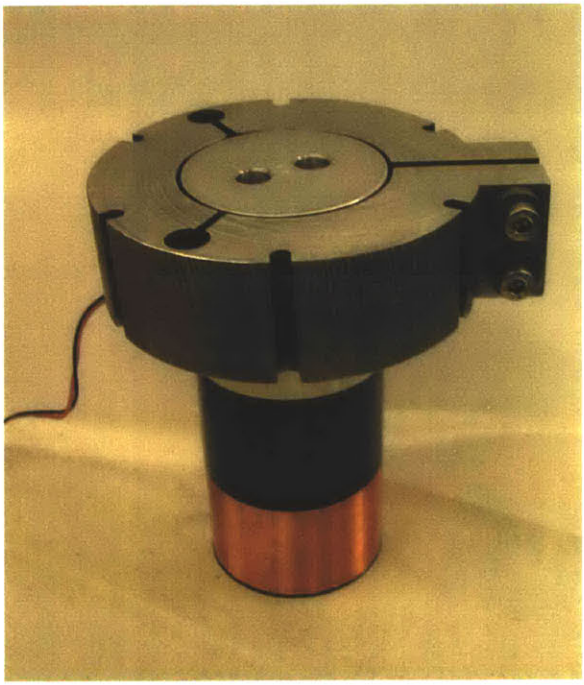

Figure 3-17: Photograph of sample holder with sample, target shaft and voice coil coil holder.

3.2.2 Sample holder

The sample holder is designed to hold three rubber specimens that are located in its inner circumference with an equal angular separation of 120^o. The rubber specimen

is constrained between the target shaft and sample holder. The sample holder is designed to allow the rubber specimen to be preloaded and assure complete surface contact, as well as provide the rubber specimen with sufficient friction force to receive shear load, and to be able to test the rubber specimen under different preload values.

The sample holder works as a three point contact clamp, due to the two built-in flexures as shown in Figure 3-18. These flexures in combination with the preload bolts permit the rubber sample to be preloaded up to 8600 N per sample. The flexures are designed so that they behave like pivots, because of their low stiffness compared to the rubber sample stiffness. Belleville springs stacked on the clamp bolts are used to adjust the preload of the rubber sample to determined values.

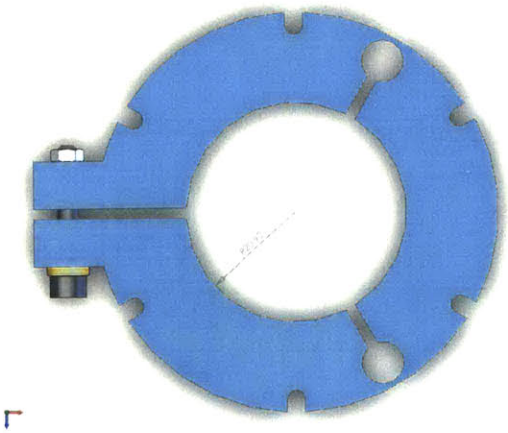

Figure 3-18: Sample holder.

The material chosen for the holder is hardened tool steel with a yield stress of 890 MPa. This material was chosen in order to both allow high compliance, high strength, and allow frequent assembly and disassembly.

3.2.3 Target shaft

The target shaft has the function of transmitting the force of the voice coil to the rubber sample in shear, and to serve as the target of the cap gage displacement sensor. To be able to test different sample thicknesses, stepped diameter shafts were fabricated, while the sample holder inner diameter was kept constant. A photograph of one of the sizes of target shaft is shown in Figure 3-19.

Figure 3-19: Target shaft.

The material chosen for the target shaft is aluminum. The shaft is required to be of non-magnetic material in order to avoid interaction with the voice coil actuator magnetic field.

The target shaft is also electrically grounded to the outer shell of the cap gage as required by the ADE electronics [1]. This is done via a flexible insulated cable connected to the side of the target shaft and then to the top plate of the test device which is electrically connected to the outer shell of the cap gage via the gage clamp.

3.3 Comments

The design of the test hardware yielded a simple and moderate price device. The most expensive hardware is the voice coil actuator and capacitance gage and related electronics. These hardware was readily available in our lab which permitted to build the test device with a budget below 2000 dollars (including the purchase of the tested rubber material).

One other important design accomplishment is that the device ended being compact in form and of relatively simple assembly and disassembly. The last permits testing of different samples in a short time.

The following chapter shows the results gathered by the test device for different materials tested under compression and shear.

Chapter 4

Rubber Compression Test Results

The rubber compression test device was used to test thin rubber samples with a thickness between $0.5 - 1.0$ mm. The materials tested under compression are Buna-N, Neoprene, Viton, Latex/Natural rubber, and Silicone rubber. The Shore A hardness of most tested samples is 40, with the exception of the Viton sample that has a Shore 75A hardness.

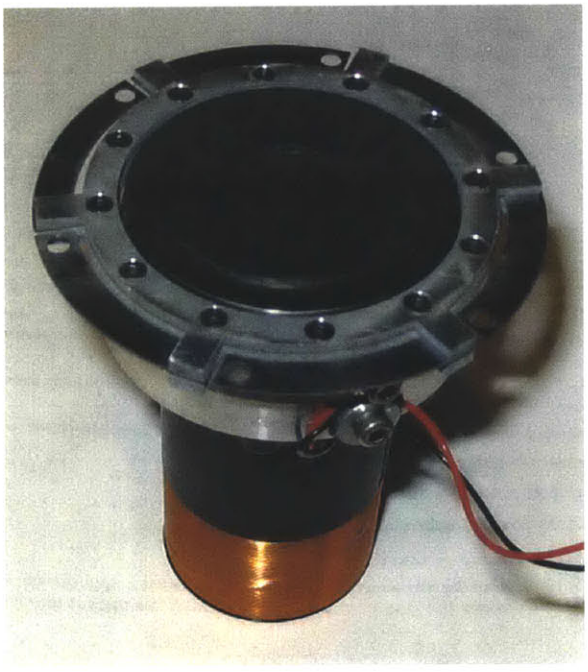

Figure 4-1: Rubber ring sample shown over target.

The design of the hardware used to perform the compression test is presented in Section 3.1. The testing of the sample is done by first applying preload between the target steel surface and the top plate of the machine with the aid of the preload flexure. The sample is subject to static and/or dynamic loading provided by the voice coil actuator, keeping the sample always in compression thanks to the preload. A photograph of the sample over the target surface and with the voice coil actuator coil holder is shown in Figure 4-1. The change in thickness of the sample is measured with the capacitance gage and the force is indirectly measured by measuring the voice coil actuator current with the aid of a sense resistor, and calculating the corresponding force via the actuator force coefficient.

4.1 Sample fabrication

The chosen sample shape is a ring of rectangular section due to the need of a central opening on the sample to let the capacitance gage measure the displacement of the target, as shown in Figure 4-2. This rings are cut with the aid of a razor blade, using hard metal as a working surface. Three main section sizes are chosen in order to study the effect of the shape factor of the sample, as shown in the Table 4.1

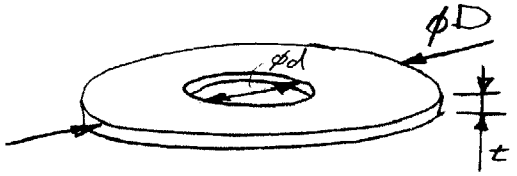

Figure 4-2: Compression sample dimensions.

4.2 Static stiffness

The static stiffness is measured by applying a compression load to the rubber samples while measuring the displacement with the aid of the capacitance gage. The applied

Table 4.1: Compression sample section sizes

Size D x d (mm x mm)
30 x 20
40 x 20
50 x 20

Table 4.2: Parameters of compression rubber samples, (1) adhesive on both sides, (2) adhesive on one side only, (3) one day of curing, (4) one week of curing

Key	Material	Shore A	D (mm)	d (mm)	t (mm)	S	Adhesive	
a	Buna-N High Grade	40	30	20	0.84	3.0	NO	
b	Buna-N High Grade	40	40	20	0.84	6.0	NO	
c	Buna-N High Grade	40	50	20	0.84	8.9	NO	
d	Buna-N High Grade	40	50	20	0.84	8.9	Cement	(1)
e	Viton Comm. Grade	75	30	20	0.74	3.4	Cement	(1)
f	Viton Comm. Grade	75	40	20	0.74	6.8	Cement	(1)
g	Viton Comm. Grade	75	50	20	0.74	10.1	Cement	(1)
h	Neoprene	?	50	20	1.65	4.5	Loctite	(2)
i	Silicone	40	40	20	0.99	5.1	Silicone	(1), (3)
j	Silicone	40	40	20	0.99	5.1	Silicone	(1), (4)
k	Latex Nat. Rubber	40	30	20	0.75	3.3	Loctite	(2)
l	Latex Nat. Rubber	40	40	20	0.75	6.7	Loctite	(2)
m	Latex Nat. Rubber	40	50	20	0.75	10.0	Loctite	(2)

compression loads range from $0 - 6$ N and are applied in an step-wise manner. The recorded displacement is the steady-state one, which is achieved in the order of seconds. Due to the high compression stiffness of the rubber samples and the limited actuator force ,static deflections on the order of 20 nm to 200 nm can be accomplished.

The static stiffness tests are done by applying a compression load to the sample, which is already under compression due to the existing preload. All the samples are tested with a preload force corresponding to two flexures which is in the order of 103 N of preload force as shown in Table 3.1.

4.2.1 Linearity

The rubber ring samples compression stiffness turned out to be fairly linear for the applied strain, as seen on the chosen examples of Figure 4-3. There exists certain non-linearities in the compression stiffness due to the lack of adhesive, and flatness of the sample which will be discussed in Section 4.2.2 and 4.2.4.

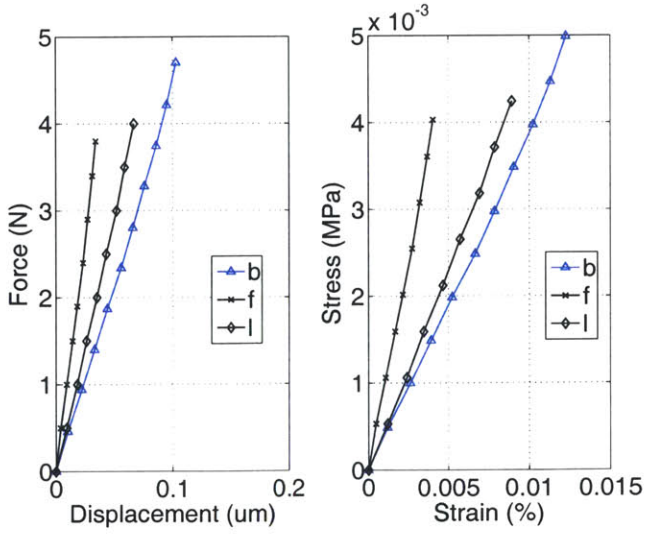

Figure 4-3: Static stiffness linearity (refer to Table 4.2 for legend).

4.2.2 Effect of bonding

As stated in Section 2.2.2 friction by itself could be sufficient to prevent slip of the load carrying surfaces. But this is only recommended for low shape factors where the shear stress that accompanies the bulging of the rubber is low.

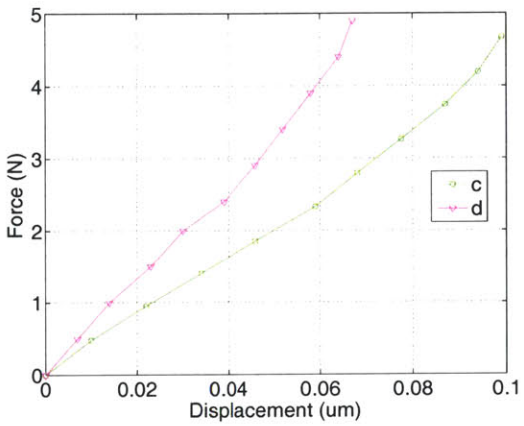

Figure 4-4: Effect of bonding on compression stiffness for Buna-N,(c) no adhesive, (d) with adhesive (refer to table 4.2 for legend).

It can be seen on figure 4-4 the difference in static stiffness due to the use of adhesive for the case of Buna-N Shore 40A with a high shape factor of $S = 8.9$. The static stiffness of the sample without adhesive is doubled with the use of adhesive. This is thought to be due to the slip of the loaded surfaces and lack of contact with the steel surfaces when no adhesive is present. Both of these reduce the compression stiffness of the tested sample.

4.2.3 Effect of curing time

Another important factor is the adhesive curing time. Some adhesives have considerably long curing times, like the case of silicone adhesives. Bonding silicone rubber to any surface is a real challenge due to its low surface energy [15]. The best adhesives for silicone are silicone-based adhesives[15].

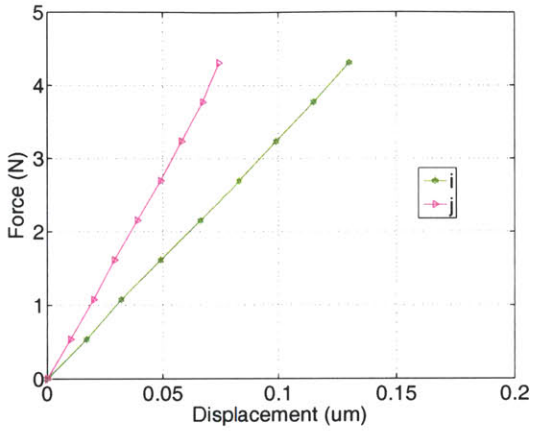

Figure 4-5: Effect of curing on compression stiffness of Silicone,(i) 1 day of curing, (j) 1 week of curing (refer to table 4.2 for legend).

Silicone adhesives take long periods of time to cure and have high viscosity which makes it really difficult to obtain a thin adhesive film. The silicone adhesives have curing times on the order of a week, which made the testing of silicone samples tedious.

Figure 4-5 shows how the compression stiffness varied in time due to the long curing time of the silicone adhesive. It shows how the compression stiffness increased about 70% due to the curing of the silicone adhesive.

4.2.4 Effect of Shape Factor

As seen in Section 2.2.2 the compression modulus E_c of a rubber ring should increase as a function of the shape factor squared (S^2) limited by the bulk modulus E_∞, as defined by (2.6)

$$E_c = \left[\frac{3}{4E_0(1+kS^2)} + \frac{1}{E_\infty} \right]^{-1} \tag{4.1}$$

Table 4.3: Calculated (using (4.1) and (4.2)) and experimental compression modulus E_c and compression stiffness k_c of the tested samples

Key	Material	Shore A	S	Calc E_c (MPa)	Calc k_c (N/μm)	Exp E_c (MPa)	Exp k_c (N/μm)
a	Buna-N High Grade	40	3.0	17.7	21.6	36.6	44.5
b	Buna-N High Grade	40	6.0	61.6	115.2	41.3	77.2
c	Buna-N High Grade	40	8.9	126.5	342.9	26.0	70.5
d	Buna-N High Grade	40	8.9	126.5	342.9	40.9	110.9
e	Viton Comm. Grade	75	3.4	119.7	165.2	79.0	109.0
f	Viton Comm. Grade	75	6.8	356.3	756.3	89.1	189.1
g	Viton Comm. Grade	75	10.1	592.9	1824.9	198.1	609.7
h	Neoprene	?	4.5			39.7	54.8
i	Silicone	40	5.1	45.7	72.5	34.8	55.2
j	Silicone	40	5.1	45.7	72.5	61.8	98.1
k	Latex Nat. Rubber	40	3.3	21.6	29.4	80.0	108.9
l	Latex Nat. Rubber	40	6.7	75.6	158.3	47.9	100.3
m	Latex Nat. Rubber	40	10.0	153.2	465.2	92.6	281.2

and the compression stiffness k_c is calculated using

$$k_c = \frac{E_c A}{t} \tag{4.2}$$

where A is the sample area, and t is its thickness.

Experimental results confirm that the compression modulus E_c does increase significantly with the shape factor S as shown in Table 4.3. Figure 4-6 shows a comparison between the experimental compression modulus and the one found using (4.1) and the data from Table 2.1. The experimental data shows 40% less Compression modulus E_c for a Shape factor $S = 10$ which is not so far off, taking into consideration the fact that the data of table 2.1 is for Natural Rubber and is used only to estimate the compression stiffness. The important thing to add is that only one load carrying surface was bonded, which reduces the bulging of the compression ring and in consequence its compression modulus E_c.

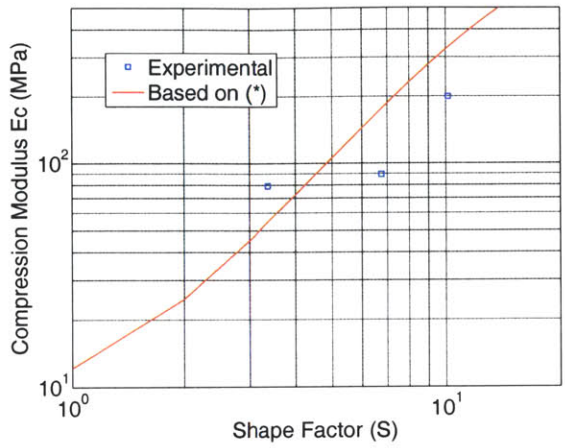

Figure 4-6: Increase in compression modulus for Viton Shore 75A with respect to shape factor S, (*) calculated using (4.1) (red line) and the data from Table 2.1.

Table 4.3 shows that the calculated compression modulus is greater than the experimental one in the majority of the cases. High shape factor samples show being considerably softer than calculated. This can be attributed to lack of contact of the whole sample loaded area due to its high compression stiffness and the use of adhesive on only one side of the sample. Other important clarification is that the compression modulus of high shape factor specimens is limited by the material bulk modulus. The bulk modulus used to calculate the compression modulus of the samples is the one provided by Table 2.1, which is for Natural rubber and serves only as a reference.

4.2.5 Settling

After the sample (with the respective adhesive) is placed in the test device and subject to preload, it experiences a settling as shown in Figure 4-7. The settling was recorded a few minutes after the sample was preloaded, so the actual settling displacement is expected to be higher. The settling time is in the order of hours, and it is important to wait for this settling to occur before testing the sample, in order to assure testing repeatability. This settling is believed to occur due to flattening of the load carrying

surfaces and the curing of the adhesive.

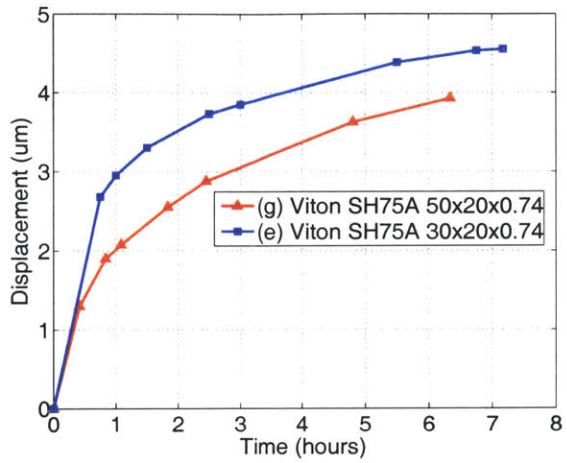

Figure 4-7: Settling of Viton compression ring samples (refer to table 4.2 for legend).

4.3 Dynamic Stiffness

The dynamic stiffness tests are performed with the sample always under compression. This is possible due to the initial preload of approximately 103 N, which is significantly higher than the applied nominal load of 6 N pk (12 N pk-pk).

The noise level from the displacement sensor accounts for about 5 nm pk-pk in a bandwidth of 50 kHz. This bandwidth is set via the panel controls on the AM502 differential amplifier. This noise becomes significant when testing the high shape factor samples, due to the high complex stiffness they achieve at high frequencies. As shown in Figure 4-9, they can reach a complex stiffness of nearly 2000 N/μm. With an applied load of 12 N pk-pk, the measured displacement will be on the order of 6 nm pk-pk, and so the cap gage noise of 5 nm pk-pk will corrupt the results.

4.3.1 Comparison of dynamic stiffness between tested materials

A comparison between samples of different materials with approximately the same shape factor and Shore hardness is shown in Figure 4-8. This figure shows how the complex modulus and its phase of different materials change with respect to frequency. It can be seen that all of the materials show the three regions (rubbery, transition, and glassy region) described in Section 2.3.9. The rubbery region is up to 10 Hz, after which the dramatic change in complex modulus starts, ending about 100 Hz. The highest phase advance takes place at the transition region within the frequency range of 20 to 40 Hz. The increase of Complex modulus from low to high frequency for the three materials is of the same order of magnitude ranging from a factor of 7 to a factor of 9.

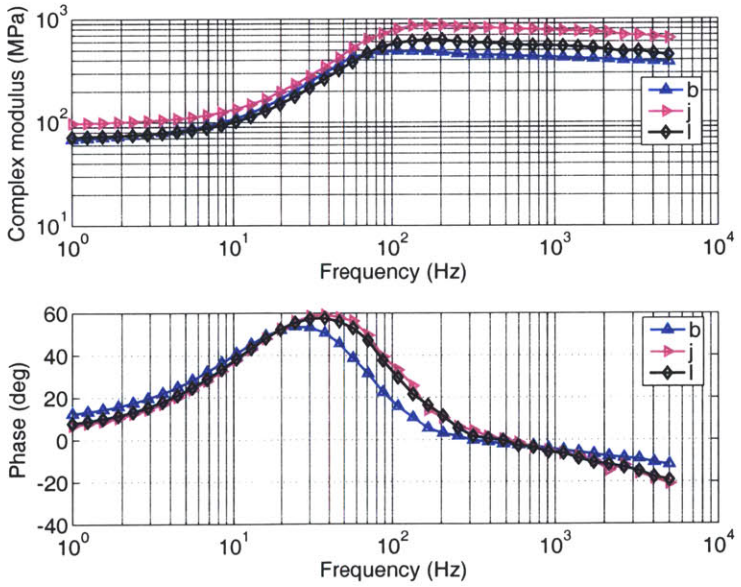

Figure 4-8: Complex modulus of different materials, all of Shore 40A, plotted against frequency (refer to table 4.2 for legend).

4.3.2 Effects of shape factor

In this section the effect of shape factor S in the dynamic properties of rubber is presented. The shape factor S of the tested rubber samples as defined previously in Section 2.2.2 is the ratio between the loaded area to the force free areas, and is defined by $S = \frac{(D-d)}{4t}$.

As the shape factor becomes large, the sample approaches the condition of bulk longitudinal deformation shown in Section 2.3.6 and so similar behavior to that of bulk compression is expected. As stated by [7] "Bulk compression would not be expected to involve changes in long-range molecular configuration or contour shape" (p.22). Viscoelastic materials of high molecular weight (including rubbers) can show drops of the bulk compliance with frequency of less than 10. Examples are given by Ferry [7] (p.49,561), including natural rubber vulcanized by sulfur which shows a drop of bulk compliance of less than a factor of 2 with increasing frequency.

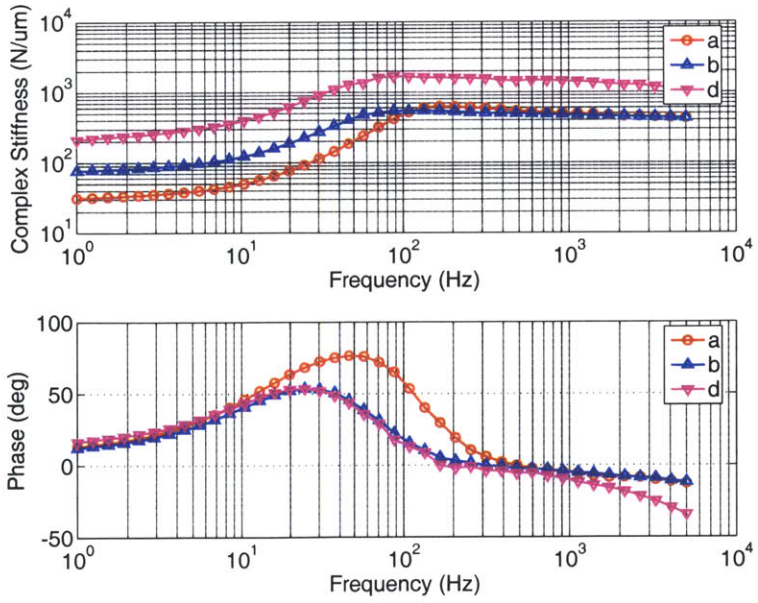

Figure 4-9: Complex modulus of Buna-N Shore 40A, plotted against frequency, (a) S=3, (b) S=6, (c) S=8.9 (refer to table 4.2 for legend).

Based on the previous argument it is expected for high shape factors that we will observe less increase of the complex modulus with frequency. Figures 4-9 and 4-10 show the complex modulus of Buna-N Shore 40A and Viton Shore 75A respectively, for different shape factors. These plots show that the increase of complex modulus is larger for smaller shape factors. It also shows higher phase advance for smaller shape factors, which is an indication of higher loss.

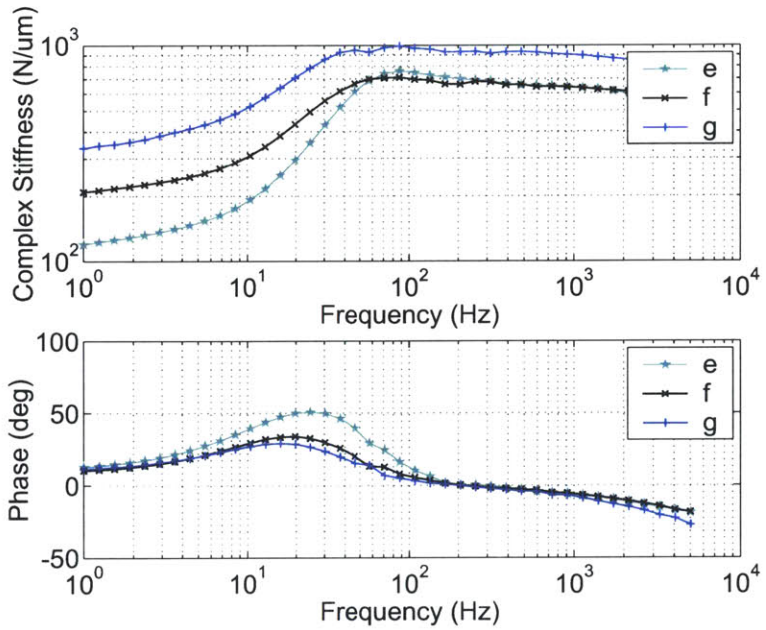

Figure 4-10: Complex modulus of Viton Shore 75A, plotted against frequency, (e) S=3.4, (f) S=6.8, (g) S=10.1 (refer to table 4.2 for legend).

4.3.3 Effect of bonding and curing time

In a similar manner as for the static stiffness, the adhesive becomes a key factor in the complex stiffness of the compression ring. It is shown in Figure 4-11 how the complex stiffness increases significantly when using an adhesive for the case of Buna-N Shore 40A with a high shape factor of $S = 8.9$, the complex stiffness is approximately doubled in its whole frequency range.

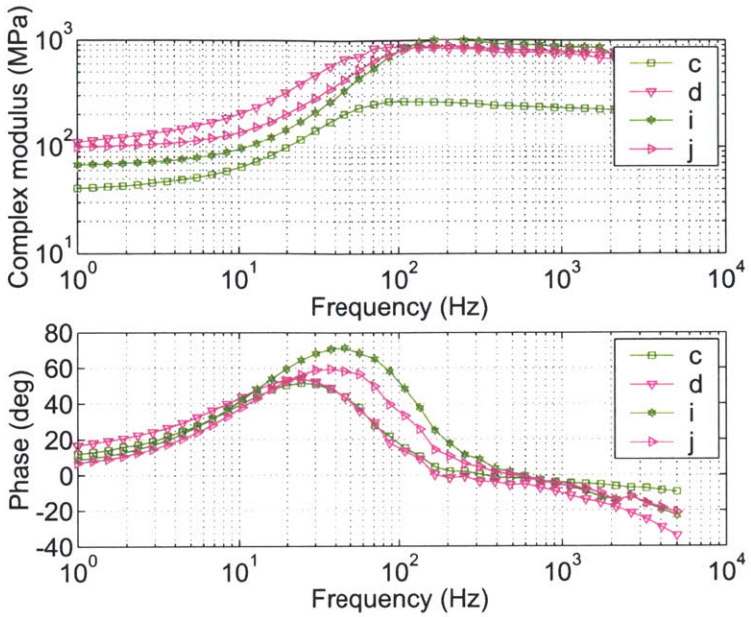

Figure 4-11: Complex modulus of Buna-N Shore 40A without adhesive (c) and with adhesive (d); and of Silicone rubber after 1 day of curing (i) and 1 week of curing (j) (refer to table 4.2 for legend).

Figure 4-11 shows as well how the curing time of the silicone adhesive affects the complex stiffness of silicone rubber. In this case the complex stiffness of the sample with the silicone adhesive cured for one week is fifty percent higher than the one with one day of curing. This increment takes place only on its low frequency range.

4.4 Step response

The step response of viscoelastic materials is characterized by a rapid rise (sometimes called the elastic zone) followed by a slow creep zone. The time characteristics of the creep process depends mainly of the material and temperature of operation [11].

All the samples shown in this Section were subject to a 0.5 Hz square wave force of 11 N pk-pk, which was accomplished by driving the voice coil actuator with a current source amplifier that had a bandwidth of about 50 kHz.

The step responses of the tested samples have shown a rapid elastic response in the order of 0.1 milliseconds, followed by a slow creep on the order of seconds. As discussed in Section 2.3.1 polymers' structure can rearrange on a local scale relatively rapid, which explains the initial rapid response, but rearrangements on the long-range scale are very slow, which explains the slow creep process. Figure 4-12 shows the step response of a Buna-N sample as reference.

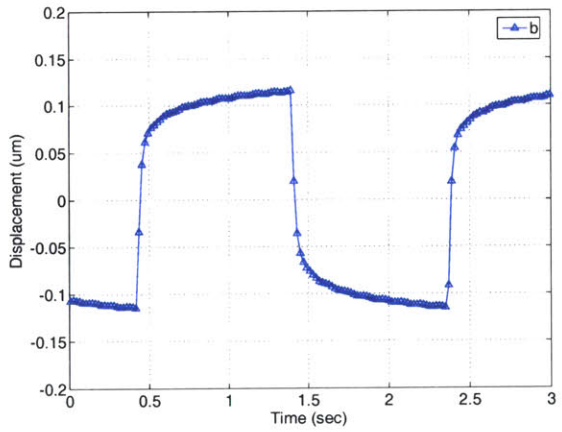

Figure 4-12: Step response of Buna-N Shore 40A (refer to table 4.2 for legend).

4.4.1 Comparison of step response between tested materials

A comparison of the step responses between tested materials with approximately equal shape factors is shown in Figure 4-13. The step responses are shown with the un-normalized and normalized displacement. It is clear in the normalized step response that the Latex/Natural Rubber Shore 40A specimen has a considerable shorter creep process, and that the Buna-N Shore 40A and Viton Shore 75A rubber show fairly similar creep properties.

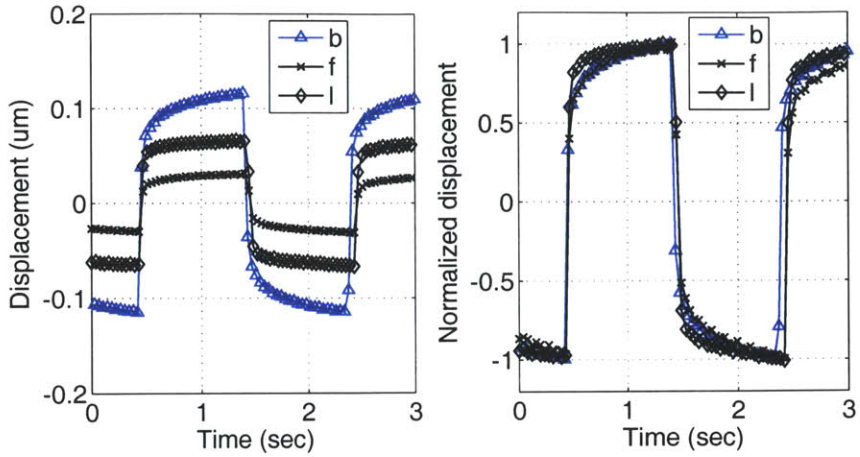

Figure 4-13: Comparison of step response for different materials, (b) Buna-N Shore 40A, (f) Viton Shore 75A, (l) Latex/Natural rubber Shore 40A (refer to table 4.2 for legend).

4.4.2 Effect of shape factor

The effect of the shape factor on the step response was found insignificant for most of the tested samples as shown in the case of Buna-N in Figure 4-14, and in the case of Latex/Natural rubber in Figure 4-16. Only Viton shows slightly less creep for smaller shape factors, as shown in Figure 4-15.

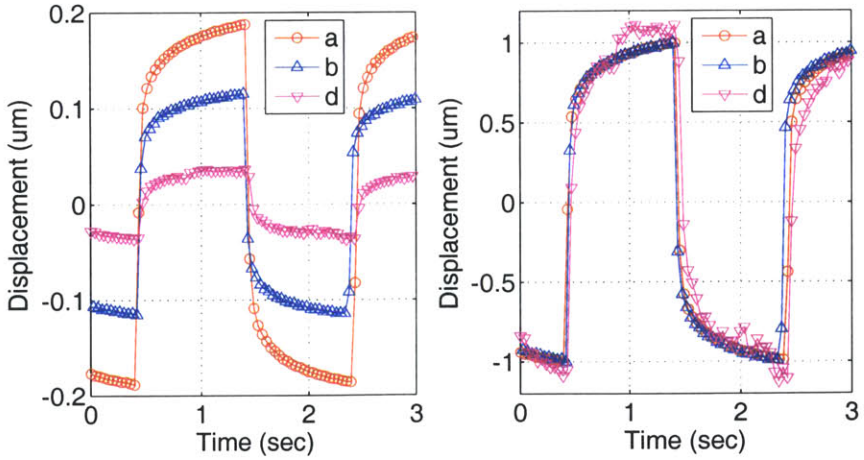

Figure 4-14: Step response for Buna-N Rubber Shore 40A for different shape factors, (a) $S = 3.6$, (b) $S = 6$, (d) $S = 8.9$ (refer to table 4.2 for legend).

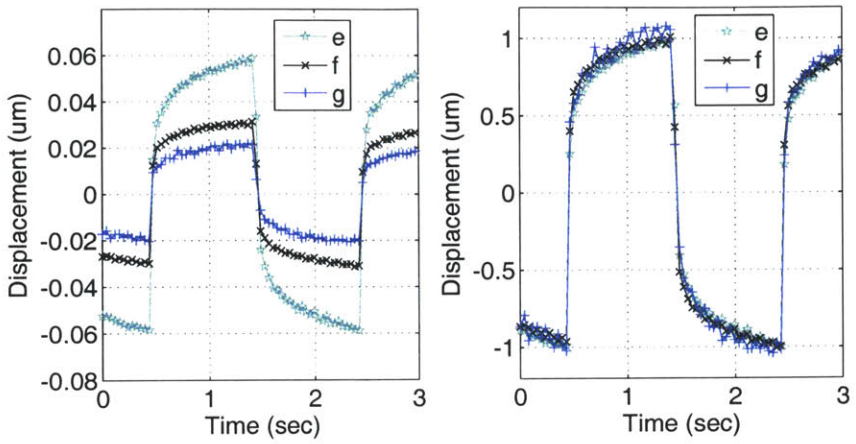

Figure 4-15: Step response for Viton Shore 75A for different shape factors, (a) $S = 3.4$, (b) $S = 6.8$, (c) $S = 10.1$ (refer to table 4.2 for legend).

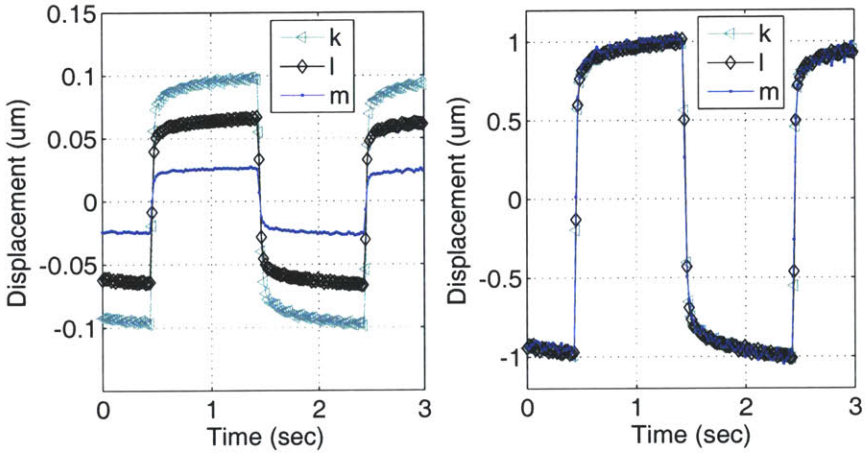

Figure 4-16: Step response for Latex/Natural Rubber Shore 40A for different shape factors, (a) $S = 3.3$, (b) $S = 6.7$, (c) $S = 10$ (refer to table 4.2 for legend).

4.5 Comments

The compression tests shown in this chapter are useful for understanding the behavior of thin rubber bearings under compression both static and dynamic. The results have shown that to assure a high compression stiffness adequate bonding of the load carrying surfaces is required. This compression stiffness is also limited by the ad-

equate contact with the steel surfaces. Samples were prepared for testing with the limitations of bonding only one side of the specimen. Both sides of the specimen could actually be bonded using metal shims. This wasn't done due to lack of time but is highly recommended.

The next Chapter will show the shear test of rubber pads both static and dynamic.

Chapter 5

Rubber Shear Test Results

The rubber shear test device is used to test thin rubber samples with a thickness between $0.5 - 1.0$ mm. The materials tested under shear are Buna-N, Viton, Silicone rubber, Neoprene and EAR C-1002. The Shore A hardness of the samples ranges from 35 to 80.

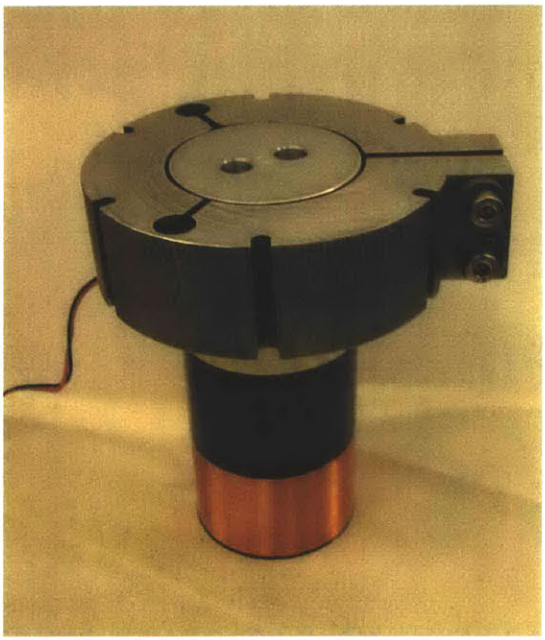

Figure 5-1: Shear test assembly of sample holder, rubber sample, target shaft, and voice coil actuator coil holder.

The design of the hardware used to perform the shear tests is presented in Section 3.2. The testing of the sample is done by first applying to it preload between the target shaft and the sample holder. The preload can be varied with the aid of the preload bolts and Belleville springs shown in Figure 5-1. The sample is subject to static and/or dynamic shear load provided by the voice coil actuator. The shear displacement is measured with the capacitance gage and the force is indirectly measured by measuring the voice coil actuator current with the aid of a sense resistor.

5.1 Sample fabrication

The rubber sample requires to be preloaded in order to provide the necessary friction and prevent slip under a shear load. The preload is as well applied in order to study its effect in the shear properties of the rubber sample. The rubber requires to have at least one load carrying surface bonded to a rigid surface to avoid creep under when preload is applied. Using an aluminum sheet as the rigid surface instead of the shaft avoids the need of constantly removing the sample from the shaft with the use of a razor blade and cleaning the adhesive from the shaft with the use of solvent.

The rubber samples for the shear tests consist of rectangular sheets cut out of rubber sheets of the desired material and formed over a round shaft. This are fabricated by first placing an aluminum sheet (0.050mm thick) over a round shaft as shown in Figure 5-2 (a). Next it follows the bonding of the oversized rectangular rubber sheets with the respective adhesive as shown in Figure 5-2 (b), applying the neccesary pressure to get rid of the excess adhesive. After waiting an adequate curing time, the bonded aluminum sheet and rubber sheet is removed. Then the rubber samples are cut out with sharp scissors or an x-acto knive to the desired dimensions. The fabricated samples are shown in Figure 5-2 (c).

Once the rubber samples are fabricated they are placed between the OD of the

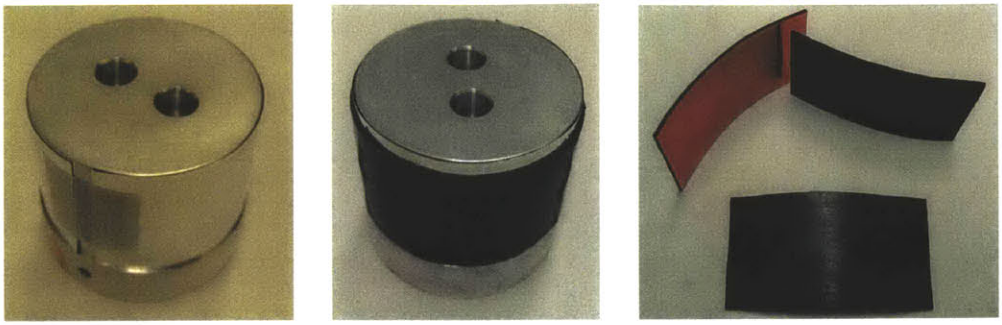

(a) (b) (c)

Figure 5-2: Shear test rubber samples fabrication

correct size shaft and the sample holder, as shown in Figure 5-3. The samples are then preloaded to the desired preload with the aid of the preload bolts and Belleville springs.

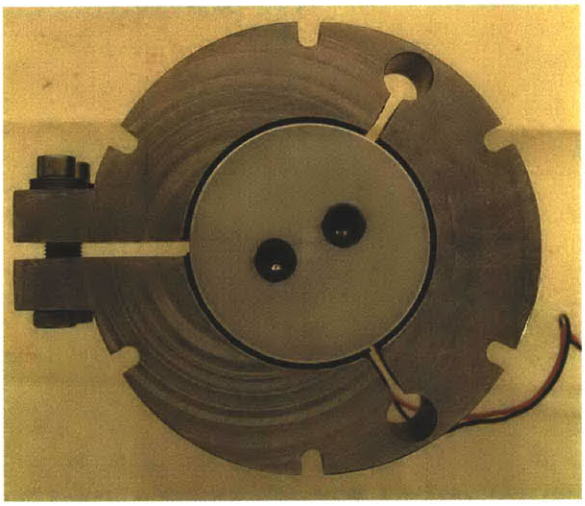

Figure 5-3: Top view of shear test assembly of sample holder, rubber sample and target shaft.

To accomodate for the different thicknesses of the rubber specimens several shafts were fabricated with different diameters ranging from ϕ38.7 mm to ϕ40.3 mm. Figure 5-3 shows the sample holder and shaft assembled with a rubber sample in place.

The tested rubber samples have an arc length dimension B, height H, and thickness t as defined in Figure 5-4. By changing the sample dimensions one can to test them at higher strains by reducing the loaded area, and also further regulate the amount of preload pressure.

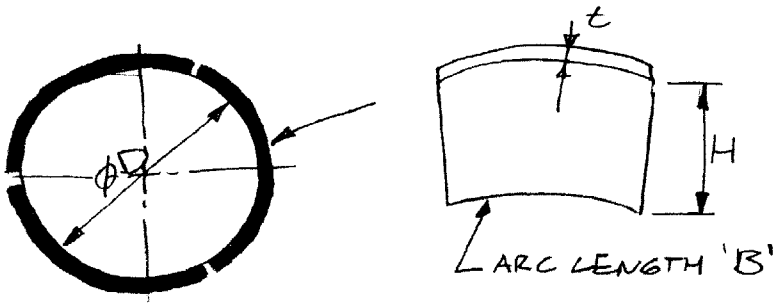

Figure 5-4: Shear sample dimensions.

Table 5.1 shows the parameters of the tested shear rubber samples.

5.2 Static Stiffness

The rubber samples are subject to a shear load while measuring their displacement with the capacitance gage. The applied shear loads range from $0-6N$ and are applied in an step-wise manner. The recorded displacement is the steady-state one which is achieved in the order of seconds. Static deflections on the order of 260 nm to 8 μm could be accomplished.

Table 5.1: Parameters of shear rubber samples,(notes: (1) after 35 days of fatigue test)

Key	Material	Shore	B (mm)	H (mm)	t (mm)	A (mm^2)	Preload (MPa)	notes
BN1	Buna-N	40A	40	20	0.84	800	6.9	
BN2	Buna-N	50A	40	20	0.85	800	6.9	
C1	EAR C-1002	50A	25	20	0.70	500	4.9	
N1	Neoprene	40A	40	20	0.80	800	0.2	
N2	Neoprene	40A	40	20	0.80	800	0.4	
N3	Neoprene	40A	40	20	0.80	700	3.4	
N4	Neoprene	50A	35	20	0.75	700	1.8	
N5	Neoprene	50A	35	20	0.75	700	3.7	
N6	Neoprene	70A	35	20	0.77	700	0.4	
N7	Neoprene	70A	35	20	0.77	700	3.7	
N8	Neoprene	80A	35	20	0.77	700	0.4	
N9	Neoprene	80A	35	20	0.77	700	1.8	
N10	Neoprene	80A	35	20	0.77	700	3.7	
S1	Silicone	35A	25	20	0.5	500	0.8	
S2	Silicone	35A	25	20	0.5	500	0.8	(1)
S3	Silicone	40A	40	20	0.99	800	3.4	
S4	Silicone	50A	40	20	0.94	800	1.7	
S5	Silicone	50A	40	20	0.94	800	3.4	
V1	Viton	75A	40	20	0.71	800	0.4	
V2	Viton	75A	40	20	0.71	800	1.0	
V3	Viton	75A	40	20	0.71	800	1.7	
V4	Viton	75A	40	20	0.71	800	3.4	
V5	Viton	75A	40	20	0.71	800	6.9	

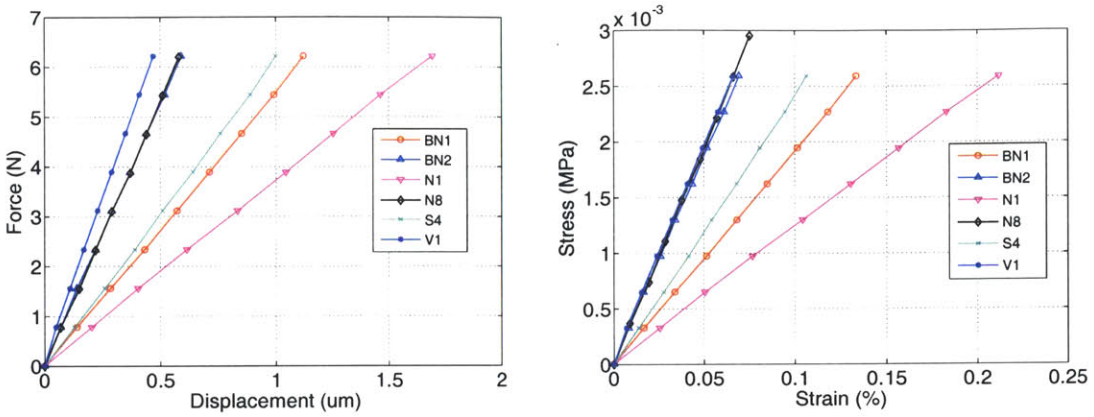

(a) (b)

Figure 5-5: Shear static stiffness results for selected materials (a) Force vs. Displacement, (b) Shear Stress vs. Strain (refer to table 5.1 for legend)

5.2.1 Linearity

As shown in Section 2.2.4 it is noted by Lindley [16] that the shear-strain curves of rubber are linear for strains below 50%.

The strains applied to the tested samples where in their majority below 0.2%. It can be seen in Figure 5-5 that the shear-strain curves of the tested samples are linear.

5.2.2 Effect of Preload

As noted by Gent [9] the shear stiffness (or shear modulus) of components of high shape factor increases as a compressive load is applied. It is further noted that the this effect increases with increasing shape factor and compressive strain.

The tested samples are subject to different compressive preload pressures with the aid of the preload mechanism shown in Figure 5-3.

The experimentally measured static shear modulus G for the different tested materials against preload pressure is shown in Figure 5-6 and Table 5.2. Table 5.2 shows a term χ_p = which is the ratio of the shear modulus of the rubber modulus with preload with respect to the theoretical one without preload (taken from Table 5.3). It can be seen in this figure how G increases with preload for all the tested samples. It is important to notice that the samples with higher Shore hardness show higher increment of Shear Modulus G with preload pressure.

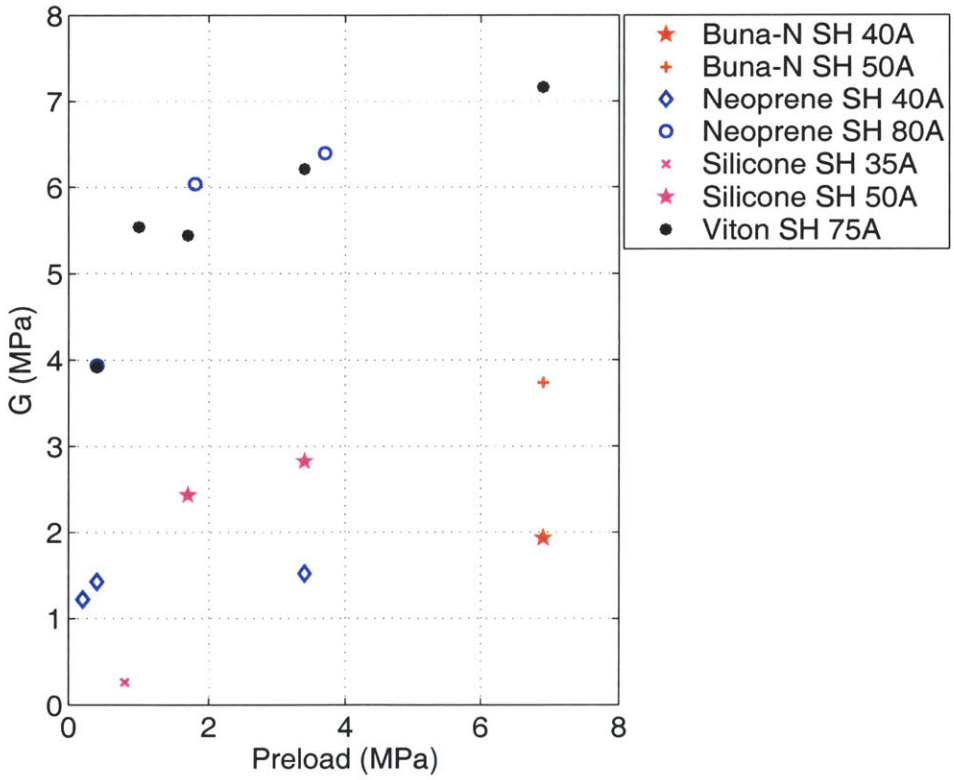

Figure 5-6: Static Shear Modulus G as a function of preload pressure.

Table 5.3 shows the shear modulus, and shear stiffness of the tested samples based on 2.11

$$k_s = 3\frac{GA}{t} \tag{5.1}$$

Table 5.2: Tabulated static shear modulus G and shear stiffness k_s as a function of preload pressure

Key	Material	Shore	Preload (MPa)	G (MPa)	k_s (N/μm)	$\chi_p =$
BN1	Buna-N	40A	6.9	1.94	10.9	4.0
BN2	Buna-N	50A	6.9	3.74	20.7	5.4
N1	Neoprene	40A	0.2	1.22	7.2	2.5
N2	Neoprene	40A	0.4	1.43	8.4	2.9
N3	Neoprene	40A	3.4	1.52	9.0	3.1
N8	Neoprene	80A	0.4	3.94	19.6	1.5
N9	Neoprene	80A	1.8	6.04	30.0	2.3
N10	Neoprene	80A	3.7	6.39	31.8	2.4
S4	Silicone	50A	1.7	2.44	12.2	3.5
S5	Silicone	50A	3.4	2.83	14.2	4.1
V1	Viton	75A	0.4	3.92	26.0	1.7
V2	Viton	75A	1.0	5.54	36.8	2.4
V3	Viton	75A	1.7	5.45	36.2	2.4
V4	Viton	75A	3.4	6.21	41.2	2.7
V5	Viton	75A	6.9	7.17	47.6	3.2

where $A = B \cdot H$ is the area of each pad, t is the thickness, and G is the shear modulus taken from the Table 2.1.

The shear modulus and shear stiffness of the rubber samples were measured under preload. To measure the shear modulus and stiffness without preload the sample requires to be bonded to the shaft and sample holder to avoid slip. To do this a new shaft and sample holder will be required for each sample, or a long adhesive removal procedure like soaking the assemble in solvent, will be required.

Comparing Table 5.2 and Table 5.3 it can be seen that the preloaded sample shows a shear modulus and stiffness higher than the theoretical shear modulus and stiffness of the sample without preload. This agrees with the increase of shear modulus and stiffness shown by the shear tests.

Table 5.3: Theoretical static shear modulus G and shear stiffness k_s without preload

Key	Material	Shore	G (MPa)	k_s (N/μm)
BN1	Buna-N	40A	0.488	2.7
BN2	Buna-N	50A	0.690	3.8
N1-N3	Neoprene	40A	0.488	2.9
N8-N10	Neoprene	80A	2.683	13.3
S1-S2	Silicone	35A	0.429	2.1
S4-S5	Silicone	50A	0.690	3.5
V1-V5	Viton	75A	2.269	15.1

5.3 Dynamic Stiffness

The dynamic stiffness tests are performed with the sample under preload. This preload is required to provide the necessary friction and avoid slip of the sample under shear load. The preload is applied as well to study its effect on the dynamic properties of the sample. This preload can be varied by stacking in different sizes and arrangements Belleville springs as shown in Figure 5-3.

5.3.1 Effect of Shore Hardness

Rubber hardness is increased by the addition of fillers like carbon black. As noted by Lindley [16] the addition of this fillers affects the dynamic properties of rubber. It is shown by Lindley that for Natural rubber the addition of fillers have a considerable stiffening effect on the low frequency complex modulus of rubber and much lower effect on the high frequency complex modulus. It is also shown that the addition of fillers to natural rubber decreases the loss factor.

The experimentally measured shear modulus G for Neoprene with different Shore hardnesses and approximately equal preload is shown in figure 5-7. The low frequency G of Neoprene increases with increasing Shore hardness, and the phase advance or loss decreases. Because the loss of the Neoprene rubber decreases with hardness along

with the increase of G with frequency. The Shear modulus of Neoprene increases by a factor of 123, 57 and 22 for Shore 50A, 70A and 80A respectively.

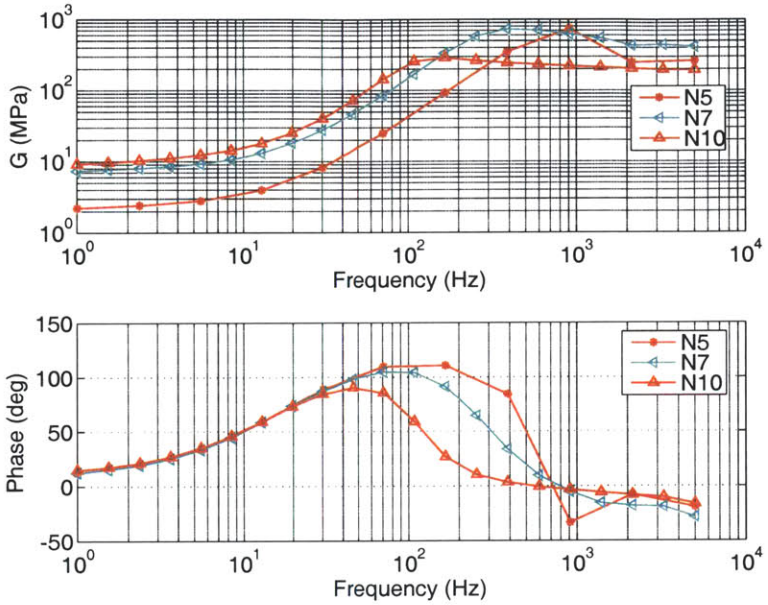

Figure 5-7: Complex shear modulus of Neoprene rubber for different Shore hardness, plotted against frequency, (N5) 50A, (N7) 70A, (N10) 80A (refer to table 5.1 for legend).

5.3.2 Effect of Preload

When a rubber shear element is subject to preload its internal pressure is increased and this results in an increase of its shear modulus and decrease of loss in the rubbery region (low frequency region) as shown in Section 2.3.12.

The experimentally measured shear modulus G for Neoprene with different preload pressures and the same Shore hardness is shown in Figure 5-8. The low frequency G for Neoprene rubber increases with increasing preload, and the phase advance decreases. Figure 5-8 (a) shows how the phase advance for Neoprene Shore 40A is significantly affected at low frequency and that the high frequency G and phase ad-

vance remain similar in magnitude. On the other hand, Figure 5-8 (b) shows how the phase advance for Neoprene Shore 80A is reduced at low frequency but has a major reduction in the transition region, and that the high frequency G and phase advance remains similar in magnitude.

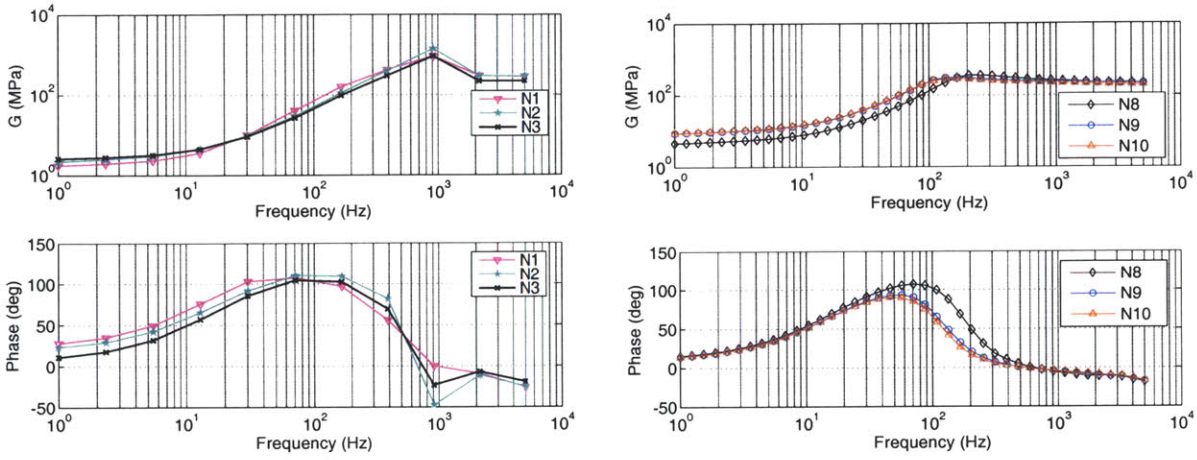

Figure 5-8: Complex shear modulus of Neoprene rubber for different preload pressures, plotted against frequency, (a) Shore 40A, (b) Shore 80A (refer to Table 5.1 for legend)

The low frequency shear modulus G of Viton rubber Shore 75A increases with increasing preload, and the phase advance decreases. Figure 5-9 shows how the phase advance for Viton Shore 75A is reduced at low frequency but has a major reduction in the transition region, and that the high frequency G and phase advance remains similar in magnitude.

The increase of Shear Modulus G with frequency for the tested materials at different preload pressures is shown in Table 5.4 and in Figure 5-10. The table shows how for a given material the low frequency (1 Hz) shear modulus increases with preload, while the high frequency (2 kHz) shear modulus remains of similar magnitude. As a

consequence the ratio of Shear modulus at high frequecy to low frequency decreases with increasing preload. The figure shows the ratio between the Shear Modulus at high frequency (2 kHz) and low frequency (1 Hz) G_{HF}/G_{LF}, and it can be seen how it decreases with preload.

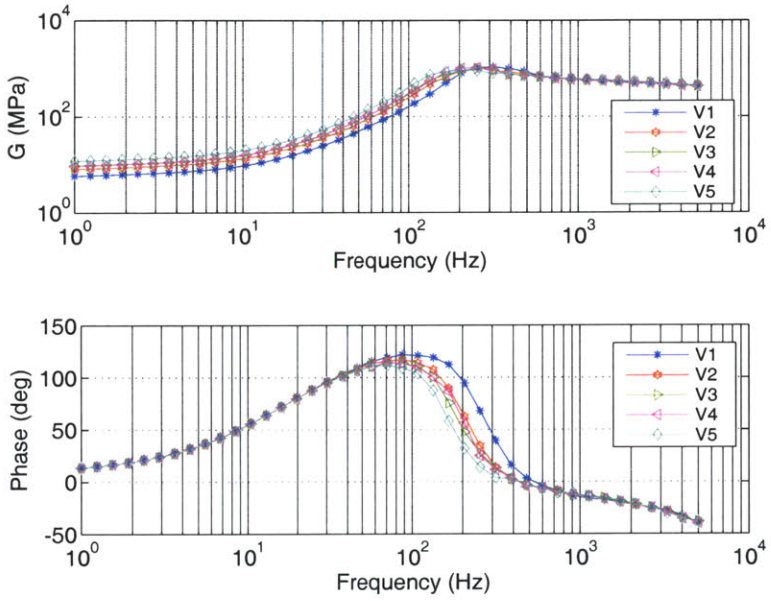

Figure 5-9: Complex shear modulus of Viton rubber Shore 75A for preload pressures, plotted against frequency (refer to table 5.1 for legend).

The higher Shore hardness materials show lower increase of shear modulus with frequency as it can be seen for the case of Neoprene in Table 5.4.

When low preload pressures are present the shear modulus strongly increases with frequency by $75 - 200$ times. When preload is applied the increase of shear modulus with frequency can be reduced to $20 - 120$ times. The strong increase of shear modulus with frequency can be a problem for high frequency designs, since it limits the high frequency strokes of a precision machine using rubber bearings. But one can design the precision machine taking this into consideration as well as being able to adjust the low frequency shear stiffness with preload.

Table 5.4: Tabulated values of low frequency shear modulus G_{LF} (at 1 Hz), high frequency shear modulus G_{HF} (at 2 kHz), and G_{HF}/G_{LF}

Key	Material	Shore	Preload (MPa)	G_{LF} (MPa)	G_{HF} (MPa)	G_{HF}/G_{LF}
BN1	Buna-N	40A	6.9	2.8	362	131
BN2	Buna-N	50A	6.9	5.0	606	121
C1	EAR C-1002	50A	4.9	1.2	278	232
N1	Neoprene	40A	0.2	1.8	285	161
N2	Neoprene	40A	0.4	2.2	285	128
N3	Neoprene	40A	3.4	2.6	223	86
N4	Neoprene	50A	1.8	2.0	186	95
N5	Neoprene	50A	3.7	2.2	260	118
N6	Neoprene	70A	0.4	5.3	397	74
N7	Neoprene	70A	3.7	7.3	411	56
N8	Neoprene	80A	0.4	4.7	217	47
N9	Neoprene	80A	1.8	9.0	217	24
N10	Neoprene	80A	3.7	9.0	193	21
S3	Silicone	40A	3.4	5.7	299	53
S4	Silicone	50A	1.7	3.2	241	76
S5	Silicone	50A	3.4	3.6	227	64
V1	Viton	75A	0.4	5.8	420	72
V2	Viton	75A	1.0	8.2	437	53
V3	Viton	75A	1.7	9.6	420	44
V4	Viton	75A	3.4	9.6	420	44
V5	Viton	75A	6.9	12.0	449	37

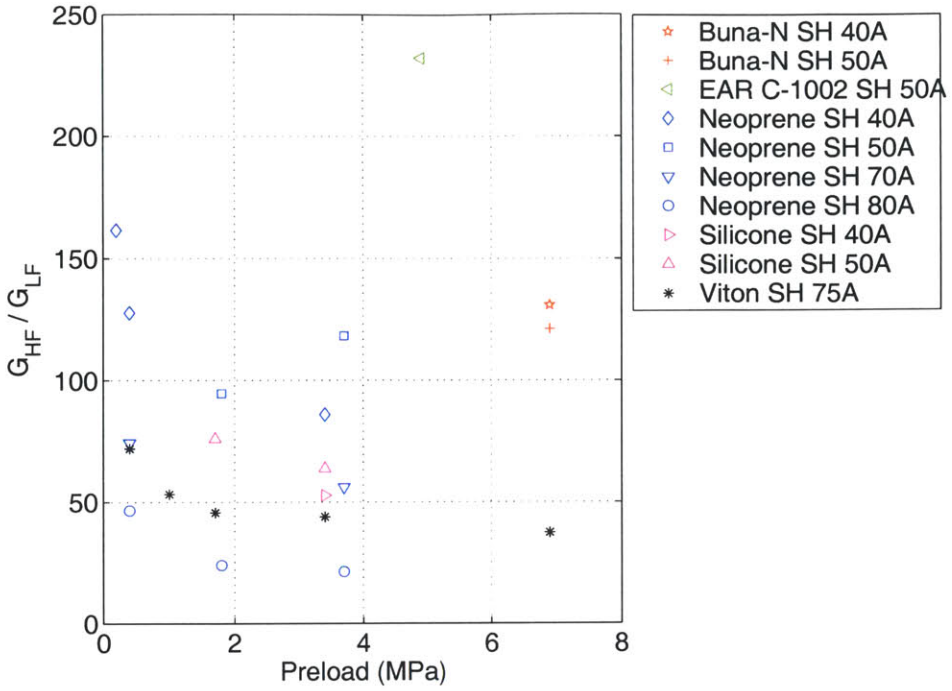

Figure 5-10: High to low frequency shear modulus ratio versus preload pressure.

5.4 Hysteresis

Hysteresis is measured for the tested materials at specifically chosen frequencies. The criteria for choosing these frequencies is based on recording the hysterisis at a low and a high frequency where loss is expected to be low, and at several frequencies within the transition region defined in Section 2.3.9, where the loss is expected to be high.

Hysteresis loops give an idea of the loss involved in the cyclic deformation of a material. As the loss η gets larger the hysteresis loop becomes thicker [14]. The hysteresis loops of the different tested materials is shown in Figures 5-11, 5-12, 5-13, and 5-14. It is hard to identify which sample shows more loss due to the different stiffness. It is easier to identify at what frequency a tested sample experiences greater loss. Section 5.4.1 calculates the loss factor based on this hysteresis loops, which helps making a better judgement of the loss involved in the cyclic deformation of the tested samples.

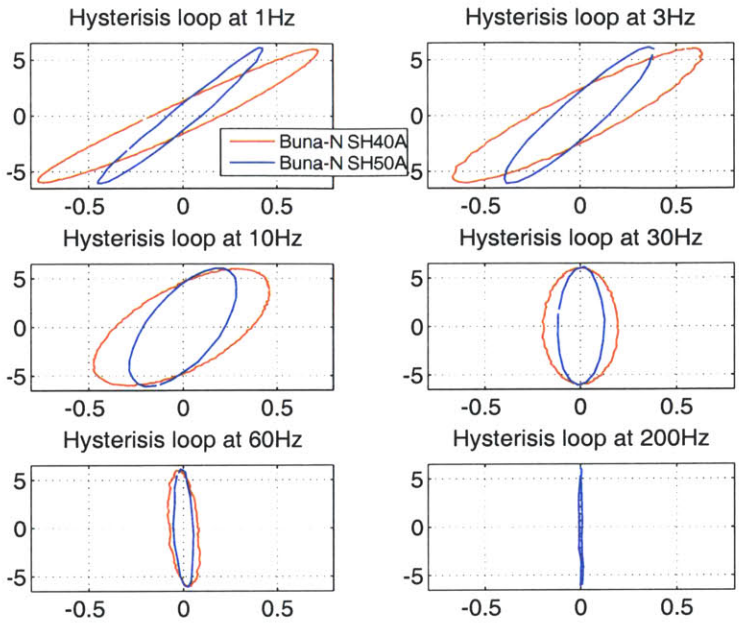

Figure 5-11: Shear Hysteresis Loops of Buna-N (Plots show Force (N) vs. Displacement (μm)).

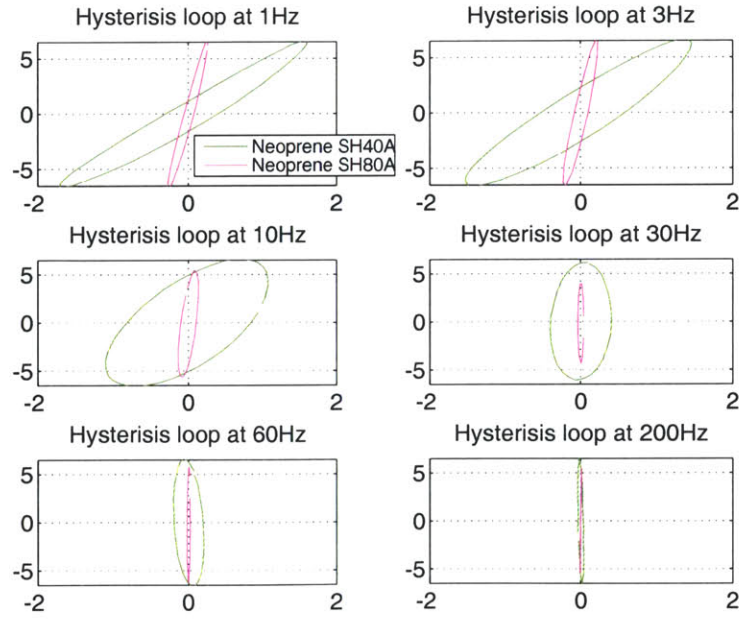

Figure 5-12: Shear Hysteresis Loops of Neoprene (Plots show Force (N) vs. Displacement (μm)).

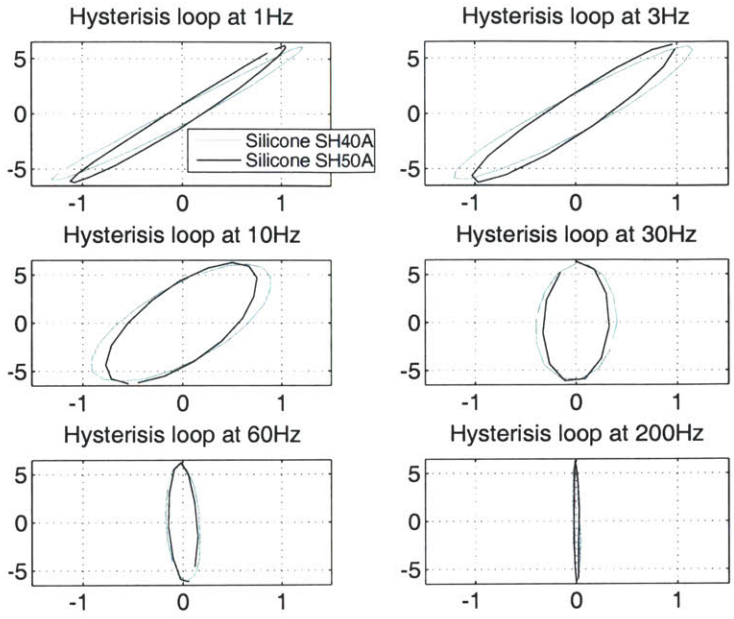

Figure 5-13: Shear Hysteresis Loops of Silicone (Plots show Force (N) vs. Displacement (μm)).

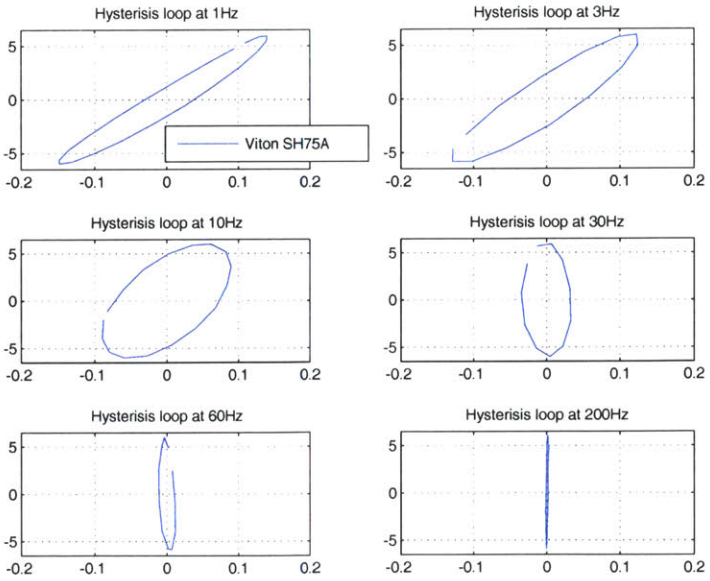

Figure 5-14: Shear Hysteresis Loops of Viton (Plots show Force (N) vs. Displacement (μm)).

5.4.1 Loss factor calculated from hysteresis

The loss factor can be calculated in several manners which are not necessarily compatible, specially when high damping is present. One method is to calculate the loss factor from the phase lag ε of the strain with respect to the applied stress with $\eta = \tan\varepsilon$. Another is by calculating the loss factor from the hysterisis loop with $\eta = D/2\pi U$, where D is the dissipated energy per cycle and U is the maximum strain energy. As stated by Nashif [11] "if the damping is high, $\tan\varepsilon$ will not be small" (p.49) and so it will differ greatly from the loss factor calculated from the hysterisis loop. One must use a single method to compare the loss properties of materials, and the value of the loss factor is usually below 1 for low loss materials but can be higher than 1 when high damping is present.

The loss factor is calculated numerically from the hysteresis loops. First the energy dissipated per cycle D is found by integrating the hysteresis loop to find its area. Second the maximum strain energy U is calculated. And finally the loss factor is found by the equation $\eta = D/2\pi U$ [14]. All this is done numerically with a developed code shown in Appendix A.1.

The highest loss takes place in the transition region, as shown in Figure 5-15. This is anticipated by the phase advance from the experimentally measured frequency responses in Section 5.3.

Tested materials with lower Shore hardness tend to have a higher loss factor than the ones with higher Shore hardness. This can be seen in Table 5.5 which shows the highest recorded loss factor of each tested material and its corresponding frequency.

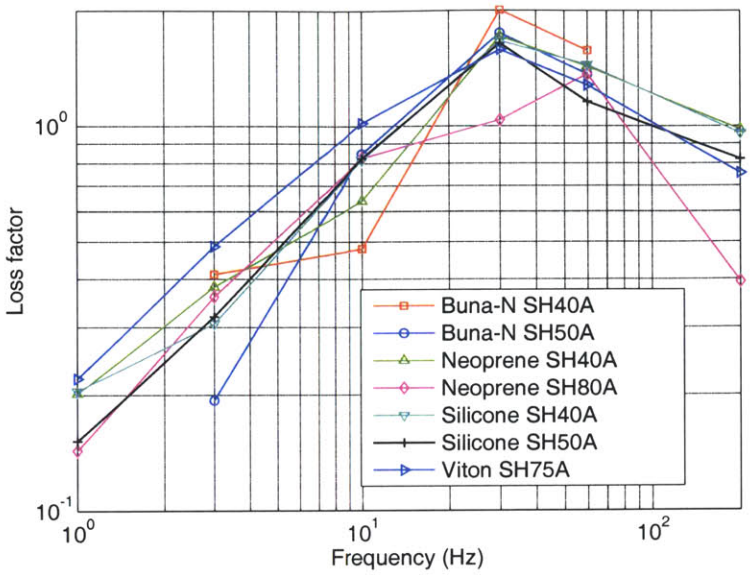

Figure 5-15: Shear Loss factor of tested samples.

Table 5.5: Highest loss factor for shear rubber samples

Material	Shore	Loss factor η	Frequency (Hz)
Buna-N	40A	2.00	30
Buna-N	50A	1.74	30
Neoprene	40A	1.71	30
Neoprene	80A	1.36	60
Silicone	40A	1.66	30
Silicone	50A	1.64	30
Viton	75A	1.57	30

5.5 Step response

All the samples are subject to a 0.5 Hz square wave force of 11 N pk-pk, which is accomplished by driving the voice coil actuator with a current source amplifier that has a bandwidth of about 50 kHz.

The step responses of the tested samples show a rapid elastic response in the order of 0.1 milliseconds, followed by a slow creep on the order of seconds, which is similar to the compression test step response behavior. As discussed in Section 2.3.1 polymers' structure can rearrange on a local scale relatively rapid, which explains the initial rapid response, but rearrangements on the long-range scale are very slow, which explains the slow creep process. Figure 5-16 shows the shear step response of a Buna-N Shore 40A sample as reference.

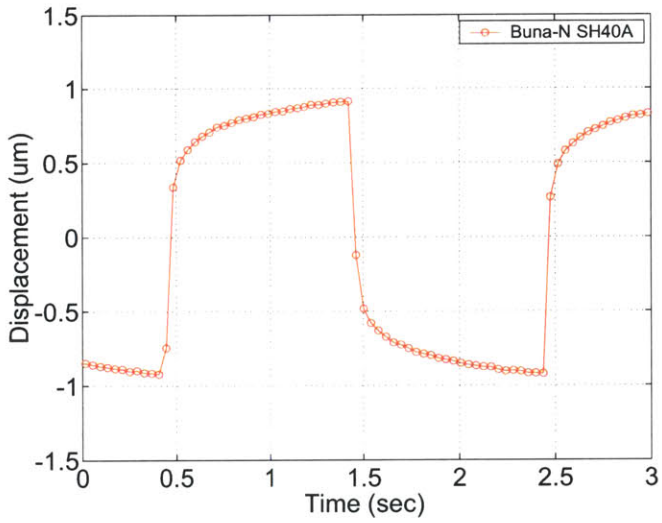

Figure 5-16: Shear Step response of Buna-N Shore 40A (refer to table 5.1 for legend).

All of the step responses for the rubber specimens are measured with a preload pressure of about 0.8 MPa. The step responses are not measured at different preload pressures.

5.5.1 Comparison of step response between tested materials

A comparison of the step responses between tested materials is shown in Figure 5-17. The step responses are shown with the un-normalized and normalized displacement. It is clear in the normalized step response that the Silicone Rubber Shore 40A spec-

imen has the shorter creep process, followed by Neoprene Shore 40A, and finally followed by Viton Shore 75A with Buna-N Shore 40A, which show fairly similar creep properties. (The idea here was to compare materials with the same Shore hardness, but Viton was unavailable in Shore 40A for the desired thickness).

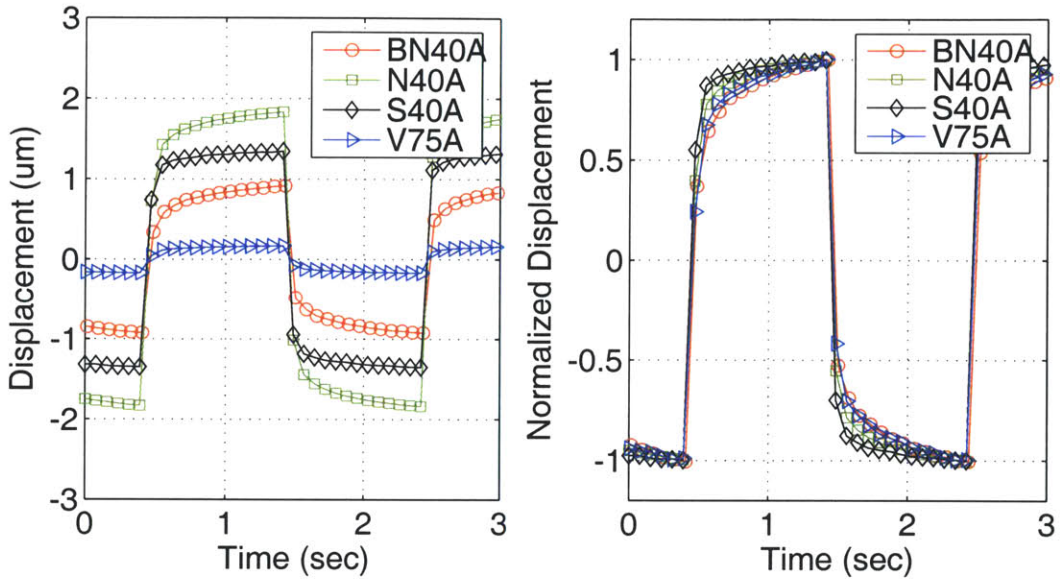

Figure 5-17: Comparison of shear step response for different materials.

5.5.2 Effect of Shore Hardness

The step response of given materials with different Shore hardness is compared in this Section. The Shore hardness has shown a minor effect on the step response.

It can be seen in Figure 5-18 how for tested silicones the normalized step response came out as being practically equal. For the case of the tested Neoprene samples as shown in Figure 5-19 the harder Shore 80A sample showed a slightly longer creep process than the softer Shore 40A sample. On the other hand the the harder Shore 50A Buna-N sample showed a slightly shorter creep response than the softer Shore 40A sample, as shown in Figure 5-20.

No actual correlation between creep response and Shore hardness can be established with the set of conducted experiments.

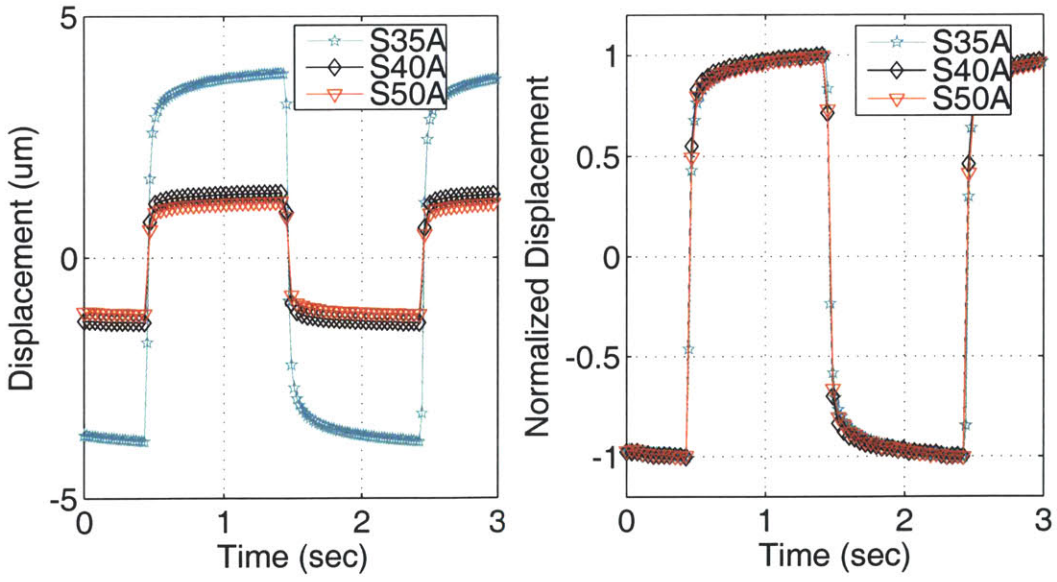

Figure 5-18: Comparison of shear step response of Silicone rubber for different Shore A hardness.

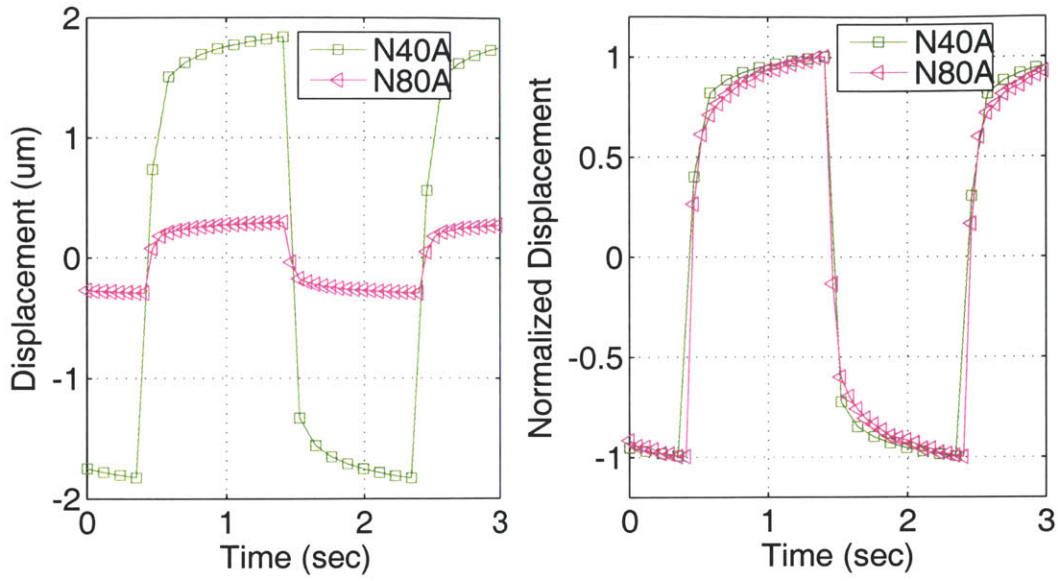

Figure 5-19: Comparison of shear step response of Neoprene rubber for different Shore A hardness.

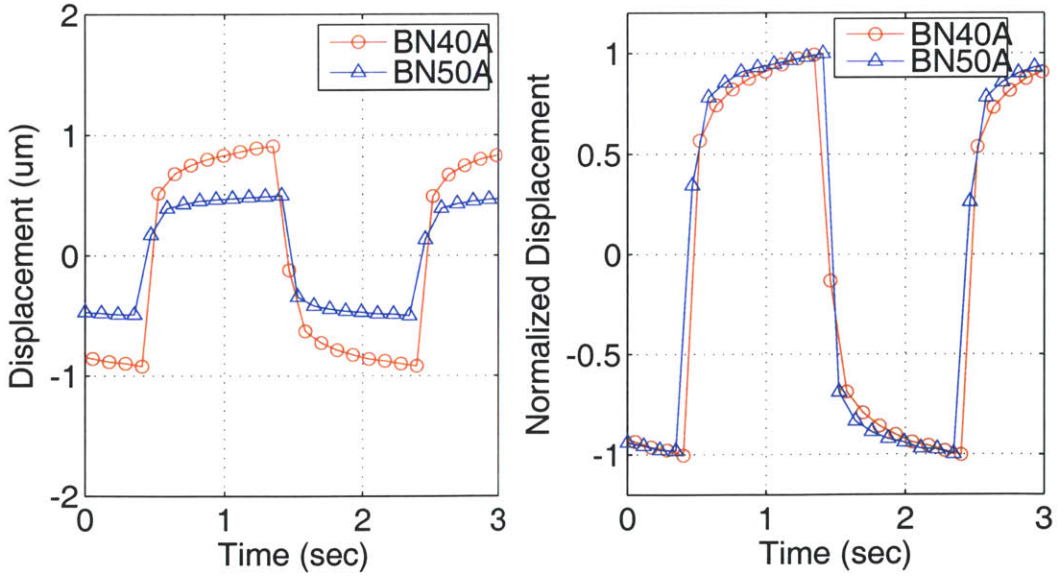

Figure 5-20: Comparison of shear step response of Buna-N rubber for different Shore A hardness.

5.6 Fatigue Tests

Reliablility of the rubber bearing is very important in order to consider it for being used in precision machines. For the bearing to be reliable is essential that its fatigue life is long enough, and if possible "infinite".

Gent [9] notes that mechanical fatigue is demonstrated in rubbery materials by a progressive weakening of physical properties as a result of slow crack growth during application of dynamic loads or deformation.

As presented in Section 2.4.1 Gent [9] observes that when reducing the dynamic stress or strain to a certain value the fatigue life of rubber approaches infinity, as shown on a typical $S - N$ curve for rubber in Figure 2-20. This concept is called limiting stress or strain. This concept is really important since if infinite life can be assured in a rubber bearing then replacement of it could be avoided, increasing the rubber bearing reliability.

The fatigue tests consists in applying a cyclic sinnusoidal force to the samples at a fixed chosen frequency. The chosen frequency is of 100 Hz because of being an intermediate frequency within the tested range that will permit a reasonable strain of the sample and at the same time a reasonable amount of cycles. The amount of cycles accomplished with this test frequency is about 8.64 million cycles per day. The strain accomplished with the chosen samples are 0.16% pk-pk for the Silicone Shore 35A (S1 from Table 5.1), and 0.004% pk-pk for the Neoprene Shore 80A (N8 from Table 5.1).

While the samples are subject to the cyclic strain, the dynamic stiffness, and phase are recorded in real-time with the aid of a developed dSpace model and Matlab code. The simple dSpace model is shown in Figure 5-21, and the matlab code is shown in Appendix A.2.

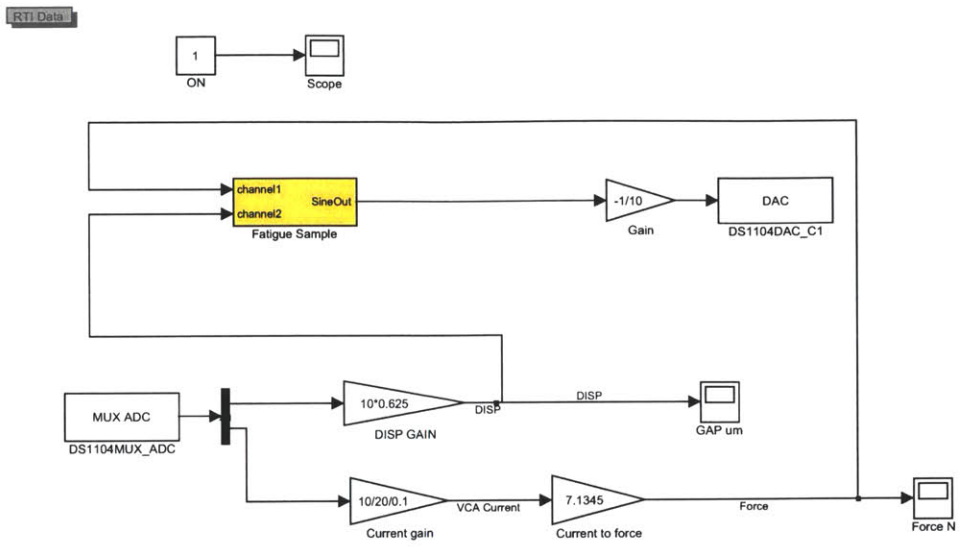

Figure 5-21: dSpace model for fatigue test.

The developed Matlab code lets you specify the testing frequency as well as the time intervals to take the dynamic stiffness and phase measurements in real-time. The dynamic stiffness is done by applying A discrete Fourier Transform of the measured cyclic force and displacement is taken, and then used to find the magnitude and phase of the tested sample complex stiffness at the given test frequency. All this is done in real-time at the user specified time intervals.

5.6.1 Silicone SH35A

The Silicone SH35A sample was subject to fatigue testing for about 35 days at 100 Hz and a strain of 0.16% pk-pk (0.8 μm pk-pk). The recorded shear stiffness and phase angle during the lapse of the fatigue test is shown in Figure 5-22. The stiffness shows a quasi-constant rise of stiffness from an initial value of 13.3 N/μm to 14.6 N/μm, which accounts for a 9.8% rise in stiffness. The phase has a quasi-constant decrement from 117.7^o to 117.1^o which accounts for a 0.5% reduction.

This result looks promising since the properties of the sample suffered just a moderate change of stiffening manner, showing no signs of an upcoming fatigue failure, after being subject to $294 \cdot 10^6$ cycles at 0.16% pk-pk strain.

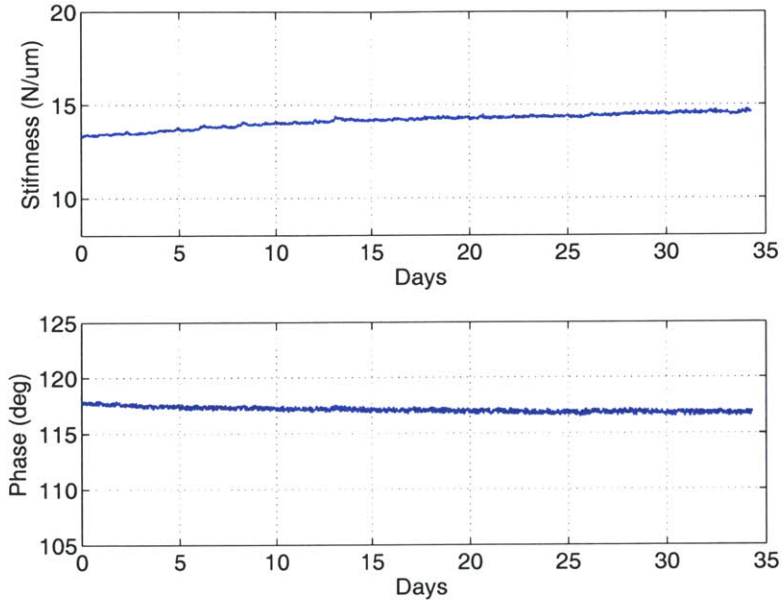

Figure 5-22: Fatigue test recorded shear stiffness and phase for Silicone SH35A.

5.6.2 Neoprene SH80A

The Neoprene SH80A sample was subject to fatigue testing for about 24 days at 100 Hz and a strain of 0.004% pk-pk (0.03 μm pk-pk). The recorded shear stiffness and phase angle during the lapse of the fatigue test is shown on figure 5-23.

The noise coming from the displacement sensor (capacitance gage) accounts for about 5 nm pk-pk, which could generate a maximum noise in our stiffness measurement of about 50 N/μm. Even with noise within the measurements the stiffnes remains between 295 N/μm to 340 N/μm which is about 14% pk-pk change in stiffness. The change in phase is practically unnoticeable being less than 0.5%.

This result looks promising as well since the properties of the sample didn't suffer an appreciable change, showing no signs of an upcoming fatigue failure, after being subject to $207 \cdot 10^6$ cycles at 0.004% pk-pk strain.

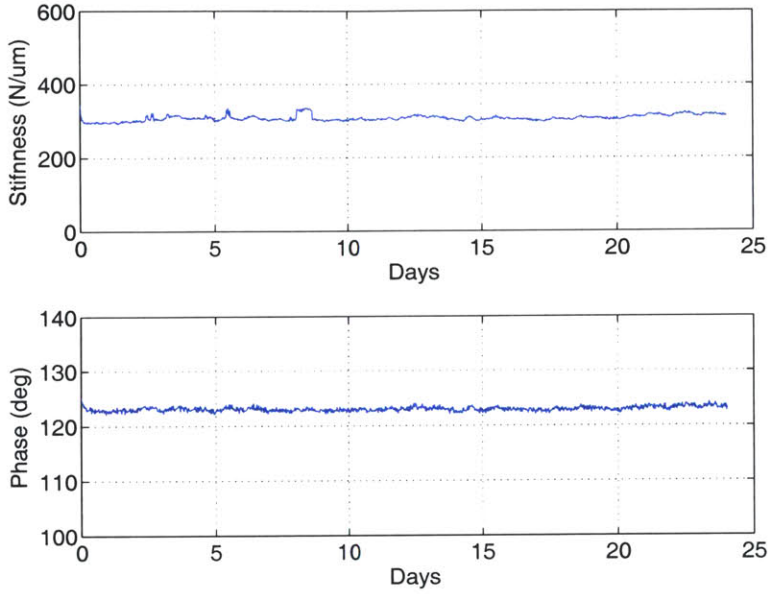

Figure 5-23: Fatigue test recorded shear stiffness and phase for Neoprene SH80A.

5.7 Comments

The shear tests have given us important information regarding the behavior of the rubber pads under shear, which serves in the design of rubber bearings.

One of the most important findings from the tests is how strongly the stiffness rises with frequency to about $75 - 200$ times with low preload. This can be regulated with preload and reduced to $20 - 120$ times. High Shore hardness materials show the lowest increase in stiffness with frequency and are a good choice when the high rise of stiffness with frequency is not desired.

As shown in Section 5.6 rubber pads can sustain hundreds of million of cycles of

under shear strain for the tested shear strains, without failure. Further fatigue tests are recommended, but the performed tests already predict the possibility of excellent fatigue properties of rubber bearings.

The next Chapter gives guidelines for the design of rubber bearings for precision machines. This Chapter takes into consideration both the results from the compression and shear tests from Chapter 4 and the current Chapter.

Chapter 6

Design of rubber bearings for precision machines

In this chapter further analysis required for the design of rubber bearings is made. Manufacturing methods for the laminate rubber bearings are also presented. Different topologies of linear and rotary bearings are shown, and compared.

6.1 Compression stiffness of bonded rectangular rubber blocks

The compression stiffness of circular disks is presented in section 2.2.2. This is taken as a reference for calculating the compression stiffness of rectangular blocks and is taken as a good estimate. A derivation of the compression stiffness of a bonded rectangular rubber block will follow.

When a bonded rectangular rubber block is subject to compression, the block will keep its volume quasi-constant due to the Poisson ratioν very close to 0.5. Because of this, bulging will occur all around the rectangular block as shown on figure 6-1. For calculating the compression stiffness the deformation of the rubber block will be

analyzed in two stages.

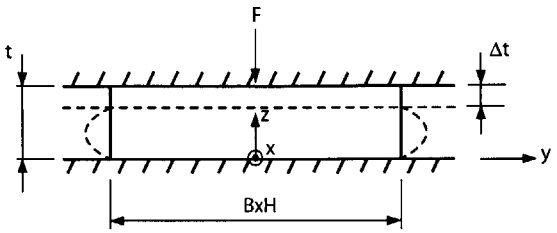

Figure 6-1: Compression of a bonded rectangular rubber block

The first stage is the homogeneous compression of the rubber block. For a homogeneous compression of a rubber block of thickness t by an amount Δt a force F_1 is required as shown on 2.2.1

$$F_1 = \frac{AE_0\Delta t}{t} \tag{6.1}$$

where $\Delta t/t = \epsilon$.

Since the upper and lower surfaces are bonded, no strain occurs on their faces and so the block must bulge around the block periphery. Taking into consideration a Poisson ratio of approximately $\nu \approx 0.5$ the volume will remain constant and the volume reduced by compression ($= BH\Delta t$) shall equal the volume of the bulge around the block V_bulge.

The bulge takes a parabolic form as it will be shown, due to the shear stress present in the bonded surface and the corresponding internal pressure which deforms the rubber outwards to keep the volume constant. Figure ($insertfigureshowingverticallinesdeformed$) shows how vertical lines in one of the planes of symmetry deform after compression. If we take a deformed differential volume $Bdxt$ as shown on figure 6-2 this will have shear stresses on the top and bottom of value $\tau_0(x)$, and a pressures acting on both sides denoted as P and $P + dP$. From this we get the following:

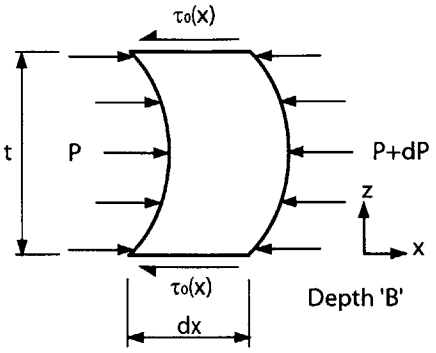

Figure 6-2: Differential bulging volume

$$\tau_0 = -\frac{t}{2}\frac{dP}{dx} \tag{6.2}$$

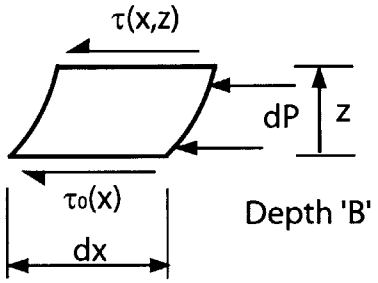

Figure 6-3: Partial differential bulging volume

Now taking a portion of the previous differential volume as shown in Figure 6-3 we can find the shear stress on the rubber as a function of the position within the thickness of the rubber as follows:

$$\tau(x,z) = \tau_0(x)\left[1 - \frac{2z}{t}\right] \tag{6.3}$$

The $Bdxdz$ element is sheared by the shear stress $\tau(x,z)$ as shown on figure 6-4 resulting in a deflection $d(\delta x)$ for an element of height dz, which integrated as shown will give the deflection δx

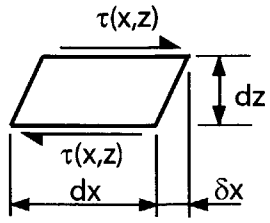

Figure 6-4: Shear of $Bdxdz$ volume

$$d(\delta x) = \frac{\tau_0(x,z)dz}{G} \tag{6.4}$$

$$\delta x = \frac{\tau_0(x)}{G}\left[z - \frac{z^2}{t}\right] \tag{6.5}$$

As mentioned earlier the bulge described by δx will take a parabolic form, and the maximum deflection will take place at $z = t/2$, as shown on figure 6-5, which we will call v_x

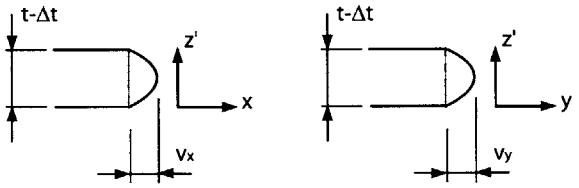

Figure 6-5: Bulge at free ends of rubber block

$$v_x = \delta_x(z = t/2) = \frac{\tau_0(x)t}{4G} \tag{6.6}$$

The shear stress $\tau_0(x)$ is taken as linear and will be defined as $\tau_0(x) = C_1 x$, giving as the following

$$v_x(x = H/2) = \frac{C_1 H t}{8G} \tag{6.7}$$

Combining (6.2) and (6.7), and taking into consideration the border condition of $P = 0$ at $x = H/2$ we get the following pressure distributions on the symmetry plains of the compression block

$$P(x, y = 0) = \frac{2GHv_x}{t^2}\left[1 - \frac{4x^2}{H^2}\right] \tag{6.8}$$

$$P(x = 0, y) = \frac{2GBv_y}{t^2}\left[1 - \frac{4y^2}{B^2}\right] \tag{6.9}$$

Now for $P(x = 0, y = 0) = \frac{2GHv_x}{t^2} = \frac{2GBv_y}{t^2}$ and so

$$Hv_x = Bv_y \tag{6.10}$$

The bulge volume can be calculated as follows:

$$V_{bulge} = BH\delta t = \frac{4}{3}(t - \delta t)[v_x(B + v_y) + v_y(H + v_x)] \tag{6.11}$$

$$BH\delta t = \frac{4}{3}(t - \delta t)[Bv_x + Hv_y] \tag{6.12}$$

where v_x and v_y have been taken as much smaller than B and H. Using (6.10) and (6.11) we find the following

$$v_x = \frac{3B^2H\epsilon}{4(B^2 + H^2)} \tag{6.13}$$

$$v_y = \frac{3BH^2\epsilon}{4(B^2 + H^2)} \tag{6.14}$$

where Δt is taken as much less than t and $\epsilon = \Delta t/t$.

So a pressure distribution of the following form is assumed

$$P(x,y) = \frac{3GB^2H^2\epsilon}{2t^2(B^2+H^2)}\left[1-\frac{4x^2}{H^2}\right]\left[1-\frac{4y^2}{B^2}\right] \tag{6.15}$$

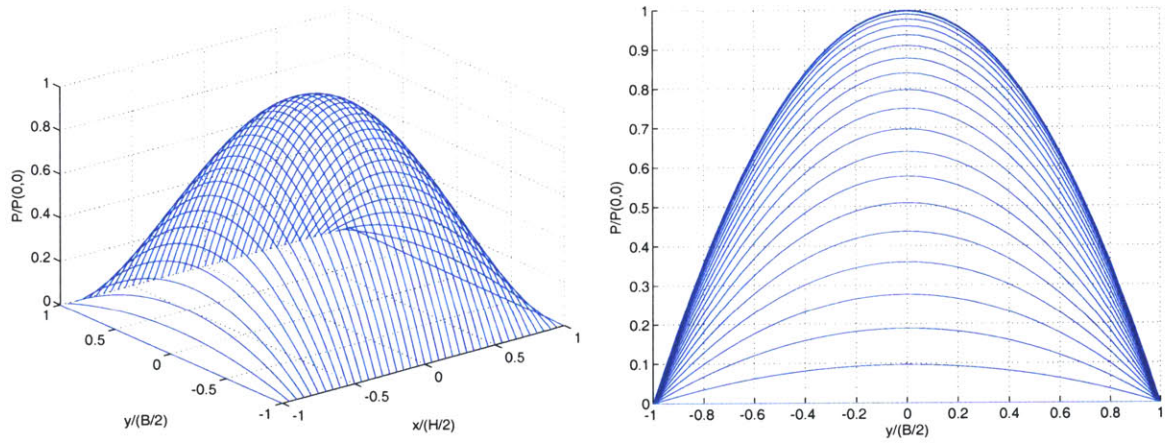

Figure 6-6: Pressure distribution related to the bulging of a rectangular rubber block under compression as defined by (6.15)

Integrating the pressure distribution defined by (6.15) and shown on figure 6-6 over the whole area will give us the force associated with the bulge $F_2 = \int_{-B/2}^{B/2}\int_{-H/2}^{H/2} P(x,y)\,dx\,dy$ which will give

$$F_2 = \frac{2GB^3H^3}{3t^2(B^2+H^2)}\epsilon \tag{6.16}$$

So adding up F_1 and F_2 from (6.1) and 6.16 we will have

$$F = E_0A\epsilon + \frac{2GB^3H^3}{3t^2(B^2+H^2)}\epsilon \tag{6.17}$$

which when taking into consideration $E_0 = 3G$ for $\nu \approx 0.5$ will reduce to the following

Table 6.1: Tabulated values for k_R

n	k_R
1	0.89
2	0.80
3	0.71
4	0.65
5	0.62
10	0.53
∞	0.44

$$F = E_0 A\epsilon \left[1 + \frac{2B^2H^2}{9t^2(B^2+H^2)}\right] \tag{6.18}$$

Taking a rectangle of sides B and $H = nB$, with n being the aspect ratio, the shape factor will be $S = \frac{nB}{2t(n+1)}$ and so (6.18) will take the form

$$F = E_0 A\epsilon \left[1 + 2k_R S^2\right] \tag{6.19}$$

$$E_c = E_0 \left[1 + 2k_R S^2\right] \tag{6.20}$$

where $k_R = \frac{4(n+1)^2}{9(n^2+1)}$, which will take the values shown on Table 6.1.

So the compression of a rectangle with the same shape factor as a circular disk can be expected to show less compression stiffness E_c being this even lower when n increases.

Taking into consideration the correction factor k given by Lindley as shown in (2.3), (6.21) becomes

$$E_c = E_0 \left[1 + 2k_R k S^2\right] \tag{6.21}$$

Taking into consideration the bulk modulus of rubber as shown in Section 2.2.2 the compression modulus of the bonded rectangular rubber block becomes

$$E_c = \left[\frac{1}{E_0 \left[1 + 2k_R k S^2\right]} + \frac{1}{E_\infty} \right]^{-1} \tag{6.22}$$

6.2 Laminate rubber bearings

Laminate rubber bearings consist of rubber and metal sheets bonded together in an alternate manner. This type of bearing has been widely used as bridge rubber bearings since the increase in compression stiffness of the rubber bearing is of great significance, while maintaining the same shear stiffness.

Rivin [17] has done research on ultra thin layered rubber-metal laminates. The results of the research have shown high compression E_c to shear modulus G ratios between 200 to 1000, utilizing rubber sheets thicknesses between 0.1 to 0.6 mm.

In this section insight will be given on why the use of rubber bearings in precision machines becomes much more attractive when the rubber-metal laminate approach is taken. Some insight will be given on how to size the intermediate metal sheets, and different alternatives of fabrication will be presented.

6.2.1 Compression to shear stiffness ratio

The compression to shear stiffness ratio of a single rectangular rubber sheet with the load carrying areas bonded to metal are given by (6.21) and (2.11) as follows,

$$\frac{k_c}{k_s} = \frac{E_0}{G} \left[1 + 2k_R k S^2\right] \tag{6.23}$$

where $S = BH/[2t(B+H)]$.

If N rubber sheets of thickness $t' = t/N$ are bonded to $(N+1)$ sheets of metal as shown in Figure (*laminatefigure*) the shape factor of each rubber sheet will be $S' = NS$. The total rubber thickness still remains the same t. The rubber-metal laminates will behave as N springs in series, each of them with the following stiffness,

$$k_{c1} = \frac{E_0 A\,[1 + 2k_R k N^2 S^2]}{t} \tag{6.24}$$

and an equivalent compression stiffness for the N springs in series of

$$k_c = \frac{E_0 A\,[1 + 2k_R k N^2 S^2]}{Nt} \tag{6.25}$$

The shear stiffness of a each rubber sheet will be

$$k_{s1} = \frac{GAN}{t} \tag{6.26}$$

and the shear stiffness of the rubber-metal laminate bearing will be

$$k_s = \frac{GA}{t} \tag{6.27}$$

So with (6.25) and (6.27) we can find the compression to shear stiffness ratio as follows

$$\frac{k_c}{k_s} = \frac{E_0\,[1 + 2k_R k N^2 S^2]}{NG} \tag{6.28}$$

Let's take as an example a rubber bearing made of a Shore 40A rubber, of the following dimensions $B = 40$mm, $H = 20$mm, and $t = 2$mm fabricated with a 1, 3

or 5 layers. Table 6.2 compares the compression to shear stiffness ratio of the three options. The increase of compression to shear stiffness becomes really significant when increasing the number of layers of the rubber-metal laminate bearing. But of course as the number of layers increases so does the fabrication complexity, especially for bearings for precision machines which are of reduced dimensions.

Table 6.2: Tabulated values for k_R

Layers	$N = 1$	$N = 3$	$N = 5$
k_c/k_s	61	172	285

6.2.2 Sizing of intermediate metal laminates

The intermediate metal laminates are subject to tension when the rubber-metal laminate bearings are subject to a compression load. Even though the strength of metal is high compared to rubber, failure can occur. Failure of the metal intermediate shims has been experienced by Rivin [17], at compression loads of 45 MPa for brass metal layers, and above 250 MPa for steel metal layers.

The metal sheets between rubber sheets are subject to shear stresses on the x-z and y-z plane, on both sides. This shear stresses can be calculated with (6.6), (6.13) and (6.14), having a maximum value of

$$\tau_{xmax} = \frac{3GnB}{(n^2+1)t_r}\epsilon \tag{6.29}$$

$$\tau_{ymax} = \frac{3Gn^2B}{(n^2+1)t_r}\epsilon \tag{6.30}$$

where n is the aspect ratio defined in Section 6.1, t_r is the rubber laminate thickness, and $\epsilon = \sigma_c/E_c$, with σ_c as the compressive stress and E_c the compression modulus of a single rubber sheet from (6.21).

By integrating the shear stress on both sides of the metal shims of thickness t_m, the normal stress acting on the shims can be found

$$\sigma_{nx} = \frac{Gn^2B^2}{2(n^2+1)t_r t_m}\epsilon \tag{6.31}$$

$$\sigma_{ny} = \frac{Gn^2B^2}{2(n^2+1)t_r t_m}\epsilon \tag{6.32}$$

The metal shims will be under a combined load condition, with a compressive stress σ_c in the z-direction, a tension stress σ_{nx} in the x-direction and a tension stress σ_{ny} y-direction. A failure criterion must be used to evaluate the resistance of the metal sheet. One of the recommended ones will be the Huber-Hencky-von Mises [10] theory as follows

$$\sigma_{eq} = \sqrt{\frac{(\sigma_1-\sigma_2)^2+(\sigma_1-\sigma_3)^2+(\sigma_2-\sigma_3)^2}{2}} < \sigma_y \tag{6.33}$$

where σ_1, σ_2 and σ_3 are the principal stresses, and σ_y the material yield strength.

6.2.3 Fabrication

The method of fabrication of laminate rubber bearings for precision machines should be effective and of low cost. The method of fabrication could range from hand-crafted to the high production rate machinery. The fabrication methods that will be presented in this section will be for curved rubber bearings, since the fabrication efforts were towards that type of configuration. The reason for this is that a rotary rubber bearing was desired to be used in a rotary precision machine.

The laminates as a finished product or part consist of sheets of rubber separated by metal plates (with the interfaces being properly bonded), and having the desired form. Different approaches can be taken for doing this. One of them will be to have

the metal shims pre-arranged with the desired arrangement to bound the form of the rubber bearing, and inject the un-vulcanized rubber between them, followed by vulcanization. A second approach will be to use vulcanized rubber sheets with the desired thickness and bond them to the metal sheets forming the desired bearing shape. The first approach gives you more freedom on the shape of the bearing, but comes along with increased fabrication hardware complexity. The second approach can be considered less expensive depending on the production volume and of the hardware complexity.

When fabricating the laminates using vulcanized rubber sheets, one bonds the rubber to the metal sheets with the aid of the proper adhesive. Also one must mould the rubber sheets into the final form before the curing of the adhesive. The problem of moulding the bonded rubber bearings is that the metal sheets prevent the bending when at two or more metal sheets are present. Small deformations of the rubber bearing after bonding might be acceptable.

OD moulding

One of the experimented methods was what we could call OD moulding. This method was utilized for fabricating the samples for the shear test as shown in section 5.1.

For fabricating rubber-metal laminate rubber bearings one places an initial metal sheet over the shaft, which is held in place by a small tension force, which can be provided by an adhesive tape adhered to the ends of the metal sheet. Over this initial metal sheet one adheres the rubber sheet with the proper adhesive, followed by another metal sheet with adhesive, and so on. Each metal sheet is held in tension with the aid of the adhesive tape. After waiting for the required curing time the bonded rubber-metal laminates are removed from the shaft, and cut out to the desired size.

As an example the rubber-metal laminate bearings fabricated with the OD moulding method, using EAR-C1002 rubber with aluminum sheets and a cynoacrolite ad-

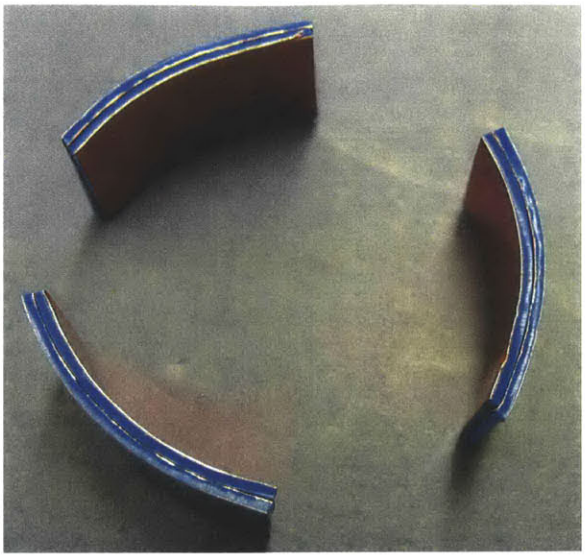

Figure 6-7: Fabricated laminate rubber bearing with the OD moulding method.

hesive is shown in Figure 6-7.

This method might be considered low-tech fabrication, but it managed to produce an acceptable laminate rubber bearing.

Pressure moulding

Another method experimented was the fabrication of laminate rubber bearings by pressure moulding. This method consists of placing the layers of metal and rubber with the proper adhesive between two moulding surfaces and under pressure.

It was proven to be more effective to mould a long oversized rubber-metal laminate, later cut to the desired size. The oversizing is required to eliminate any excess or lack of adhesive on the edges of the original oversized laminate.

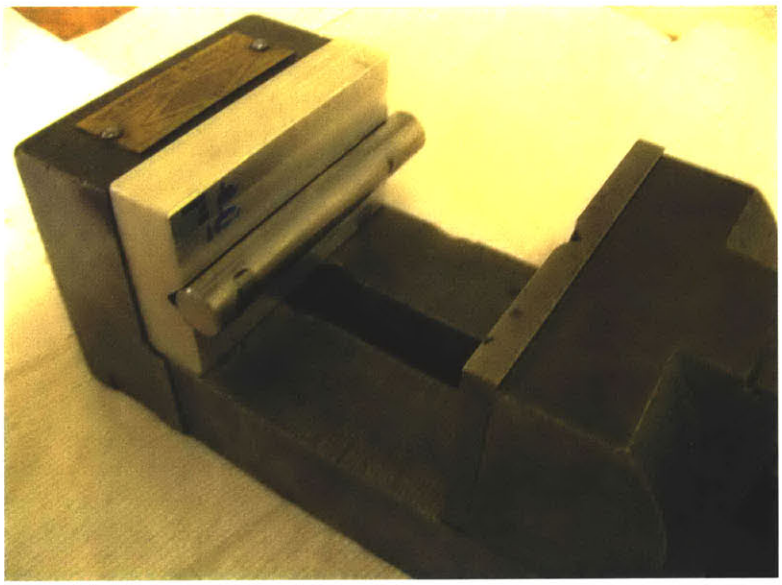

Figure 6-8: Mould shaft for fabrication of rubber bearings.

A simple device was designed to fabricate the laminate rubber bearings by this method. The design included using a commercial vise with adapted jaws that will hold the moulding parts. One of the moulding part is a ground steel shaft as shown in Figure 6-8, and the other a semi-cylindrical cavity as shown in Figure 6-9. Once the metal and rubber laminates are placed into the moulding cavity a pressure is exerted between the shaft and cavity with the aid of the vise as shown in Figure 6-11 and Figure 6-10. The bearings are cut out of the oversized rubber-metal laminates using an x-acto knife. An example of bearings fabricated using the pressure moulding method are shown in Figure 6-12.

This method proved to be really effective and reduced the amount of hand-crafting in the fabrication of the bearings. One of the downsides is that to obtain nice cut edges the x-acto blade needs to be replaced each time the cutting of a new bearing is required.

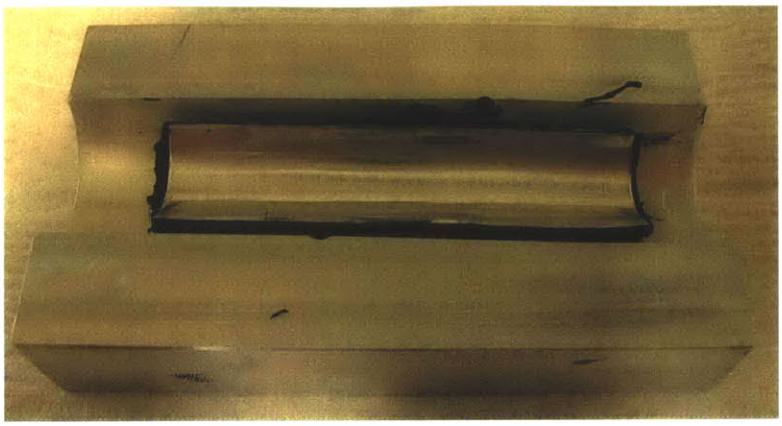

Figure 6-9: Mould semi-cylindrical cavity with oversized rubber-metal laminate and cured adhesive.

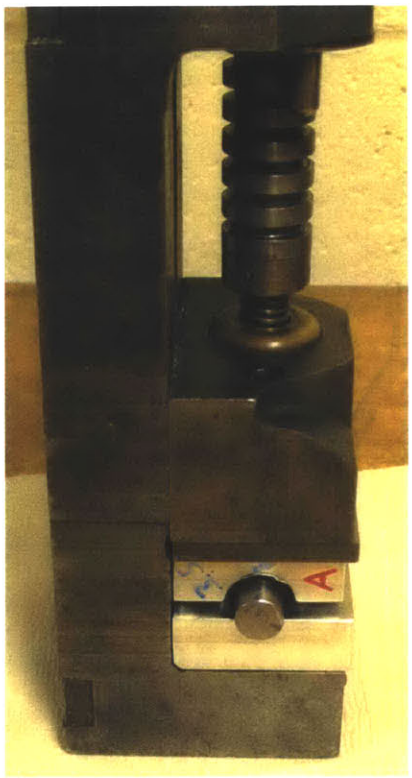

Figure 6-11: Vise exerting pressure for moulding or rubber bearings.

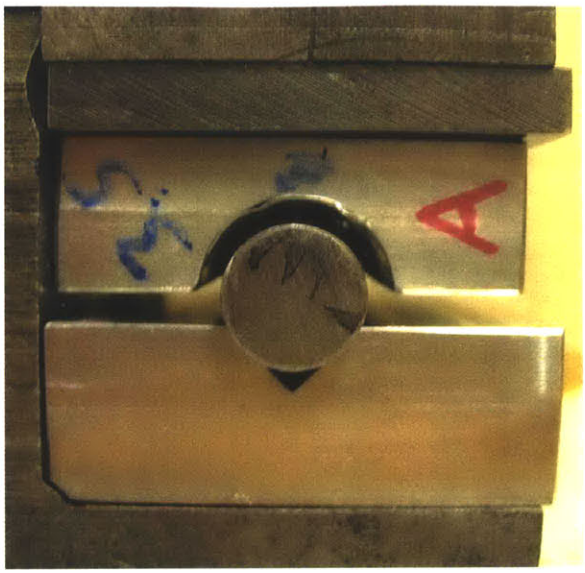

Figure 6-10: Moulding parts exerting pressure on rubber-metal laminates under curing.

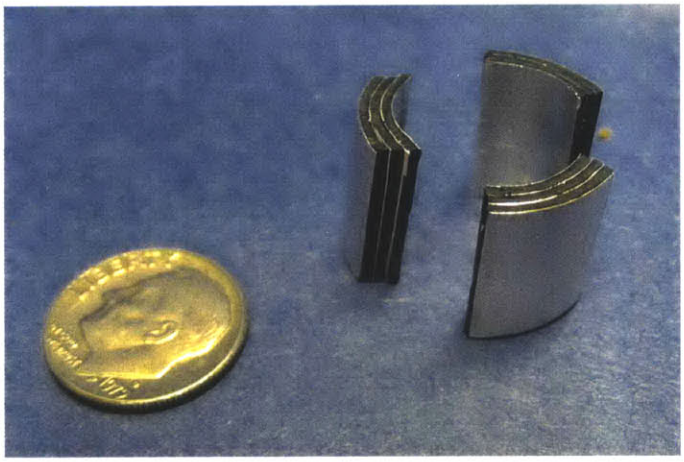

Figure 6-12: Finished bearing after pressure moulding and cutting.

6.3 Linear rubber bearing

The design of any linear rubber bearing must comply with the following general functional requirements: be compliant in the axial direction, provide restraint in the transverse directions, and provide adjustable preload to the rubber bearings.

6.3.1 Topologies

Different topologies of the linear rubber bearing will be presented here stating in a qualitative manner their advantages and disadvantages.

The first topology shown in Figure 6-13 consists of four rubber bearings in a square arrangement. This bearing is for a shaft of square section. The preload of the rubber is accomplished by bringing together the two parts of the body with the aid of preload bolts. Several approaches could be taken assure a given preload, for example the use of Belleville Springs. The axial compliance is given by the shear of the rubber bearings in that direction. The transverse restraint is given by the compression stiffness of the rubber bearings, which is high. However the torsional stiffness will be moderate in this design.

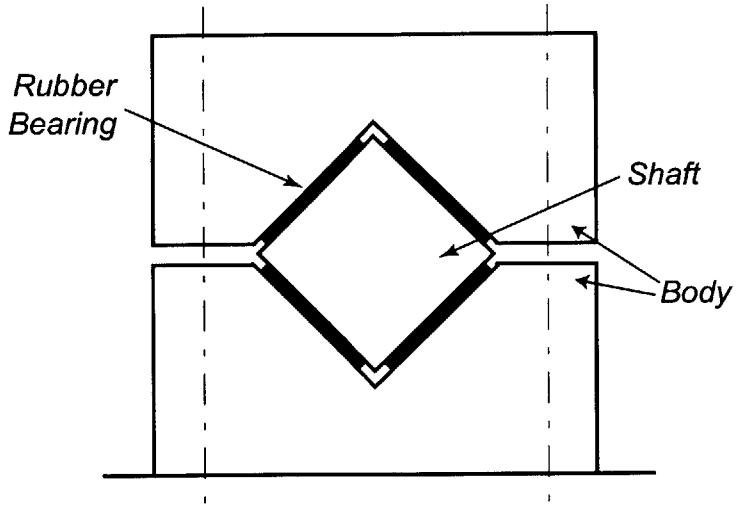

Figure 6-13: Linear rubber bearing option No. 1.

The second topology shown in Figure 6-14 consists of three rubber bearings in a triangular arrangement. This is intended of course for a triangular section shaft. Preload is accomplished with the aid of the top and bottom part of the body and the

aid of preload bolts, in similar manner as the first topology. The axial compliance is given by the shear of the rubber bearings. The transverse restraint will be mainly provided by the compression stiffness of the rubber bearings, and is considered high, and the torsional restraint of will be moderate.

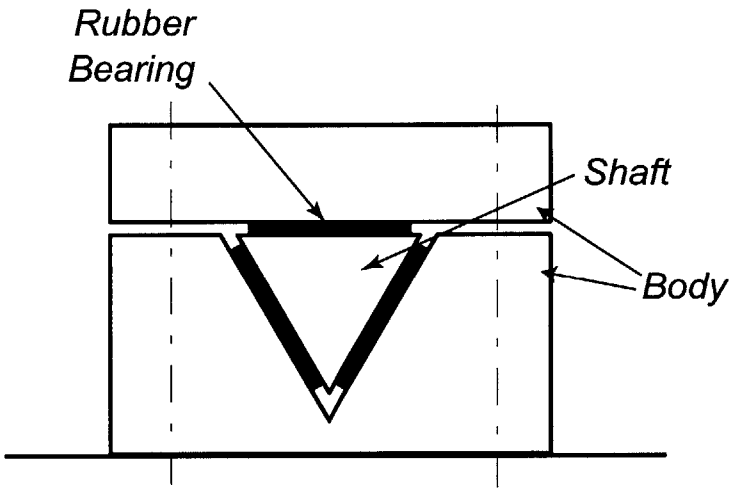

Figure 6-14: Linear rubber bearing option No. 1.

If torsional compliance of the rubber bearing is not an issue then all the rotary rubber bearings shown in Figures 6-15 and 6-16 may be used as linear rubber bearings.

6.3.2 Stiffness calculations

Calculating the axial shear stiffness of any of these bearings is fairly easy since one needs to take into the consideration the loaded area of each rubber pad A, the cummulative rubber thickness of the rubber t (considering the bearing is of laminate type), and the shear modulus G yielding

$$k_s = \frac{\chi_p GA}{t} \tag{6.34}$$

where χ_p is the stiffening due to the compressive preload, which can be found experimentally. Experimental values of χ_p are shown for several materials is shown in Table 5.2.

For calculating the transverse stiffness of the different topologies one needs to consider the geometric arrangement of the rubber pads and their compression stiffness, which can be calculated with 6.21. One important aspect to consider is that the preload pressure must be sufficiently large so that the rubber pads remain under compression while the working load is applied. This is necessary to prevent slip, as well as maintaining the entire area of the pad loaded, and so assure a high compression stiffness.

The presented topologies show the use of rubber pads around the shaft instead of a rubber continuum. The advantage of using rubber pads is the ease of uniform preload of the rubber pads. A continuum can only be subject to preload by methods described by Gent [9] (p.238): Enlarging the inner member dimensions after bonding; reducing the outer member dimensions after bonding; or Molding at high pressures to induce pre-compression in the elastomer.

Here the lateral stiffness of square section shaft with four rubber pads and a rubber continuum will be compared. The lateral stiffness of the four padded case will be basically defined by the compression stiffness of the rubber bearings. When the rubber bearings are under compression load their loaded free areas can bulge and so its compression modulus is defined by (6.21)

$$E_c = E_0 \left[1 + 2k_R k S^2\right] \tag{6.35}$$

with $S = \frac{BH}{2t(B+H)}$

In the case of the rubber continuum when a lateral load is applied an axial bulge

can occur without restraint. If we consider the lateral load being an upward load then the top portion of the rubber continuum will be subject to a compression load which creates an outward bulge, while the bottom one will be subject to a tension load which creates an inward bulge. Both bulges to occur will require to deform the lateral part of the rubber continuum, which implies a restraint.

The upper bound of the lateral stiffness of the rubber continuum bearing can be found when considering that no bulge occurs either on the top or bottom portion of the rubber continuum. For that case the top and bottom portion will be under a one-dimensional strain as defined by (2.4)

$$E_c = \frac{4}{3} E_0 (1 + kS^2) \tag{6.36}$$

with $S = H/2t$

The increase of compression modulus due to the continuum is shown in Table 6.3, were the dimensions B and H are considered equal, and a compression coefficient $k = 1$ is assumed. It can be seen that the compression modulus could be increased by a factor of 3 for high shape factors. The actual increase of compression modulus and so lateral stiffness of the continuum type bearing will be less than the values found here, but it gives as an idea on how the lateral stiffness of the rubber bearing can be increased by the use of a continuum rubber.

When designing a rubber bearing one will have to take into consideration the benefit versus the effort (or cost) of making the continuum type rubber bearing, instead of a rubber pad one.

Table 6.3: Compression stiffness comparison between 4 pad and continuum rubber bearing

$H/2t$	$\frac{E_c(Continuum)}{E_c(4Pads)}$
$\ll 1$	1.3
1	1.85
5	2.86
10	2.96

6.4 Rotary rubber bearing

The design of any rotary rubber bearing must comply with the following general functional requirements: be compliant in the axial direction, provide restraint in the transverse directions, and provide adjustable preload to the rubber bearings.

6.4.1 Topologies

Different topologies of the linear rubber bearing will be presented here stating in a qualitative manner their advantages and disadvantages.

The first topology shown in Figure 6-15 consists of three rubber bearings in a circular arrangement. The preload of the rubber is accomplished by the reduction of the preload clamp inner diameter with the aid of preload bolts and Belleville springs. The rotary compliance is given by the shear of the rubber bearings in a diametrical manner. The transverse restraint is given by the compression stiffness of the rubber bearings, which is high. This type of bearing is compliant in the axial direction and so it requires an accompanying thrust bearing if this compliance is not desired.

The second topology shown in Figure 6-16 consists of three rubber bearings in a circular arrangement. The preload of the rubber is accomplished by sliding the taper collet into its holder with the aid of a preload part, preload bolts and Belleville springs. The rotary compliance is given by the shear of the rubber bearings in a

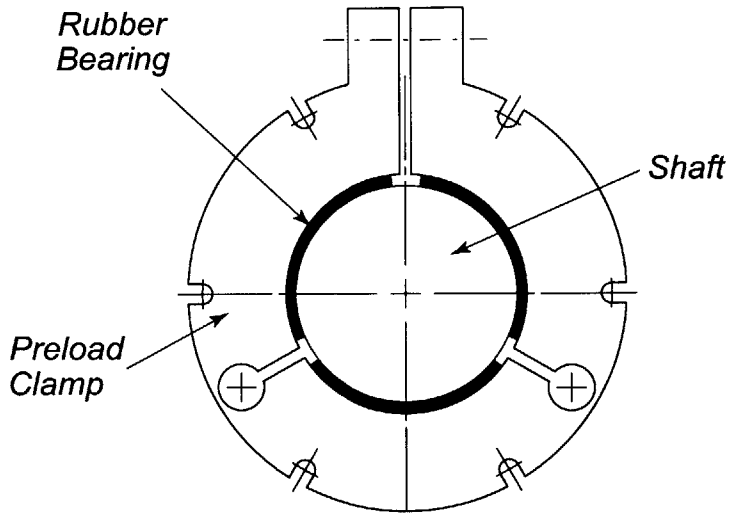

Figure 6-15: Linear and rotary rubber bearing with self-preloading body.

diametrical manner. The transverse restraint is given by the compression stiffness of the rubber bearings,which is high. This type of bearing is compliant in the axial direction and so it requires an accompanying thrust bearing if this compliance is not desired.

6.4.2 Stiffness calculations

To calculate the torsional stiffness k_θ of a three pad type rotary rubber bearing, the dimensions of each rubber pad are taken as the width B (measured along its curvature), the height H, the cumulative rubber thickness t (considering the bearing is of laminate type), the shear modulus G, and the stiffening due to the preload which we will call χ_p as shown in section 6.3.2 and is given as follows

$$k_\theta = \frac{3D^2}{4}\frac{\chi_p GA}{t} \tag{6.37}$$

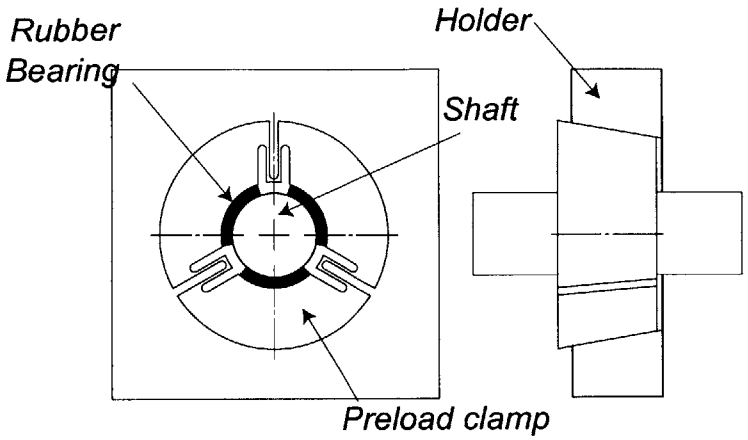

Figure 6-16: Linear and rotary rubber bearing with taper collet type preload.

where $A = BH$

The radial stiffness k_{rad} of the three pad type rotary rubber bearing is calculated based on the fact that the three rubber bearings remain under compression, due to a sufficient amount of preload. The lateral stiffness will be defined as follows

$$k_{rad} = 1.5\psi\chi_p k_c \tag{6.38}$$

where $\psi = D/B\sin(D/B)$ is a correction factor due to the non-uniform loading of the rubber bearing, and $k_c = \frac{E_0 A\left[1+2k_R kN^2S^2\right]}{Nt}$, with $S = \frac{nB}{2t(n+1)}$ and $H = nB$.

In similar manner as stated in section 6.3.2 the topologies shown use rubber pads instead of a rubber continuum. A rubber continuum will increase the radial stiffness, but the fabrication and uniform preload of rubber laminate bearings must be taken into consideration. Here a comparison of the radial stiffness between the three rubber pad option and the rubber continuum is shown.

Freakley [8] (p.137) presents an expression for calculating the radial stiffness of annular rubber units in radial compression taken from an analysis made by Adkins

and Gent (1954)

$$k_{rad} = \frac{4\pi G[(r2/r1)^2 - 1]}{[(r2/r1)^2 + 1]ln(r2/r1) - [(r2/r1)^2 - 1]} \tag{6.39}$$

This expression is for an infinite long unit which is adequate when considering thin rubber units.

If we take as example a single layer rubber bearing with $G = 0.5$ MPa, $E_0 = 1.5$ MPa, an inner radius $r_1 = 6$ mm, an outer radius $r_2 = 7.5$ mm, and a length $L = 15$ mm, we calculate the radial stiffness for the three rubber pad option using (6.38) and for the continuum option using (6.39) giving 2663 N/mm for the three rubber pad option, and 5697 N/mm for the continuum option. This case shows an increment of a factor of 2.1 due to the use of the rubber continuum.

6.5 Rubber bearing design guide

In this section the necessary equations needed for static rubber bearing design will be summarized, for the case of a single rubber-metal laminate rectangular linear bearing and three-pad ubber-metal laminate rotary bearing.

6.5.1 Linear rubber-metal laminate bearing

First we need to size the bearing of width B, length H and thickness t, for the required shear stiffness k_s using

$$k_s = \frac{GA}{t} \tag{6.40}$$

where $A = BH$ is the bearing loaded area, t the cumulative rubber thickness of

the rubber (considering the bearing is of laminate type), and G the shear modulus which can be found in Table 2.1.

Second the number of laminates N of the rubber bearing must be specified to assure a desired compression stiffness using

$$k_c = \left[\frac{1}{E_0[1+2k_R k N^2 S^2]} + \frac{1}{E_\infty}\right]^{-1} \frac{A}{Nt} \tag{6.41}$$

where E_0 is the Young's modulus, E_{inf} is the Bulk modulus, and k a compressibility factor (all of this having reference values which can be taken from Table 2.1); k_R is shown in Table 6.2, and $S = BH/[2t(B+H)]$ is the shape factor of the rubber bearing without considering the laminations.

6.5.2 Three pad rotary rubber-metal laminate bearing

First we need to size the bearing of width B, length H and thickness t, for the required rotary shear stiffness k_θ when used in a diameter D shaft using

$$k_\theta = \frac{3D^2}{4}\frac{GA}{t} \tag{6.42}$$

where $A = BH$ is the bearing loaded area, t the cumulative rubber thickness of the rubber (considering the bearing is of laminate type), and G the shear modulus which can be found in Table 2.1.

Second the number of laminates N of the rubber bearing must be specified to assure a desired compression stiffness using

$$k_c = \left[\frac{1}{E_0[1+2k_R k N^2 S^2]} + \frac{1}{E_\infty}\right]^{-1} \frac{1.5\psi A}{Nt} \tag{6.43}$$

where $\psi = D/B\sin(D/B)$ is a correction factor due to the non-uniform loading of the rubber bearing. E_0 is the Young's modulus, E_{inf} is the Bulk modulus, and k a compressibility factor (all of this having reference values which can be taken from Table 2.1). k_R is shown in Table 6.2, and $S = BH/[2t(B+H)]$ is the shape factor of the rubber bearing without considering the laminations.

6.6 Comments

This chapter has presented tools to be used in the design of rubber bearings for precision machines. The tools presented here are used in the next Chapter for designing a rotary fast tool servo using rubber bearings.

Chapter 7

Design of rotary FTS using rubber bearings

The design of a Rotary Fast Tool Servo (FTS) using rubber bearings was undertaken in order to prove the applicability of rubber bearings in precision positioning systems using rubber bearings. This is seen as a low-cost alternative versus the use of flexural bearings.

The performance of the FTS designed and fabricated by Montesanti [13] was used as a reference for the design of ours. His FTS uses metal flexural bearings, and is driven by the same actuator used in our design. Montesanti's FTS has a maximum stroke of 50 μm pk-pk at low frequencies and has demonstrated a 2.5 μm pk-pk stroke at 2 kHz while under operation.

The use of the FTS designed by Montesanti is for diamond turning, area in which he has significant experience. Montesanti [13] learned from experience that when designing a precision machine tool "the stiffness at the tool tip relative to the machine base needed to be at least 20 N/μm, and that the same stiffness was required for the workpiece relative to the machine base." The basis for this recommendation is discussed further in Montesanti's thesis [13], and it its based in a 4.5 N cutting force.

For the design of our FTS the tool tip stiffness of 20 N/μm (for a design work load of 4.5 N) was taken into consideration. The goal of our design will be to obtain a maximum stroke of 50 μm pk-pk at low frequencies and a stroke on the order of 1 μm pk-pk at 1 kHz. A closed-loop bandwidth within the range of 1 - 10 kHz is desired. Also because of possible overloads, a design radial load of 20 N will be taken into consideration.

The work piece which the FTS is intended to machine on consists of a ϕ9 mm and 5 mm, which is held in a work piece holder which is mounted in a spindle. The design of the FTS must permit the work piece to approach the diamond tool to perform the machining of the work piece.

The design of the FTS will include preload of the rubber bearings with the aid of a compact preload mechanism to assure the bearing radial stiffness.

7.1 Rubber Bearing material selection

The experimental results from Chapter 5 shown that the increase in complex shear modulus with frequency G_{HF}/G_{LF} was significant, ranging from 30 up to 240. It is of our interest to obtain as much stroke at high frequency as possible, for which a low G_{HF}/G_{LF} is desired. Silicone, Viton, and Neoprene show the lowest complex shear modulus increment, as shown in Figure 5-10.

A comparison between the use of Silicone, Viton, and Neoprene rubber materials as a rubber bearing is made, based on the type A bearing shown in Figure 7-2. The basis of comparison is using the same rubber sheet thickness $t_r = 0.77$ mm, a shaft diameter of $D = 20$ mm, and bearing of dimensions $B = 20$ mm and $H = 25$ mm. A tool radius r_T of 10 mm was considered for this calculation. The number of laminates is varied to obtain a bearing radial stiffness K_{rad} of approximately 100 N/μm. The

desired stroke at low frequency is of the order of 20 μm pk, and the stroke at 2 kHz is desired to be on the order of 1 μm pk.

The comparison between materials shows that the highest DC stroke is accomplished with the softer materials of Shore 40A, being this stroke of about 40 μm pk, while the harder materials of Shore 75/80A accomplish DC strokes of about 20 μm pk. The stroke accomplished at 2 kHz with Silicone Shore 40A is of 0.4 μm pk, while the one accomplished with Viton Shore 75A is 0.3 μm pk, and with Neoprene Shore 80A is 0.5 μm pk. The results of this comparison are shown in Figure 7-1.

Softer materials have lower DC stiffness which helps accomplish higher DC strokes but requires the use of thinner rubber layers to accomplish a desired radial stiffness. Also softer materials have a higher increment of shear stiffness with frequency which limits the stroke at high frequencies.

Harder materials have higher DC stiffness which lets you accomplish lower DC strokes but thicker rubber layers can be used to compensate for the higher shear stiffness, and still maintain the desired radial stiffness.

Silicone rubbers although being promising have a downside with regard to the bonding of the rubber to metal surfaces. As noted by Petrie [15], silicone rubber is characterized of being a low surface energy material, which are generally difficult to bond with adhesives. Petrie recommends the use of "room temperature curing, one-part silicone sealant adhesives (RTV Silicone)" (p.625) for medium to high strength bonds.

		Type A					Type B	Type C
	Material	Silicone	Viton	Neoprene	Neoprene	Neoprene	Neoprene	Neoprene
	Shore	40A	75A	40A	70A	80A	80A	80A
	Jshaft+motor (kgm^2)	5.79E-06	5.79E-06	5.79E-06	5.79E-06	5.79E-06	5.79E-06	2.70E-05
	D (mm)	20	20	20	20	20	20	10
	B (mm)	20	20	20	20	20	20	10
	H (mm)	25	25	25	25	25	25	40
	tr (mm)	0.77	0.77	0.77	0.77	0.77	0.77	0.77
	n	2	5	2	4	5	5	2
	t (mm)	1.54	3.85	1.54	3.08	3.85	3.85	1.54
	A (mm2)	500	500	500	500	500	500	400
	S	7.2	7.2	7.2	7.2	7.2	7.2	5.2
	Ec (MPa)	125.0	391.6	125.0	268.9	391.6	391.6	242.5
	G (Mpa)	0.524	2.366	0.524	1.344	2.366	2.366	2.366
	Shear HF factor @ 2 kHz	100	75	150	100	43	43	43
	Shear HF factor @ 10 kHz	100	75	150	100	43	43	43
DC	ktors (N.m/rad)	51.0	92.2	51.0	65.5	92.2	92.2	46.1
DC	krad (N/um)	102.5	128.4	102.5	110.2	128.4	108.5	159.0
DC	krad/ktors	2.0	1.4	2.0	1.7	1.4	1.2	3.5
DC	Max stroke (um P) (for 10mm tool offset)	39.2	21.7	39.2	30.6	21.7	21.7	43.4
(2kHz)	ktors (N.m/rad)	5103.9	6913.8	7655.8	6545.5	3963.9	2100.0	1982.0
(2kHz)	Max stroke (um P) (for 10mm tool offset)	0.39	0.29	0.26	0.31	0.50	0.95	0.47
(2kHz)	Stiffness or Inertia driven	Stiffness	Stiffness	Stiffness	Stiffness	Stiffness	Stiffness	Inertia
(10kHz)	ktors (N.m/rad)	5103.9	6913.8	7655.8	6545.5	3963.9	2100.0	1982.0
(10kHz)	Max stroke (um P) (for 10mm tool offset)	0.09	0.09	0.09	0.09	0.09	0.09	0.02
(10kHz)	Stiffness or Inertia driven	Inertia	Inertia	Inertia	Inertia	Inertia	Inertia	Inertia
	Est. Nat. frequency (Hz)	4.7E+03	5.5E+03	5.8E+03	5.4E+03	4.2E+03	3.0E+03	2.9E+03

Limited by flexure (Type B)

Figure 7-1: Material and bearing type comparison.

When experimenting with the use of this adhesives the bond thickness resulted in being excessive due to its high viscosity. A three layer sample fabricated with Silicone rubber, aluminum shims and a Silicone adhesive (Dow Corning 737 RTV Sealant) is taken as an example. This sample cured with and without an applied pressure at room temperature. The resulting bond without an applied pressure while curing was of adequate strength and with a bond thickness of about 0.1 mm. On the other hand the bond obtained with curing under pressure resulted of low stiffness with a bond thickness of about 0.04 mm. The silicone adhesives cure on exposure to moisture as stated by Petrie [15]. It is thought that the applied pressure avoided the proper exposure to moisture of the curing adhesive. The bond thickness of the properly cured adhesive of 0.1 mm is excessive in relation to the rubber thickness of the rubber laminates that are desired for our design.

The use of Silicone rubber as material for our rubber bearing was discarded mainly because of its poor bonding properties. The bonding properties of Neoprene and Viton proved to be outstanding, obtaining thin and strong bonds when using a rubber toughened cynoacrylate (Loctite 380). Bonds as thin as 0.02 mm could be obtained experimentally under an applied pressure with the setup shown in Figure 6-10

Neoprene Shore 80A was preferred in comparison with Viton Shore 75A because of its lower shear complex stiffness at high frequencies as shown in Figure 7-1. This permits to obtain higher strokes at high frequencies.

7.2 Rubber bearing type selection

Three rubber bearing types were compared based on the selected material Neoprene Shore 80A.

The type A bearing consists of three rubber bearings in a circular arrangement

preloaded on their outside diameter, as shown in Figure 7-2.

The Type B bearing consists on a shaft with added flexures as shown in Figure 7-3. While the rubber bearing increases it complex shear stiffness at high frequency the flexures torsional stiffness remain constant. So if the flexure torsional stiffness is sized to be lower than the rubber bearing torsional stiffness at high frequency then the flexure torsional stiffness will dominate at high frequencies. With this one could size the flexures to obtain a desired stroke.

The Type C bearing consists on a long bearing between a solid and a hollow shaft as shown in Figure 7-4. The hollow shaft is the rotating shaft that carries the tool.

The comparison between the Type A and B bearing shows that the Type B has half the high frequency torsional stiffness and so double the stroke, as shown in Figure 7-1. This is accompanied by a 20% decrease in the radial stiffness due to the radial compliance of the flexures. This alternative is an interesting approach but the added complexity in the fabrication makes it unattractive.

The Type C bearing adds complexity in the design of the coupling between the rotating shaft and the motor, and the added inertia makes the stroke at 2 kHz limit the stroke to approximately the same as the Type A bearing, as shown in Figure 7-1.

Based on the comparison shown here the Type A bearing was chosen as the bearing for the design of our rotating precision machine.

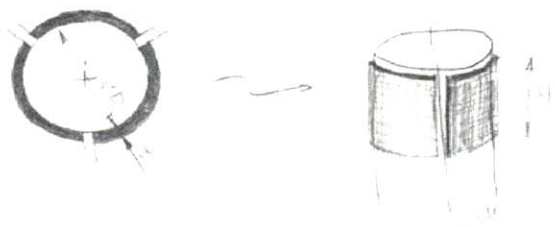

Figure 7-2: Type A bearing.

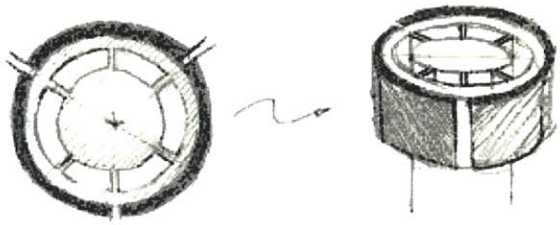

Figure 7-3: Type B bearing.

Figure 7-4: Type C bearing.

7.3 Optimization of rubber bearing and shaft dimensions

The optimization was based on achieving the maximum possible stroke with a minimum radial tool tip stiffness of 25 N/μm. The desired DC stroke was on the order of 50 μm pk-pk and a 2 μm pk-pk stroke at 1 kHz, taking into consideration the

actuator as a torque source, of maximum torque of 0.4 Nm pk-pk.

The following dimensions of the shaft-bearing-tool-holder assembly were considered for the optimization: length from the coupling to the bottom of the bearing L_x, bearing height H, spacing from top of bearing to bottom of tool holder e, height of tool from bottom of tool holder h_{th}, tool radius r_T, the rubber sheets thickness t_r, the width of the rubber bearing B (measured at the inner arc), and the number of laminates n. Based on this dimensions the following general dimensions can be found: the length from the bearing center to the tool tip $L_b = H/2 + e + h_{th}$, and the length from the coupling to the tool tip $L_T = L_x + H/2$.

For the optimization the following dimensions were fixed: the spacing $e = 4$ mm, to provide enough space for a top sealing plate with its respective o-ring, the dimension $h_{th} = 5$ mm, to provide enough space for the tool, and the rubber sheet thickness $t_r = 0.77$ mm, for being the thickness available for Neoprene Shore 80A. The rest of the dimensions were considered as variables, leaving a total of 6 variables: d, B, r_T, L_x, n, and H. To reduce the number of variables and so make the optimization process less extensive the width of the bearing was taken as $B = d$. This leaves us with only 5 variables.

The optimization was done for three different diameters of $\phi 12$, $\phi 14$ and $\phi 15$ mm, each diameter with four to five different tool radius r_T, each tool radius with three different values of L_x, and each length L_x with a rubber bearing of $n = 1$, 2, 3 and 4 rubber layers. The remainder dimension H is found by maximizing the stroke at 2 kHz limiting the tool tip stiffness to a minimum of 25 N/μm.

The radial tool tip stiffness is calculated by considering the radial compliance of the rubber bearing, the bending of the shaft length from the center of the bearing to the tool tip, and the compliance of the tool holder.

The bearing stiffness at the tool tip k_{brad} is found by considering the model shown

in Figure 7-5, were the radial stiffness at the motor shaft is taken into consideration, giving us the following

$$k_{brad} = \frac{k_A k_B (L_T - L_b)^2}{(k_A L_T^2 + k_B L_b^2)} \tag{7.1}$$

where k_A is the radial stiffness at the motor shaft and k_B is the radial stiffness of the rubber bearing.

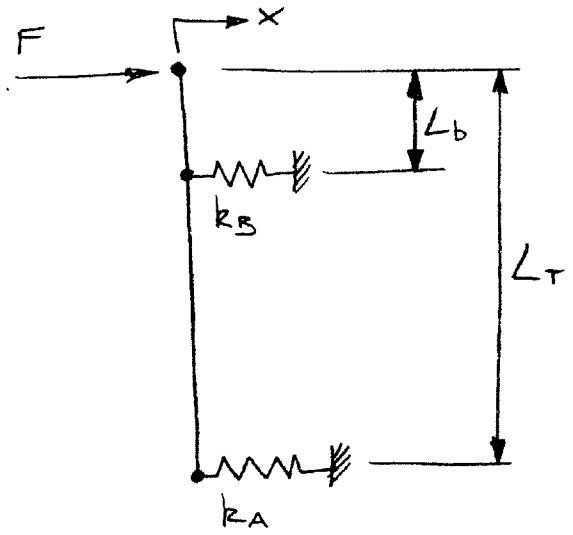

Figure 7-5: Model used to calculate tool tip stiffness.

The compliance of the tool holder and shaft bending are calculated by considering a cantilever beam which has a compliance of $x/F = L^3/(3EI)$ where E is the Young's modulus of aluminum, I the respective moment of inertia, and $L = r_T - d/2$ for the case of the tool holder and $L = L_b - h_{th} - H/2$ for the case of the shaft bending.

The optimization considered a total of 160 cases with a total of 6 spreadsheets to calculate the different parameters. The summary spreadsheet is shown in Appendix B.

When increasing the diameter d from $\phi 12$ to $\phi 14$ mm the maximum possible stroke

reduces. This is shown in Figure 7-6 (a) which shows the maximum stroke at 2 kHz of all the cases plotted against d. Higher bearing stiffness at the tool tip K_{brad} can be accomplished for $d = 12$ mm as shown in Figure 7-6 (b).

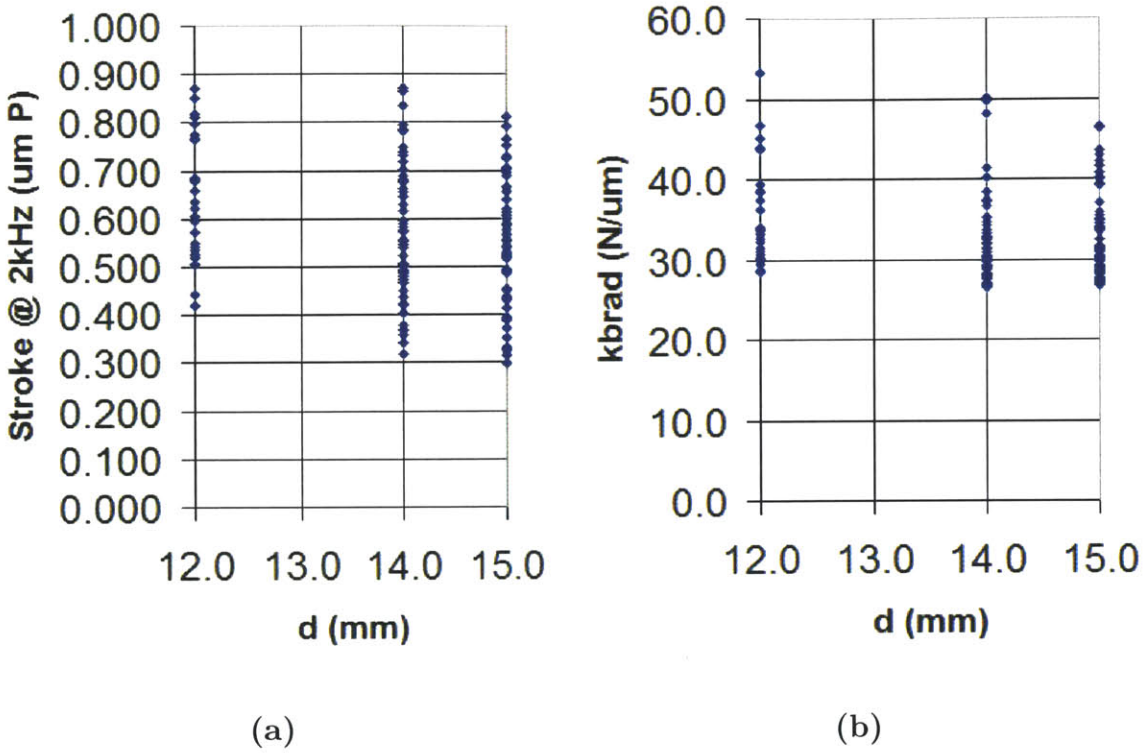

(a) (b)

Figure 7-6: Plots of (a) Stroke at 2 kHz and (b) k_{brad} against d

It is interesting to notice that when increasing the number of layers n higher strokes can be accomplished, as shown in Figure 7-7. But the maximum strokes achieved with 3 and 4 layers similar in magnitude.

The chosen configuration was actually the one with the highest stroke, since the dimensions of the shaft and bearing were reasonable, as well as having an acceptable bearing stiffness. The dimensions of the chosen configuration are as follows

$d = 12$mm, $r_T = 12$mm, $L_T = 54.5$mm, $L_b = 16.7$mm, $B = 12$mm, $H = 15.5$mm, $t_r = 0.77$mm, $n = 3$

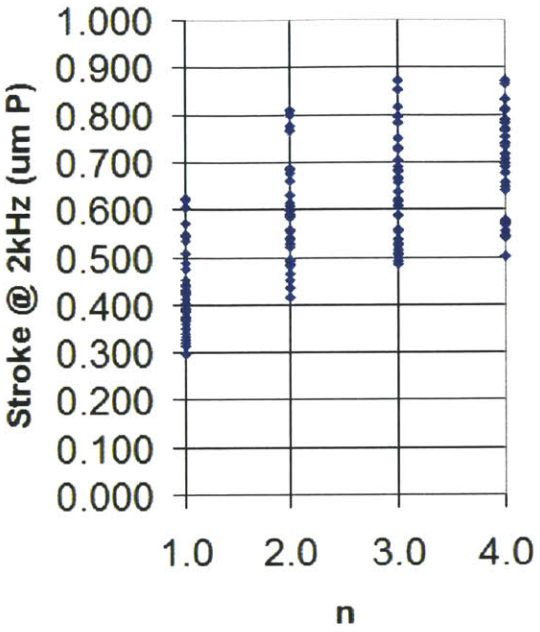

Figure 7-7: Maximum stroke at 2 kHz plotted against number of layers n.

The chosen configuration is expected to have a radial stiffness at the tool tip $k_{rad} = 25$ N/μm, a DC stroke of 31.4 μm pk, and a stroke at 2kHz of 0.9 μm pk.

7.4 Rubber Bearing metal laminates sizing

The selected material for the rubber bearing metal laminates was aluminum. Aluminum shims are light, readily available, easy to handle an bend to a desired form, as well as being much easier to cut than steel shims.

The sizing of this metal laminates is based basically on the preload pressure exerted to the rubber bearings. The reason for this is that the preload pressure exerts a compressive stress on the rubber bearings which consequently stresses the metal shims in compression in the direction of its thickness and in tension along it length

and width. This has been shown in 6.2.2 along with the necessary equations to size the metal laminates.

The normal stress acting on the metal laminates can be found using (6.31) and (6.32)

$$\sigma_{nx} = \frac{Gn^2B^2}{2(n^2+1)t_r t_m}\epsilon \tag{7.2}$$

$$\sigma_{ny} = \frac{Gn^2B^2}{2(n^2+1)t_r t_m}\epsilon \tag{7.3}$$

where $\epsilon = \sigma_c/E_c$.

The design preload pressure applied to the rubber bearings is $\sigma_c 1.6$ MPa, and the Neoprene Shore 80A rubber laminates of thickness $t_r = 0.77$ mm, have a compression and shear modulus of $E_c = 175$ MPa and $G = 2.4$ MPa respectively. When considering aluminum laminates of thickness $t_m = 0.076$ mm the resultant tension stress along their lengths come out to be on the order of 16.7 MPa on both directions. The equivalent stress found using (6.33) is $\sigma_{eq} = 15$ MPa. The material chosen for the metal laminates is Aluminum 1145 with a yield strength of 115 MPa which satisfies the strength requirements.

7.5 Preload mechanism

The preload mechanism must be able to preload the rubber bearings in compression with a preload pressure on the order of 1.6 MPa, allow variation of the preload pressure to desired values with an acceptable tolerance, not compromise the rubber bearing stiffness, and be compact.

7.5.1 Options

The first considered option was having single part capable of holding the motor and to house the rubber bearing. The housing of the rubber bearing will deform to preload the rubber bearing, thanks to the compliance provided by the built in flexures as shown in Figure 7-8. The problem with this option is that the built in flexures add compliance to housing, and so requires reinforcing plates to make it stiff under operation.

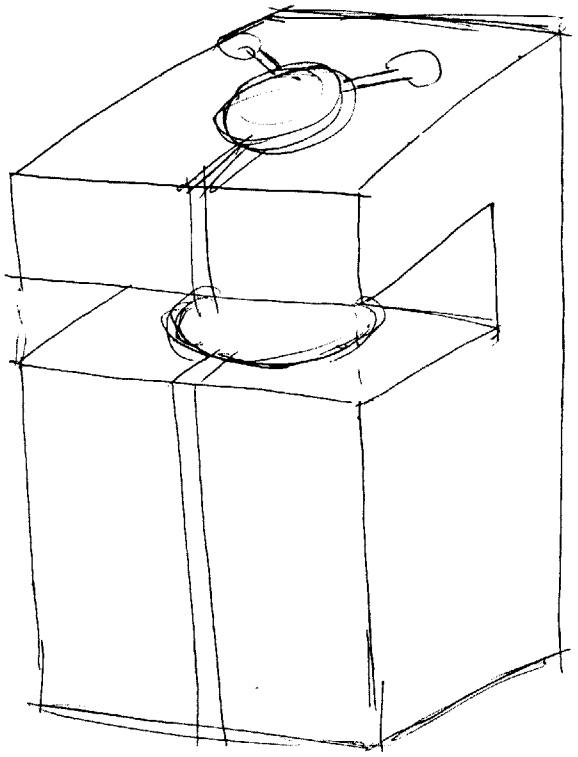

Figure 7-8: Preload mechanism option No.1.

The second considered option was to fabricate a flexure within the housing as shown in Figure 7-9, which will preload the rubber bearing. This option does not reduce the housing stiffness but is a challenge to design a way to deform the inner flexure, as well as being not a practical solution.

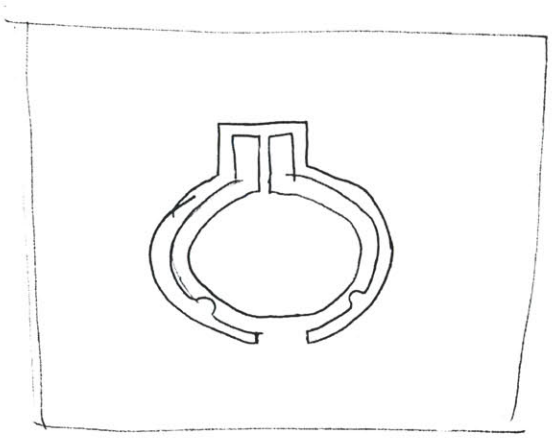

Figure 7-9: Preload mechanism option No.2.

The third option shown in Figure 7-10 considered was the use of a collet with a nut at one end, which when tightened will reduce its inner diameter to preload the rubber. To assure a uniform preload on the rubber bearing it is required that the collet deforms uniformly in its clamping zone. To assure that the collet length becomes excessive. But this option gave rise to other type of solutions.

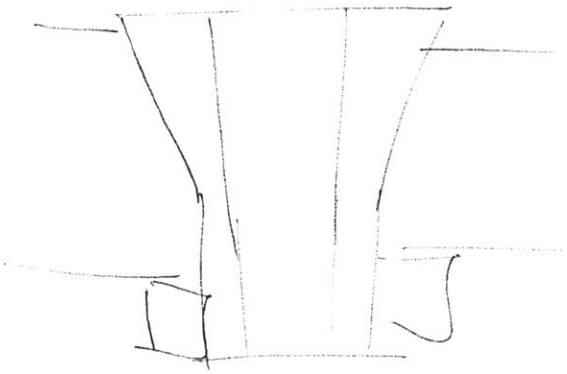

Figure 7-10: Preload mechanism option No.3.

The fourth option derived from the collet idea was the one shown in Figure 7-11. This collet is deform with the aid of a tapered preload part, and preload bolts with springs to exert a pre-defined force. This option looked promising but an option with

less friction involved was desired.

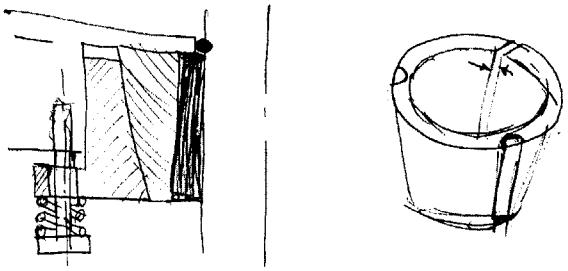

Figure 7-11: Preload mechanism option No.4.

The last and chosen option is shown in Figure 7-12, is a taper collet with built in flexures which permit its deformation when pushed into a tapered holder. This collet is geometrically held into place, being rigid and compact.

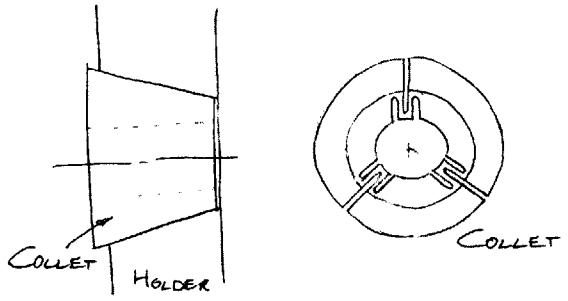

Figure 7-12: Chosen Preload mechanism option.

7.5.2 Sizing of collet flexures

The stiffness of the collet must be low enough so as to prevent the oversizing of the preload bolts, and make the preload force more deterministic. The compression stiffness of the rubber bearings was taken as a reference. The compression stiffness of one rubber bearing is in the order of 50 N/μm, and the collet stiffness was desired to be less than 5% of that, so below 2.5 N/μm.

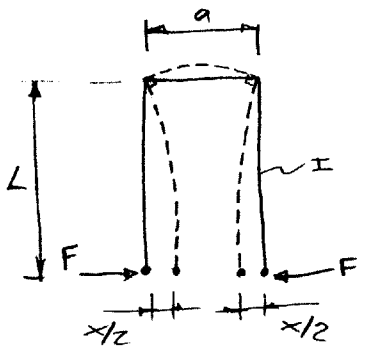

Figure 7-13: Collet flexure model.

Each flexure was modeled as shown in Figure 7-13, and is stiffness was derived as

$$k_x = \frac{EI}{2L^2\left[\frac{L}{3} + \frac{a}{2} - \frac{(L+a)^2}{(4L+2a)}\right]} \tag{7.4}$$

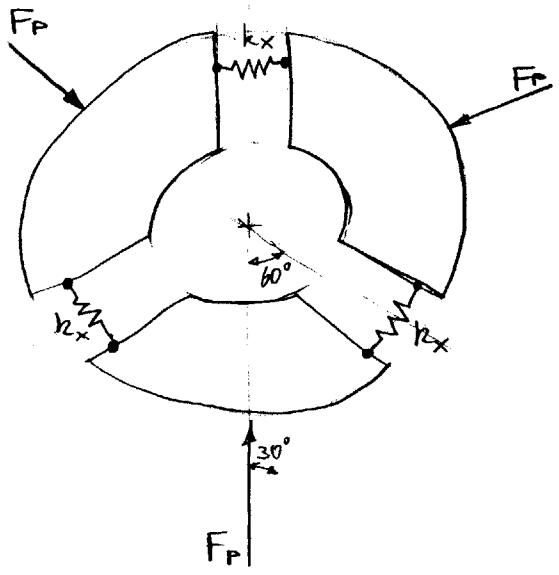

Figure 7-14: Collet model.

Having the stiffness of each flexure defined then the collet could be modeled as shown in Figure 7-14. The three springs in the model with stiffness k_x represent the flexures. When a preload force F_p is applied the collet will deform radially by an

amount δ_r which is related to the x of each flexure by $x = \sqrt{3}\delta_r$. And so the radial stiffness of the collet k_r becomes

$$k_r = 3k_x \tag{7.5}$$

The flexures will be subject to a moment and flexural stress defined by (check words)

$$M = k_x\sqrt{3}\delta_r\frac{(L+a)L}{(2L+a)} \tag{7.6}$$

$$\sigma_f = \left[\frac{\sqrt{3}k_x t}{2I}\frac{(L+a)L}{(2L+a)}\right]\delta_r \tag{7.7}$$

The chosen material for the collet was brass since its resistance was adequate, and because of its increased machinability. The final dimensions of the flexure, its stiffness and applied stress under operation is shown in Figure 7-15. The resultant collet stiffness was k_r = 820 N/mm which is less than 2% of the rubber bearing, and the stress of the flexure under operation was of 7 MPa which is way below the minimum yield stress of ASTM B16 brass of 103 MPa.

7.5.3 Determination of collet taper angle and preload force

The collet was designed to be self-locking to prevent it from coming loose in the presence of an overload. Also if the collet was designed to be self-releasing, then the stiffness of the bearing will be compromised, since it will be limited by the stiffness of the preload springs.

The collet is pushed into the holder with the aid of a preload part as shown in Figure 7-17, and preload bolts with Belleville springs. A rubber sheet is placed between the preload part and the collet to permit the collet to deform radially without the presence of friction in the interface.

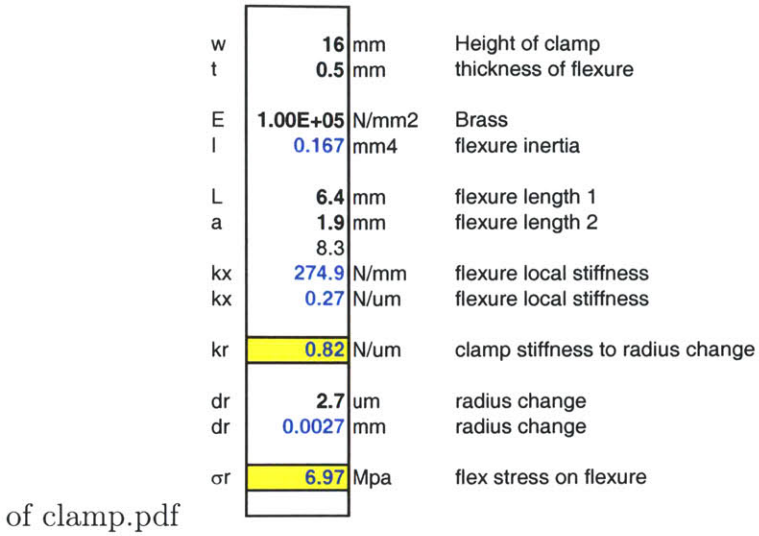

Figure 7-15: Preload Collet flexure sizing.

In order to make the collet self-locking the friction coefficient between the collet (brass) and the holder (steel) must be considered. The friction coefficient does not only depend on the materials but as well as their surface finish. A better surface finish comes along with a lower coefficient of friction as shown by Marks [6]. Because of the lack of information about the coefficient of friction between brass and steel with surface finish 63 R_a or better, information about measurement of coefficient of friction between brass and stainless steel with different surface finishes was taken into consideration. This information was found in the following website (http://www.varmintal.com/afric.htm), which shows tests performed by Dick Hatfield (2004). Based on this reference a coefficient of friction of $\mu = 0.2 - 0.3$ was used for our analysis.

The model shown in Figure 7-16 was used to find the taper angle required to make the collet self-locking. If the collet is already in the holder taper and a force F is required to pull it out, then it is self-locking, so F must be greater than zero. Doing the sum of forces gives

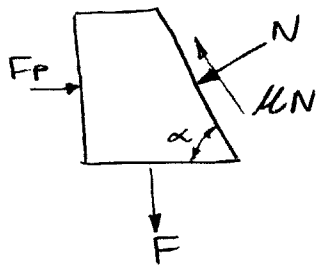

Figure 7-16: Collet model to evaluate self-locking.

$$F = N(\sin\alpha - \mu\cos\alpha) \tag{7.8}$$

which for $F > 0$ requires that

$$\mu > \tan(90 - \alpha) \tag{7.9}$$

For $\mu = 0.2$ the taper angle α requires to be greater than 79^o for the collet to be self-locking.

So $\alpha = 80^o$ was used for the design of the collet.

The model shown in Figure 7-17 was used to calculate the relationship between the preload force applied to the rubber bearing F_P and the bolt force

$$F_P = \frac{(\sin\alpha - \mu\cos\alpha)}{(\mu\sin\alpha + \cos\alpha)} F_B - F_c - F_s = k_b\delta_r \tag{7.10}$$

where $F_c = k_r\delta_r$ is the force required to deform the collet being k_r its stiffness as defined in (7.5), and $F_s = k_s\delta_r$ is the force required to deform the rubber interface being k_s its shear stiffness.

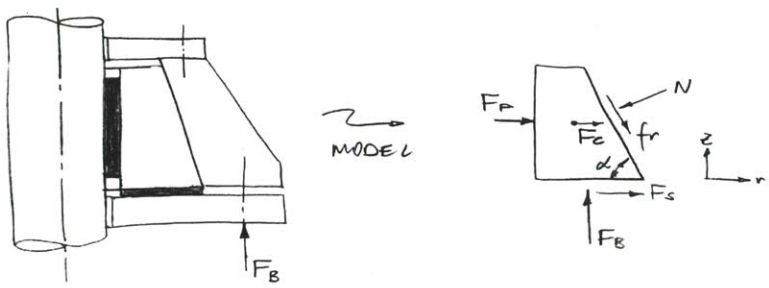

Figure 7-17: Collet preload model.

The force required per bolt to preload each rubber bearing with a radial force $F_P = 270$ N, is calculated as shown in 7-18, being $F_B = 124$ N.

α	80	deg	
α	1.396	rad	
sin α	0.985		
cos α	0.174		
tan α	5.671		
mu	0.25 (0.20 - 0.30)		
kb	50000	N/mm	
kc	825	N/mm	
ks	700	N/mm	
dr	0.00540	mm	
Fc	4.453098073	N	Clamp force
Fs	3.78	N	Interface rubber force
Fp	270.0	N	Rubber bearing preload force
F_B	124.1	N	Preload bolt force
N	295.6	N	

Figure 7-18: Calculation of rubber bearing preload mechanism.

7.6 Collet Holder

The holder's main function is to house the taper collet within its own taper. Other functions included the support the cap gage holder rests on its top surface, support the sealing top plate, attachment to the separator, provide space for a part holder to

reach the tool, for which the necessary features were provided. Pictures of the holder with the collet in place are shown in Figure 7-19.

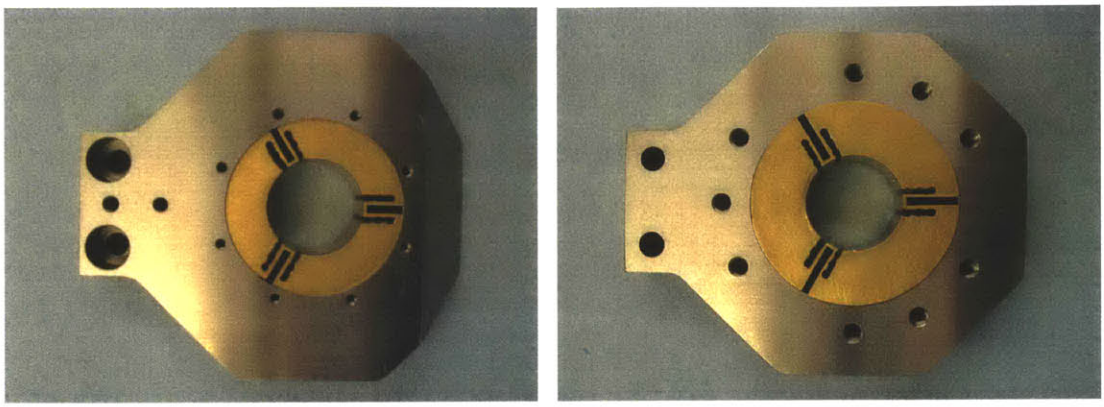

(a) (b)

Figure 7-19: Holder with the collet in place (a) Top view (b) Bottom view

7.7 Tool holder

The tool holder was designed to hold in a firm manner a diamond tool (with its steel shank), and provide the necessary space for the $\phi 9$ mm diameter work-piece. The diamond tool used as a reference for the design was designed by Montesanti [13] with collaboration from Chardon Tools. The diamond tool and tool shank weighs 0.4 grams and the tool shank has a 30^o taper angle to assure a stiff connection with the tapered slot of the tool holder.

The tool tip is aligned with the rotating axis as shown in Figure 7-20. This reduces the lateral displacement of the tool tip to a minimum. The amount of lateral displacement for this position of the tool tip is defined by $r_T(1 - \cos\theta)$ while the tool travel is defined by $r_T \sin\theta$, where r_T is the tool radial position and θ is the angular rotation of the shaft. For a tool travel of 25 μm and $r_T = 12$ mm, the lateral displacement will be 26 nm. Since this is three orders of magnitude less than the tool

travel we avoid the need of some type of compensation.

The closer the tool tip is to the center of the rubber bearing, higher radial tool tip stiffness can be accomplished. Because of this the diamond tool was placed on the end of the tool holder arm with is top plane aligned with the shaft axis as shown in Figure 7-20. Another important feature about placing the tool at the end of the tool holder arm is the compliance provided by the tapered slot allowing the slot to deform when the tool shank is bolted to the tool holder.

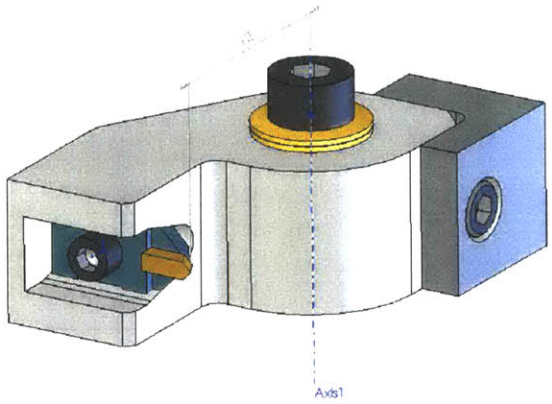

Figure 7-20: Assembly of tool holder, diamond tool and balance mass.

The calculation of the stiffness of tool holder arm was considered in Section 7.3. The calculated stiffness of the tool arm for the final dimensions is 207 N/μm as shown in Appendix B.

The tool holder design includes a balance mass as shown in Figure 7-20 in order to keep the center of mass of the tool holder assembly within an acceptable eccentricity. This eccentricity was limited with the criteria that at the maximum operating frequency, the inertial force generated by the mass of the tool holder assembly with its eccentricity will be lower than 5% of the design operating load of 4.5 N.

The position of the center of mass of the tool holder is defined in polar coor-

dinates by $\bar{x} = r\hat{e_r}$, its velocity $\bar{v} = \dot{r}\hat{e_r} + r\dot{\theta}\hat{e_\theta}$, and its acceleration $\bar{a} = (\ddot{r} - r\dot{\theta}^2)\hat{e_r} + (2\dot{r}\dot{\theta} + r\ddot{\theta})e_{\hat{theta}}$. Since the center of mass moves in a fixed radius then $\bar{a} = (-r\dot{\theta}^2)\hat{e_r} + (r\ddot{\theta})e_{\hat{theta}}$, where $\dot{\theta} = \theta_M\omega\cos(\omega t)$ and $\ddot{\theta} = -\theta_M\omega^2\sin(\omega t)$, with θ_M as the maximum angle.

If we consider an eccentricity of the center of mass of $r = 1$ mm, a tool holder mass $m_{th} = 0.007$ kg, and a maximum angle $\theta_M = 8 \cdot 10^{-5}$ rad at $w = 12566$ rad/s (corresponding to a 1 μm stroke at 2000 Hz). The maximum radial and circumferential inertial force comes out to $8 \cdot 10^{-6}$ N and 0.1 N respectively. The last one is 2% of the design operating load of 4.5 N, so a center of mass eccentricity below 1 mm will be acceptable.

With the aid of the balance mass a tool holder center of mass eccentricity of $r = 0.007$ mm was obtained in the design, which is so low that the fabrication tolerances might actually alter it. But even the fabrication tolerances won't give a center of mass eccentricity near 1 mm, since they are on the order of 10 μm.

7.7.1 Tool holder and shaft interface

The tool holder and shaft interface required of centering type, and permit adjustment of the angular position of the tool holder for alignment. To suit this purpose the tool holder was provided with a counter bore to mate with the shaft end. The tool holder counter bore was provided with an adequate tolerance to adequately center it to the shaft axis, and permit its angular adjustment.

The tool holder was coupled to the shaft with the aid of a single centered bolt. The joint force provided by this bolt required to be sufficient to work with the design load. The design load used for the joint calculation was $F_R = F_T = F_A = 25$ N as shown in Figure 7-21. This design loads exceed the design operating load, since it must be able to sustain possible overloads.

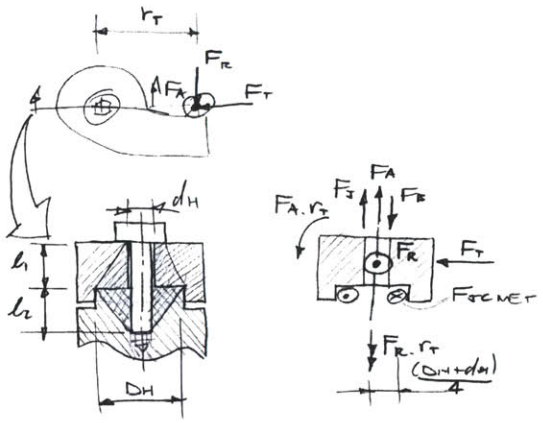

Figure 7-21: Model to analyze tool holder and shaft interface.

When the joint is subject to shear stress $\tau_1 = \frac{F_R r_T}{A r_M}$ due to the $F_R r_T$ moment, a shear stress $\tau_2 = F_T/A$ due to the transverse force F_T, and a shear stress $\tau_3 = F_R/A$ due to the radial force F_R, as shown in Figure 7-22 (a), (b), and (c) respectively.

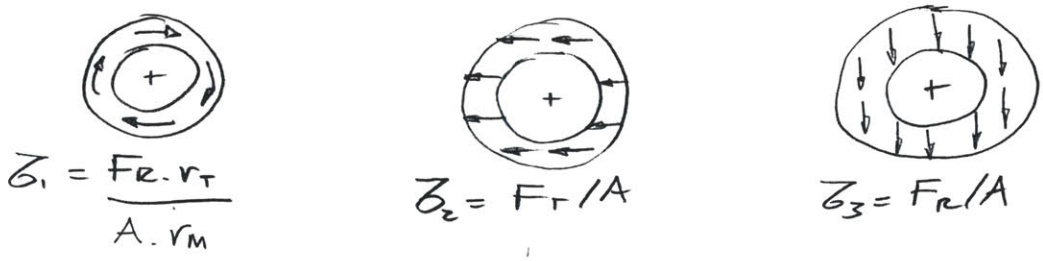

Figure 7-22: Shear stress acting on tool holder and shaft interface

Defining $|F_R| = |F_T| = F$ the maximum shear stress will be defined by

$$\tau_{max} = \frac{F r_T}{A r_M} + \frac{\sqrt{2}F}{A} \tag{7.11}$$

With $F = 25$ N, $A = 71.5$ mm^2, $r_M = 6.5$ mm and $r_T = 12$ mm, the maximum

shear stress becomes $\tau_{max} = 1.14$ N/mm^2. The required joint force F_{Jreq} to prevent slip is defined by $F_{Jreq} = \frac{\tau A}{\mu_{AL-AL}}$, which with $\mu_{AL-AL} = 1.0$ becomes $F_{Jreq} = 81.5$ N.

With an M2.5x10 Class 12.9 Socket Head Cap Screw taken into consideration and taking into consideration the joint and bolt compliances the force ratio $\Phi = \frac{F_{eB}}{F_{eB}+F_{eJ}}$ becomes $\Phi = 0.27$. Also the bolt settling force becomes $F_z = 163.4$ N.

Finally the minimum, the maximum bolt mounting force, and the maximum bolt force are calculated as follows:

$$F_{Mmin} = F_{Jreq} + F_z + F_A(1 - \Phi) \tag{7.12}$$

$$F_{Mmax} = \alpha_A \cdot F_{Mmin} \tag{7.13}$$

$$F_{Bmax} = F_{Mmax} + \Phi F_A \tag{7.14}$$

where $\alpha = 2.5$ for mounting with a wrench, giving $F_{Mmin} = 263.2$ N, $F_{Mmax} = 657.9$ N, and $F_{Bmax} = 664.6$ N. The yield strength is matched with a bolt force equal to 3970N so the M2.5x10 Class 12.9 is adequate. Using a smaller screw might be possible, but impractical, so the M2.5x10 was used.

To assure the correct preload of the screw the use of Belleville springs was considered. This also helps prevents the loosening of the screw under alternating loads as well as prevent its damage due to excessive preload.

7.8 Shaft

The shaft consisted of a solid aluminum round shaft with its general dimensions as defined in the Section 7.3. The shaft must provide a centering mating feature with the tool holder at one end and a coupling at the opposite end.

Since the capacitance gage used requires the target to be grounded to its case, a grounding connection was provided at the coupling end of the shaft. A hole to insert the grounding cable in conjunction with a set screw, and then a connection to the separator was used for this purpose, as shown in Figure 7-23.

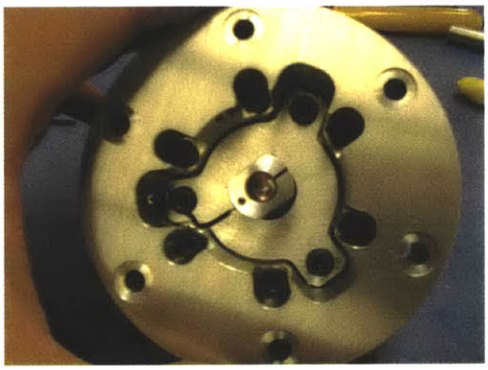

Figure 7-23: Ground cable connection for capacitance gage.

The final design of the shaft is shown in Figure 7-24.

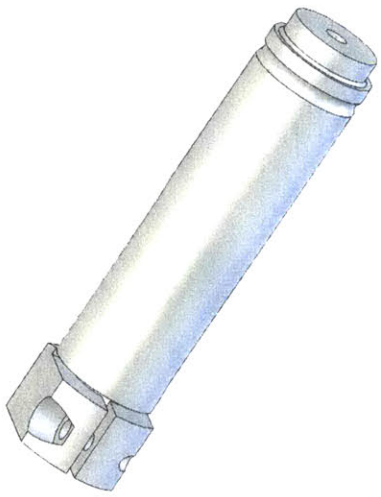

Figure 7-24: Solid model of shaft.

The design of the mating surface with the tool holder is discussed in Section 7.7.1,

and the coupling design will be discussed in the following subsection.

7.9 Shaft coupling

The shaft coupling was designed as an integral part of the shaft. This assures a better alignment between the shaft and the motor and provides an stiffer coupling. The coupling was designed as a rigid coupling, since there is no over-constraint problem when following a correct assembly procedure as shown in Section 7.17.

7.9.1 Options

Three options were considered for the design of the shaft coupling. The first one shown in Figure 7-25 consisted in providing the shaft with a reduced diameter, including a bore for the motor shaft and slit cuts. Then with the aid of a standard clamp in combination the bore is reduced to couple with the motor shaft. This type of coupling is low cost and adds moderate inertia, but provides low coupling stiffness.

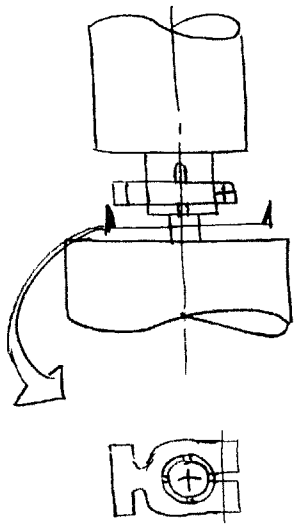

Figure 7-25: Shaft coupling (First Option).

The second option considered the use of a nut with a taper bore to clamp a taper slit cut feature to the motor shaft, as shown in Figure 7-26. This coupling provides high stiffness, but its fabrication is expensive and adds a reasonable amount of inertia.

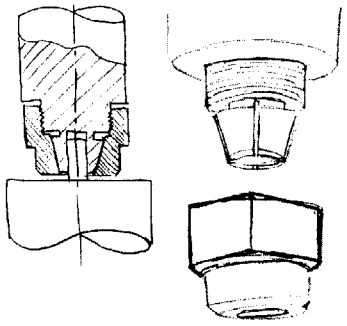

Figure 7-26: Shaft coupling (Second Option).

The third and chosen option consists on a built-in clamp as shown in Figure 7-27. This clamp adds low inertia and its fabrication is less expensive than the second option, providing an acceptable stiffness.

7.9.2 Sizing

The clamp requires to deform radially the maximum radial difference between the shaft and the coupling bore. This is calculated using both the shaft and coupling tolerances. The measured shaft diameter was $\phi 6.980$ mm, which required an electrical insulation shim, being this a 76 μm thick plastic shim. The coupling bore was designed with a diameter of $\phi 7.144 - 7.149$ mm, which is the tolerance given by a commercial reamer. So the minimum and maximum diametral gap is of 11 μm and 16 μm respectively.

For the calculation of the clamp a point of contact near the center of the shaft was considered, as shown in Figure 7-27. The coupling needs to deform radially at that point $\delta r = 8$ μm. This will be accomplished with the deformation of the highlighted

zone shown in Figure 7-27, due to the transverse force F coming from the bolt, and the moment $F(L-B)$. The displacement δr will be defined by

$$\delta r = \frac{F}{3EI/B^3} + \frac{F(L-B)}{EI/B} \tag{7.15}$$

An equivalent moment of inertia $I = 7.8$ mm^4 was used, which resulted in a force $F = 344$ N being required to deform the coupling as desired. The maximum stress was found to be of 241 MPa due to the deformation of the coupling.

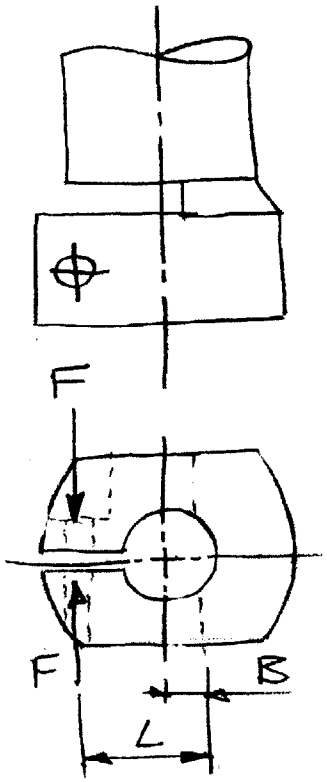

Figure 7-27: Model of shaft coupling.

Additional force is required to prevent slip of the coupling shaft interface. For that a torque $T = 300$ Nmm was considered (due to a design load applied to the tool tip of 25 N and the tool radius of 12 mm). A conservative coefficient of friction

of $\mu = 0.1$ was used due to the plastic shim, which gave a required normal force to prevent slippage on the ϕ7mm diameter shaft of $F_{nreq} = 429$ N

The total required bolt mounting force becomes $F_{mreq} = F + F_{nreq} = 773$ N. The maximum required bolt mounting force is $F_{mmax} = 2304$ N for an M2 bolt, as shown in Figure 7-28. The yield strength on an M2 Class 12.9 Socket Head Cap Screw is met with a 2421 N preload force, which makes it an acceptable choice.

	Fmreq	772.6	N
Bolt	d	2	mm
	L	6	mm
	Am	1.539	mm^2
	fz	4.780E-03	mm
	Eb	2.10E+05	N/mm^2
	δb	2.351E-05	mm/N
Joint	EJ	7.00E+04	N/mm^2
	As	10	mm^2
	δJ	8.57E-06	mm/N
	Fz	1.490E+02	N
	αA	2.5	
	Fmmin	921.6	N
	Fmmax	2303.9	N

Figure 7-28: Calculation of coupling bolt.

7.10 Rotational modal analysis

A rotational modal analysis of the assembly of the tool holder, shaft, shaft coupling, and galvanometer was made. A discrete model which consisted of rotational inertias J_i connected with rotational springs k_i was considered as shown in Figure 7-29.

The modal analysis is based on the following matrix model

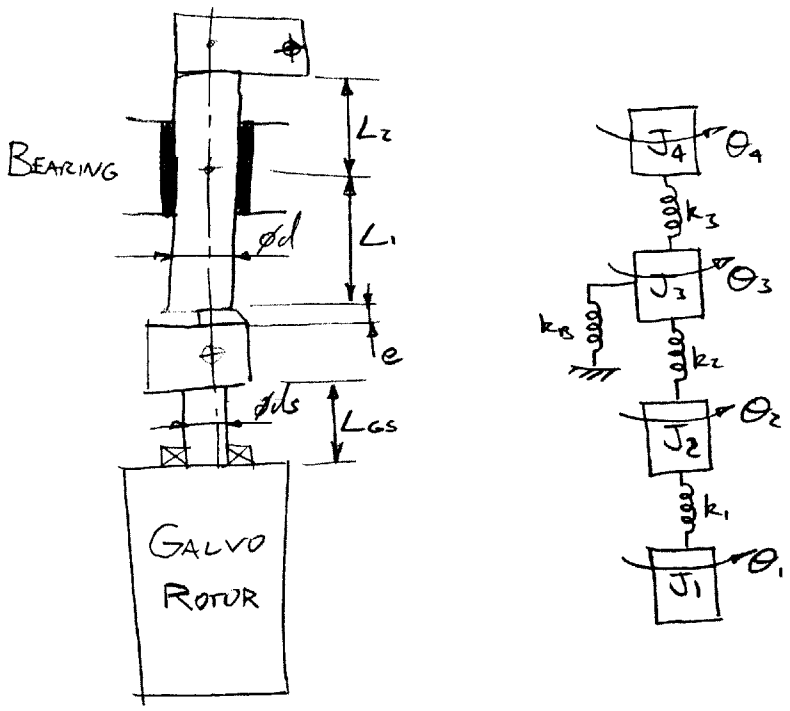

Figure 7-29: Rotational Modal Analysis model.

$$\mathbf{J}\ddot{\bar{\theta}} + \mathbf{K}\bar{\theta} = \bar{\tau} \tag{7.16}$$

where $\mathbf{J}$ and $\mathbf{K}$ are the inertia and stiffness matrix, defined by

$$\mathbf{J} = \begin{bmatrix} J_1 & 0 & 0 & 0 \\ 0 & J_2 & 0 & 0 \\ 0 & 0 & J_3 & 0 \\ 0 & 0 & 0 & J_4 \end{bmatrix}, \tag{7.17}$$

$$\mathbf{K} = \begin{bmatrix} k_1 & -k_1 & 0 & 0 \\ -k_1 & k_1 + k_2 & -k_2 & 0 \\ 0 & -k_2 & k_2 + k_3 + k_B & -k_3 \\ 0 & 0 & -k_3 & k_3 \end{bmatrix}, \tag{7.18}$$

and the $\bar{\theta}$ and $\bar{\tau}$ are the rotational displacement and torque input vector defined as

$$\bar{\theta} = \begin{bmatrix} \theta_1 \\ \theta_2 \\ \theta_3 \\ \theta_4 \end{bmatrix} \tag{7.19}$$

$$\bar{\tau} = \begin{bmatrix} \tau_1 \\ \tau_2 \\ \tau_3 \\ \tau_4 \end{bmatrix} \tag{7.20}$$

The discrete model considers the rotational inertias shown in Table 7.1.

Table 7.1: Rotational Inertias for Modal Analysis

J_i	(kgm^2)	Rotational Inertia considered
J_1	$6.40 \cdot 10^{-7}$	Galvanometer rotor
J_2	$1.46 \cdot 10^{-7}$	Coupling plus $L_1/2$ of shaft
J_3	$1.42 \cdot 10^{-7}$	$L_1/2 + L_2/2$ of shaft
J_4	$4.98 \cdot 10^{-7}$	$L_2/2$ of shaft plus tool holder

The discrete model considers the rotational springs shown in Table 7.6.

The eigenvalue and eigenvector problem is defined by

Table 7.2: Rotational Springs for Modal Analysis

k_i	(Nm/rad)	Rotational Stiffness considered
k_1	$3.81 \cdot 10^3$	Galvanometer shaft
k_2	$1.15 \cdot 10^3$	Coupling in series with stiffness L_1 of shaft
k_3	$4.20 \cdot 10^3$	Stiffness of L_2 of shaft
k_B	$76.5 \cdot 10^3$	Rubber bearing DC stiffness

$$(\mathbf{A} - \lambda \mathbf{I})\phi = 0 \tag{7.21}$$

with $\mathbf{A} = \mathbf{J}^{-1}\mathbf{K}$, the eigenvalue $\lambda = \omega^2$ where ω is the natural frequency in rad/s, and the eigenvector ϕ defining the mode shape.

The following eigenvectors, and corresponding natural frequencies $f = \omega/2\pi$ are found

Table 7.3: Rotational Springs for Modal Analysis

Eigenvector 1	Eigenvector 2	Eigenvector 3	Eigenvector 4
0.090	-0.207	-0.793	1.000
-0.659	1.000	-0.476	0.991
1.000	0.616	0.718	0.956
-0.205	-0.199	1.000	0.961
f_1 (Hz)	f_2 (Hz)	f_3 (Hz)	f_4 (Hz)
35450	29616	7764	1151

The first mode occurs at 1151 Hz with the actuator rotor and shaft rotating as a rigid body. The second one at 7763 Hz is the one with the tool holder and the actuator rotating out of phase. The third and fourth mode are higher order modes which occur far beyond the working frequency range.

7.11 Flexural modal analysis

A flexural modal analysis was done in order to verify the non-existence of excitable modes within the working frequency range that could compromise the machine performance. The model shown in Figure 7-30 was used for the analysis.

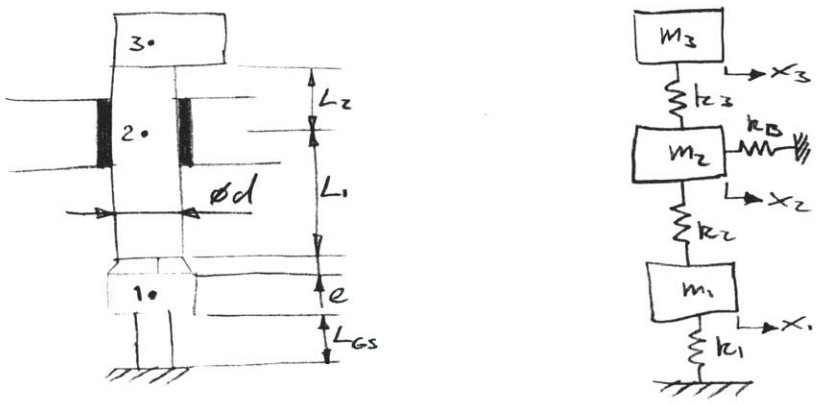

Figure 7-30: Rotational Modal Analysis model.

The modal analysis is based on the following matrix model

$$\mathbf{M}\ddot{\bar{x}} + \mathbf{K}\bar{x} = \bar{f} \tag{7.22}$$

where $\mathbf{M}$ and $\mathbf{K}$ are the mass and stiffness matrix, defined by

$$\mathbf{M} = \begin{bmatrix} m_1 & 0 & 0 \\ 0 & m_2 & 0 \\ 0 & 0 & m_3 \end{bmatrix}, \tag{7.23}$$

$$\mathbf{K} = \begin{bmatrix} k_1 + k_2 & -k_2 & 0 \\ -k_2 & k_2 + k_3 + k_B & -k_3 \\ 0 & -k_3 & k_3 \end{bmatrix}, \tag{7.24}$$

and the $\bar{x}$ and $\bar{f}$ are the rotational displacement and torque input vector defined as

$$\bar{x} = \begin{bmatrix} x_1 \\ x_2 \\ x_3 \end{bmatrix} \tag{7.25}$$

$$\bar{f} = \begin{bmatrix} f_1 \\ f_2 \\ f_3 \end{bmatrix} \tag{7.26}$$

The discrete model considers the masses shown in Table 7.4.

Table 7.4: Masses for Modal Analysis

m_i	(kg)	Masses considered
m_1	$9.32 \cdot 10^{-3}$	Actuator shaft plus coupling plus $L_1/2$ of shaft
m_2	$7.89 \cdot 10^{-3}$	$L_1/2 + L2/2$ of shaft
m_3	$9.20 \cdot 10^{-3}$	Tool holder plus $L_2/2$ of shaft

The discrete model considers the lateral springs shown in Table 7.5.

Table 7.5: Lateral Springs for Modal Analysis

k_i	(N/m)	Stiffness considered
k_1	$2.38 \cdot 10^9$	Actuator shaft
k_2	$1.58 \cdot 10^7$	Coupling in series with stiffness L_1 of shaft
k_3	$1.07 \cdot 10^8$	Stiffness of L_2 of shaft
k_B	$7.60 \cdot 10^7$	Rubber bearing DC stiffness

The eigenvalue and eigenvector problem is defined by

$$[\mathbf{A} - \lambda \mathbf{I}]\,\phi = 0 \tag{7.27}$$

with $\mathbf{A} = \mathbf{M}^{-1}\mathbf{K}$, the eigenvalue $\lambda = \omega^2$ where ω is the natural frequency in rad/s, and the eigenvector ϕ defining the mode shape.

The following eigenvectors, and corresponding natural frequencies $f = \omega/2\pi$ are found

Table 7.6: Rotational Springs for Modal Analysis

Eigenvector 1	Eigenvector 2	Eigenvector 3
1.000	0.008	0.004
-0.009	1.000	0.644
0.000	-0.552	1.000
f_1 (Hz)	f_2 (Hz)	f_3 (Hz)
80651	28757	10235

The first mode occurs at 10235 Hz which is the coupling moving laterally while the tool holder stays practically still. To excite this mode a lateral inertial force due to an unbalance needs to be present, which will be low. Also the natural frequency of this mode is outside the working frequency range. The second and third modes are of higher order and occur at 28757 Hz and 80651 Hz which is far beyond the working frequency range.

7.12 Actuator

The chosen actuator for the precision machine is a Model 6880 Galvanometer Optical Scanner from Cambridge Technology, INC. As stated by Cambridge Technologies [2], this actuator consists of a moving-magnet actuator, having very little electrical inductance. Consequently extremely high torque can be generated very quickly, which

is essential for systems that require short step response times.

As stated further by Cambridge Technologies [2] the torque is limited by the mechanical failure limits of the rotor assembly. The rms torque is limited by the maximum power that can be dissipated by the actuator coming from the stator coils (I^2R with $R = 1\ \Omega$) when working at the maximum rms current. It is further noticed that adequate heat sinking is required to work at the maximum rms current.

Cambridge Technologies [2] further states that the maximum temperature that actuator body should attain is 50°C, to avoid personal injury. Also that the actuator body must be electrically insulated from chassis ground. For that electrical insulating Mylar and plastic sheets are used for the actuator body and shaft respectively. The Mylar used for the actuator body is also provided with heat transfer paste to assure a good heat transfer interface.

7.12.1 Holder clamping design

The holder design is required to serve two basic functions: first hold the actuator firmly so as to not compromise the whole machine stiffness, and to require adequate heat transfer from the actuator body to the environment. The chosen material for the holder was aluminum since its strength is sufficient and its heat transfer properties are good as well. Also this type of material for the holder was recommended by Cambridge Technologies [2].

To design the holder to clamp firmly the actuator the model shown in Figure 7-31. This model considers that the compliance of the holder is mainly provided by the flexure formed by slit cut of the holder. This slit cut is sized so as to permit the holder deform the inner diameter of the holder to fit the outer diameter of the actuator. The outer diameter of the actuator (considering an insulation film 127 μm thick) is ϕ30.704 - 30.734 mm, and the design inner diameter of the holder is ϕ30.810

- 30.835 mm. This means that the inner diameter of the holder must reduce by a maximum of 0.131 mm.

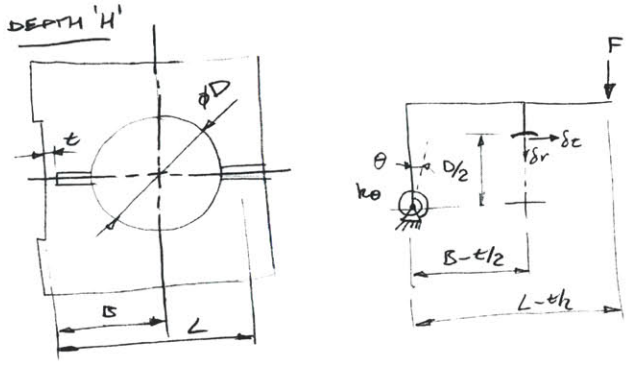

Figure 7-31: Model of Actuator Holder.

Considering the angular stiffness of the flexure k_θ and the model of Figure 7-31, the radial displacement δr of the holder is found by

$$\delta r = \theta \sqrt{(B - t/2)^2 + (D/2)^2} \cos \alpha \tag{7.28}$$

$$\alpha = \arctan\left(\frac{D/2}{B - t/2}\right) \tag{7.29}$$

$$\theta = \frac{FL}{k_\theta} \tag{7.30}$$

The calculation of the actuator holder flexure is shown in Figure 7-32. The force required by the holder bolts to clamp the actuator is of 278 N. This is easily obtained with the chosen M6 Class 12.9 used.

F	278	N
E	7.00E+04	MPa
H	70	mm
t	5.00	mm
I	729.2	mm4
h	3.0	mm
kteta	17013889	N.mm/rad
M	20989	N.mm
teta	0.001234	rad
D	30.8	mm
B	46	mm
L	78	mm
alpha	0.340	rad
dr	0.054	mm
dt	0.019	mm
stress	71.962	N/mm2

Figure 7-32: Calculation of actuator holder flexure.

7.12.2 Holder heat transfer analysis

The holder heat sinking capabilities were analyzed with the aid of the model and line graph shown in Figure 7-33. Note that both T_1 and T_2 are temperatures above the ambient temperature T_amb. The thermal resistance Coil-to-Case given by the manufacturer is $R_1 = 0.66°C/W$. The calculated thermal resistance from the Case to the outer surface of the Holder was on the order of $0.05°C/W$, reason for which the temperature of the holder was considered uniform. The calculated thermal resistance from the Holder-to-Ambient and the Holder thermal capacitance were $6.67°C/W$ and 1220 J/degC respectively.

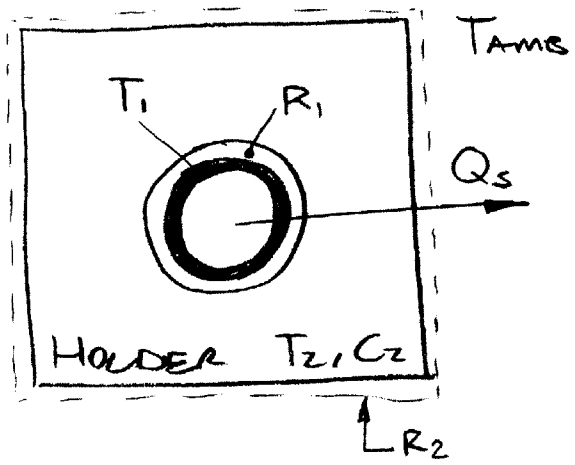

Figure 7-33: Heat transfer model of actuator holder.

The derived transfer functions relating the dissipated heat from the actuator $Q_s(t)$ with the Holder temperature T_2 and the coil temperature T_1 in transfer function form are

$$\frac{T_2(s)}{Q_s(s)} = \frac{R_2}{R_2C_2s + 1} \tag{7.31}$$

$$\frac{T_1(s)}{Q_s(s)} = \frac{R_1R_2C_2s + (R_1 + R_2)}{R_2C_2s + 1} \tag{7.32}$$

With a constant heat dissipation $Q(t) = 1$ W the coil temperature is expected to rise to $T_1 = 7.3^oC$ above ambient temperature but the time constant associated with this rise is in the order of 2 hours, as shown in 7-34. The Bode plot shown in Figure 7-35 shows how the temperature rise associated with a heat source at frequencies higher than 0.001 Hz is only on the order of $T_1 = 0.7^oC$ above ambient temperature.

If the actuator was working with at with a current $I(t) = 10\text{A}\sin(2\pi ft)$ with a frequency $f \geq 1$ Hz the coil heat dissipation will be $Q_s(t) = |I^2R| = 100\text{W}|\sin(2\pi ft)|$. And the coil temperature could reach $T_1 = 70^oC$ above ambient, which corresponds

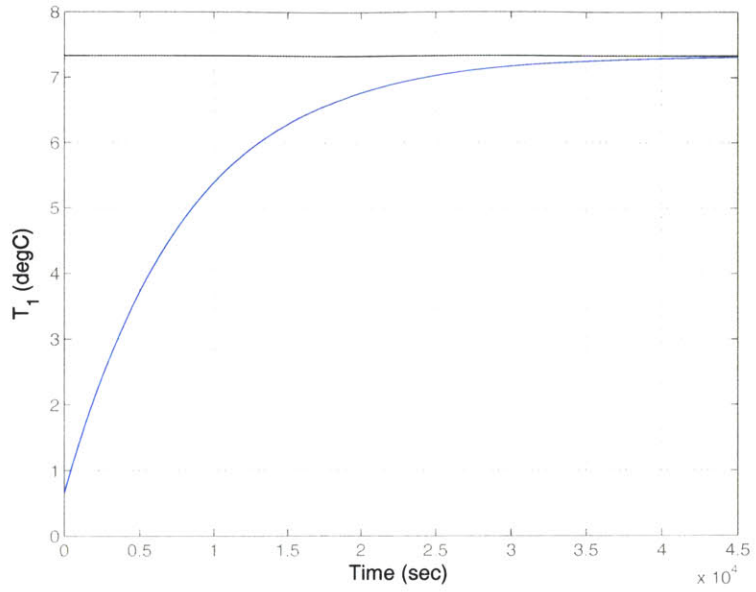

Figure 7-34: Step response of T_1 for a coil heat dissipation $Q_s = 1$ W.

to a coil temperature of 95^{o}C for an ambient temperature of 20 deg C.

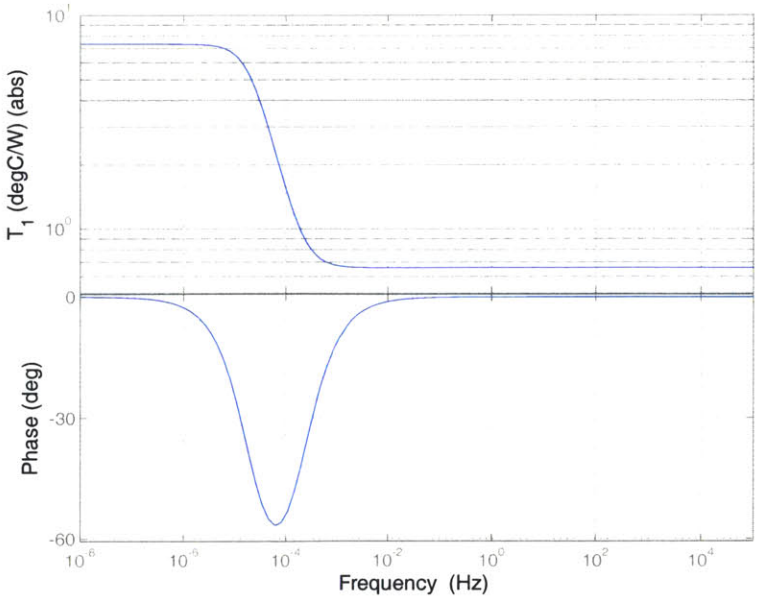

Figure 7-35: Bode Plot of $T_1(s)/Q_s(s)$.

The maximum allowable actuator coil temperature of the actuator is given by the

manufacturer as 110°C. So the holder will let you work with currents of up to 10 A-pk provided with frequencies above 1 Hz. Also if the holder is bolted to another structure this one will acts as an additional heat sink. This situation is not considered in our heat transfer analysis.

7.12.3 Electrical Dynamics

The chosen actuator for the precision machine is a Model 6880 Galvanometer Optical Scanner from Cambridge Technology, INC. The actuator has a torque constant of $K_m = 0.0245$ Nm/A, a coil resistance $R_m = 1\ \Omega$, a coil inductance $L_m = 280$ uH, and a rotor inertia $J = 0.64 \cdot 10^{-6}$ kgm^2.

The actuator circuit model is shown in Figure 7-36, yielding the following differential equation:

$$v_m(t) - i(t)(R_s + R_m) - L_m \frac{d}{dt} i(t) - e(t) = 0 \tag{7.33}$$

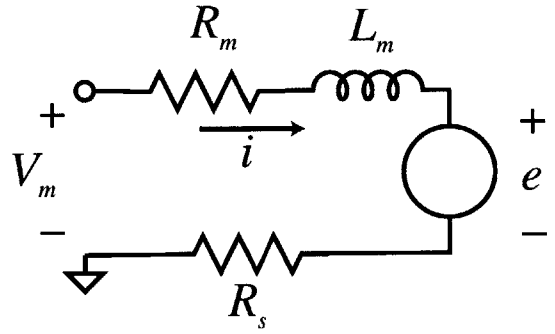

Figure 7-36: Actuator electrical circuit.

where $e(t) = K_m \frac{d}{dt}\theta(t)$ is the back-emf, and $R_s = 0.1\ \Omega$ is the current sensing resistance. The magnitude of the back-emf is defined by $|e(t)| = K_m w|\theta(t)|$. The angular rotation will be $|\theta(t)| < 2.5$ mrad up to around 10 Hz, and then drops to $|\theta(t)| < 83.3$ urad around 1 kHz. The magnitude of the back-emf has a maximum value of 4 mV at 10 Hz, with a voltage $v_m = 8$ V driving the actuator. The magnitude

of the back-emf has a maximum value of 6 mV at 1 kHz, with a voltage $v_m = 15$ V driving the actuator. So the back-emf is insignificant enough to simplify (7.33) as follows:

$$v_m(t) - i(t)(R_s + R_m) - L_m \frac{d}{dt} i(t) = 0 \tag{7.34}$$

Taking the Laplace transform of 7.34:

$$V_m(s) - I(s)(R_s + R_m) - L_m s I(s) = 0 \tag{7.35}$$

$$\frac{I(s)}{V(s)} = \frac{1/(R_s + R_m)}{(L_m/(R_s + R_m))s + 1} \tag{7.36}$$

For the given values of $R_s = 0.1\ \Omega$, $R_m = 1\ \Omega$, and $L_m = 280\ \mu$H, gives as a breakpoint frequency at $625Hz$ and the Bode plot for $I(s)/V(s)$ as shown on Figure 7-37.

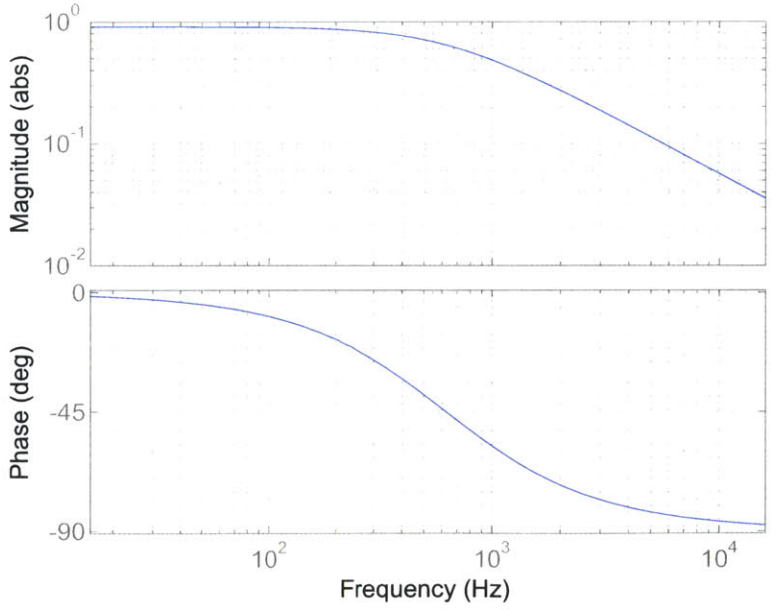

Figure 7-37: Bode plot of $I(s)/V(s)$ for FTS actuator.

7.13 Cap gage holder

The cap gage holder serves the purpose of holding the cap gage with is axis aligned with the tool tip and it sensing surface perpendicular to the tool holder target face. The holder part was provided with an extension to mount the holder on.

The cap holder design is a part that can be mounted with two screws in one side and a built-in collet that is clamped with the aid of two additional screws, as shown in Figure 7-38.

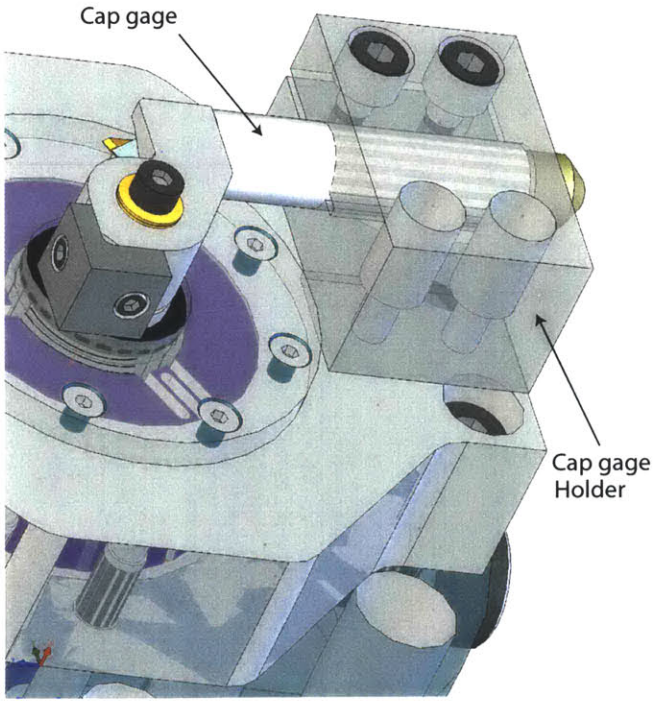

Figure 7-38: Capacitance gage holder.

The clamp of the cap gage holder was calculated using a similar procedure as the one for the shaft coupling shown in Section 7.9.2.

7.14 Separator

The separator serves the main function of a transition piece between the collet holder and the galavanometer holder. This part was made of aluminum, making it easy to machine and a light part.

This part permits removal of the preload part and re-adjustments if necessary. A grounding point is provided to connect a cable to the shaft, in order to provide the necessary grounding between the cap gage and the tool holder. Also a hole is provided on the side of the part to permit the tightening of the shaft coupling to the galvanometer shaft. A solid model of the separator is shown in Figure 7-39.

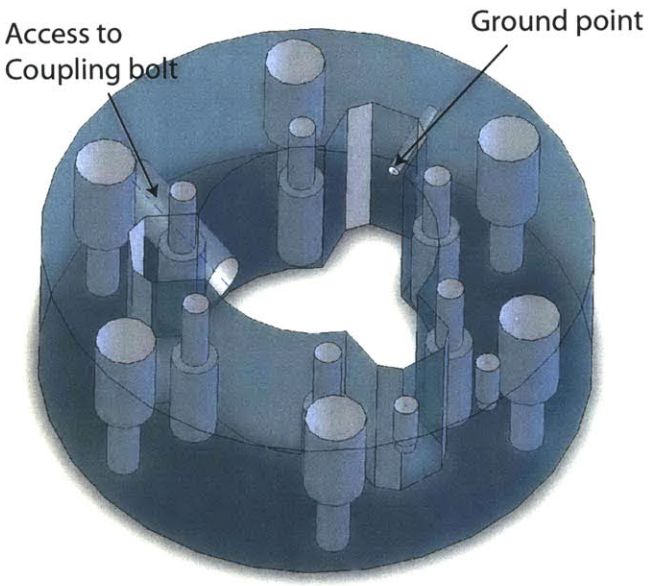

Figure 7-39: Solid model of Separator.

7.15 Sealing

Sealing of the machine is important to avoid any cutting oil or lubricant getting into the rubber bearing, although the Neoprene rubber has a good resistance to oil. A

sealing plate with an o-ring is provided to seal the top opening of the machine as shown in Figure 7-48. The use of a plastic plug in the hole provided in the separator to access the coupling bolt was considered, as well as in all other exposed counter bores that could permit oil from getting into the rubber bearing area. In the case of the drilled and tapped hole of the separator to provide a ground point the use of silicone sealant or epoxy on the outer side will be sufficient.

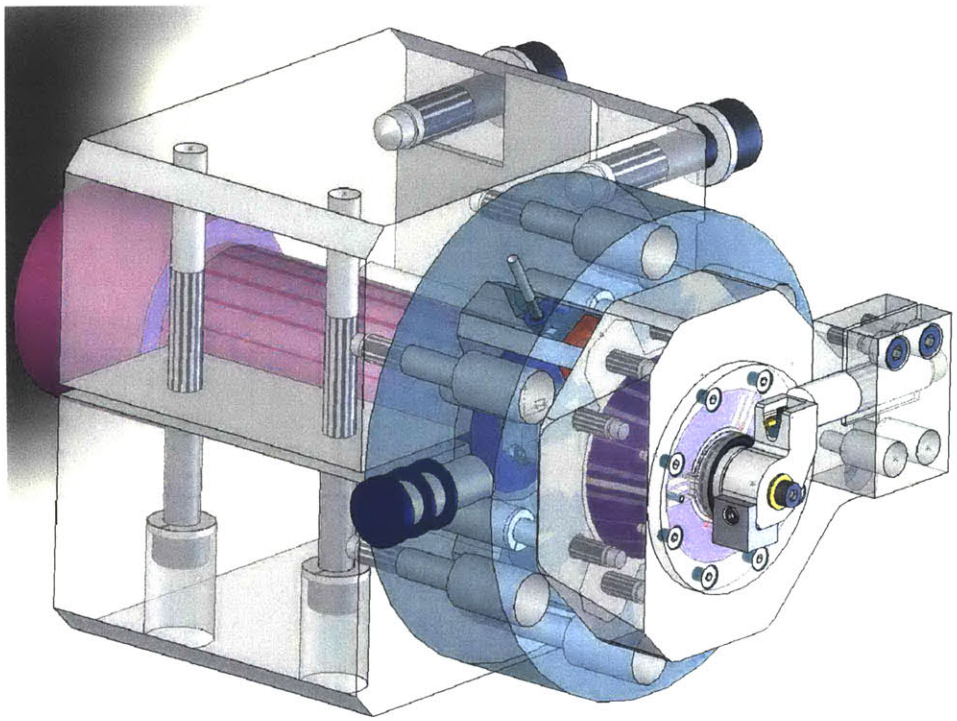

Figure 7-40: FTS Solid model.

7.16 Final design

A preliminary set of general dimensions and first order performance parameters are presented in Section 7.3. Here the general dimensions of the FTS, as a result of the detailed design shown in Figure 7-40, will be taken into consideration. A summary of the general dimensions and performance parameters are shown in Figure 7-41.

Dimensions

Shaft diam1 d1 (mm)	tool radius rT (mm)	length from tool to bearing center Lb (mm)	Spacing between top of bearing and tool e (mm)	Length from bearing bottom to galvo Lx (mm)	length from tool to galvo LT (mm)	Width of Bearing B (mm)	Height of bearing H (mm)	Thickness of rubber laminate t (mm)	Number of laminates n
12.0	**12.0**	**16.7**	**4.6**	**30.4**	**55.1**	**12.0**	**15.5**	**0.77**	**3**

Actuator torque 0.2 Nm
(The actuator is considered as a torque source for this analysis)

Actuator shaft stiffness 2.38E+06 N/um

Rotational inertia 1.44E-06 kg.m2
(Considers shaft + tool holder + Actuator Rotor)

Performance

Radial Tool Tip Stiffness krad (N/um)	Max DC Stroke (umP)	Max Stroke @ 2kHz (umP)	Max Stroke @ 10kHz (umP)	Est. rigid body nat. frequency fn (Hz)
19.3	31.39	0.87	0.42	1161
		Stiffness Driven	Inertia Driven	

Rubber Bearing Calculation

Material	Shore	Stiffness factor due to preload	A (mm2)	ϕ	S	kr	Ec (MPa)	G (MPa)	kc (N/um)	ks (N/um)	kc/ks
Neoprene	**80A**	**3.72**	185.8	0.9	4.4	0.9	477.4	8.8	38.4	0.7	54.2

krad DC (N/um)	kaxial DC (N/um)	ktors DC (N.m/rad)	ktors @2 kHz (N.m/rad)	ktors @10 kHz (N.m/rad)
52.4	2.124	76.5	2752.6 Estimate	2752.6 Estimate

Shear Strain (%) DC	Shear Strain (%) @ 2 kHz	Shear Strain (%) @ 10 kHz
0.68	0.019	0.009

DC Stiffness Calculations
(Stiffness referred to tool tip)

Rubber bearing kbrad (N/um)	Tool holder bending kthrad (N/um)	Shaft bending ksbrad (N/um)
25.4	331.9	106.9

Figure 7-41: Final Design calculation.

7.17 Assembly procedure

To assure the correct operation of the FTS an assembly process is required. Following this assembly process avoids over-constraints of the rotating shaft.

The FTS consists of about 17 parts excluding fasteners and mounting accesories. A photograph with all the FTS parts is shown in Figure 7-42.

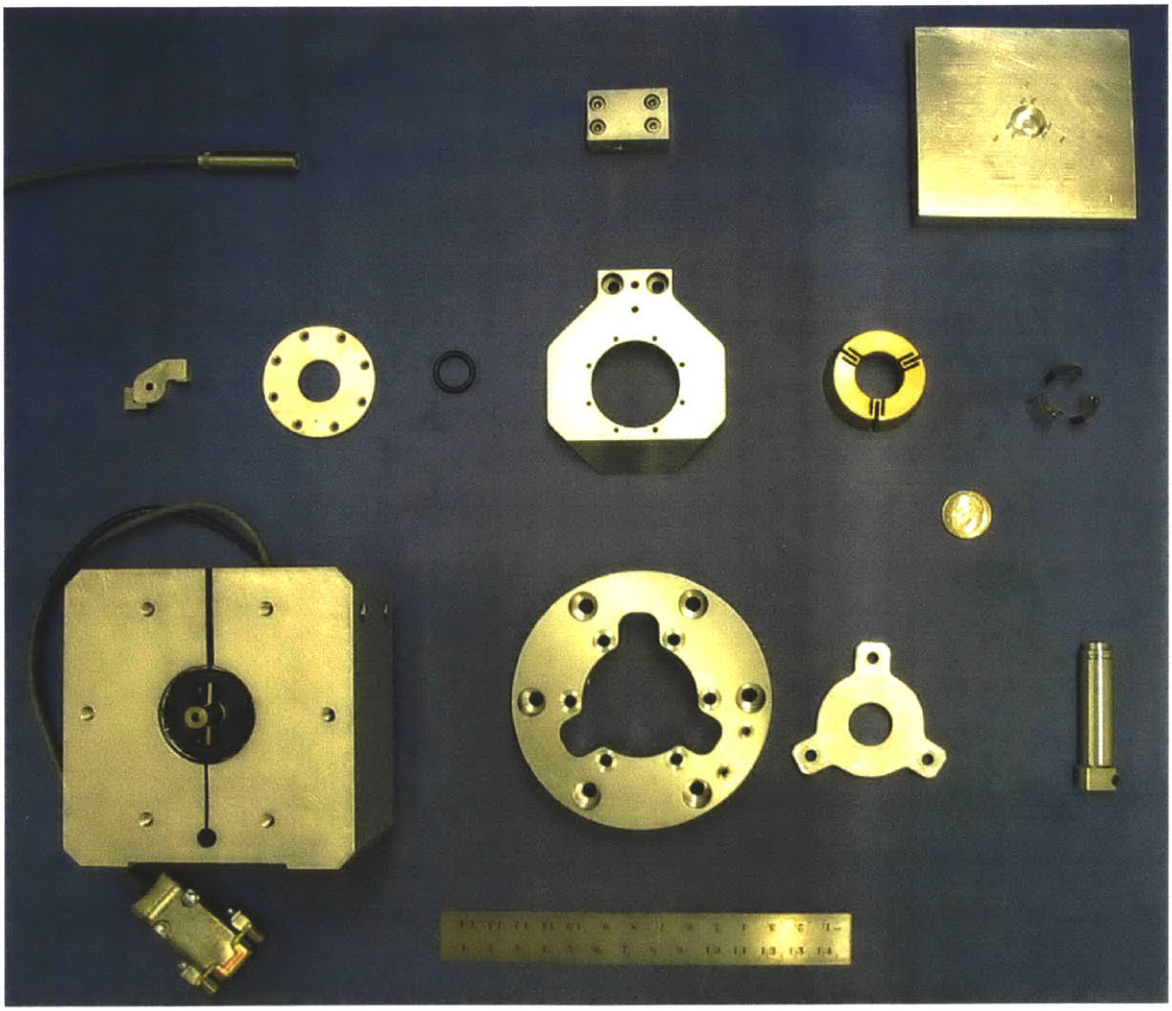

Figure 7-42: Photograph of all the parts of the FTS.

The assembly steps of the FTS are presented as follows:

Step 1

The first step is to assemble the rubber bearings with the shaft and collet. The rubber bearings are undersized on purpose and so the use of an aluminum shim is required. The bearings must first be positioned in the bearing assembler unit as shown on Figure 7-43.

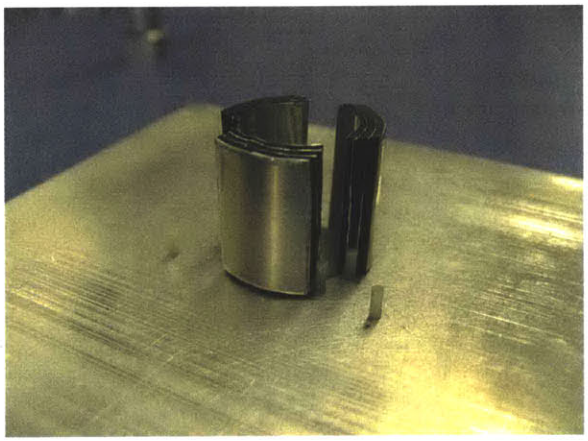

Figure 7-43: Bearings in bearing assembler unit.

Step 2

An adequate aluminum shim is first placed in the inner diameter of the collet. The collet is positioned with the correct alignment in the bearing assembler unit as shown in Figure 7-44.

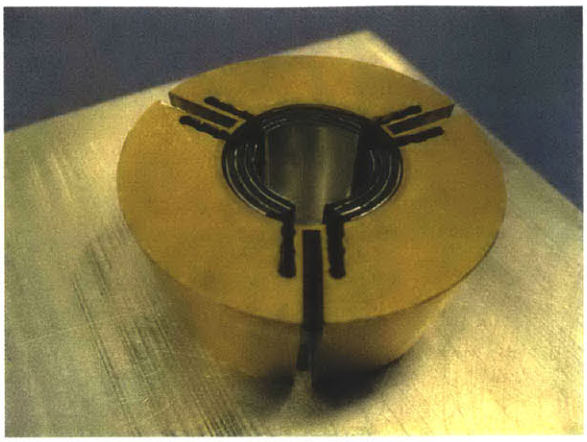

Figure 7-44: Bearings and Collet in bearing assembler unit.

Step 3

Slide the shaft into the inner diameter of the rubber bearings until it reaches the bearing assembler stop, which sets up the axial position of the shaft with respect to the rubber bearings, as shown in Figure 7-45. The rubber bearings must be lightly pressed into the collet before the assembly removal.

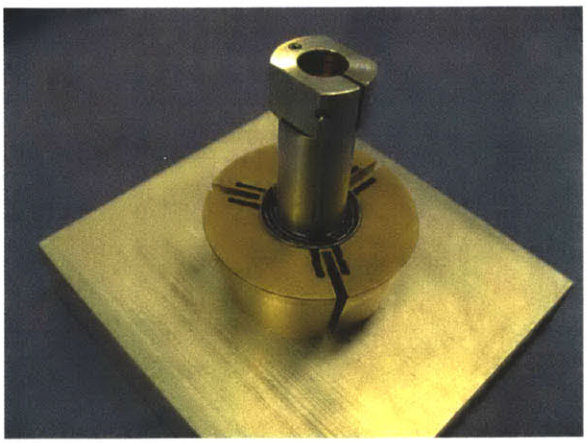

Figure 7-45: Bearings, Collet and Shaft in bearing assembler unit.

Step 4

Remove the collet-bearing-shaft assembly from the bearing assembly unit by gripping the collet with three fingers providing pressure. The resulting assembly is shown in Figure 7-46.

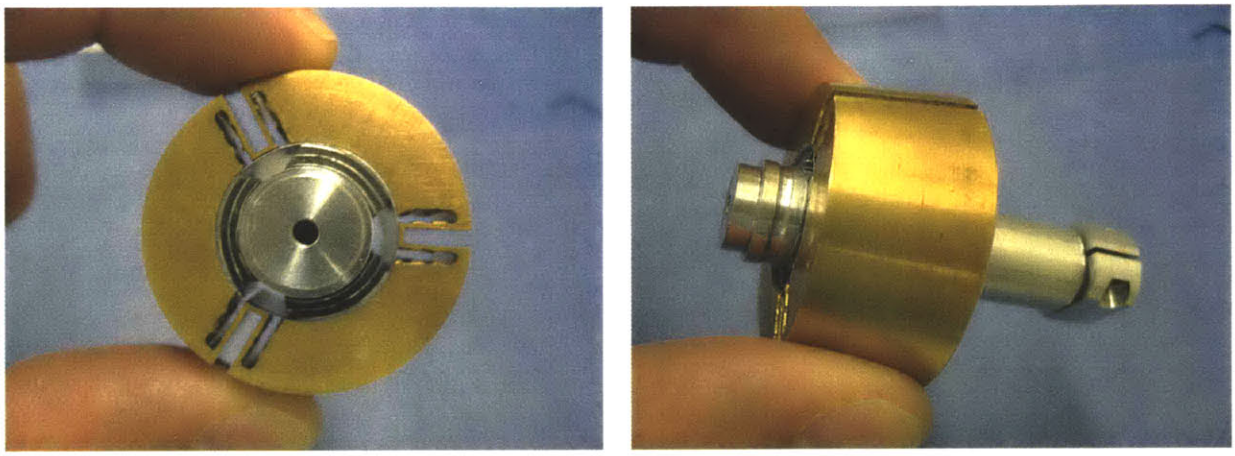

Figure 7-46: Bearings, Collet and Shaft assembled!

Step 5

Assemble the top sealing on the collet holder with its respective alignment pin, followed by the installation of the collet collet-bearing-shaft assembly.

Step 6

Preload the collet with the aid of the preload part, rubber sheet interface, and the corresponding preload bolts and Belleville Springs, as shown in Figure 7-47.

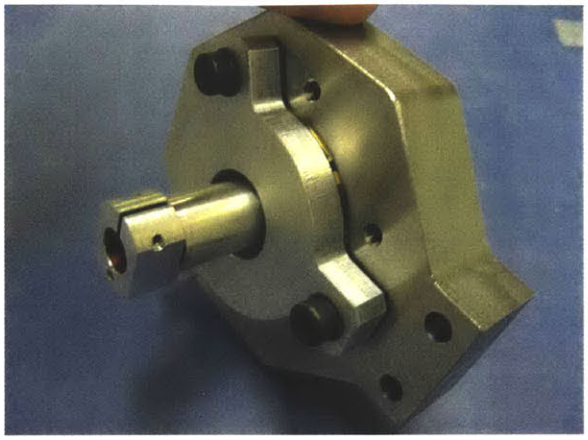

Figure 7-47: Collet preload.

Step 7

Remove the the top plate, and reinstall it with the o-ring in installed in the shaft, as shown in Figure 7-48.

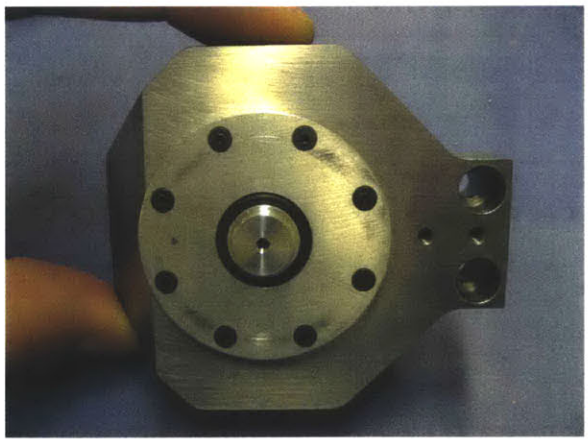

Figure 7-48: O-ring installation.

Step 8

Install the tool holder assembly on the shaft and align it with the aid of parallels. The resultant assembly is shown in Figure 7-49.

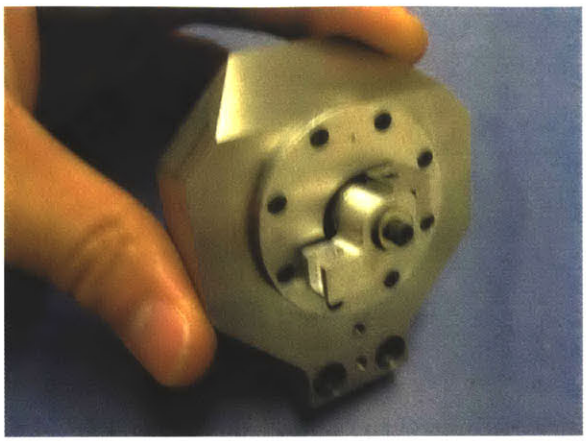

Figure 7-49: Tool holder installation.

Step 9

Connect the ground cable to the shaft and the separator, and then assemble the separator to the current assembly, as shown in Figure 7-50.

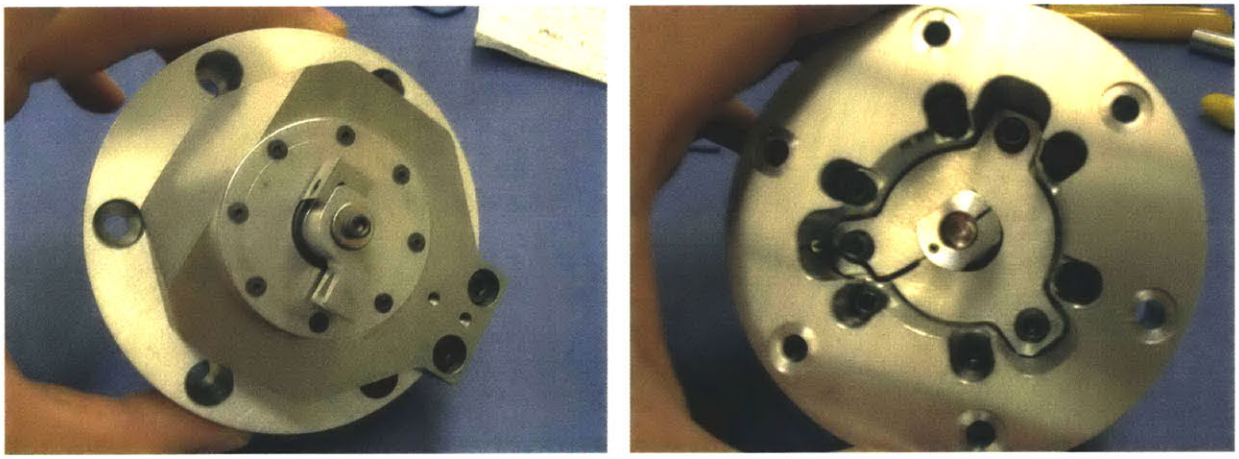

Figure 7-50: Separator installation.

Step 10

Install the actuator in the actuator holder and then assemble it with the assembly of the previous step. The shaft coupling must assemble aligned with the actuator

shaft letting to self center while assembling. Tighten the assembly bolts in a cross manner by tightening all of them first with light torque. Place the assembly on a flat surface and align with the aid of shims the collet holder as shown in Figure 7-51. After the alignment tighten all bolts with medium torque and finally with full torque. Full torque is the bolt manufacturer recommended torque. If tightening by hand then you tighten according to experience.

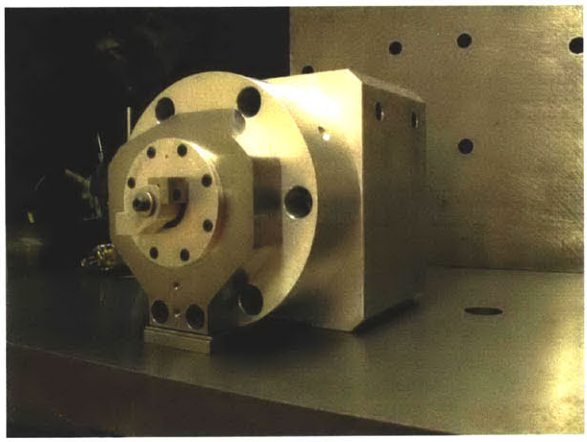

Figure 7-51: Alignment of collet holder to actuator holder.

7.18 Power Amplifier and Current Control

The Power Amplifier and Current control used to drive the actuator were the same used by Montesanti [13] to drive his actuator. The Current control was designed and built by Montesanti.

The Power Amplifier is an Apex Microtechnology Corporation PA04 with a non-inverting DC gain $K_{pa} = 3$. This amplifier is a high voltage, high current amplifier with a maximum power supply voltage of ± 100 V, and a maximum output current of 20 A-pk. A power supply of ± 35 V was provided to the amplifier by two Lambda LK 343A FM connected in series, with a maximum output current of 10 A. The amplifier output current was also limited to 10 A with the aid of a current limit resistor.

The PA04 power amplifier frequency response was measured using an HP 35665 A Dynamic Signal Analyzer up to 50 kHz showing a constant gain of 2.95 and practically constant phase with only a phase lag of 0.56^o at 50 kHz.

Additional high-frequency bypass capacitance was added to the amplifier power supply bypassing. The amplifier had only 0.01 uF high-frequency ceramic capacitors installed for the positive and negative part of the power supply, when it is recommended to have between 0.1 uF and 1 uF. A total of 0.4 uF capacitance was installed.

7.19 Displacement measurement

The tool tip displacement was measured with the aid of a capacitance gage. The capacitance gage an module used is the same used in the rubber test device as described in Section 3.1.7. The capacitance gage module outputs ± 10 V for ± 25 μm.

7.20 Simulink and Control desk models for test

The tests of the FTS were done using a dSpace ds1104 board as an analog to digital interface between our electronics and the dSpace environment. A Simulink model was created to perform all the necessary experimentation, and to control the FTS, as well as provide the necessary safety features.

Safety features where included in the Simulink model to avoid the overheating of the voice coil actuator and the damage of the tool holder or capacitance gage resulting from an excessive stroke. The current was limited to a maximum of 10 A pk, and the stroke to a maximum of 25 μm-pk. Whenever any of this limiting factors was exceeded the voltage supplied to the actuator was zeroed with the aid of a trigger.

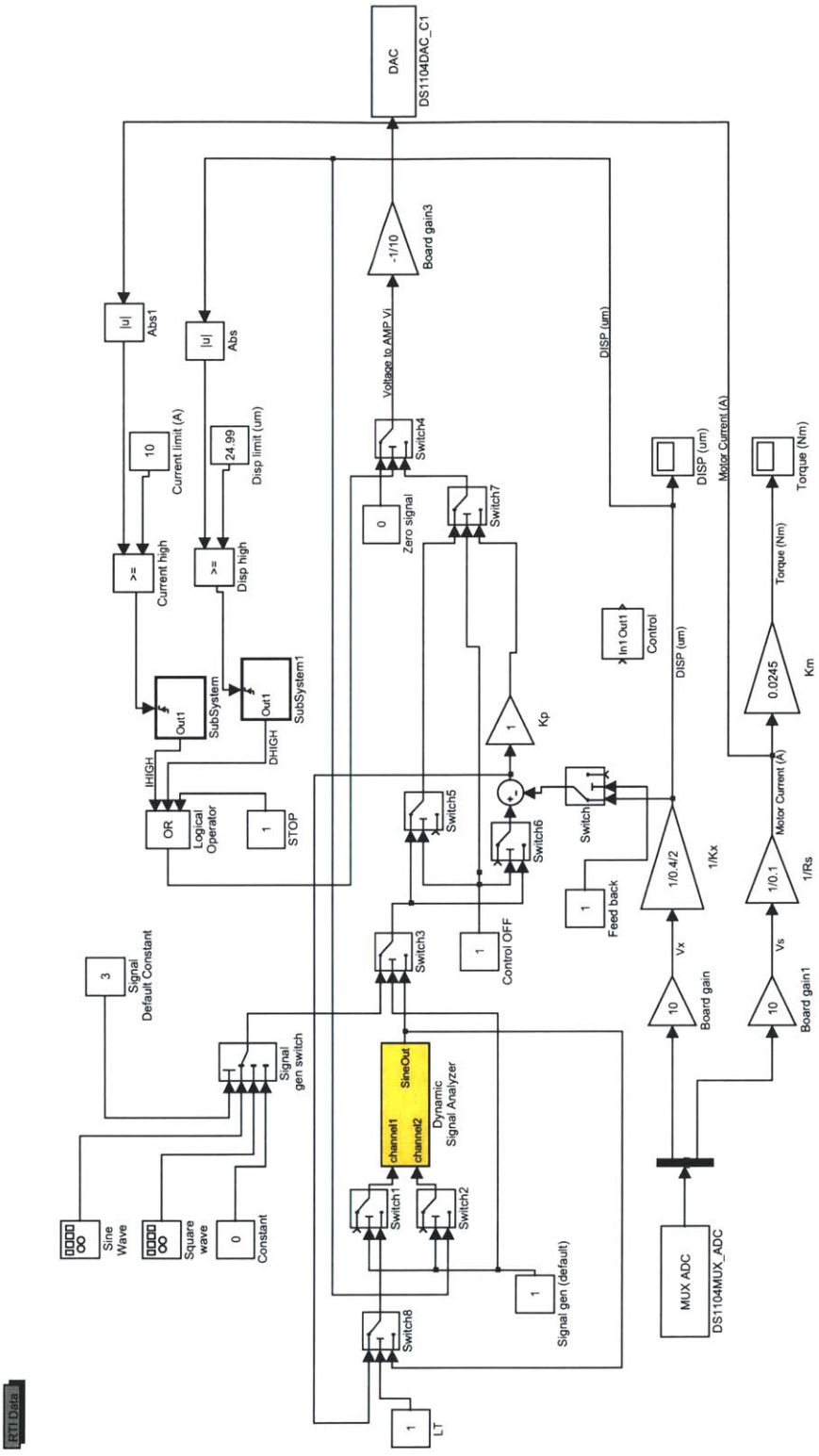

Figure 7-52: Simulink model used for the testing of the FTS.

The developed Simulink model is shown in Figure 7-52.

7.21 Electrical connections

The electrical connections between all the electronic equipments where done to achieve low noise level measurements and assure proper safety.

7.21.1 Avoiding ground loops

To avoid ground loops a grounding technique was followed as shown in Figure 7-53. The technique followed is to keep supply commons separate and meet only at one single point connected to ground. As a result "each supply current returns only on its associated common, and not on other commons or the ground wire." as stated by Trumper [18] (Sec. 5.5.1)

To keep the supply commons separate it is necessary isolate the subsystems. Unity gain INA154 differential amplifiers are used to isolate the current control circuit from the dSpace board (which is referenced to earth ground), the power amplifier, and the actuator electronics. All this INA154 differential amplifiers were already included in the current control electronics designed and built by Montesanti [13].

The capacitance gage module is used in differential mode with the shielding provided by the a floating common (ARTN), the positive and negative gage module are connected to the positive and negative input of a Tektronix AM502 differential amplifier. This differential amplifier is connected to earth ground, reason for which the shielding of the gage module outputs with the provided floating common was chosen.

All the power supply commons where connected to a single earth ground as shown in Figure 7-53.

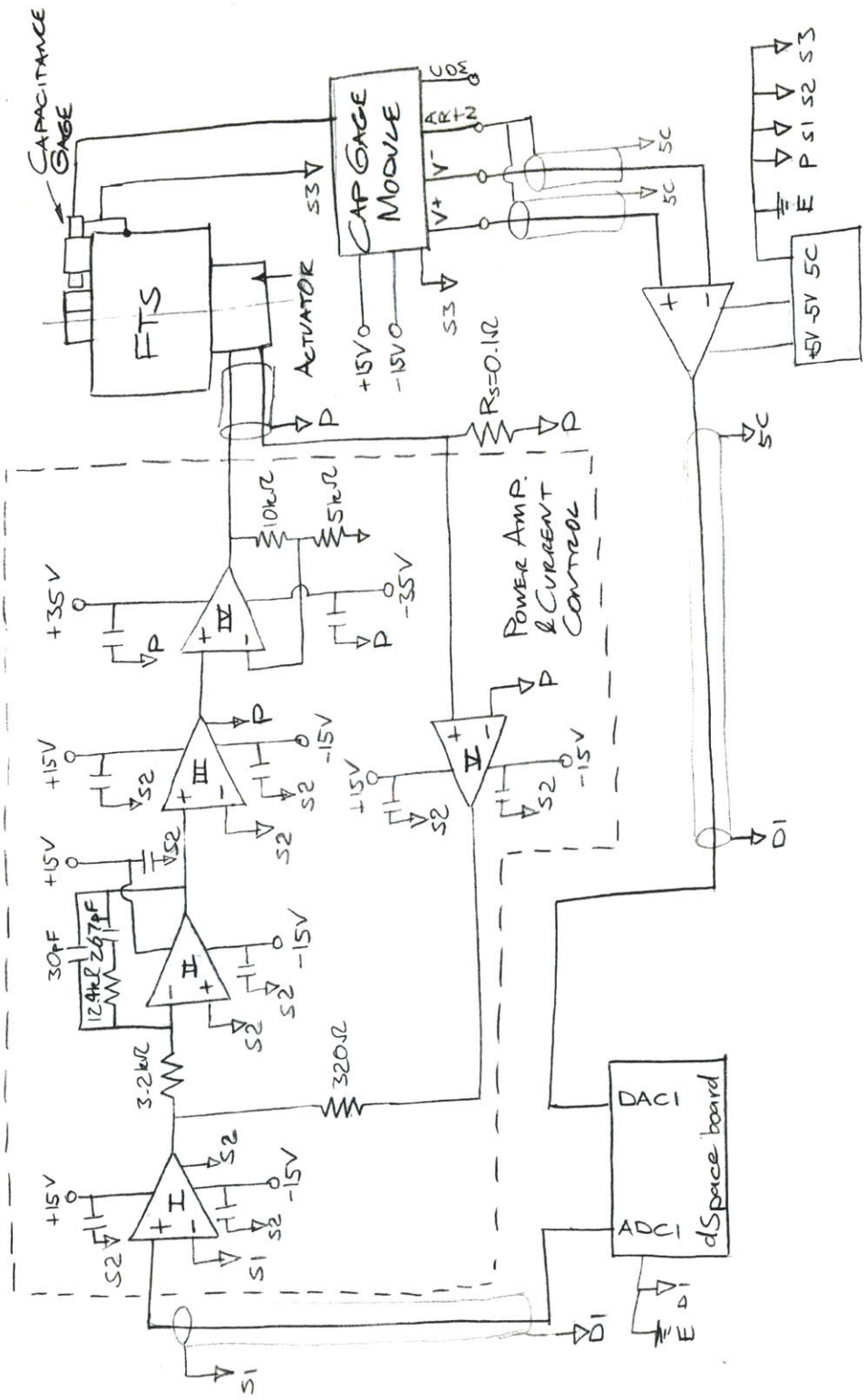

Figure 7-53: Schematic of electrical connections showing grounding technique (legend: I, III, and V are INA154 High-Speed Precision Difference Amplifiers; II is an OPA602 High-Speed Precision Operational Amplifier; and III is the APEX PA04 Power Amplifier).

This grounding technique helped reduce the ground loops and electrical noise of the position signal to a minimum. The measured electrical noise from the cap gage shown in Figure 7-54, is on the order of 2 mV pk-pk, which is equivalent to 5 nm pk-pk displacement of the tool tip.

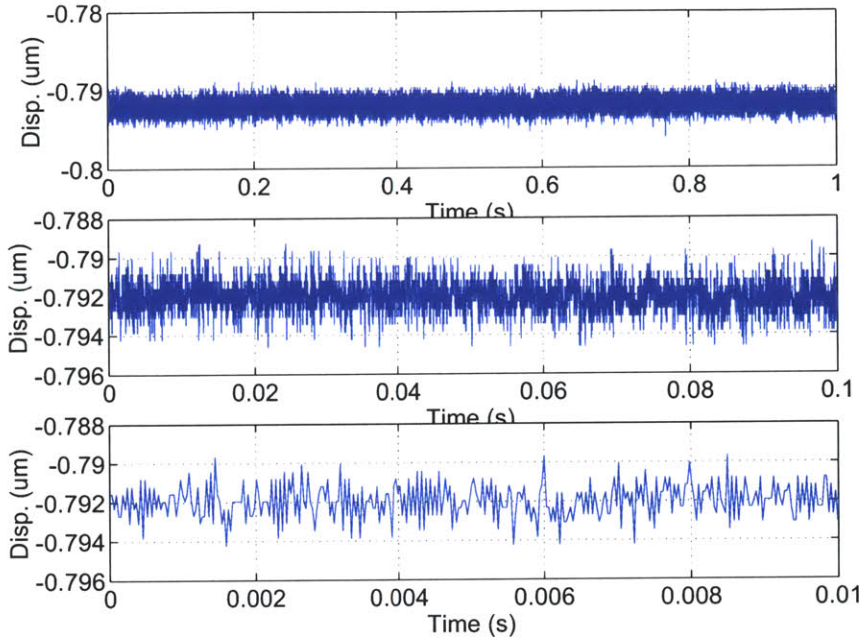

Figure 7-54: Electrical noise from capacitance gage module represented as measurement noise (Three different time scales shown).

7.22 Open loop behavior

Preliminary measurements where done open loop to understand the open loop behavior of the FTS, as well as solving any electronic or mechanical issues, as well as to serve as a basis for the design of a controller.

7.22.1 Tool tip stiffness

When measuring the open loop stiffness of the tool tip in the stroke direction, the displacement comes mainly from the torsion of the rubber bearing, secondary dis-

placement comes from the radial displacement of the tool holder. The second one must be reduced to a minimum.

A digital force gage in combination with the capacitance gage was used to measure the stiffness. The measured open loop tool tip stiffness was on the order of 0.62 N/μm.

Measurements of the radial stiffness of the tool holder where not successful with the current setup. An adequate surface to apply a force aligned with the centerline was not available, and only the tool tip displacement could be measured. Any eccentricity of the applied force creates rotation of the shaft and so adds up to the measurement of the displacement of the tool tip. Indirect measurements of the radial stiffness were done by applying a force at different eccentricities. The predicted radial stiffness based on the indirect measurements ranges between 10 N/μm and 100 N/μm.

7.22.2 Step response

The step response of the FTS shows a rapid rise to around 60% of the maximum displacement within the order of 100's of milliseconds, followed by a creep response which takes place in the order of seconds, as shown in Figure 7-55. This step response is basically a representation of the rubber bearing dynamics, which can be seen in Section 5.5. The dynamics of the rotational inertia become secondary due to the low rotational inertia.

7.22.3 Frequency response

The open loop frequency response of the FTS driven basically by a current source, being current the input, and tool tip displacement the output was measured. The open loop frequency response of the FTS is shown in Figure 7-56. The frequency response shows a reduction of output stroke with an increase in frequency which is

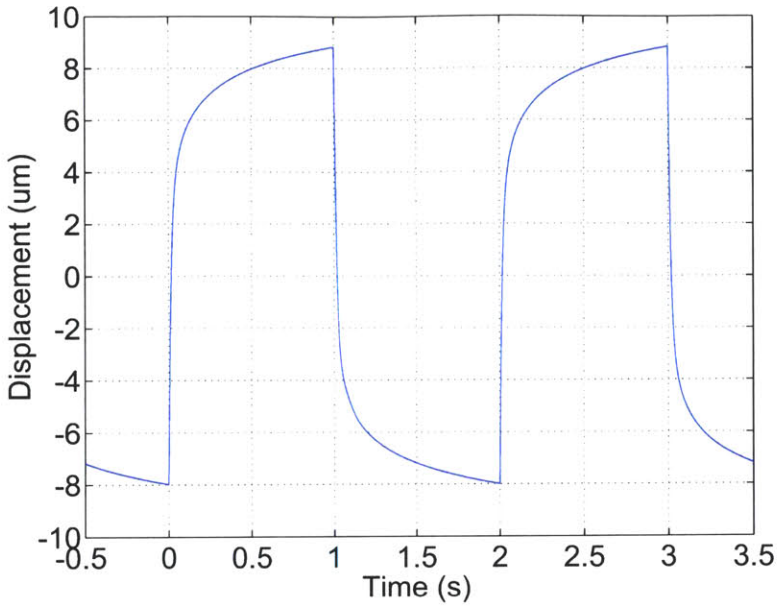

Figure 7-55: FTS Step response.

due to the increase of complex stiffness of the rubber bearing. The phase lag due to the rubber bearing should get to a maximum within the transition zone, and then drop as shown in Section 5.3.

The rotational modal analysis predicted a rigid body resonance at around 1.2 kHz and a out of phase resonance between the actuator rotor and the tool holder at around 7.8 kHz. The rigid body resonance is actually highly over-damped due to the damping from the rubber bearing. The rotational inertia of the FTS rotor is $J = 1.426 \cdot 10^{-6}$ kgm^2 which accounts for a rotational dynamic stiffness at 1 kHz of about 56 Nm/rad. While the predicted rubber bearing rotational dynamic stiffness at 1 kHz is on the order of 1000 Nm/rad. The Bode plot shown in Figure 7-56 shows how the dynamic stiffness approaches a maximum, being this usual for rubber dynamic stiffness, and it is reached around 2 kHz. A resonance peak is seen around 3 kHz which is considered as the out of phase resonance predicted with the rotational modal analysis happening at lower frequency. The lower resonant frequency is foreseen as been due to an overestimate of the coupling stiffness. The phase lag associated with an out of phase resonance is 180^o at the resonance frequency and

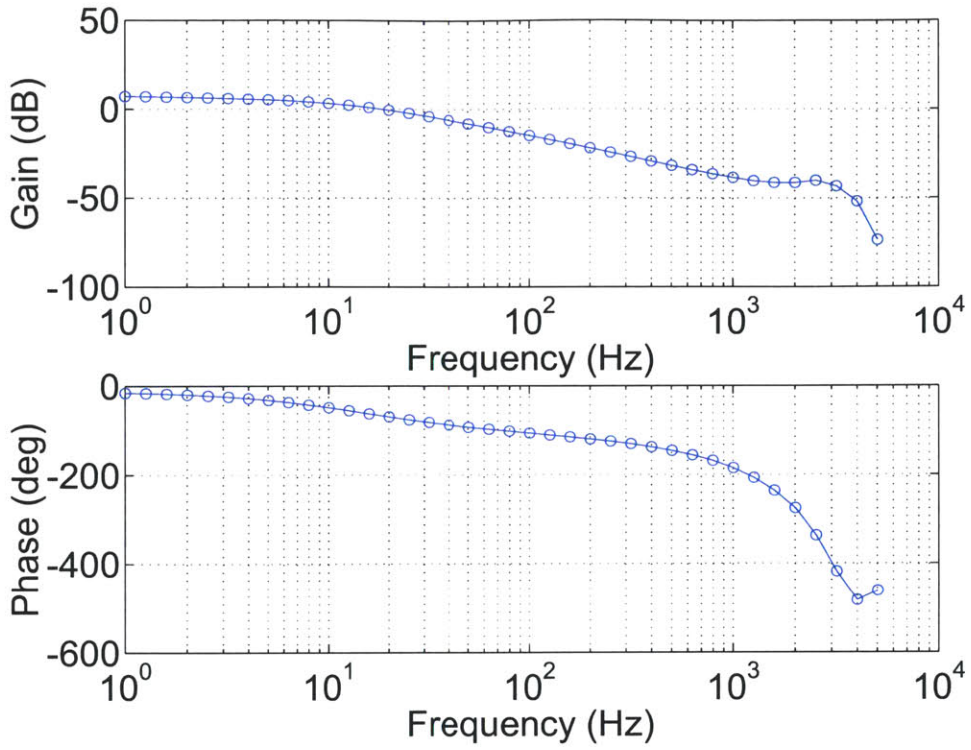

Figure 7-56: FTS Open Loop frequency response.

360^o at higher frequencies. Being this considered as the reason of the phase of the measured frequency response.

7.22.4 Maximum Stroke

The maximum open loop strokes as a function of frequency are shown in Table 7.7. The predicted open loop maximum stroke was of 60 μm pk-pk at 1 Hz and 1.6 μm pk-pk at 1 kHz. The maximum stroke prediction are of the same order of magnitude than the experimental ones, being 30% off on the case of the one at 1 Hz and 100% off for the stroke at 1 kHz.

Table 7.7: Maximum open loop strokes as a function of frequency (with the actuator driven at 20 A pk-pk)

f (Hz)	Stroke (μm pk-pk)
1	45
10	33
100	6.3
1000	0.8

7.23 Controller Design

From the open loop frequency response it is seen that -180^o are reached around 1 kHz, and then drops significantly. Also the frequency response magnitude is practically flat between 1 kHz and 3 kHz, which makes it really hard to design a controller with a cross-over frequency higher than 1 kHz.

7.23.1 Proportional Controller

The open loop frequency response shows a pole with an associated break-point frequency at around 10 Hz, followed by a zero with an associated break-point frequency at around 1 kHz. Being this due to the rubber bearing dynamics. At frequencies below 1 KHz the rubber bearing acts like an integrator which is limited by the low frequency bearing rotational stiffness.

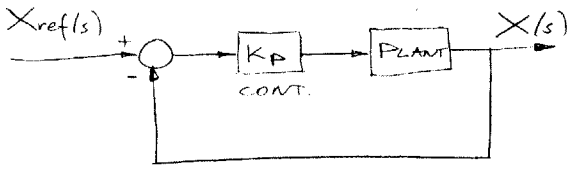

Figure 7-57: Proportional Controller.

Adding a proportional controller as shown in Figure 7-57, with a cross-over frequency within the 100's of Hertz range is easily accomplished. This proportional

controller will provide sufficient disturbance rejection without the use of an integrator, thanks to the rubber bearing dynamics.

The gain of the proportional controller was chosen by first experimenting with three proportional gains K, being this 30, 40, and 50. The associated cross-over frequencies f_c, phase margin PM and gain margin GM are shown in Table 7.8, and the loop transmission frequency response is shown in Figure 7-58.

Table 7.8: Proportional controller design

K	f_c (Hz)	PM	GM
30	380	45^o	10 dB
40	500	33^o	6.7 dB
50	700	20^o	2 dB

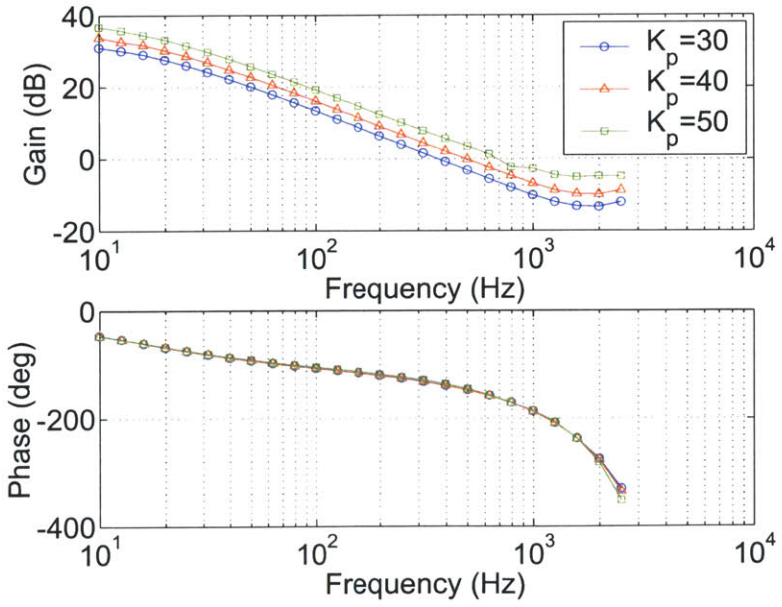

Figure 7-58: Loop Transmission frequency response with a proportional controller at different gains.

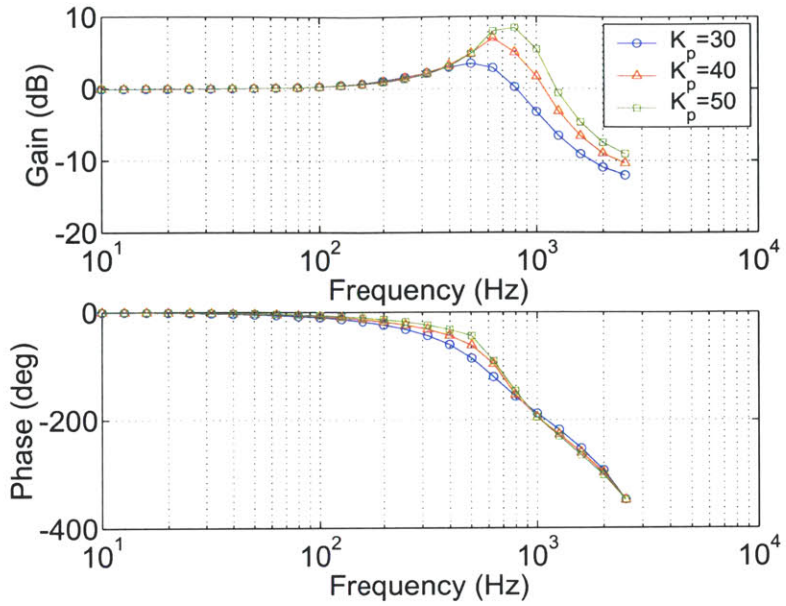

Figure 7-59: Closed loop frequency response with a proportional controller at different gains.

The resulting closed loop frequency responses for the different proportional gains are shown in Figure 7-59. The associated damping coefficient ζ and bandwidth BW are shown in Table 7.9. The chosen proportional controller gain was $K = 35$ so as to obtain a bandwidth close to 1 kHz with a damping ratio close to $\zeta = 0.3$. The resulting loop transmission and closed loop frequency response with a proportional controller $K = 35$ is shown in Figure 7-60 and Figure 7-61 respectively.

Table 7.9: FTS Closed loop bandwidth and damping coefficient with proportional controller

K	BW (Hz)	ζ
30	900	0.4
40	1200	0.2
50	1500	0.15

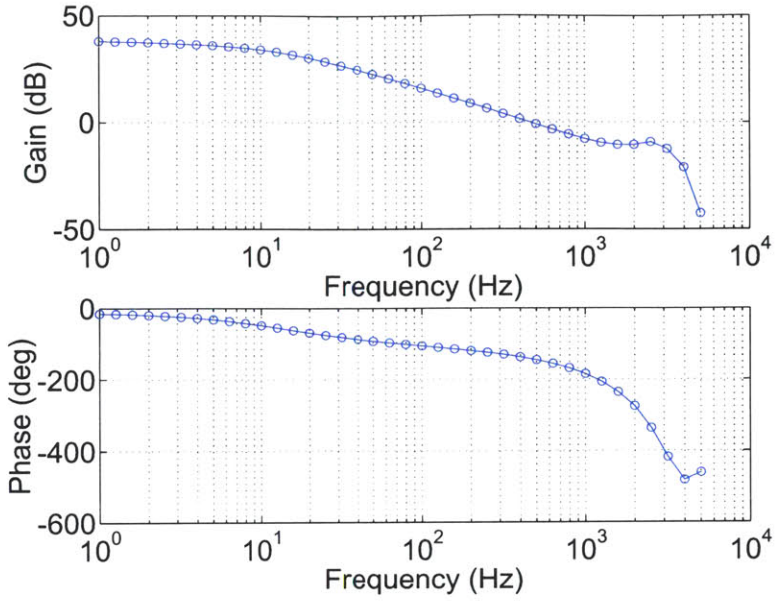

Figure 7-60: Loop Transmission frequency response with a proportional controller ($K_p = 35$).

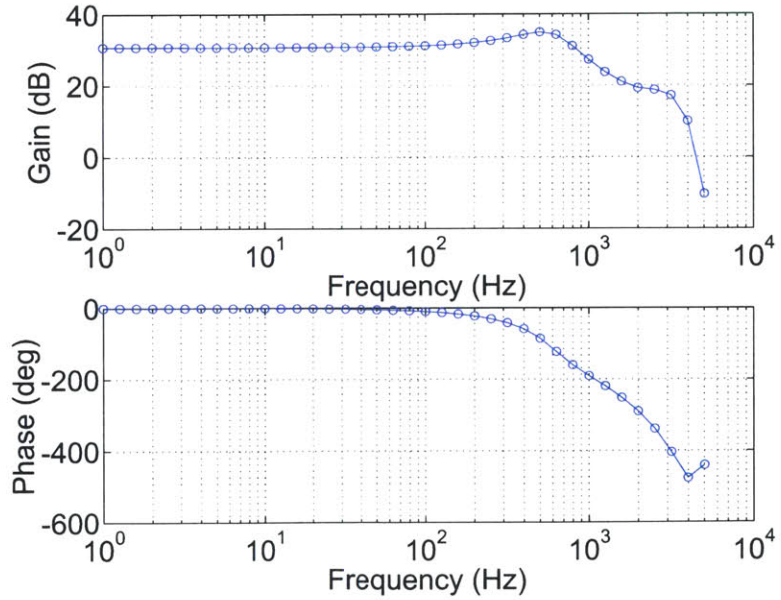

Figure 7-61: Closed loop frequency response with a proportional controller ($K_p = 35$).

The small signal step response of the FTS with the implemented proportional controller is shown in Figure 7-62. It can be seen that the rise time is about $t_r = 0.5 \cdot 10^{-3}$

s, the time to the first peak is about $t_p = 0.7 \cdot 10^{-3}$ s, and the overshoot is about 35% which is correspondent to the closed loop frequency response shown in Figure 7-61. It can be seen in the small signal step response how the creep behavior of the rubber bearing shown in Figure 7-55 is no longer present, and that the time constant of the system has reduced significantly from an order of seconds to an order of milliseconds.

The large signal step response of the FTS is shown in Figure 7-63. The time constant associated to this step response is larger than the small signal step response due to the saturation of the A/D converter and further limited by the power amplifier and power supplies current limit.

The measured closed loop tool tip DC stiffness was between 66 N/μm and 79 N/μm, with an average of 70 N/μm. This was measured with the aid of a force gage and by reading the measured displacement with the capacitance gage.

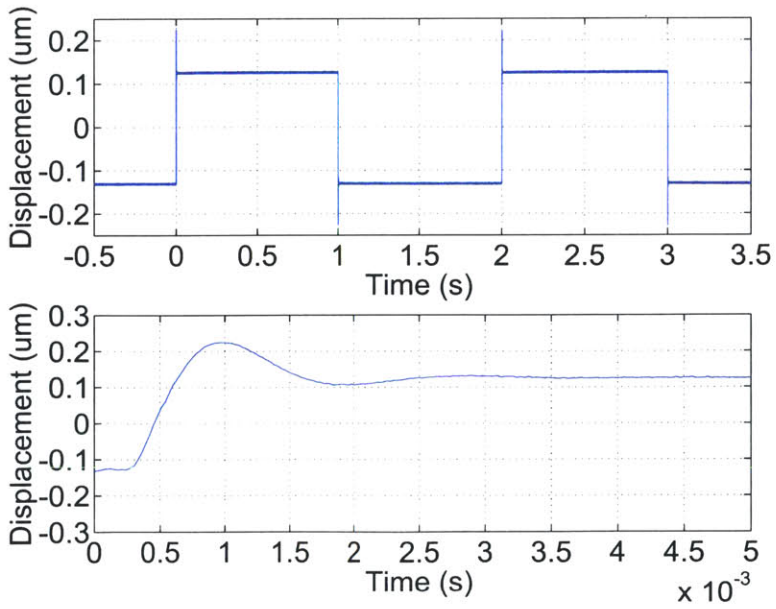

Figure 7-62: FTS small step (0.26 μm) using a proportional controller ($K_p = 35$).

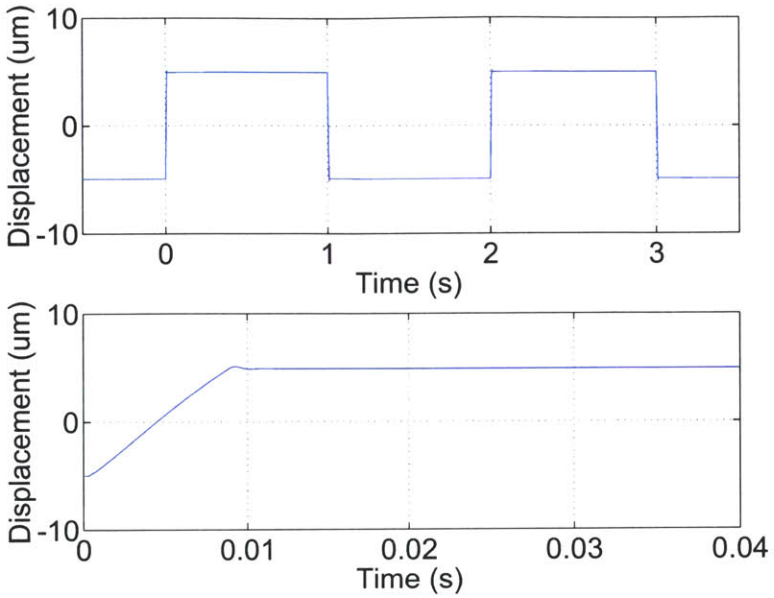

Figure 7-63: FTS large step (10 μm) using a proportional controller ($K_p = 35$).

The expected tool tip stiffness can be calculated by considering the simplified system model shown in Figure 7-64. The DC tool tip stiffness F_d/X is defined by

$$\frac{F_d}{X} = \frac{1 + \frac{r_T}{K_B} 10^6 K_p K_m}{\frac{r_T^2}{K_B}} \tag{7.37}$$

where $r_T = 0.012$ m is the tool radius; $K_B = 76.5$ Nm/rad is the rubber bearing DC torsional stiffness; $K_p = 35$ Nm/μm is the DC gain of the combined proportional controller plus power amplifier and current control; and $K_m = 0.0245$ Nm/rad is the actuator torque constant.

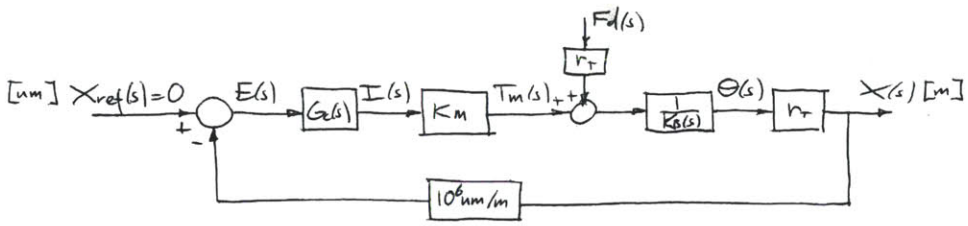

Figure 7-64: Simplified system model to predict DC tool tip stiffness.

Solving (7.37) gives a tool tip DC stiffness of 72 N/μm, which is surprisingly close to the measured tool tip stiffness. Any decrease of the tool tip stiffness is due to the radial displacement of the tool holder. The controller will try to compensate this displacement up to certain extent but the rubber bearing radial stiffness will eventually limit this compensation.

The maximum closed loop strokes as a function of frequency are shown in Table 7.10 (actuator driven at 20 A pk-pk).

Table 7.10: Proportional controller design

f (Hz)	Stroke (μm pk-pk)
1	31
10	21
50	7.8
100	2.5
200	1.7
500	0.6
1000	0.3

7.23.2 Lead Controller

The design of a lead controller for the FTS to obtain a higher bandwidth was undertaken. As stated earlier the flat magnitude of the frequency response between 1 kHz and 3 kHz, makes it really hard to design a controller with a cross-over frequency higher than 1 kHz.

The lead controller defined by 7.38 was implemented with an $\alpha = 2$ and a time constant $\lambda = 159 \cdot 10^{-6}$. The maximum phase of this lead controller occurs at around 700 Hz and corresponds to 19.5°.

$$G_{lead}(s) = K_c \frac{\alpha\lambda s + 1}{\lambda + 1} \tag{7.38}$$

Due to the added phase a higher cross-over frequency than the one with the proportional controller can be achieved. Two controller gains K_c where tried with their respective cross-over frequency f_c, phase margin PM and gain margin GM are shown in Table 7.11. The resulting loop transmission frequency response for the lead controller is shown in Figure 7-65.

Table 7.11: Lead controller design

K	f_c (Hz)	PM	GM
25	400	60^o	6.5 dB
27	480	55^o	6 dB

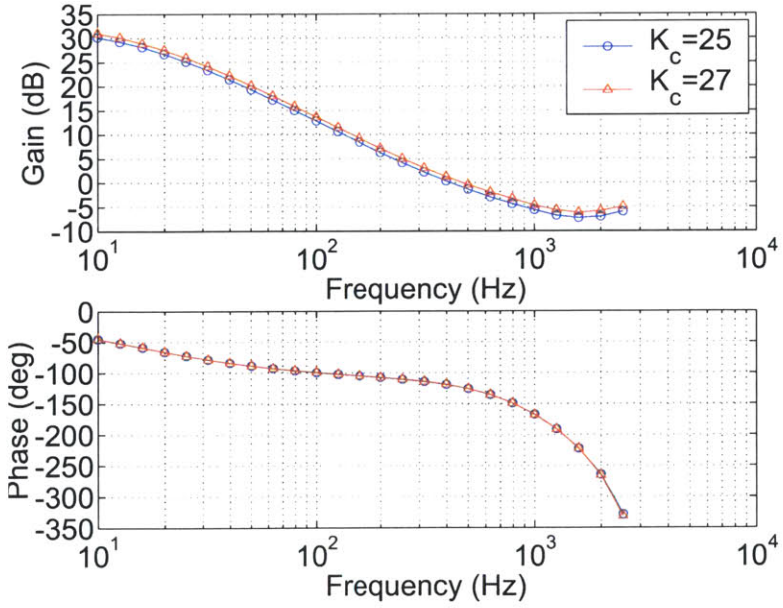

Figure 7-65: Loop Transmission frequency response with a lead controller at different gains.

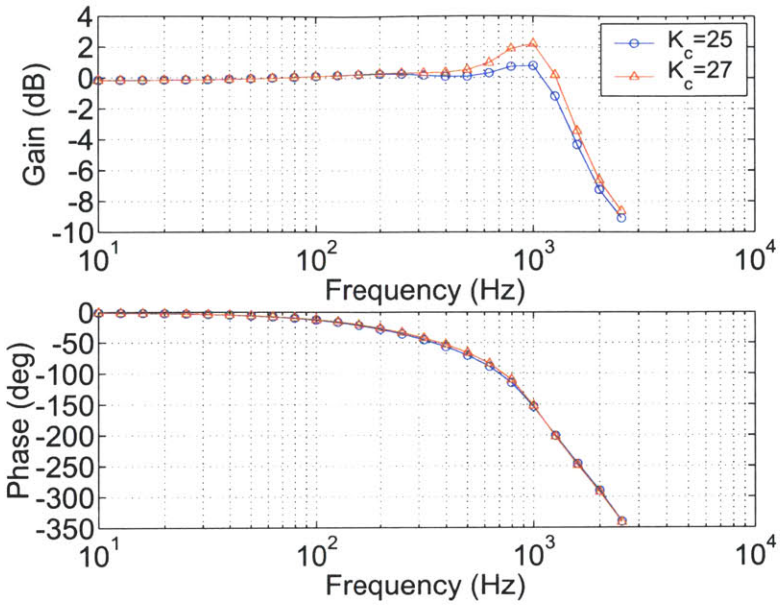

Figure 7-66: Closed loop frequency response with a lead controller at different gains.

The resulting closed loop frequency responses for the different gains K_c of the lead controller are shown in Figure 7-66. The associated damping coefficient ζ and bandwidth BW for the different lead controller gains K_c are shown in Table 7.9.

Table 7.12: FTS Closed loop bandwidth and damping coefficient with lead controller

K_c	BW (Hz)	ζ
25	1400	0.50
27	1500	0.45

The small signal step response of the FTS with the lead controller with a gain $K_c = 27$ is shown in Figure 7-67. It can be seen that the rise time is about $t_r(10\% - 90\%) = 0.25$ ms, the time to the first peak is about $t_p = 0.5$ ms, and the overshoot is about 8% which is correspondent to the closed loop frequency response. It can be seen here as well that the creep behavior of the rubber bearing shown in Figure 7-55 is no longer present, and that the time constant of the system has reduced significantly from an order of seconds to an order of milliseconds.

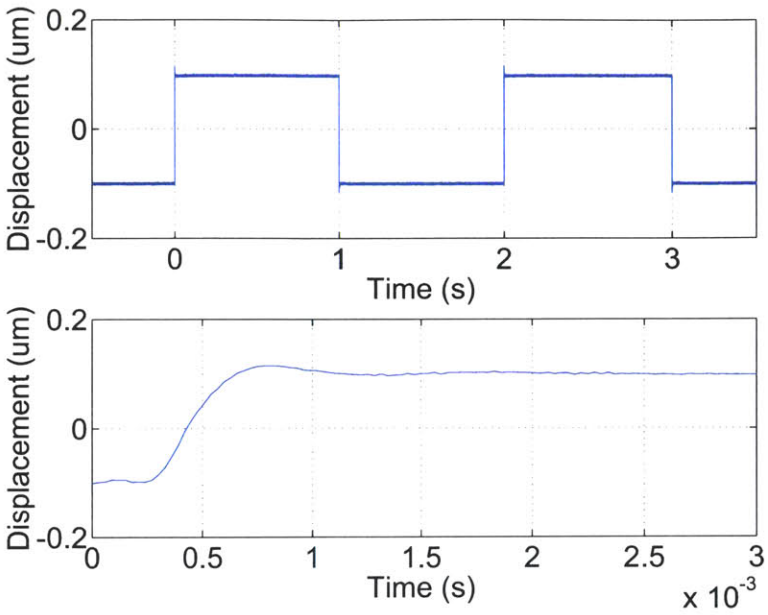

Figure 7-67: FTS small step (0.20 μm) using the designed lead controller ($K_c = 27$).

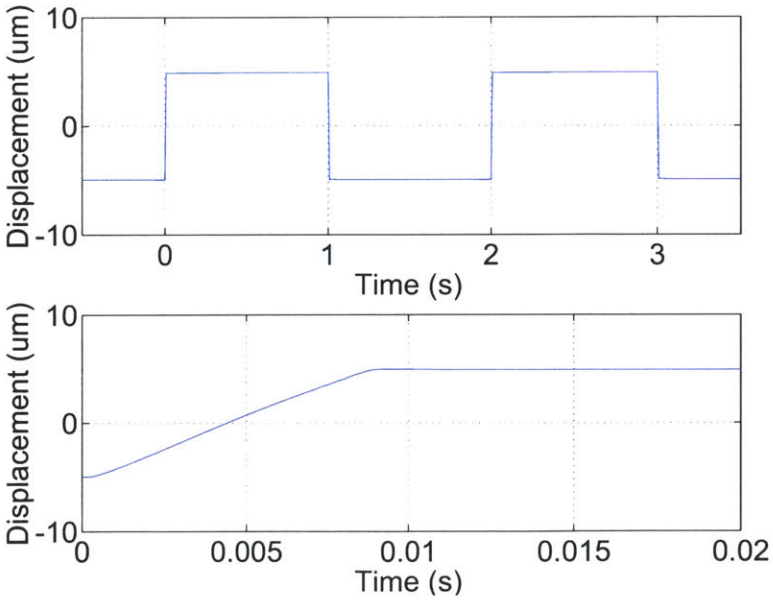

Figure 7-68: FTS large step (10 μm) using the designed lead controller ($K_c = 27$).

The large signal step response of the FTS is shown in Figure 7-68. The time

constant associated to this step response is larger than the small signal step response due to the saturation of the A/D converter and further limited by the power amplifier and power supplies current limit.

The measured closed loop tool tip DC stiffness was between 52 N/μm and 60 N/μm, with an average of 57 N/μm.

7.24 Comments

This chapter has shown an extensive design effort made in the design of a precision machine using rubber bearings. The tests of the actual machine have confirmed that the prediction of the static properties of the rubber bearings is somewhat accurate. This tests have also shown that the high frequency rubber bearing properties can be predicted within an order of magnitude.

The use of the collected data from the rubber compression and shear tests from Chapter 4 and 5 has been really useful in the design of the precision machine shown in this Chapter. Further experimentation is encouraged in order to get a better understanding of the high frequency properties of rubber bearings.

Chapter 8

Conclusions and Suggestions for Future Work

As part of our research we have designed and fabricated two machines, with the purpose of gaining better understanding of the properties of rubber bearings. The first machine is a test fixture, which served the purpose of testing rubber specimens in compression and shear. The second machine is a Rotary Fast Tool Servo that used laminate rubber-metal bearings.

8.1 Rubber Compression Test

The tests of the rubber specimens in compression have shown a fairly linear behavior of the compression stiffness within the tested strain of 0.013%. Experimental results show that the compression stiffness increases significantly with the shape factor S, with this increment proportional to the shape factor squared S^2. Also the results have shown that this increase of compression stiffness depends strongly on the adequate bonding of the load carrying surfaces. The ratio of the high to low frequency complex compression modulus E_{HF}/E_{LF} has shown to be between 7 and 9 for the tested samples. Samples of higher shape factors show lower E_{HF}/E_{LF}, since its behavior becomes more close to that of bulk modulus compression.

8.2 Rubber Shear Test

The tests of rubber specimens in shear have shown a linear behavior of the shear stiffness within the tested strain of 1.6%. Also the application of preload pressure increases the static and low frequency shear modulus G, and decreases the ratio of the high to low frequency complex shear modulus G_{HF}/G_{LF}. The measured G_{HF}/G_{LF} of the tested materials ranges from 30 to 240. The preferred rubber materials for rubber bearings, when trying to obtain higher displacements at high frequencies, are the ones with lower G_{HF}/G_{LF}. The loss factor calculated from the measured hysteresis loops have shown that materials with lower Shore hardness exhibit higher loss factor η than the ones with higher Shore hardness. The shear step response of the rubber specimens have a rapid elastic-type response within the order of 0.1 ms followed by a slow creep process lasting seconds. Variation in the Shore hardness has shown practically no effect on the shear step response of the tested specimens.

Fatigue tests performed on Silicone SH35A and Neoprene SH80A have shown no signs of fatigue after being subject to $294 \cdot 10^6$ and $207 \cdot 10^6$ cycles, while subject to cyclic shear strains on the order of 0.16% and 0.004%, respectively. These fatigue tests show the tested rubber specimens possess remarkable fatigue life properties for the tested strains.

8.3 Rotary FTS using rubber bearings

Testing of the rotary fast tool servo shows an open loop maximum stroke of 45 μm pk-pk at 1 Hz and 0.8 μm pk-pk at 1 kHz. The predicted open loop maximum stroke was of 60 μm pk-pk at 1 Hz and 1.6 μm pk-pk at 1 kHz. The maximum stroke prediction is within one order of magnitude of the experimental ones, being 30% off on the

case of the stroke at 1 Hz and 100% off for the stroke at 1 kHz. This is an acceptable prediction of performance for the first prototype of this type of machine using rubber bearings. But further testing of the rubber bearings with testing conditions closer to the operating conditions is suggested, to make more accurate predictions.

The closed loop bandwidth of the rotary fast tool servo obtained with a simple proportional controller is 970 Hz, which is close to the desired 1 kHz to 10 kHz bandwidth. The maximum strokes obtained when using the proportional controller are of 31 μm pk-pk at 1 Hz and 0.3 μm pk-pk at 800 Hz. Also the closed loop tool tip stiffness is around 70 N/μm, which is well within the required 20 N/μm for precision diamond turning [13].

The preload mechanism (collet) used to preload the rubber bearings of the rotary fast tool servo has proved in being effective. The assembly and alignment of the rubber bearings, collet and shaft, is an easy task due to the bearing assembler unit. The preload mechanism provides the necessary normal force in the rubber bearings to prevent slip. It also permits an easy adjustment of the preload force with the aid of the preload bolts and Belleville springs, which regulates the torsional stiffness of the torsional rubber bearings.

The rubber bearings have shown great potential as bearings for precision positioning systems. These bearings are a low cost and compact form alternative versus conventional flexure bearings. Flexure bearings provide a DC stiffness, while the rubber bearings have a rising with frequency complex stiffness, which may make it an unattractive option as a bearing for some engineers. But rubber bearings provide high damping, while flexure bearings have very low damping. When using flexure bearings additional damping elements are often needed to damp unwanted resonances. Another advantage of rubber bearings is that they permit an increase in the low frequency shear stiffness by applying higher preload compressive loads with the aid of a preload mechanism.

8.4 Suggestions for Future Work

A re-design of the current rubber test fixture is suggested as future work. It is suggested to re-design the device to obtain strains higher than 1% in shear and being able to drive at frequencies of at least 10 kHz. For that it is suggested to use the proper actuator and power amplifier that will permit higher force output. Also it is required to re-design the current bearing holder so as to obtain a stiffer connection with the machine top plate. Another option is to use the design of the FTS preload mechanism to test smaller laminate rubber bearings. The use of a displacement sensor with a higher bandwidth than the current capacitance sensor with 5 kHz bandwidth is recommended. Higher strains of the rubber bearings would also reduce the noise to signal ratio of the displacement sensor output.

It is suggested as well that for the design of any future precision positioning system using rubber laminate bearings, that more adequate information related to the performance of the rubber bearings be collected. For this the testing conditions of the rubber bearings must be as similar as possible to the operating conditions.

The design of a linear positioning system using rubber bearings is suggested. The rubber bearings can provide with the adequate topology the necessary lateral and torsional stiffness and be compliant in the desired longitudinal direction of motion.

Appendix A

Matlab codes

A.1 Code for calculating the loss factor of hysteresis loops

```
function [D,U,loss] = hystdu(xv,fv,ds)

%Calculates the dissipated energy per cycle D, the strain energy U, and loss factor

[xmin,nxmin]=min(xv); [xmax,nxmax]=max(xv); ntm=size(xv);
nt=ntm(1,2);

%U=0.5*fv(nxmax)*xmax %This is the usual approach which I didn't take for
%not been applicable for all cases

UV=abs(fv.*xv./2); [U,nUmax]=max(UV); xv(nUmax); fv(nUmax);

D=0;D1=0;D2=0;D3=0;

if nxmin<nxmax
```

```
    for n = nxmin:ds:(nxmax-ds),
        D1=D1+(fv(n)+fv(n+ds))/2*abs(xv(n+ds)-xv(n));
    end
        D1=D1+(fv(n+ds)+fv(nxmax))/2*abs(xv(nxmax)-xv(n+ds));
    if (nxmin~=1)&((1+ds)>=(nxmin-ds))
        for n = 1:ds:(nxmin-ds),
            D2=D2+(fv(n)+fv(n+ds))/2*(abs(xv(n+ds)-xv(n)));
        end
            D2=D2+(fv(n+ds)+fv(nxmin))/2*(abs(xv(nxmin)-xv(n+ds)));
    end
    if (nxmin~=1)&((1+ds)<(nxmin-ds))
        D2=D2+(fv(1)+fv(nxmin))/2*(abs(xv(nxmin)-xv(1)));
    end
    if (nxmax~=size(xv))&((nxmax+ds)<=(nt-ds))
        for n = nxmax:ds:(nt-ds),
            D3=D3+(fv(n)+fv(n+ds))/2*(abs(xv(n+ds)-xv(n)));
        end
            D3=D3+(fv(n+ds)+fv(nt))/2*(abs(xv(nt)-xv(n+ds)));
    end
    if (nxmax~=size(xv))&((nxmax+ds)>(nt-ds))
        D3=D3+(fv(nxmax)+fv(nt))/2*(abs(xv(nt)-xv(nxmax)));
    end
end

if nxmin>nxmax
    for n = nxmax:ds:(nxmin-ds),
        D1=D1+(fv(n)+fv(n+ds))/2*abs(xv(n+ds)-xv(n));
    end
        D1=D1+(fv(n+ds)+fv(nxmin))/2*abs(xv(nxmin)-xv(n+ds));
    if (nxmax~=1)&((1+ds)<=(nxmax-ds))
```

```
        for n = 1:ds:(nxmax-ds),
            D2=D2+(fv(n)+fv(n+ds))/2*(abs(xv(n+ds)-xv(n)));
        end
            D2=D2+(fv(n+ds)+fv(nxmax))/2*(abs(xv(nxmax)-xv(n+ds)));
    end
    if (nxmax~=1)&((1+ds)>(nxmax-ds))
        D2=D2+(fv(1)+fv(nxmax))/2*(abs(xv(nxmax)-xv(1)));
    end
    if (nxmin~=size(xv))&((nxmin+ds)<=(nt-ds))
        for n = nxmin:ds:(nt-ds),
            D3=D3+(fv(n)+fv(n+ds))/2*(abs(xv(n+ds)-xv(n)));
        end
            D3=D3+(fv(n+ds)+fv(nt))/2*(abs(xv(nt)-xv(n+ds)));
    end
    if (nxmin~=size(xv))&((nxmin+ds)>(nt-ds))
        D3=D3+(fv(nxmin)+fv(nt))/2*(abs(xv(nt)-xv(nxmin)));
    end
end

D1; D2; D3;

D=abs(D1)+abs(D2)+abs(D3);

loss=D/(2*pi*U);
```

A.2 Code for calculating in real-time the complex shear stiffness magnitude and phase of a tested sample during fatigue testing

```
function [FR,my_data] = fs_1104(A,f,sett,dts)
% function [FR] = fs_1104(A,f,sett,dts)
% ---------------------(Aug 27, 2004)---------------------
% % A : Sine wave amplitude (Voltage input to amplifier)
% f : frequency tested (Hz)
% sett : Settling time (min)
% dts : Time interval to take samples (min)

%-------------------------------------------------------------------------
% OUTPUTs: The output is a (3 x 1) vector.
%    Row 1:  time (min)
%    Row 2:  GAIN, as the ratio of channel2/channel1
%    Row 3:  PHASE, in degrees
%-------------------------------------------------------------------------

%clear all;

%Initializing board
mlib('SelectBoard','ds1104');
%mlib('StartDSP');

%Starting sine wave and clock
[amp_freq_start]=mlib('GetTrcVar',...
        {'Model Root/Fatigue Sample/Swept\nSine/Amplitude';...
```

```
        'Model Root/Fatigue Sample/Swept\nSine/Frequency';
        'Model Root/Fatigue Sample/Start/Value'});

mlib('Write', amp_freq_start, 'Data', {A;f;1});

%Defining force and displacement variables to trace
 y_addr=mlib('GetTrcVar',...
            {'Model Root/Fatigue Sample/channel1/Out1';...
                'Model Root/Fatigue Sample/channel2/Out1';...
                'Model Root/Fatigue Sample/Swept\nSine/Out1'});

%Tracking time
time=mlib('GetTrcVar',...
        {'Model Root/Fatigue Sample/Integrator/Out1'});

%Defining the number of samples
samp_per=mlib('GetTrcVar',...
            {'Task Info/Timer Task 1/sampleTime'}); % KAL 3/13/02
dt=mlib('Read',samp_per)
T=1/f; %Wave period
NC=2; %Number of cycles
st=NC*T; Nsamples=floor(st/dt);

time_trigger=sett*60; N=1;

ON=mlib('GetTrcVar',...
        {'Model Root/ON/Value'});

mlib('CaptureState')
```

```
while mlib('Read',time)<(sett*60), end

while mlib('Read',ON)==1,

    while mlib('Read',time)<time_trigger, end

    mlib('Set', ...
                'Downsampling', 1, ...
                'Delay', 0, ...
                'NumSamples', Nsamples);
            mlib('Set','Trigger', 'On',...
                'TriggerVariable', y_addr(3),...
                'TraceVars', y_addr,...
                'TriggerLevel', 0,...
                'TriggerEdge', 'rising');
            mlib('LockProgram');
            mlib('StartCapture');
            %while mlib('CaptureState')==or(0,2)
                %'wait'
                %end
            while mlib('CaptureState')~=0, end

            mlib('CaptureState')

            my_data= mlib('FetchData');

            force=my_data(1,1:Nsamples);
            disp=my_data(2,1:Nsamples);

            mlib('UnlockProgram');
```

```
F=fft(force);
D=fft(disp);

L=length(F);

Fk=F(2:(L/2+1));
[Fm,k]=max(abs(Fk))
k1=k+1;
Fm=F(k1);
f1=(k1-1)/(Nsamples*dt)
fv=2*Fm/Nsamples

Dk=D(2:(L/2+1));
[Dm,k]=max(abs(Dk))
k2=k+1;
Dm=D(k2);
f2=(k2-1)/(Nsamples*dt)
dv=2*Dm/Nsamples
xdc=D(1)/Nsamples

gain=abs(fv/dv)
phase=angle(fv/dv)
phasedeg=phase*180/pi

G(1,N)=gain;
P(1,N)=phasedeg;
XDC(1,N)=xdc;
tv(1,N)=dts*(N-1);
```

```
save G;
save P;
save XDC;
save tv;

time_trigger=time_trigger+dts*60;

N=N+1;

figure(1)
subplot(3,1,1);
plot(tv,G);
xlabel('Time (min)');
ylabel('Stifnness (N/um)');
title('Fatigue test');
subplot(3,1,2);
plot(tv,P);
xlabel('Time (min)');
ylabel('Phase (deg)');
subplot(3,1,3);
plot(tv,XDC);
xlabel('Time (min)');
ylabel('Disp DC (um)');

figure(2)
subplot(2,1,1);
plot(force);
xlabel('Sampling points');
ylabel('Force (N)');
title('Force and displacement measurements');
```

```
    subplot(2,1,2);
    plot(disp);
    xlabel('Sampling points');
    ylabel('Disp (um)');

    pause(dts*60-5);
end

mlib('Write', amp_freq_start, 'Data', {0;0;0});
'Fatigue analysis finished by user'
```

Appendix B

Optimization of Rubber Bearing and Shaft dimensions results

Data											Rubber bearing dimer				Stiffnesses at tool tip				Max Stroke				
Shaft diam1 d1 (mm)	Shaft diam2 d2 (mm)	tool radius rT (mm)	(rT-d/2) (mm)	height of tool holder hth (mm)	length from tool to bearing center Lb (mm)	e (mm)	Lx (mm)	length from tool to galvo LT (mm)	Shaft length Lshaft (mm)	Shaft length up to bearing center Lshaftb (mm)	B=d1 B (mm)	H (mm)	t (mm)	n	Rubber bearing kbrad (N/um)	Tool holder bending kthrad (N/um)	Shaft bending ksbrad (N/um)	tool tip stiffness (w/o torsion) krad (N/um)	DC xmax (umP)	@2kHz xmax (umP)		@10kHz xmax (umP)		fn (Hz)
12.0	12.0	11.0	5	5	13.89149	4	12	30.8	25.78	8.891488	12.0	9.8	0.77	1	29.48	358.40	304.08	25.00	15.18	0.42	Stiffness	0.42	Stiffness	10877
12.0	12.0	11.0	5	5	16.91681	4	12	36.8	31.83	11.91681	12.0	15.8	0.77	2	34.14	358.40	126.31	25.00	18.76	0.52	Stiffness	0.48	Inertia	9637
12.0	12.0	11.0	5	5	9	4	12																	
12.0	12.0	11.0	5	5	9	4	12																	
12.0	12.0	11.0	5	5	13.06576	4	20	37.1	32.13	8.065764	12.0	8.1	0.77	1	28.77	358.40	407.36	25.00	18.26	0.51	Stiffness	0.48	Inertia	9760
12.0	12.0	11.0	5	5	15.25464	4	20	41.5	36.51	10.25464	12.0	12.5	0.77	2	31.09	358.40	198.22	25.00	23.74	0.66	Stiffness	0.47	Inertia	8469
12.0	12.0	11.0	5	5	18.09409	4	20	47.2	42.19	13.09409	12.0	18.2	0.77	3	37.44	358.40	95.21	25.00	24.49	0.68	Stiffness	0.46	Inertia	8226
12.0	12.0	11.0	5	5	20.4262	4	20	51.9	46.85	15.4262	12.0	22.9	0.77	4	38.95	358.40	58.23	21.91	25.99	0.72	Stiffness	0.45	Inertia	7899
12.0	12.0	11.0	5	5	12.60368	4	30	46.2	41.21	7.603678	12.0	7.2	0.77	1	28.45	358.40	486.23	25.00	20.60	0.57	Stiffness	0.46	Inertia	8989
12.0	12.0	11.0	5	5	14.39738	4	30	49.8	44.79	9.397377	12.0	10.8	0.77	2	30.01	358.40	257.57	25.00	27.51	0.76	Stiffness	0.45	Inertia	7714
12.0	12.0	11.0	5	5	16.25795	4	30	53.5	48.52	11.25795	12.0	14.5	0.77	3	32.75	358.40	149.81	25.00	30.69	0.85	Stiffness	0.45	Inertia	7241
12.0	12.0	11.0	5	5	19.72707	4	30	60.5	55.45	14.72707	12.0	21.5	0.77	4	43.75	358.40	66.92	24.63	27.69	0.77	Stiffness	0.43	Inertia	7506
12.0	12.0	12.0	6	5	14.07697	4	12	31.2	26.15	9.076971	12.0	10.2	0.77	1	31.57	207.41	285.82	25.00	15.95	0.44	Stiffness	0.44	Stiffness	11071
12.0	12.0	12.0	6	5	17.54067	4	12	38.1	33.08	12.54067	12.0	17.1	0.77	2	38.53	207.41	108.38	25.00	18.97	0.53	Stiffness	0.52	Inertia	9979
12.0	12.0	12.0	6	5	20.65578	4	12	44.3	39.31	15.65578	12.0	23.3	0.77	3	41.27	207.41	55.70	21.28	20.85	0.58	Stiffness	0.51	Inertia	9376
12.0	12.0	12.0	6	5	9	4	12																	
12.0	12.0	12.0	6	5	13.20707	4	20	37.4	32.41	8.207073	12.0	8.4	0.77	1	30.68	207.41	386.68	25.00	19.25	0.53	Stiffness	0.53	Inertia	9921
12.0	12.0	12.0	6	5	15.56837	4	20	42.1	37.14	10.56837	12.0	13.1	0.77	2	33.72	207.41	181.09	25.00	24.66	0.69	Stiffness	0.51	Inertia	8665
12.0	12.0	12.0	6	5	19.61359	4	20	50.2	45.23	14.61359	12.0	21.2	0.77	3	46.78	207.41	68.49	24.51	22.90	0.64	Stiffness	0.50	Inertia	8823
12.0	12.0	12.0	6	5	9	4	20																	
12.0	12.0	12.0	6	5	12.72204	4	30	46.4	41.44	7.722042	12.0	7.4	0.77	1	30.28	207.41	464.21	25.00	21.76	0.60	Stiffness	0.50	Inertia	9131
12.0	12.0	12.0	6	5	14.62755	4	30	50.3	45.26	9.627555	12.0	11.3	0.77	2	32.25	207.41	239.53	25.00	28.79	0.80	Stiffness	0.50	Inertia	7868
12.0	12.0	12.0	6	5	16.74207	4	30	54.5	49.48	11.74207	12.0	15.5	0.77	3	36.23	207.41	132.03	25.00	31.39	0.87	Stiffness	0.49	Inertia	7462
12.0	12.0	12.0	6	5	19.88981	4	30	60.8	55.78	14.88981	12.0	21.8	0.77	4	44.66	207.41	64.75	23.44	29.75	0.83	Stiffness	0.47	Inertia	7557
12.0	12.0	13.0	7	5	13.43596	4	20	37.9	32.87	8.435963	12.0	8.9	0.77	1	33.86	130.61	356.05	25.00	19.78	0.55	Stiffness	0.55	Stiffness	10176
12.0	12.0	13.0	7	5	16.14569	4	20	43.3	38.29	11.14569	12.0	14.3	0.77	2	38.66	130.61	154.38	25.00	24.56	0.68	Stiffness	0.55	Inertia	9013
12.0	12.0	13.0	7	5	19.6748	4	20	50.3	45.35	14.6748	12.0	21.3	0.77	3	47.15	130.61	67.64	22.91	24.66	0.69	Stiffness	0.54	Inertia	8846
12.0	12.0	13.0	7	5	9	4	20																	
12.0	12.0	13.0	7	5	12.91168	4	30	46.8	41.82	7.911683	12.0	7.8	0.77	1	33.30	130.61	431.63	25.00	22.43	0.62	Stiffness	0.55	Inertia	9352
12.0	12.0	13.0	7	5	15.02133	4	30	51.0	46.04	10.02133	12.0	12.0	0.77	2	36.19	130.61	212.39	25.00	29.15	0.81	Stiffness	0.53	Inertia	8124
12.0	12.0	13.0	7	5	17.95837	4	30	56.9	51.92	12.95837	12.0	17.9	0.77	3	45.12	130.61	98.23	25.00	29.39	0.82	Stiffness	0.52	Inertia	7983
12.0	12.0	13.0	7	5	19.95889	4	30	60.9	55.92	14.95889	12.0	21.9	0.77	4	45.04	130.61	63.86	21.97	32.03	0.89	Stiffness	0.51	Inertia	7579
12.0	12.0	14.0	8	5	13.82243	4	20	38.6	33.64	8.822431	12.0	9.6	0.77	1	39.43	87.50	311.28	25.00	19.60	0.54	Stiffness	0.54	Stiffness	10590
12.0	12.0	14.0	8	5	17.78845	4	20	46.6	41.58	12.78845	12.0	17.6	0.77	2	53.23	87.50	102.20	25.00	21.51	0.60	Stiffness	0.59	Inertia	9918
12.0	12.0	14.0	8	5	9	4	20																	
12.0	12.0	14.0	8	5	9	4	20																	

Figure B-1:

Data											Rubber bearing dimer				Stiffnesses at tool tip				Max Stroke					
Shaft diam1 d1 (mm)	Shaft diam2 d2 (mm)	tool radius rT (mm)	(rT-d/2) (mm)	height of tool holder hth (mm)	length from tool to bearing center Lb (mm)	e (mm)	Lx (mm)	length from tool to galvo LT (mm)	Shaft length Lshaft (mm)	Shaft length up to bearing center Lshaftb (mm)	B=d1 B (mm)	H (mm)	t (mm)	n	Rubber bearing kbrad (N/um)	Tool holder bending kthrad (N/um)	Shaft bending ksbrad (N/um)	tool tip stiffness (w/o torsion) krad (N/um)	DC xmax (umP)	@2kHz xmax (umP)		@10kHz xmax (umP)		fn (Hz)
12.0	12.0	14.0	8	5	13.22495	4	30	47.4	42.45	8.224951	12.0	8.4	0.77	1	38.51	87.50	384.16	25.00	22.37	0.62	Stiffness	0.59	Inertia	9705
12.0	12.0	14.0	8	5	15.78368	4	30	52.6	47.57	10.78368	12.0	13.6	0.77	2	44.04	87.50	170.46	25.00	27.86	0.77	Stiffness	0.57	Inertia	8593
12.0	12.0	14.0	8	5	19.02854	4	30	59.1	54.06	14.02854	12.0	20.1	0.77	3	53.05	87.50	77.42	23.15	28.27	0.79	Stiffness	0.55	Inertia	8406
12.0	12.0	14.0	8	5	19.86	4	30	60.7	55.72	14.86	12.0	21.7	0.77	4	44.49	87.50	65.14	20.30	34.81	0.97	Stiffness	0.55	Inertia	7548
14.0	14.0	11.0	4	5	13.07433	4	12	29.1	24.15	8.074335	14.0	8.1	0.77	1	26.85	700.00	752.28	25.00	11.48	0.32	Stiffness	0.32	Stiffness	11946
14.0	14.0	11.0	4	5	14.94843	4	12	32.9	27.9	9.948434	14.0	11.9	0.77	2	27.71	700.00	402.20	25.00	15.72	0.44	Stiffness	0.44	Stiffness	10045
14.0	14.0	11.0	4	5	16.6796	4	12	36.4	31.36	11.6796	14.0	15.4	0.77	3	28.95	700.00	248.55	25.00	18.27	0.51	Stiffness	0.43	Inertia	9187
14.0	14.0	11.0	4	5	18.53559	4	12	40.1	35.07	13.53559	14.0	19.1	0.77	4	30.95	700.00	159.69	25.00	19.61	0.54	Stiffness	0.42	Inertia	8735
14.0	14.0	11.0	4	5	12.44432	4	20	35.9	30.89	7.444315	14.0	6.9	0.77	1	26.65	700.00	959.90	25.00	13.58	0.38	Stiffness	0.38	Stiffness	10677
14.0	14.0	11.0	4	5	13.97188	4	20	38.9	33.94	8.971881	14.0	9.9	0.77	2	27.21	700.00	548.34	25.00	18.81	0.52	Stiffness	0.42	Inertia	8960
14.0	14.0	11.0	4	5	15.32702	4	20	41.7	36.65	10.32702	14.0	12.7	0.77	3	27.94	700.00	359.57	25.00	22.17	0.62	Stiffness	0.41	Inertia	8166
14.0	14.0	11.0	4	5	16.67322	4	20	44.3	39.35	11.67322	14.0	15.3	0.77	4	28.94	700.00	248.96	25.00	24.38	0.68	Stiffness	0.40	Inertia	7707
14.0	14.0	11.0	4	5	12.08651	4	30	45.2	40.17	7.086505	14.0	6.2	0.77	1	26.54	700.00	1112.77	25.00	15.15	0.42	Stiffness	0.40	Inertia	9746
14.0	14.0	11.0	4	5	13.40605	4	30	47.8	42.81	8.40605	14.0	8.8	0.77	2	26.97	700.00	666.69	25.00	21.23	0.59	Stiffness	0.39	Inertia	8153
14.0	14.0	11.0	4	5	14.5422	4	30	50.1	45.08	9.542204	14.0	11.1	0.77	3	27.49	700.00	455.78	25.00	25.31	0.70	Stiffness	0.39	Inertia	7403
14.0	14.0	11.0	4	5	15.62909	4	30	52.3	47.26	10.62909	14.0	13.3	0.77	4	28.14	700.00	329.77	25.00	28.21	0.78	Stiffness	0.38	Inertia	6957
14.0	14.0	12.0	5	5	13.15387	4	12	29.3	24.31	8.15387	14.0	8.3	0.77	1	27.90	358.40	730.48	25.00	12.28	0.34	Stiffness	0.34	Stiffness	12053
14.0	14.0	12.0	5	5	15.08696	4	12	33.2	28.17	10.08696	14.0	12.2	0.77	2	28.89	358.40	385.85	25.00	16.76	0.47	Stiffness	0.47	Stiffness	10150
14.0	14.0	12.0	5	5	16.89945	4	12	36.8	31.8	11.89945	14.0	15.8	0.77	3	30.34	358.40	235.03	25.00	19.37	0.54	Stiffness	0.47	Inertia	9301
14.0	14.0	12.0	5	5	18.91212	4	12	40.8	35.82	13.91212	14.0	19.8	0.77	4	32.88	358.40	147.07	25.00	20.59	0.57	Stiffness	0.45	Inertia	8880
14.0	14.0	12.0	5	5	12.50932	4	20	36.0	31.02	7.509317	14.0	7.0	0.77	1	27.67	358.40	935.19	25.00	14.54	0.40	Stiffness	0.40	Stiffness	10772
14.0	14.0	12.0	5	5	14.07993	4	20	39.2	34.16	9.07993	14.0	10.2	0.77	2	28.31	358.40	529.00	25.00	20.08	0.56	Stiffness	0.46	Inertia	9049
14.0	14.0	12.0	5	5	15.4863	4	20	42.0	36.97	10.4863	14.0	13.0	0.77	3	29.16	358.40	343.43	25.00	23.59	0.66	Stiffness	0.45	Inertia	8257
14.0	14.0	12.0	5	5	16.90372	4	20	44.8	39.81	11.90372	14.0	15.8	0.77	4	30.35	358.40	234.78	25.00	25.82	0.72	Stiffness	0.44	Inertia	7808
14.0	14.0	12.0	5	5	12.14309	4	30	45.3	40.29	7.143092	14.0	6.3	0.77	1	27.56	358.40	1086.53	25.00	16.23	0.45	Stiffness	0.44	Inertia	9830
14.0	14.0	12.0	5	5	13.49687	4	30	48.0	42.99	8.496865	14.0	9.0	0.77	2	28.04	358.40	645.54	25.00	22.69	0.63	Stiffness	0.43	Inertia	8231
14.0	14.0	12.0	5	5	14.67061	4	30	50.3	45.34	9.670606	14.0	11.3	0.77	3	28.63	358.40	437.87	25.00	26.99	0.75	Stiffness	0.42	Inertia	7482
14.0	14.0	12.0	5	5	15.8036	4	30	52.6	47.61	10.8036	14.0	13.6	0.77	4	29.39	358.40	314.05	25.00	29.99	0.83	Stiffness	0.41	Inertia	7039
14.0	14.0	13.0	6	5	13.28284	4	12	29.6	24.57	8.282842	14.0	8.6	0.77	1	29.64	207.41	696.89	25.00	12.90	0.36	Stiffness	0.36	Stiffness	12225
14.0	14.0	13.0	6	5	15.31608	4	12	33.6	28.63	10.31608	14.0	12.6	0.77	2	30.86	207.41	360.71	25.00	17.50	0.49	Stiffness	0.49	Stiffness	10319
14.0	14.0	13.0	6	5	17.27735	4	12	37.6	32.55	12.27735	14.0	16.6	0.77	3	32.78	207.41	213.99	25.00	20.03	0.56	Stiffness	0.50	Inertia	9492
14.0	14.0	13.0	6	5	19.64732	4	12	42.3	37.29	14.64732	14.0	21.3	0.77	4	36.71	207.41	126.02	25.00	20.76	0.58	Stiffness	0.48	Inertia	9151
14.0	14.0	13.0	6	5	12.61431	4	20	36.2	31.23	7.614312	14.0	7.2	0.77	1	29.36	207.41	897.04	25.00	15.29	0.42	Stiffness	0.42	Stiffness	10923
14.0	14.0	13.0	6	5	14.25688	4	20	39.5	34.51	9.256883	14.0	10.5	0.77	2	30.14	207.41	499.24	25.00	21.02	0.58	Stiffness	0.49	Inertia	9193
14.0	14.0	13.0	6	5	15.7523	4	20	42.5	37.5	10.7523	14.0	13.5	0.77	3	31.21	207.41	318.57	25.00	24.55	0.68	Stiffness	0.48	Inertia	8408
14.0	14.0	13.0	6	5	17.30284	4	20	45.6	40.61	12.30284	14.0	16.6	0.77	4	32.81	207.41	212.66	25.00	26.62	0.74	Stiffness	0.47	Inertia	7979

Figure B-2:

Data											Rubber bearing dimer				Stiffnesses at tool tip				Max Stroke				
Shaft diam1 d1 (mm)	Shaft diam2 d2 (mm)	tool radius rT (mm)	(rT-d/2) (mm)	height of tool holder hth (mm)	length from tool to bearing center Lb (mm)	e (mm)	Lx (mm)	length from tool to galvo LT (mm)	Shaft length Lshaft (mm)	Shaft length up to bearing center Lshaftb (mm)	B=d1 B (mm)	H (mm)	t (mm)	n	Rubber bearing kbrad (N/um)	Tool holder bending kthrad (N/um)	Shaft bending ksbrad (N/um)	tool tip stiffness (w/o torsion) krad (N/um)	DC xmax (umP)	@2kHz xmax (umP)		@10kHz xmax (umP)		fn (Hz)
14.0	14.0	13.0	6	5	12.23428	4	30	45.5	40.47	7.234278	14.0	6.5	0.77	1	29.22	207.41	1045.96	25.00	17.09	0.47	Stiffness	0.47	Inertia	9965
14.0	14.0	13.0	6	5	13.64476	4	30	48.3	43.29	8.644764	14.0	9.3	0.77	2	29.81	207.41	612.98	25.00	23.80	0.66	Stiffness	0.46	Inertia	8356
14.0	14.0	13.0	6	5	14.88252	4	30	50.8	45.77	9.882521	14.0	11.8	0.77	3	30.54	207.41	410.30	25.00	28.18	0.78	Stiffness	0.45	Inertia	7608
14.0	14.0	13.0	6	5	16.09725	4	30	53.2	48.19	11.09725	14.0	14.2	0.77	4	31.52	207.41	289.77	25.00	31.15	0.87	Stiffness	0.45	Inertia	7174
14.0	14.0	14.0	7	5	13.48772	4	12	30.0	24.98	8.487717	14.0	9.0	0.77	1	32.47	130.61	647.63	25.00	13.26	0.37	Stiffness	0.37	Stiffness	12492
14.0	14.0	14.0	7	5	15.69366	4	12	34.4	29.39	10.69366	14.0	13.4	0.77	2	34.18	130.61	323.83	25.00	17.78	0.49	Stiffness	0.49	Stiffness	10590
14.0	14.0	14.0	7	5	17.95506	4	12	38.9	33.91	12.95506	14.0	17.9	0.77	3	37.24	130.61	182.13	25.00	19.94	0.55	Stiffness	0.53	Inertia	9820
14.0	14.0	14.0	7	5	22.15317	4	12	47.3	42.31	17.15317	14.0	26.3	0.77	4	50.09	130.61	78.46	24.77	18.10	0.50	Stiffness	0.50	Inertia	9979
14.0	14.0	14.0	7	5	12.78005	4	20	36.6	31.56	7.78005	14.0	7.6	0.77	1	32.10	130.61	840.92	25.00	15.74	0.44	Stiffness	0.44	Stiffness	11155
14.0	14.0	14.0	7	5	14.54298	4	20	40.1	35.09	9.54298	14.0	11.1	0.77	2	33.17	130.61	455.67	25.00	21.47	0.60	Stiffness	0.53	Inertia	9418
14.0	14.0	14.0	7	5	16.19908	4	20	43.4	38.4	11.19908	14.0	14.4	0.77	3	34.73	130.61	281.94	25.00	24.80	0.69	Stiffness	0.52	Inertia	8652
14.0	14.0	14.0	7	5	18.03141	4	20	47.1	42.06	13.03141	14.0	18.1	0.77	4	37.38	130.61	178.95	25.00	26.36	0.73	Stiffness	0.50	Inertia	8276
14.0	14.0	14.0	7	5	12.37762	4	30	45.8	40.76	7.377616	14.0	6.8	0.77	1	31.92	130.61	986.18	25.00	17.62	0.49	Stiffness	0.49	Stiffness	10173
14.0	14.0	14.0	7	5	13.88152	4	30	48.8	43.76	8.881522	14.0	9.8	0.77	2	32.71	130.61	565.25	25.00	24.38	0.68	Stiffness	0.50	Inertia	8551
14.0	14.0	14.0	7	5	15.23006	4	30	51.5	46.46	10.23006	14.0	12.5	0.77	3	33.74	130.61	369.89	25.00	28.66	0.80	Stiffness	0.49	Inertia	7810
14.0	14.0	14.0	7	5	16.59809	4	30	54.2	49.2	11.59809	14.0	15.2	0.77	4	35.21	130.61	253.83	25.00	31.33	0.87	Stiffness	0.48	Inertia	7397
14.0	14.0	15.0	8	5	13.82055	4	12	30.6	25.64	8.820549	14.0	9.6	0.77	1	37.26	87.50	577.05	25.00	13.23	0.37	Stiffness	0.37	Stiffness	12911
14.0	14.0	15.0	8	5	16.35566	4	12	35.7	30.71	11.35566	14.0	14.7	0.77	2	40.20	87.50	270.44	25.00	17.34	0.48	Stiffness	0.48	Stiffness	11041
14.0	14.0	15.0	8	5	19.55424	4	12	42.1	37.11	14.55424	14.0	21.1	0.77	3	48.11	87.50	128.45	25.00	18.12	0.50	Stiffness	0.50	Stiffness	10528
14.0	14.0	15.0	8	5	9	4	12																	
14.0	14.0	15.0	8	5	13.04614	4	20	37.1	32.09	8.046145	14.0	8.1	0.77	1	36.69	87.50	760.22	25.00	15.76	0.44	Stiffness	0.44	Stiffness	11516
14.0	14.0	15.0	8	5	15.02372	4	20	41.0	36.05	10.02372	14.0	12.0	0.77	2	38.42	87.50	393.20	25.00	21.17	0.59	Stiffness	0.56	Inertia	9781
14.0	14.0	15.0	8	5	17.01917	4	20	45.0	40.04	12.01917	14.0	16.0	0.77	3	41.34	87.50	228.08	25.00	23.85	0.66	Stiffness	0.55	Inertia	9074
14.0	14.0	15.0	8	5	19.95709	4	20	50.9	45.91	14.95709	14.0	21.9	0.77	4	49.70	87.50	118.35	25.00	23.28	0.65	Stiffness	0.52	Inertia	8988
14.0	14.0	15.0	8	5	13.04614	4	20	37.1	32.09	8.046145	14.0	8.1	0.77	1	36.69	87.50	760.22	25.00	15.76	0.44	Stiffness	0.44	Stiffness	11516
14.0	14.0	15.0	8	5	15.02372	4	20	41.0	36.05	10.02372	14.0	12.0	0.77	2	38.42	87.50	393.20	25.00	21.17	0.59	Stiffness	0.56	Inertia	9781
14.0	14.0	15.0	8	5	17.01917	4	20	45.0	40.04	12.01917	14.0	16.0	0.77	3	41.34	87.50	228.08	25.00	23.85	0.66	Stiffness	0.55	Inertia	9074
14.0	14.0	15.0	8	5	19.95709	4	20	50.9	45.91	14.95709	14.0	21.9	0.77	4	49.70	87.50	118.35	25.00	23.28	0.65	Stiffness	0.52	Inertia	8988
15.0	15.0	12.0	4.5	5	12.87036	4	12	28.7	23.74	7.870358	15.0	7.7	0.77	1	27.00	491.63	1070.46	25.00	10.72	0.30	Stiffness	0.30	Stiffness	12532
15.0	15.0	12.0	4.5	5	14.56102	4	12	32.1	27.12	9.56102	15.0	11.1	0.77	2	27.55	491.63	597.09	25.00	14.92	0.41	Stiffness	0.41	Stiffness	10435
15.0	15.0	12.0	4.5	5	16.04662	4	12	35.1	30.09	11.04662	15.0	14.1	0.77	3	28.26	491.63	387.14	25.00	17.66	0.49	Stiffness	0.44	Inertia	9447
15.0	15.0	12.0	4.5	5	17.50251	4	12	38.0	33.01	12.50251	15.0	17.0	0.77	4	29.22	491.63	267.03	25.00	19.51	0.54	Stiffness	0.43	Inertia	8859
15.0	15.0	12.0	4.5	5	12.28462	4	20	35.6	30.57	7.284623	15.0	6.6	0.77	1	26.86	491.63	1350.00	25.00	12.63	0.35	Stiffness	0.35	Stiffness	11145
15.0	15.0	12.0	4.5	5	13.68053	4	20	38.4	33.36	8.680528	15.0	9.4	0.77	2	27.24	491.63	797.84	25.00	17.72	0.49	Stiffness	0.42	Inertia	9279
15.0	15.0	12.0	4.5	5	14.87767	4	20	40.8	35.76	9.877669	15.0	11.8	0.77	3	27.69	491.63	541.49	25.00	21.17	0.59	Stiffness	0.41	Inertia	8393
15.0	15.0	12.0	4.5	5	16.01385	4	20	43.0	38.03	11.01385	15.0	14.0	0.77	4	28.24	491.63	390.60	25.00	23.65	0.66	Stiffness	0.41	Inertia	7856

Figure B-3:

Data											Rubber bearing dimer				Stiffnesses at tool tip				Max Stroke					
Shaft diam1 d1 (mm)	Shaft diam2 d2 (mm)	tool radius rT (mm)	(rT-d/2) (mm)	height of tool holder hth (mm)	length from tool to bearing center Lb (mm)	e (mm)	Lx (mm)	length from tool to galvo LT (mm)	Shaft length Lshaft (mm)	Shaft length up to bearing center Lshaftb (mm)	B=d1 B (mm)	H (mm)	t (mm)	n	Rubber bearing kbrad (N/um)	Tool holder bending kthrad (N/um)	Shaft bending ksbrad (N/um)	tool tip stiffness (w/o torsion) krad (N/um)	DC xmax (umP)	@2kHz xmax (umP)		@10kHz xmax (umP)		fn (Hz)
15.0	15.0	12.0	4.5	5	11.95148	4	30	44.9	39.9	6.951482	15.0	5.9	0.77	1	26.79	491.63	1553.54	25.00	14.05	0.39	Stiffness	0.39	Stiffness	10105
15.0	15.0	12.0	4.5	5	13.16775	4	30	47.3	42.34	8.167746	15.0	8.3	0.77	2	27.08	491.63	957.74	25.00	19.90	0.55	Stiffness	0.39	Inertia	8398
15.0	15.0	12.0	4.5	5	14.18773	4	30	49.4	44.38	9.187729	15.0	10.4	0.77	3	27.41	491.63	672.87	25.00	23.98	0.67	Stiffness	0.38	Inertia	7582
15.0	15.0	12.0	4.5	5	15.13385	4	30	51.3	46.27	10.13385	15.0	12.3	0.77	4	27.80	491.63	501.45	25.00	27.05	0.75	Stiffness	0.38	Inertia	7081
15.0	15.0	13.0	5.5	5	12.96169	4	12	28.9	23.92	7.961688	15.0	7.9	0.77	1	28.31	269.27	1034.05	25.00	11.34	0.32	Stiffness	0.32	Stiffness	12667
15.0	15.0	13.0	5.5	5	14.71176	4	12	32.4	27.42	9.711763	15.0	11.4	0.77	2	28.96	269.27	569.72	25.00	15.73	0.44	Stiffness	0.44	Stiffness	10559
15.0	15.0	13.0	5.5	5	16.26636	4	12	35.5	30.53	11.26636	15.0	14.5	0.77	3	29.81	269.27	364.93	25.00	18.55	0.52	Stiffness	0.47	Inertia	9572
15.0	15.0	13.0	5.5	5	17.8154	4	12	38.6	33.63	12.8154	15.0	17.6	0.77	4	31.00	269.27	247.95	25.00	20.39	0.57	Stiffness	0.46	Inertia	8993
15.0	15.0	13.0	5.5	5	12.3601	4	20	35.7	30.72	7.360096	15.0	6.7	0.77	1	28.15	269.27	1308.89	25.00	13.37	0.37	Stiffness	0.37	Stiffness	11264
15.0	15.0	13.0	5.5	5	13.80123	4	20	38.6	33.6	8.801226	15.0	9.6	0.77	2	28.59	269.27	765.47	25.00	18.72	0.52	Stiffness	0.46	Inertia	9387
15.0	15.0	13.0	5.5	5	15.04702	4	20	41.1	36.09	10.04702	15.0	12.1	0.77	3	29.12	269.27	514.57	25.00	22.29	0.62	Stiffness	0.45	Inertia	8500
15.0	15.0	13.0	5.5	5	16.241	4	20	43.5	38.48	11.241	15.0	14.5	0.77	4	29.79	269.27	367.40	25.00	24.82	0.69	Stiffness	0.44	Inertia	7966
15.0	15.0	13.0	5.5	5	12.01768	4	30	45.0	40.04	7.017677	15.0	6.0	0.77	1	28.07	269.27	1509.99	25.00	14.89	0.41	Stiffness	0.41	Stiffness	10211
15.0	15.0	13.0	5.5	5	13.2707	4	30	47.5	42.54	8.270705	15.0	8.5	0.77	2	28.41	269.27	922.42	25.00	21.04	0.58	Stiffness	0.42	Inertia	8493
15.0	15.0	13.0	5.5	5	14.32832	4	30	49.7	44.66	9.328318	15.0	10.7	0.77	3	28.79	269.27	642.90	25.00	25.30	0.70	Stiffness	0.41	Inertia	7674
15.0	15.0	13.0	5.5	5	15.31629	4	30	51.6	46.63	10.31629	15.0	12.6	0.77	4	29.25	269.27	475.32	25.00	28.45	0.79	Stiffness	0.41	Inertia	7174
15.0	15.0	14.0	6.5	5	13.10672	4	12	29.2	24.21	8.106724	15.0	8.2	0.77	1	30.44	163.13	979.53	25.00	11.78	0.33	Stiffness	0.33	Stiffness	12877
15.0	15.0	14.0	6.5	5	14.95501	4	12	32.9	27.91	9.955005	15.0	11.9	0.77	2	31.27	163.13	528.97	25.00	16.25	0.45	Stiffness	0.45	Stiffness	10755
15.0	15.0	14.0	6.5	5	16.62933	4	12	36.3	31.26	11.62933	15.0	15.3	0.77	3	32.41	163.13	331.81	25.00	19.03	0.53	Stiffness	0.50	Inertia	9773
15.0	15.0	14.0	6.5	5	18.35467	4	12	39.7	34.71	13.35467	15.0	18.7	0.77	4	34.12	163.13	219.11	25.00	20.69	0.57	Stiffness	0.49	Inertia	9216
15.0	15.0	14.0	6.5	5	12.47953	4	20	36.0	30.96	7.479532	15.0	7.0	0.77	1	30.24	163.13	1247.19	25.00	13.91	0.39	Stiffness	0.39	Stiffness	11449
15.0	15.0	14.0	6.5	5	13.99458	4	20	39.0	33.99	8.994576	15.0	10.0	0.77	2	30.79	163.13	717.16	25.00	19.38	0.54	Stiffness	0.49	Inertia	9556
15.0	15.0	14.0	6.5	5	15.32231	4	20	41.6	36.64	10.32231	15.0	12.6	0.77	3	31.48	163.13	474.49	25.00	22.96	0.64	Stiffness	0.48	Inertia	8669
15.0	15.0	14.0	6.5	5	16.61798	4	20	44.2	39.24	11.61798	15.0	15.2	0.77	4	32.40	163.13	332.78	25.00	25.41	0.71	Stiffness	0.47	Inertia	8142
15.0	15.0	14.0	6.5	5	12.12217	4	30	45.2	40.24	7.122166	15.0	6.2	0.77	1	30.14	163.13	1444.50	25.00	15.50	0.43	Stiffness	0.43	Stiffness	10377
15.0	15.0	14.0	6.5	5	13.43489	4	30	47.9	42.87	8.434892	15.0	8.9	0.77	2	30.56	163.13	869.59	25.00	21.82	0.61	Stiffness	0.45	Inertia	8643
15.0	15.0	14.0	6.5	5	14.55492	4	30	50.1	45.11	9.554924	15.0	11.1	0.77	3	31.06	163.13	598.24	25.00	26.13	0.73	Stiffness	0.44	Inertia	7820
15.0	15.0	14.0	6.5	5	15.61432	4	30	52.2	47.23	10.61432	15.0	13.2	0.77	4	31.67	163.13	436.39	25.00	29.26	0.81	Stiffness	0.44	Inertia	7323
15.0	15.0	15.0	7.5	5	13.33612	4	12	29.7	24.67	8.336116	15.0	8.7	0.77	1	33.93	106.19	900.87	25.00	11.96	0.33	Stiffness	0.33	Stiffness	13199
15.0	15.0	15.0	7.5	5	15.35112	4	12	33.7	28.7	10.35112	15.0	12.7	0.77	2	35.14	106.19	470.54	25.00	16.33	0.45	Stiffness	0.45	Stiffness	11062
15.0	15.0	15.0	7.5	5	17.24904	4	12	37.5	32.5	12.24904	15.0	16.5	0.77	3	36.95	106.19	283.95	25.00	18.85	0.52	Stiffness	0.52	Stiffness	10101
15.0	15.0	15.0	7.5	5	19.38039	4	12	41.8	36.76	14.38039	15.0	20.8	0.77	4	40.19	106.19	175.49	25.00	19.98	0.55	Stiffness	0.51	Inertia	9614
15.0	15.0	15.0	7.5	5	12.66734	4	20	36.3	31.33	7.667338	15.0	7.3	0.77	1	33.65	106.19	1157.77	25.00	14.14	0.39	Stiffness	0.39	Stiffness	11732
15.0	15.0	15.0	7.5	5	14.3051	4	20	39.6	34.61	9.305095	15.0	10.6	0.77	2	34.44	106.19	647.73	25.00	19.54	0.54	Stiffness	0.52	Inertia	9820
15.0	15.0	15.0	7.5	5	15.7767	4	20	42.6	37.55	10.7767	15.0	13.6	0.77	3	35.48	106.19	416.96	25.00	22.95	0.64	Stiffness	0.51	Inertia	8937
15.0	15.0	15.0	7.5	5	17.26761	4	20	45.5	40.54	12.26761	15.0	16.5	0.77	4	36.97	106.19	282.67	25.00	25.08	0.70	Stiffness	0.50	Inertia	8432

Figure B-4:

Data											Rubber bearing dimer				Stiffnesses at tool tip				Max Stroke					
Shaft diam1 d1 (mm)	Shaft diam2 d2 (mm)	tool radius rT (mm)	(rT-d/2) (mm)	height of tool holder hth (mm)	length from tool to bearing center Lb (mm)	e (mm)	Lx (mm)	length from tool to galvo LT (mm)	Shaft length Lshaft (mm)	Shaft length up to bearing center Lshaftb (mm)	B=d1 B (mm)	H (mm)	t (mm)	n	Rubber bearing kbrad (N/um)	Tool holder bending kthrad (N/um)	Shaft bending ksbrad (N/um)	tool tip stiffness (w/o torsion) krad (N/um)	DC xmax (umP)	@2kHz xmax (umP)		@10kHz xmax (umP)		fn (Hz)
15.0	15.0	**15.0**	7.5	**5**	12.28579	**4**	**30**	45.6	40.57	7.285794	15.0	**6.6**	**0.77**	**1**	33.51	106.19	1349.35	25.00	15.78	0.44	Stiffness	0.44	Stiffness	10630
15.0	15.0	**15.0**	7.5	**5**	13.69639	**4**	**30**	48.4	43.39	8.696386	15.0	**9.4**	**0.77**	**2**	34.10	106.19	793.49	25.00	22.08	0.61	Stiffness	0.48	Inertia	8873
15.0	15.0	**15.0**	7.5	**5**	14.92288	**4**	**30**	50.8	45.85	9.922878	15.0	**11.8**	**0.77**	**3**	34.83	106.19	534.12	25.00	26.26	0.73	Stiffness	0.47	Inertia	8049
15.0	15.0	**15.0**	7.5	**5**	16.11102	**4**	**30**	53.2	48.22	11.11102	15.0	**14.2**	**0.77**	**4**	35.77	106.19	380.45	25.00	29.16	0.81	Stiffness	0.46	Inertia	7561
15.0	15.0	**16.0**	8.5	**5**	13.71344	**4**	**12**	30.4	25.43	8.713443	15.0	**9.4**	**0.77**	**1**	39.96	72.95	788.83	25.00	11.73	0.33	Stiffness	0.33	Stiffness	13707
15.0	15.0	**16.0**	8.5	**5**	16.04261	**4**	**12**	35.1	30.09	11.04261	15.0	**14.1**	**0.77**	**2**	42.17	72.95	387.56	25.00	15.70	0.44	Stiffness	0.44	Stiffness	11568
15.0	15.0	**16.0**	8.5	**5**	18.47903	**4**	**12**	40.0	34.96	13.47903	15.0	**19.0**	**0.77**	**3**	46.30	72.95	213.10	25.00	17.50	0.49	Stiffness	0.49	Stiffness	10699
15.0	15.0	**16.0**	8.5	**5**	9	**4**	**12**																	
15.0	15.0	**16.0**	8.5	**5**	12.97294	**4**	**20**	36.9	31.95	7.972945	15.0	**7.9**	**0.77**	**1**	39.49	72.95	1029.67	25.00	13.92	0.39	Stiffness	0.39	Stiffness	12174
15.0	15.0	**16.0**	8.5	**5**	14.83097	**4**	**20**	40.7	35.66	9.830967	15.0	**11.7**	**0.77**	**2**	40.86	72.95	549.25	25.00	18.97	0.53	Stiffness	0.53	Stiffness	10243
15.0	15.0	**16.0**	8.5	**5**	16.59429	**4**	**20**	44.2	39.19	11.59429	15.0	**15.2**	**0.77**	**3**	42.91	72.95	334.83	25.00	21.84	0.61	Stiffness	0.53	Inertia	9389
15.0	15.0	**16.0**	8.5	**5**	18.59335	**4**	**20**	48.2	43.19	13.59335	15.0	**19.2**	**0.77**	**4**	46.56	72.95	207.77	25.00	23.06	0.64	Stiffness	0.52	Inertia	8976
15.0	15.0	**16.0**	8.5	**5**	12.55014	**4**	**30**	46.1	41.1	7.550141	15.0	**7.1**	**0.77**	**1**	39.27	72.95	1212.52	25.00	15.58	0.43	Stiffness	0.43	Stiffness	11022
15.0	15.0	**16.0**	8.5	**5**	14.13203	**4**	**30**	49.3	44.26	9.132034	15.0	**10.3**	**0.77**	**2**	40.27	72.95	685.26	25.00	21.55	0.60	Stiffness	0.51	Inertia	9240
15.0	15.0	**16.0**	8.5	**5**	15.5606	**4**	**30**	52.1	47.12	10.5606	15.0	**13.1**	**0.77**	**3**	41.61	72.95	443.09	25.00	25.29	0.70	Stiffness	0.50	Inertia	8425
15.0	15.0	**16.0**	8.5	**5**	17.02651	**4**	**30**	55.1	50.05	12.02651	15.0	**16.1**	**0.77**	**4**	43.56	72.95	300.01	25.00	27.56	0.77	Stiffness	0.49	Inertia	7971

Figure B-5:

Bibliography

[1] Anonymous. *Model 3800 OEM Gaging System User Manual.* ADE Corporation, 80 Wilson Way, Westwood, MA 02090, USA, revision e edition.

[2] Anonymous. *Model 6880 Galvanometer Optical Scanner Instruction Manual.* Cambridge Technology, INC., 109 Smith Place, Cambridge, MA 02138, USA, revision 0 edition.

[3] Anonymous. *Unbrako Engineering Guide.* Unbrako.

[4] Christian R. Brackbill. *Helicopter Rotor Aeroelastic Analysis using a refined Elastomeric Damper Model.* The Pennsylvania State University, 2000.

[5] E.A.R. Specialty composites. *Dynamic mechanical analysis (http://www.earsc.com/).*

[6] Theodore Baumeister III Eugene A. Avallone. *Mark's Standard Handbook for Mechanical Engineering (10th Edition).* McGraw-Hill, 1996.

[7] John D. Ferry. *Viscoelastic properties of polymers.* Wiley, 1980.

[8] P K Freakley. *Theory and Practice of Engineering with rubber.* Applied Science, 1978.

[9] Alan N. Gent. *Engineering with Rubber.* Hanser, 2001.

[10] Archie I. Higdon. *Mechanics of Materials.* John Wiley and Sons, 1985.

[11] David I. G. Jones. *Viscoelastic Vibration Damping.* Wiley, 1992.

[12] P. B. Lindley. *Engineering Design with Natural Rubber.* The Malaysian Rubber Producers' Research Association, 1970.

[13] Richard C. Montesanti. *High Bandwidth Rotary Fast Tool Servos and a Hybrid Rotary and Linear Electromagnetic Actuator.* PhD thesis, Massachusetts Institute of Technology, 2005.

[14] Ahid D. Nashif. *Vibration Damping.* Jon Wiley and Sons, 1985.

[15] Edward M. Petrie. *Handbook of Adhesives and Sealants.* McGraw-Hill, 2000.

[16] A.R. Payne P.W. Allen, P.B. Lindley. *Use of rubber in Engineering.* Maclaren and Sons London, 1996.

[17] Eugene I. Rivin. *Stiffness and Damping in Mechanical Design.* Marcel Dekker, 1999.

[18] David L. Trumper. *ASPE Tutorial.* 1999.

[19] R.G. Young, W.C.; Budynas. *Roark's Formulas for Stress and Strain (7th Edition).* McGraw-Hill, 2002.